Montanuniversität Leoben

Carbon-based nanoporous materials for hydrogen storage

MSc. Nikolaos Kostoglou

Doctorate thesis submitted to the Department of Physical Metallurgy and Materials Testing (Chair of Functional Materials and Materials Systems) of the Montanuniversität Leoben in partial fullfilment of the requirements of the degree of a Doktor der montanistischen Wissenschaften (Dr. mont.)

Leoben, November 2017

The current thesis was not funded by any kind of project within its course of three years, instead, was significantly supported by a worldwide network of collaborators, including scientific institutions and companies, in terms of materials availability and experimental measurements.

Statutory declaration

I declare in lieu of oath that the present thesis was created by myself independently and only using the literature cited.

Leoben, November 2017 Signature

Acknowledgments

This study would have not been feasible without the contribution of certain people from various institutions and companies worldwide. My deep and sincere gratitude goes to my mentor/supervisor Prof. Claus Rebholz (Department of Mechanical and Manufacturing Engineering, University of Cyprus, Nicosia, Cyprus), and my supervisor Prof. Christian Mitterer (Chair of Functional Materials and Materials Systems, Montanuniversität (MU) Leoben, Austria), for their proper guidance and endless support during the three years of my doctoral studies. Both had faith and confidence in me, offered drastic solutions on important issues, and I have benefited greatly from their advice.

I sincerely acknowledge the significant contribution of researchers, collaborators and friends from different universities and institutes in terms of materials availability and experimental studies. At first, I am truly grateful to Prof. Biljana Babic and Prof. Branko Matovic from the University of Belgrade in Serbia (Institute of Physics and Vinča Institute of Nuclear Sciences, respectively) for their constant support in this work by providing promising carbon-based materials and invaluable feedback. In addition, I am very obliged to Prof. Georgios Constantinides from the Cyprus University of Technology (Lemesos, Cyprus), Prof. Kyriaki Polychronopoulou from the Khalifa University of Science and Technology (KUST, Abu Dhabi, UAE) as well as Dr. Mark Baker and Dr. Steve Hinder from the University of Surrey (Guildford, UK) for providing important experimental data and knowledge related to advanced characterization methods. Furthermore, my doctoral work has been significantly supported by the Institute of Nanoscience and Nanotechnology of the National Center of Scientific Research (NCSR) ''Demokritos'' (Athens, Greece). More specifically, I am truly thankful to the research director of the HYSORB laboratory, Dr. Theodore Steriotis, for providing a constant and constructive feedback during the course of my doctoral studies and his Ph.D. student, Mr. Christos Tampaxis, for performing a great number of gas adsorption measurements. Referring to the same institute, I also express my gratitude to Dr. Athanassios Kontos, Dr. Konstantinos Giannakopoulos and Dr. Vasileios Tzitzios for all the structural characterization studies performed in their laboratories as well as the useful experimental data provided by their side. Sincere acknowledgments are given to Dr. Vladislav Ryzhkov from Fibrtec Inc. (Atlanta, USA) for the endless discussions on the interpretation of data derived from diffraction and spectroscopy methods and his very interesting ideas, as well as Mr. Ian Walters and Dr. Afshin Tarat from Perpetuus Carbon Technologies (Ammanford, UK) for providing a series of graphene-based materials

for our studies. Finally, I express my appreciation to the rest of the co-authors included in my papers that contributed to the completion of my work, including Mrs. Velislava Terziyska, Mr. Christian Koczwara, Dr. Christian Prehal and Prof. Oskar Paris from MU Leoben, Dr. Georgia Charalambopoulou, Dr. Aggeliki Papavasiliou, Dr. Maria Giannouri and Dr. Georgia Basina from NCSR Demokritos, as well as Prof. Charalabos Doumanidis, Dr. Yuanqing Li and Prof. Kin Liao from KUST.

On a personal level, I would like to thank my parents, Konstantinos and Evgenia, my sisters, Kyriaki and Sofia, and my girlfriend Stela, for their constant support and encouragement in every aspect of my life. I am aware that my parents make tremendous sacrifices to ensure that we achieve our goals and this is the reason why I dedicate the current work to them.

Nikolaos K. Kostoglou

Table of Contents

List of abbreviations and symbols

APS ..... Average Pore Size
APW ..... Average Pore Width
BDC ..... BenzeneDiCarboxylate
BET ..... Brunauer-Emmet-Teller
BJH ..... Barret-Joyner-Halenda
CFRP ..... Carbon Fiber Reinforced Plastic
CNT ..... Carbon NanoTube
FC ..... Fuel Cell
FLG ..... Few-Layer Graphene
GAI ..... Generalized Adsorption Isotherm
GO ..... Graphene Oxide
HHV ..... Higher Heating Value
ICE ..... Internal Combustion Engine
ISO ..... International Standardization Organization
IUPAC ..... International Union of Pure and Applied Chemistry
LHV ..... Lower Heating Value
LH_2 ..... Liquid Hydrogen
LN_2 ..... Liquid Nitrogen
MH ..... Metal Hydride
MOF ..... Metal-Organic Framework
MWCNT ..... Multi-Walled Carbon NanoTube
PEM ..... Proton Exchange Membrane
PSD ..... Pore Size Distribution
QSDFT ..... Quenched Solid Density Functional Theory
SA ..... Specific Area
SPV ..... Specific Pore Volume
STP ..... Standard Temperature Pressure
SWCNT ..... Single-Walled Carbon NanoTube
US DoE ..... United States Department of Energy

"Energy can be neither created nor destroyed, it can be transferred from one location to another and converted from one form to another"

1st Law of Thermodynamics

1. Introduction

1.1. The alternative of hydrogen energy

The efficient storage of energy combined with a minimum carbon footprint as well as the effective capture and conversion of unwanted greenhouse emissions are considered the major challenges towards a progressive, sustainable and environmental friendly society on a global scale [1]. Besides the classic route of storing energy by electrochemical means using batteries, supercapacitors and hybrid devices, energy can be also stored in pure chemical form using gaseous substances with high heating values (energy per mass content). In this respect, hydrogen (H_2) is considered the ideal carbon-free energy carrier for future stationary and mobile power applications as well as the most promising alternative to the combustion of finite, carbon-rich and environmental harmful fossil fuels, such as diesel and gasoline. H_2 is not characterized as an energy source because it cannot be found at a free-state in nature, but as a highly-dense carrier of chemical energy it needs to be produced by other sources (same as electricity) [2]. The most remarkable features that H_2 exhibits include: (a) abundancy in various chemical compounds, such as water (H_2O) and different forms of organic matter (hydrocarbons, biomass, etc.), (b) environmental friendliness, as its combustion produces only pure H_2O with almost no pollutants to the environment; only a small concentration of nitric oxides (NO_x) may be produced, (c) highly-efficient electrochemical combination with oxygen (O_2) in a fuel cell to produce electricity; efficiencies up to 60 % can be reached, while an ultimate efficiency of 90 % is possible if the waste heat from the fuel cell is captured [3], (d) greater energy per mass content than other fuels, as it exhibits the highest heating value of ~143 MJ/kg in ambient conditions; in comparison 1 kg of H_2 has the same energy content with ~3 kg of gasoline [2].

The transition to a worldwide energy network based on H_2 could resolve both the environmental and energy issues arising from the use of fossil fuels. Such a vision is widely known as *Hydrogen Economy* [4] and its principles are based on the operation of the water-H_2 cycle, as shown in Fig. 1. According to this closed cycle, H_2 is first generated from the electrolysis of H_2O (dissociation into H_2 and O_2) by applying a direct electric current. The necessary energy input for electrolysis should be produced only by renewable energy sources (solar, wind, geothermal, hydroelectric and waves) to minimize the carbon footprint. In a following stage, the O_2 produced from the electrolysis is released to the

atmosphere, while the produced H_2 could be stored in a molecular or atomic form using solid materials. The cycle is completed by using the stored H_2 as a fuel either in internal combustion engines (ICEs) or fuel cells (FCs) to produce mechanical work or electric power, respectively. For both cases, H_2 reacts with the atmospheric O_2 and emits only pure water to the environment. Through this concept, H_2O and H_2 can be exchanged renewably and indefinitely, with H_2O acting as a H_2 carrier and H_2 as an energy carrier.

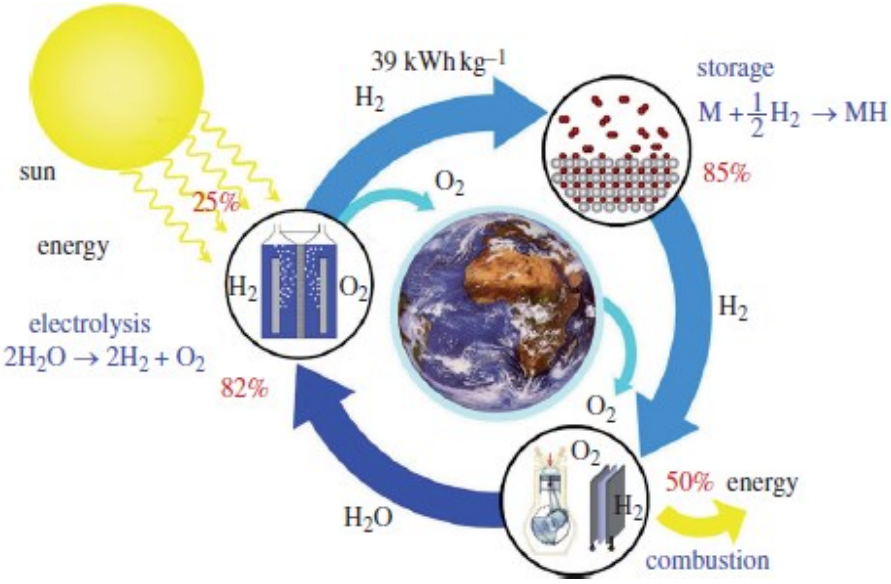

Fig. 1.1: The closed water-hydrogen cycle as a vision of the Hydrogen Economy [2].

The dynamic transition from a fossil fuel-based economy to a H_2 economy requires significant progress in all four fields of the H_2 technology, including production, storage, distribution and use. The industrial production of H_2 is mainly achieved by fossil fuels, while renewable sources are also used on a small scale. The worldwide H_2 production is estimated to more than 50 million metric tons/year with most of it consumed in petroleum refining and production of chemicals, such as ammonia (NH_3) and methanol (CH_3OH) [5]. Steam reforming of natural gas and gasification of coal are the most common methods of producing H_2 [4]. It is obvious that such non-renewable fossil fuel-based production routes will deteriorate even more the existing problems by reducing the available fossil fuel reserves and emitting more pollutants to the environment. Instead, H_2 production by clean and renewable means (e.g. electrolysis using solar energy) does not have a negative impact to the environment. Theoretically, electrolysis of water under ambient conditions requires a minimum energy of 39.7 kWh in order to produce 1 kg of H_2 [2]. Currently, large electrolyzers can dissociate water with more than 80 % efficiency, as they consume 47

kWh/kg of (H_2) by operating at 90 ^oC [6]. In any case, a further development of the renewable energy technologies is required in order to increase their energy conversion efficiency.

The field of distribution requires a reliable H_2-delivery infrastructure, which includes a pipeline network, transportation-supply vehicles and refueling stations. The storage process implies the reduction of the great volume that H_2 occupies as a gas. The conventional methods of H_2 compression and liquefaction cannot offer a convenient, safe, low-cost and efficient storage. In contrary, storing H_2 in solid materials with the ability to physically or chemically bind molecular H_2 is considered an attractive and promising alternative [7-10]. Finally, using H_2 in fuel cells is the most efficient and environmental friendly method of converting chemical energy into electricity, as efficiencies of up to ~60 % can be reached in comparison to a gasoline engine that produces mechanical work with much lower efficiencies of 25-30 %. However, the cost of the fuel cells is 100 times higher to that of a conventional gasoline engine due to the use of precious metal catalysts (e.g. platinum) and membranes [3]. In addition, H_2 can power internal combustion engines with a minor NO_x emission. Thus, the high specific energy of H_2 in combination with its compatibility with electricity makes it quite attractive for several applications, such as replacing conventional fuels in transportation, producing electricity in power stations and replacing batteries in portable electronic devices.

Each field of the H_2 technology exhibits important challenges and further advancements are required in its production, distribution and use with the aim to (a) reduce the cost of electrolysis and increase the efficiency of renewable energy technologies, (b) develop a global infrastructure for H_2 delivery and (c) reduce the cost and enhance the performance and durability of fuel cells. However, the field of H_2 storage still exhibits the most significant technical challenges, especially for on-board automotive applications. This is attributed to the close-to-absolute zero boiling point of H_2 (~20 K) and its extremely low density in gaseous state (~0.084 kg/m^3) under atmospheric conditions. More precisely, H_2 tends to occupy large volumes as a gas (i.e. 1 kg of H_2 occupies ~12 m^3), has the lowest energy per volume content compared to other fuels (i.e. 0.01 MJ/L for H_2 vs. 34.2 MJ/L for gasoline) and requires large amounts of energy for liquefaction (i.e. 30-35% of its energy content) [2]. The currently available technologies of compression using high-pressure cylinders (up to 700 bar) and liquefaction using cryogenic tanks (operating at 20 K) cannot be considered as viable storage solutions due to practical reasons related to the large

weight and volume of these systems, as well as other issues arising during their operation (e.g. large pressure-drops, evaporation losses, safety issues, etc.). Hence, the transition to a worldwide H_2-fueled community necessitates an innovative, convenient, efficient and safe H_2 storage method.

1.2. The unique properties of hydrogen

Hydrogen is the simplest, lightest and most abundant chemical element in nature. Its monatomic form (H) corresponds to the 75 % of the known mass in the universe; even the stars are composed of hydrogen in a plasma-state. The most common isotope is protium (^{1}H or H) which consists of a single proton in its nucleus. The other two isotopes, which are found rarely in nature, are deuterium (^{2}H or D) having a proton and a neutron and the unstable-radioactive tritium (^{3}H or T) with one proton and two neutrons. All three hydrogen isotopes form covalent diatomic molecules (H_2, D_2 and T_2) due to the single electron of their atoms. Hydrogen's physical and chemical properties are described in detail within the H_2-related modules provided by the United States Department of Energy (US DoE) [11-14]. At standard temperature and pressure (STP) conditions (i.e. 0 ^{o}C or 273 K and 100 kPa or 1 bar), it is a colorless, odorless, tasteless, non-toxic, non-metallic and highly flammable diatomic gas with a molecular formula H_2. Diatomic H_2 is rarely found in a free-state on earth because it tends to form mainly covalent bonds with other elements. Hence, it can be found in various chemical substances, as for example H_2O and organic compounds, such as carbohydrates (biomass) and fossil hydrocarbons (crude oil, natural gas and coal). It can also exhibit a metal-like behavior by forming intermetallic compounds or behaving as an anion (H^-) or cation (H^+) in ionic compounds. It demonstrates a very small volumetric density (i.e. 0.084 kg/m^3) in ambient conditions (i.e. 25 ^{o}C or 298 K and 100 kPa or 1 bar) and therefore it tends to occupy large volumes; i.e. 1 kg of H_2 under those conditions occupies a volume of ~12 m^3. In addition, it exhibits a low boiling point at -252.8 ^{o}C (or 20.3 K) and a melting point at -259 ^{o}C (or 14 K) under ~1.01 bar. This means that H_2 can exist as a liquid below 20.3 K and as a solid below 14 K under atmospheric pressure. The density of liquid H_2 at its boiling point (20.3 K) under 1 atm is 70.8 kg/m^3 (i.e. ~843 times higher than its gas form in ambient conditions). The point of temperature and pressure at which the three states of H_2 (gas, liquid and solid) coexist in a thermodynamic equilibrium is known as the *triplepoint* and can be found at -259.3 ^{o}C (or 13.8 K) and ~0.07 bar. The boiling point of H_2 can be increased up to a certain point by increasing the

applied pressure. Thus, the *critical point* of H_2, representing the temperature and pressure above which it can only exist as a gas, is located at -240.2 °C (or 32.9 K) and ~12.87 bar. The strong repulsion interactions between H_2 molecules are responsible for this low critical point [15]. Beyond that point, H_2 cannot maintain its liquid state even by further increasing the pressure (> 12.87 bar). As shown in the phase diagram of Fig. 1.2, H_2 can only exist as a liquid in a narrow temperature region between its triplepoint (13.8 K) and its critical point of (32.9 K).

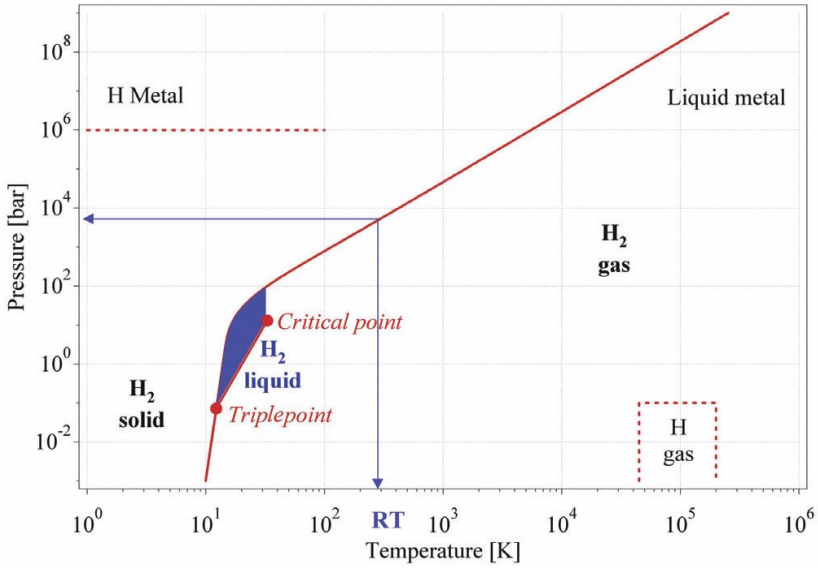

Fig. 1.2: Primitive phase diagram of hydrogen [15].

Regarding the specific energy content of H_2, it is characterized by a higher (HHV) and a lower heating value (LHV) of ~142 MJ/kg and ~120 MJ/kg, respectively, in ambient conditions. The first value represents the amount of heat produced upon complete combustion of H_2, while the latter results by subtracting the latent heat of vaporization of water vapor formed by the combustion [4]. Hydrogen's specific energy is the highest compared to all the other conventional fuels (see Fig. 1.3). Characteristically, based on the HHV, 1 kg of H_2 has the same energy content with 3.1 kg of gasoline or 2.6 kg of natural gas. However, in terms of volume, H_2 has a very low energy density of ~0.01 MJ/m^3 (or 10^{-5} MJ/L) under ambient conditions, a fact that is attributed to its small volumetric density and hence to its large occupied volume. In fact, the energy density of H_2 is the lowest among all conventional fuels (see Fig. 1.3). Based on the HHV, 1 L of H_2 has ~3400 times smaller energy content than 1 L of gasoline. A comparison between the gravimetric and volumetric energy densities of several type of fuels is shown in Fig. 1.3.

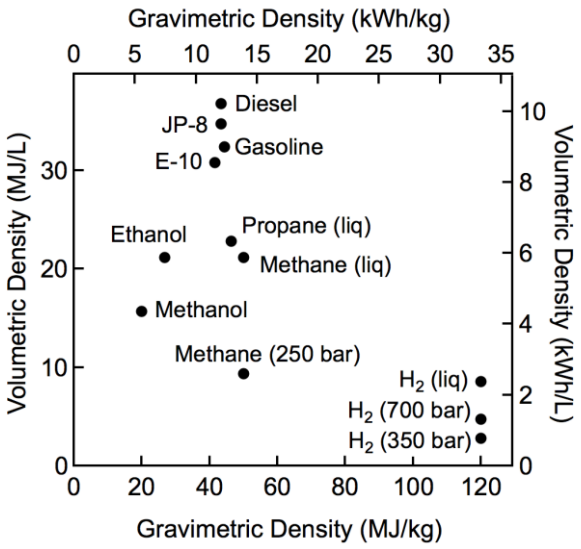

Fig. 1.3: Volumetric and gravimetric energy densities of several fuels based on their LHVs [16].

Hydrogen can be used as a fuel for the exploitation of its chemical energy either by employing modified ICEs and turbines or FCs. In the case of ICEs, H_2 reacts with the O_2 of the air and releases only heat and pure water. In some cases a small amount of NO_x may also be produced at quite high temperatures (~2000 ^oC). The combustion of H_2 at 25 ^oC is quite exothermic as it demonstrates a reaction enthalpy of - 286 kJ/mol and can be described by the following reaction:

$$2H_2(g) + O_2(g) \rightarrow 2H_2O(l) + [572\ kJ/mol]$$

In the case of FCs, the electrochemical combination between H_2 and O_2 produces electricity, H_2O and heat. The simplest FC type has a proton exchange membrane (PEM). The function of a PEM fuel cell, as shown in Fig. 1.4, is based on two electrochemical reactions, (a) oxidation of H_2 in the anode and (b) reduction of H_2 in the cathode, both due to the presence of a platinum (Pt) catalyst. Both reactions can be described as,

$$H_2 \rightarrow 2H^+ + 2e^- \text{ (oxidation)}$$

$$4H^+ + 4e^- + O_2 \rightarrow 2H_2O \text{ (reduction)}$$

During oxidation, molecular H_2 dissociates in the anode into protons (H^+) and electrons (e^-). The released e^- generate electric current by traveling through an external circuit to the cathode, while H^+ enter through the PEM and reach the cathode due to ionic conduction. During reduction, H^+, e^- and molecular O_2 react all together in the cathode and form H_2O molecules.

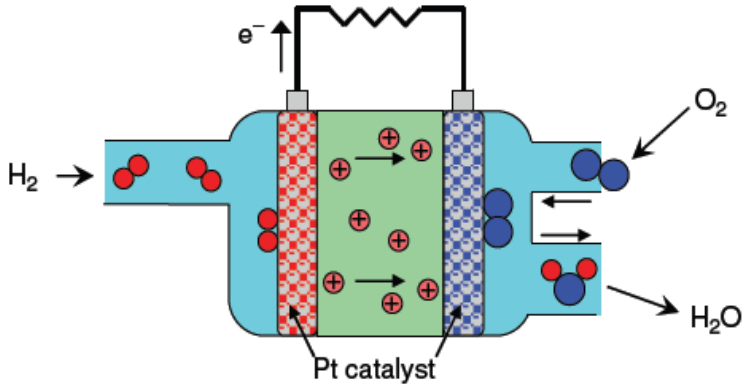

Fig. 1.4: The basic function of a PEM fuel cell using H_2 and O_2 [3].

H_2 is a highly flammable gas and can be burned in the presence of air in concentrations ranging from 4 to 75 % by volume; for comparison gasoline needs 1-7.5 % by volume. The thermal activation energy of H_2, defined as the minimum energy needed to ignite a stoichiometric H_2/O_2 mixture, is only 0.02 mJ. This value is quite small compared to those of other fuel mixtures (e.g. the gasoline/O_2 mixture requires 0.2 mJ). On the other side, the auto-ignition temperature of H_2, corresponding to the lowest temperature at which it can spontaneously ignite without any external ignition source, is as high as 585 ^oC. This temperature is the highest compared to all the other fuels (e.g. gasoline auto-ignites at 280 ^oC). Table 1.1 summarizes the most important physical properties of H_2.

Table 1.1: Selected properties of H_2 in ambient conditions (25 ^oC and 1 bar).

Atomic number	1
Atomic mass	1.00784 amu
Molecular mass	2.01568 amu
Volumetric density	0.08376 kg/m^3
Boiling point	-252.87 ^oC
Melting point	-259 ^oC
Triple point	-259.3^oC at 0.07 atm
Critical point	-240.2^oC at 12.7 atm
Auto-ignition point	585 ^oC
Higher heating value	141.86 MJ/kg
Lower heating value	119.93 MJ/kg
Energy density	10.05 MJ/ m^3
Minimum Activation Energy	0.02 mJ

“The secret of change is to focus all of your energy, not on fighting the old, but on building the new.”

Socrates, Classical Greek Philosopher (470-399 B.C.)

2. The challenge of hydrogen storage

2.1 Terminology and definitions

An increased research activity in the field of H_2 storage has been observed since the early 2000's, mainly due to the need for a practical storage method that could be applied in the residential, industrial, and more importantly, automotive sector. The use of H_2 as a fuel in internal combustion engine and fuel cell vehicles requires a reliable and effective storage medium. The storage of H_2 as a process implies the minimization of its great volume with a high efficiency and minimal losses. The ultimate challenge is the development of a safe, low-cost and lightweight on-board storage system with a rapid refuel rate that could store large amounts of H_2 (about 4-7 kg) [17,18]. The technical specifications of an ideal H_2 storage system should be comparable to those of a conventional fossil fuel-based storage technology to enable a similar driving performance.

There are certain concepts in the comparison of different H_2 storage technologies towards their efficiency and performance. The H_2 content of a storage system can be expressed on the basis of its mass or volume. The *gravimetric capacity* is defined as the amount of stored H_2 relative to the total mass of the system, expressed as wt.% or kg (H_2)/kg (system). The *volumetric capacity* is defined as the amount of stored H_2 relative to the total volume of the system, expressed as kg (H_2)/m^3 or kg (H_2)/L. Otherwise, the H_2 content can be expressed as energy content in terms of mass or volume. The *gravimetric energy density* is defined as the amount of stored energy relative to the mass of the system (kWh/kg), while the *volumetric energy density* is the amount of stored energy relative to the system's volume (kWh/L). Another important term is the *reversibility* of the storage system, which corresponds to the ability to switch between the H_2 charge and discharge processes. Therefore, the sorbed/desorbed H_2 amount between the lower and upper operating pressure is known as *reversible storage capacity*. The *cyclic stability* represents the ability of the storage system to retain its reversible capacity during its lifetime (charge/discharge cycle performance). According to their reversibility, H_2 storage systems can be distinguished into *reversible* and *non-reversible*. Reversible systems can release H_2 and in reverse store it without any external intervention, while non-reversible systems can only release H_2 and then must be re-charged again through a regeneration process. Thus, reversible systems are convenient for on-board applications, in contrast with the non-reversible ones that need to be regenerated off-board. More specifically, H_2 compression

and liquefaction systems, as well as metal hydrides and porous materials, are considered reversible technologies, while chemical storage methods are non-reversible. Finally, the *kinetics* represents the rate at which a storage system can take and release H_2. Alternatively, it can be defined as the time period required for H_2 charge and discharge between a minimum and a maximum operating pressure.

2.2 Technical targets and milestones

The US DoE and the Council for Automotive Research have established the FreedomCAR partnership [19] a program for developing energy efficient and environmentally friendly highway-transportation technologies. The technical targets for the year 2020 concerning the on-board H_2 storage systems in light-duty vehicles, as shown in Table 2.1, are summarized in the renewed version of the *Multi-Year Research, Development and Demonstration Plan (2015)*. The main target is the design of a lightweight storage system (5-13 kg) that could enable a conventional driving range of 500 km (or ~300 miles). The minimum H_2 gravimetric capacity is set to 5.5 wt.% or 0.055 kg (H_2)/kg (system) which is equivalent to 1.8 kWh/kg, while the minimum H_2 volumetric capacity is set to 0.04 kg (H_2)/L or 40 g (H_2)/L which is equivalent to 1.3 kWh/L. The system should have a 90 % *on-board efficiency*, which describes the energy efficiency for delivering H_2 from the storage system to the fuel cell and a 60 % *well-to-power plant efficiency*, which includes both the on-board and off-board energy efficiency (i.e. accounting also for H_2 production, delivery, compression, etc.).

Furthermore, the minimum and maximum delivery temperatures should be -40 and 85 ^{o}C, respectively, while the minimum and maximum delivery pressures from the storage system should be 5 and 12 bar, respectively. Additionally, a refueling time of 3.3 min is needed for 5 kg of H_2 which is equivalent to a charging/discharging rate of 1.5 kg (H_2)/min, as well as a minimum lifetime of 1500 charge/discharge cycles which is equivalent to 5000 operating hours or 150.000 miles (~240.000 km). Finally, the storage system should have a cost of 10 $/kWh or 333 $/kg ($H_2$). Besides the aforementioned targets, there are also the so called *ultimate targets* for H_2 storage systems. Meeting these targets will contribute to the faster commercialization and significant penetration of the H_2-fueled vehicles in the automotive market. The ultimate H_2 gravimetric capacity is set at 7.5 wt.% or 0.075 kg (H_2)/kg (system) that is equivalent to 2.5 kWh/kg, while the ultimate H_2 volumetric capacity is set at 0.07 kg (H_2)/L (system) or 70 g (H_2)/L (system) that is equivalent to 2.3

kWh/L. It should be noted that these targets are based on hydrogen's LHV which is 120 MJ/kg (or 33.3 kWh/kg). In addition, they refer to a complete H_2 storage system and not only to the storage material itself. A complete system may consist of a tank, storage material, valves, regulators, piping, mounting brackets, insulation, cooling system and other components.

Table 2.1: Technical targets for the on-board H_2 storage systems in light-duty vehicles set by the US DoE for the year 2020 [19].

Storage Parameter	Units	2020	Ultimate
System Gravimetric Capacity	kWh/kg	1.8	2.5
• Usable, specific-energy from H_2 (net useful energy/max system mass)[b]	(kg H_2/kg system)	(0.055)	(0.075)
System Volumetric Capacity	kWh/L	1.3	2.3
• Usable energy density from H_2 (net useful energy/max system volume)[b]	(kg H_2/L system)	(0.040)	(0.070)
Storage System Cost	$/kWh net	10	8
	($/kg $H_{2\ stored}$)	333	266
• Fuel cost[c]	$/gge at pump	2–4	2–4
Durability/Operability			
• Operating ambient temperature[d]	°C	-40/60 (sun)	-40/60 (sun)
• Min/max delivery temperature	°C	-40/85	-40/85
• Operational cycle life (1/4 tank to full)	Cycles	1,500	1,500
• Min delivery pressure from storage system	bar (abs)	5	3
• Max delivery pressure from storage system	bar (abs)	12	12
• Onboard efficiency[e]	%	90	90
• "Well" to power plant efficiency[e]	%	60	60
Charging/Discharging Rates			
• System fill time (5 kg)	min	3.3	2.5
	(kg H_2/min)	(1.5)	(2.0)
• Minimum full flow rate	(g/s)/kW	0.02	0.02
• Start time to full flow (20 °C)	s	5	5
• Start time to full flow (-20 °C)	s	15	15
• Transient response at operating temperature 10%–90% and 90%–0%	s	0.75	0.75
Fuel Quality (H_2 from storage)f	% H_2	SAE J2719 and ISO/PDTS 14687-2 (99.97% dry basis)	
Environmental Health & Safety			
• Permeation & leakage[g]	-	Meets or exceeds applicable standards, for example SAE J2579	
• Toxicity	-		
• Safety	-		
• Loss of usable H_2[h]	(g/h)/kg $H_{2\ stored}$	0.05	0.05

2.3 Technologies and methods

The existing H_2 storage methods can be classified on the basis of their (a) reversibility, (b) H_2 storage mechanism and (c) operating conditions. The reversibility describes the ability to switch between the H_2 charge and discharge processes and thus *reversible* or *non-reversible/irreversible* systems can be distinguished. The H_2 storage mechanism refers to the method of storing/releasing H_2 and is distinguished to *physical H_2 storage* via *compression* or *liquefaction*, *solid-state H_2 storage* in metal hydrides and porous materials by absorption or adsorption, respectively, and *chemical H_2 storage* via chemical reactions with other substances. The operating conditions refer to the necessary temperature (cryogenic, ambient or elevated) and pressure (atmospheric or higher) for H_2 storage.

On the one side, H_2 can be stored and fully released in a reversible manner by three methods, (a) as a gas in high-pressure cylinders, (b) as a liquid in cryogenic tanks and (c) by physical or chemical interaction with solid materials, a method known as *solid-state or materials-based H_2 storage* [7-10]. By combining the first two methods, H_2 can be stored in a cryo-compressed form as well. Nevertheless, the techniques of H_2 compression and liquefaction are considered only as temporary storage solutions mainly due to their large weight and volume as well as high operating cost. H_2 storage materials, however, seem to be more promising, as they minimize the great volume that H_2 occupies as a gas by binding it reversibly onto their porous surface or inside their bulk structure and possess a more convenient and safe method for transportation.

On the other side, irreversibility is encountered in *chemical H_2 storage* [20]. Materials known as *chemical hydrides* can generate H_2 through a chemical reaction with H_2O or alcohol-based solutions (i.e. hydrolysis or alcoholysis, respectively). Such hydrides can release large amounts of H_2 upon their oxidation since their structure possesses a high H-content. Characteristic examples are the sodium borohydride ($NaBH_4$), lithium hydride (LiH) or sodium hydride (NaH). Other techniques involve H_2 generation either by reacting such hydrides between each other (destabilization) or by heating solid compounds or organic liquids up to their decomposition temperature (thermolysis) [3]. Nevertheless, chemical H_2 storage is a one-way route, as H_2 can only be released by the material, while it requires a regeneration process under very high temperatures and pressures in order to be recharged again. Therefore, such an approach cannot have a viable character for on-board H_2-fueled applications as regeneration can only take place off-board. All the

available H_2 storage technologies in terms of reversibility, storage mechanism and operating conditions (temperature and pressure) are summarized in Table 2.2.

Table 2.2: Main characteristics of the available H_2 storage methods.

H_2 storage technologies	**Reversibility**	**H_2 storage mechanism**	**Operating conditions**	
			Temperature (K)	**Pressure (bar)**
*High-pressure gas cylinders	Fully reversible	Physical storage	298	350-700
*Cryogenic liquid tanks	Fully reversible	Physical storage	20	1
Conventional metal hydrides	Reversible upon heating	Absorption	298	0-100
Complex metal hydrides	Usually reversible	Absorption	373-673	0-100
Porous materials	Fully reversible	Adsorption	77	0-100
Chemical hydrides	Non-reversible	Chemical reaction	298	1

*Cryo-compression can be also included as a combination of compressed gas and cryogenic liquid H_2 storage.

2.3.1 Compressed hydrogen

In the method of compression, H_2 gas is pressurized from 350 up to 700 bar (or 35 to 70 MPa) inside high-pressure cylinders at room temperature (Fig. 2.1). The cylinders are made of carbon fiber reinforced plastic (CFRP) to withstand these pressures. The volumetric capacity of compressed H_2 can reach 17.6 g/L at 350 bar and 27.2 g/L at 700 bar [20]; i.e. it increases by increasing the pressure. Instead, the H_2 gravimetric capacity can reach 5.5 wt.% at 350 bar and 5.2 wt.% at 700 bar [20]; i.e. decreases by increasing the pressure as the walls of a 700 bar CFRP cylinder are thicker (larger mass for the system). Based on hydrogen's HHV (~142 MJ/kg), the equivalent volumetric energy density is 2.5 MJ/L (or 0.7 kWh/L) at 350 bar and 3.9 MJ/L (or 1.1 kWh/L) at 700 bar, while the gravimetric energy density is 7.8 MJ/kg (or 2.2 kWh/kg) at 350 bar and 7.4 MJ/kg (or 2.1

kWh/kg) at 700 bar. In comparison, gasoline has a volumetric capacity equivalent to 31.6 MJ/L (or 8.8 kWh/L); i.e. 8 times higher than compressed H_2 at 700 bar. The technology of H_2 compression is already applied in demonstration FCVs, but is generally considered a bulk storage method due to the significant space occupied inside a conventional vehicle and the large weight of the cylinders. In addition, high costs are involved in manufacturing a 700 bar vessel, as well as in compressing H_2 at 700 bar which requires almost 15 % of its energy content [17]. Other important issues arising during operation are the large pressure-drops as well as the H_2 embrittlement phenomena; i.e. the metallic parts become more brittle upon long-term exposure to H_2.

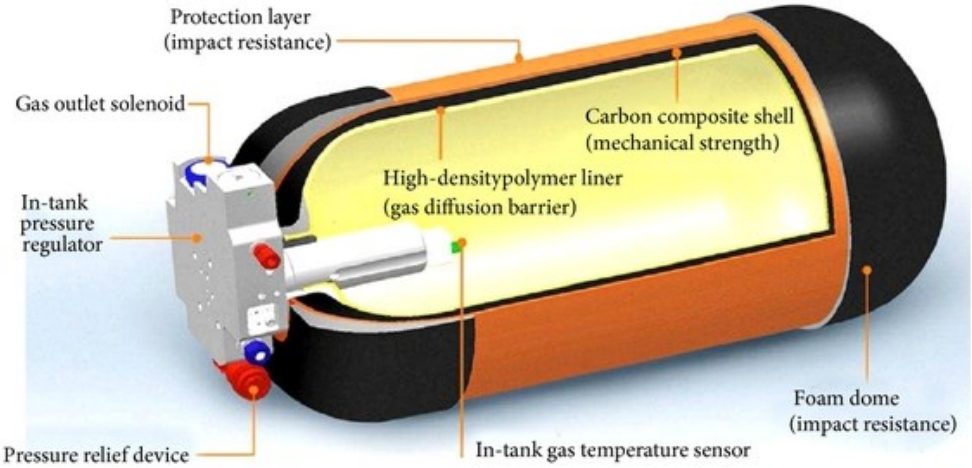

Fig. 2.1: Components of a high-pressure cylinder for compressed H_2 storage [21].

2.3.2 Liquefied hydrogen

In the method of liquefaction, H_2 is cooled down to 20.3 K (boiling point of H_2) under atmospheric pressure using cryogenic tanks to maintain its liquid state (Fig. 2.2). Liquid H_2 has a greater volumetric capacity than compressed H_2, reaching 70.8 g/L that is equivalent to 10 MJ/L (or 2.8 kWh/L) in terms of energy density [20]; i.e. 2.6 times higher than compressed H_2 at 700 bar. The gravimetric capacity, however, is dependent on the size of the tank. The most important issues associated with liquefaction are the non-viable requirements of the process in terms of energy and cost. More specifically, liquefaction requires 30-35 % of hydrogen's energy content [17], i.e. 10 kWh are needed to liquefy 1 kg of H_2. Furthermore, it is considered a bulk storage method because the tanks have a significant volume and weight (similar to compressed cylinders). Another major issue refers to potential losses due to evaporation of H_2 from the tank, usually described as a

boil-off mechanism [7]. As the heat enters into the system due to thermal conduction through the tank's components (e.g. pipes and cables) or thermal radiation from the environment, it causes a significant evaporation of the liquid H_2. In its turn, the evaporated H_2 gas causes an increase of pressure inside the tank and therefore some of the H_2 must be ventilated by opening a valve as soon as the pressure reaches a maximum level (usually at ~10 bar).

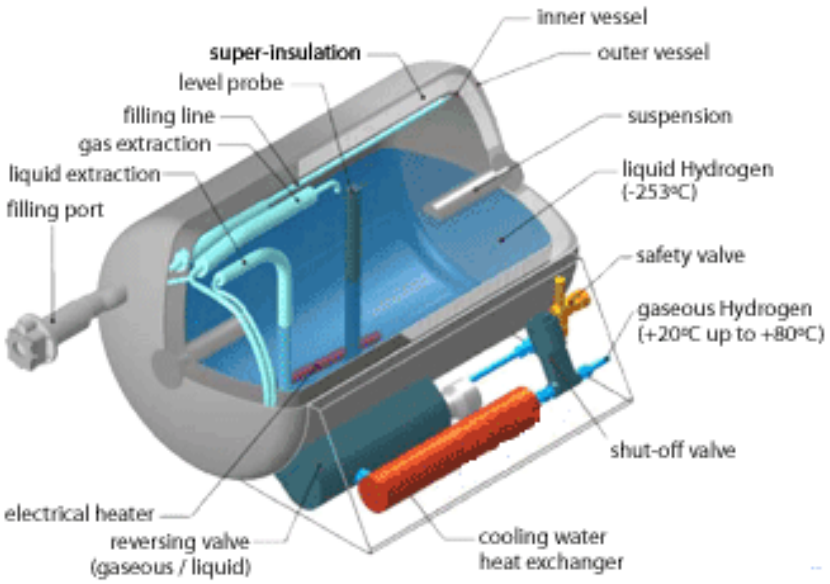

Fig. 2.2: Components of a cryogenic tank for liquid H_2 storage [22].

2.3.3 Cryo-compressed hydrogen

Both methods of compression and liquefaction can be combined in hybrid tanks of *cryo-compressed H_2*. The technology of cryo-compression may include (a) pressurized liquid H_2, (b) cooled-compressed H_2 gas or (c) two-phase systems of liquid-vapor H_2. On the one side, compressing liquid H_2 at ~240 bar (~24 MPa) increases the volumetric capacity up to 87 g/L [20], which is equivalent to 12.3 MJ/L (or 3.4kWh/L) in terms of energy density; i.e. additional 2.3 MJ/L (or 0.6 kWh/L) to the non-compressed liquefaction. On the other side, upon cooling the compressed H_2 gas using liquid N_2 at 77K, it becomes denser and more H_2 can be stored inside the tank; i.e. ~3 times more than the non-cooled compression. A novel technique also involves the incorporation of microporous adsorbents (carbon substrates) inside the tank in order to decrease further the storage pressure of H_2 gas. Therefore, the necessary temperatures for cryo-compression are higher than the temperature of liquid H_2 (i.e. 77 K instead of 20 K) and consequently less energy is required for liquefaction, while fewer evaporative losses are observed.

2.3.4 Solid-state hydrogen storage

There are several solid materials with the ability to store H_2 onto their porous surface or inside their crystal structure and reversibly release it by varying the pressure and temperature conditions. The requirements of this method seem to be more viable than compression and liquefaction. The associated materials can be classified primarily by their H_2 storage mechanism and the required operating temperatures into two main groups, the *metal hydrides* and the *porous adsorbents*. As indicated in previous studies [3,4,22], the ideal H_2 storage material should satisfy the following requirements in order to be commercialized on a larger scale:

- H_2 gravimetric and volumetric capacity greater than that of liquid H_2.
- Complete reversibility of the H_2 charge and release cycle.
- Operation under moderate pressures and ambient temperatures.
- Fast kinetics with minimum energy demands in H_2 charge and release.

Several materials have been found to satisfy certain of those requirements, but none has proven to satisfy them all. Nevertheless, abundance, low-cost, lightweight, reliable lifetime/performance, safety and non-toxicity are some additional factors that should be taken into consideration. The H_2 gravimetric capacities of various materials versus their operating temperatures are shown in Fig. 2.3, in comparison to the US DoE targets.

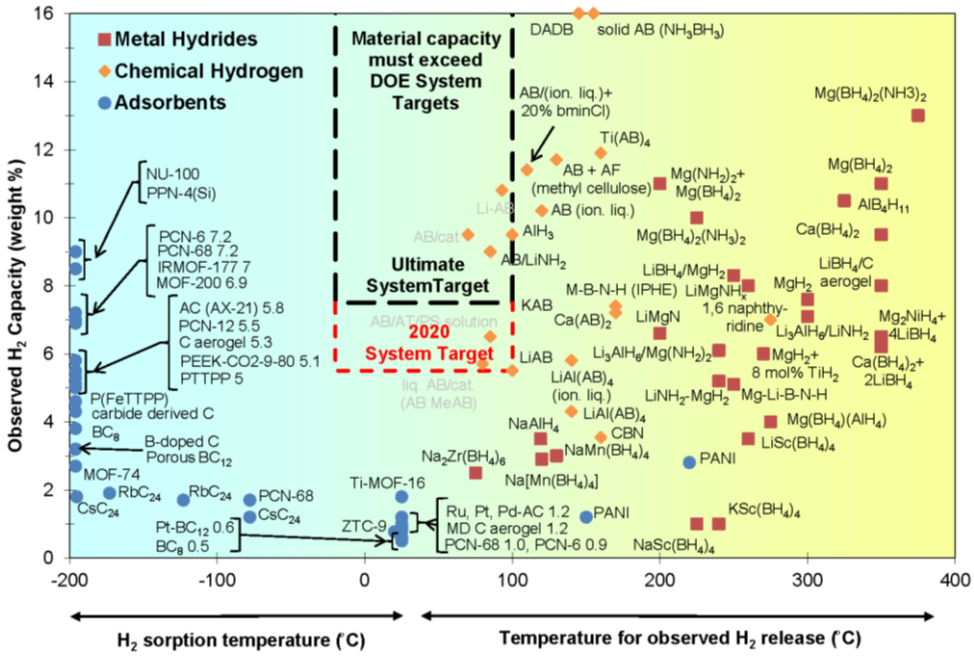

Fig. 2.3: Gravimetric capacity of the existing H_2 storage materials relative to their operating temperature and capacity targets described by the US DoE [23].

2.3.4.1 Metal hydrides

Metal hydrides (MHs) store atomic H inside their crystal structure by the mechanism of *absorption*. Molecular H_2 is attached onto the surface of the metal, where it dissociates into atomic H and then diffuses into the bulk of the metal by occupying interstitial sites of the crystal lattice [9]. Most MHs store H_2 exothermically by releasing heat upon absorption, while in reverse H_2 desorption is an endothermic process requiring a heat input, as shown in Fig. 2.4. There are two main categories of MHs, the *conventional* and the *complex* ones. The first retain their crystal structure upon H_2 absorption/desorption, while for the latter a crystal structure exists as long as the H atoms are bonded in the ionic compound (metal cation-complex anion) and then decomposes in two or more substances upon H_2 desorption [20].

Conventional MHs are distinguished into (a) those containing a single metal (MH_x) and (b) *intermetallic*s containing two or more metals ($A_xB_yH_z$) [24]. The most promising conventional MH is magnesium hydride (MgH_2) that demonstrates a H_2 gravimetric capacity of up to ~7.5 wt.% combined with a good reversibility, but it needs to be heated at high temperatures (> 300 ^oC) to release the stored H_2 under atmospheric pressure and also demonstrates slow kinetics. In contrary, some intermetallics operate at temperatures close to ambient, but they exhibit H_2 gravimetric capacities below 2 wt.% and have a high cost as they consist of heavy and rare earth metals (e.g. lanthanum (La)). Therefore, the advantages of storing H_2 in conventional MHs are the high volumetric capacities, good reversibility and indefinite storage without losses, while major drawbacks are related to low gravimetric capacities, heavy weight, high cost, increased decomposition temperatures to H_2 release and heat conductivity issues [25]. Complex MHs are distinguished into (a) alanates (Al-based) (b) amides or imides (N-based) and (c) borohydrides (B-based) [24]. The most promising is sodium alanate ($NaAlH_4$) that reversibly stores ~5.5 wt.% H_2 but requires high temperatures (i.e. 240-300^oC) to release it in a two-step decomposition process under atmospheric pressure; using a catalyst can lower significantly the desorption temperatures (i.e. 30-110^oC). Complex MHs show sufficient gravimetric and volumetric capacities but exhibit slow absorption/desorption kinetics, release H_2 in two or more decomposition stages under elevated temperatures, may produce toxic byproducts and usually require the presence of a catalyst upon absorption to be reversible [25].

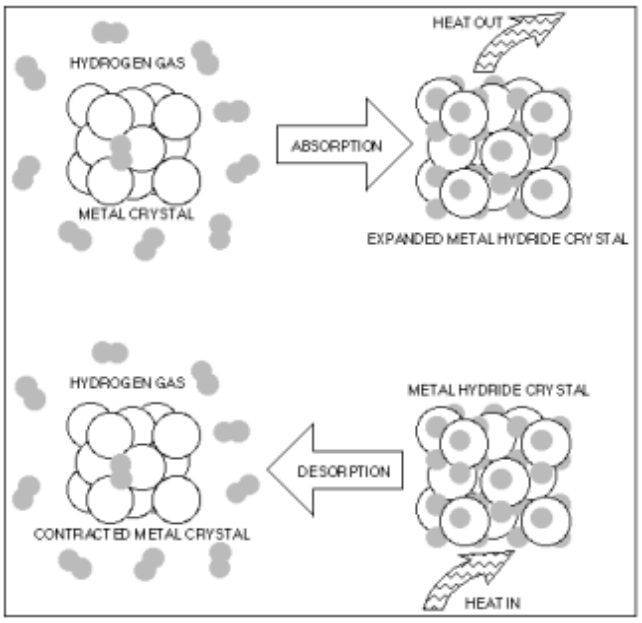

Fig. 2.4: Representation of H_2 absorption and desorption in a metal hydride crystal [26].

2.3.4.2 Porous adsorbents

Porous materials, the subject of the current thesis, can store H_2 onto their surface by the mechanism of *physical adsorption* or *physisorption*. Molecular H_2 is attached onto the external surface and fills the pores of the material by increasing the pressure (see Fig. 2.5). A great variety of adsorbents have been already investigated in the literature as potential H_2 storage mediums, including amorphous activated carbons, various carbon nanostructures (e.g. nanotubes, nanofibers, fullerenes, etc.) and zeolites, while novel materials currently draw attention, such as porous graphene or graphene oxide, metal-organic frameworks (MOFs) and polymers of intrinsic microporosity [8-10,20]. The physical adsorption and desorption of H_2 is fully reversible and characterized by fast kinetics due to the weak nature of interactions between the solid surface of the porous material and the molecular H_2 gas (i.e. van der Waals interactions) [15]. The structure of the porous surface (e.g. pore size distribution, average pore size, etc.) has an important impact on the adsorption mechanism. Specifically, microporous materials characterized by pore widths less than 2 nm are more desirable for H_2 storage as they demonstrate large specific areas and provide stronger binding sites for the H_2 molecules [9]. However, the cryogenic temperatures (i.e. less than 100 K) required to reach sufficient H_2 gravimetric capacities is the most important drawback of the physisorption method. Liquid nitrogen (LN_2) is usually employed to cool down the operating temperature to 77 K.

Even though cryogenic adsorbent-based systems operating at 77 K are more favorable in terms of energy and cost than cryogenic tanks of liquid H_2 operating at 20 K, the efficient H_2 storage at room temperature (298 K) still remains the ultimate challenge. However, the H_2 storage capacity of porous materials in ambient conditions is considered too low for practical applications, a fact mainly attributed to the weak quadrupole moment and poorly polarizable nature of the molecular H_2 gas [27]. Different strategies have been suggested in the literature during the past years to enhance the interactions between the H_2 gas and the solid surface and consequently increase the available H_2 storage capacity at 298 K, but none has been found to be of great significance. These include (a) high-specific area materials with optimized interlayer distance (e.g. graphene stacks, metal-organic frameworks, etc.) [28], (b) formation of complexes between molecular H_2 and various transition metals, known as *Kubas complexes* [29], (c) functionalization of porous surfaces with active heterogeneous groups [30] and (d) doping of carbon materials with catalytic nanosized metal additives (nanoparticles) [31]. The latter has been proposed to initiate *weak chemical adsorption* mechanisms and/or potential synergetic effects between the carbon support and the hosted nanoparticles, allegedly known as "spillover" effect; i.e. the nanoparticles act as catalysts for the dissociation of H_2 molecules into H atoms, which in turn migrate onto the carbon surface and form covalent bonds with the carbon atoms.

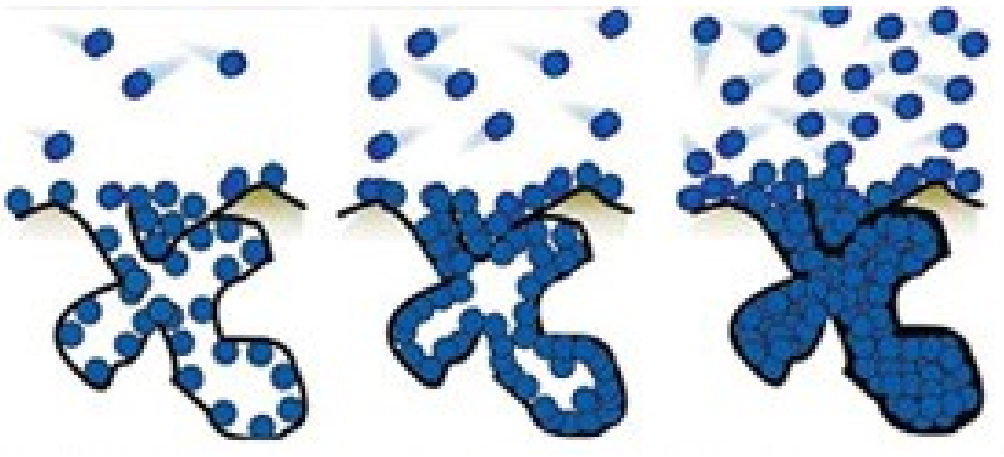

Fig. 2.5: Physical adsorption of gas molecules inside the pore cavities by gradually increasing the applied pressure (from left to right).

"Yes my friends, I believe that water will one day be employed as fuel, that hydrogen and oxygen which constitute it, used singly or together, will furnish an inexhaustible source of heat and light, of an intensity of which coal is not capable.... When the deposits of coal are exhausted we shall heat and warm ourselves with water. Water will be the coal of the future."

Jules Verne, The Mysterious Island (1874)

3. Hydrogen adsorption in porous materials

3.1 Terminologies and definitions

According to the International Union of Pure and Applied Chemistry (IUPAC) [32], the general term *adsorption* is defined as the enrichment of one or more components in an interfacial layer. The specific term of *H_2 adsorption* describes the phenomenon at which molecular H_2 is attracted onto or close to the surface of a solid material. In other words, the density of the H_2 gas increases as it gets closer to a solid surface. The inverse process in which the H_2 molecules are removed from the solid surface while the H_2 gas density decreases is known as *H_2 desorption*. The adsorbed H_2 gas is the *adsorbate*, the solid material that adsorbs H_2 is the *adsorbent* and the free H_2 gas which is capable of being adsorbed is known as the *adsorptive*. However, the general term *sorption* can be used to describe either the adsorption on a porous surface or the absorption inside the crystal structure of a metal hydride. There are two types of H_2 adsorption, (a) *physical adsorption* or *physisorption*, which occurs due to weak Van der Waals interactions between the molecular H_2 and the solid surface, and (b) *chemical adsorption* or *chemisorption* which involves the formation of strong covalent bonds due to dissociation of molecular H_2 onto the solid surface [9]. Physisorption is characteristic in porous materials where H_2 molecules are adsorbed weakly onto their external surface area and inside their pores, while chemisorption is encountered in metal hydrides or metal-doped adsorbents due to the fact that metal catalysts cause the dissociation of molecular H_2 into atomic H.

From a thermodynamic aspect, adsorption is an exothermic process that involves an interaction potential between the adsorbate and the adsorbent, while desorption is an endothermic one. The *heat or enthalpy of H_2 adsorption* describes the strength of interaction between the H_2 molecule and the solid surface. Physisorption mainly occurs at low temperatures (< 100 K) due to the weak nature of interactions and exhibits an adsorption enthalpy of 1-10 kJ/mol, while chemisorption is observed at higher temperatures (above ambient) due to the strong nature of interactions with an adsorption enthalpy of 50-100 kJ/mol [33]. The optimum interaction/binding energy for reversible and effective H_2 storage at room temperature and moderate pressures lies between physisorption and chemisorption (i.e. 10-50 kJ/mol), as illustrated in Fig. 3.1. The isosteric enthalpy of H_2 adsorption (Q_{st}) at a constant surface coverage (θ) can be estimated by using the Clausius-Clapeyron equation [34]. Hence,

$$Q_{st} = -R\left[\frac{\partial \ln(P)}{\partial(1/T)}\right]_{\theta} \qquad (3.1)$$

where R is the universal gas constant (i.e. 8.314 J mol^{-1} K^{-1}), P is the pressure and T is the temperature. To sum up, physisorption has the advantages of complete reversibility and fast adsorption/desorption kinetics and allows H_2 to retain its molecular form with a minimum activation energy, but the cryogenic temperatures needed to achieve significant H_2 storage capacities represents a major drawback. Chemisorption on the other hand results in larger amounts of stored H_2 but is not fully reversible and high temperatures are needed to release the stored H_2 gas. Therefore, the ideal H_2 adsorbent material should be microporous (pore widths < 2 nm), combine a high specific area and micropore volume as well as exhibit strong adsorbate-adsorbent interactions (between 10-50 kJ/mol) to satisfy the basic requirements for an effective H_2 storage under ambient conditions.

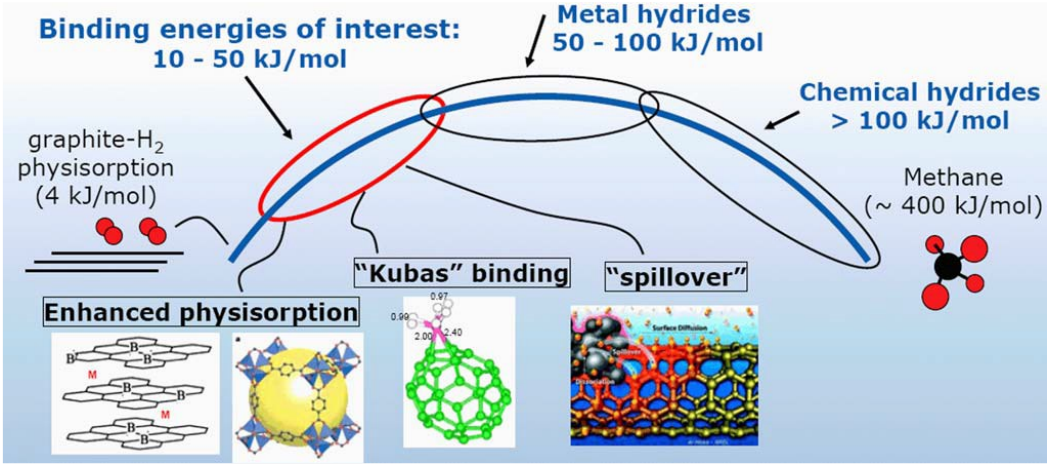

Fig. 3.1: The binding energies of the currently available H_2 storage material [33].

3.2 The basic principles of adsorption

On a molecular level, the physical adsorption of H_2 gas by a solid adsorbent is due to weak interaction forces between the H_2 molecules and the atoms or ions of the solid surface, known as *van der Waals forces*, arising from resonant fluctuations in charge distributions [15]. In fact, a H_2 molecule interacts with several atoms on the adsorbent's surface. These interactions include both attractive dispersion forces, known as *London dispersion forces*, and short-range repulsion forces. The dispersion forces arise due to the rapid fluctuation in the electron density within each individual atom, which induces an electrical moment in a near neighbor atom and leads to an attraction between the two atoms [35]. If the solid adsorbent is polar, which means that its atoms have a permanent electrical dipole moment,

then electrostatic forces are arising too, known as *Coulomb forces*. The potential energy (U_r) between two individual atoms separated by a distance (r) is known as Lennard-Jones potential [35] and its simplified form is given as following,

$$U(r) = -\frac{C}{r^6} + \frac{B}{r^{12}} \qquad (3.2)$$

where C is the dispersion constant associated with the dipole-dipole interactions (the negative sign implies attraction) and B is an empirical constant associated with the short-range repulsive forces due to the overlapping of the electron clouds (the positive sign implies repulsion). In the case of physisorption, the potential energy of the H_2 molecule shows a minimum value of 1 to 10 kJ/mol (or 0.01 to 0.1eV) at a distance equal to its molecular radius (r) [15]; i.e. half of the distance between the two atomic nuclei of the molecule. There is no energy barrier for the H_2 molecule to be adsorbed on the surface which leads to fast kinetics [37]. On the other hand, chemisorption is associated with an *activation energy*, which means that the attracted-to-the-surface gas molecules must overcome an energy barrier before becoming strongly bonded to the surface. The difference in the potential energy between physisorption and chemisorption as a function of the distance from the adsorbent's surface is shown in Fig. 3.2.

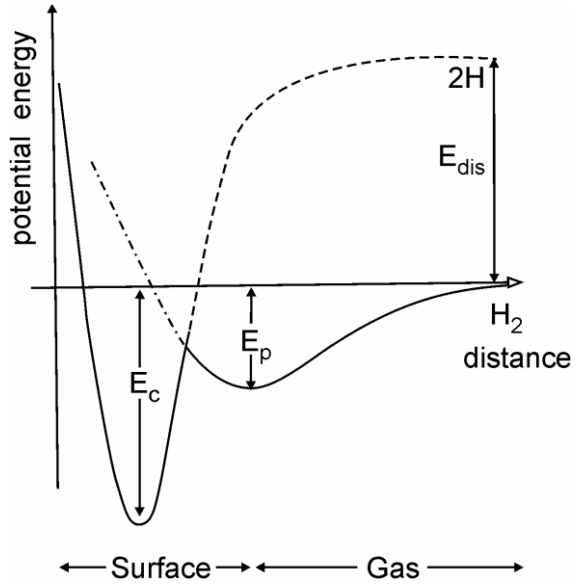

Fig. 3.2: Potential energy curves for physisorption (E_p) and chemisorption (E_c) of molecular H_2 as a function of the distance from the solid surface [37].

3.3 Classification of porous materials

The term *porous medium* describes a solid material that contains pores (i.e. voids, cavities, slits, channels, etc.) on its surface with a depth greater than their width. Many physical properties of the solid, such as density, thermal conductivity and mechanical strength are dependent on its pore structure. The term *porosity (ε)* describes the pore space inside a material and is defined as the ratio between the total pore volume (V_p) and the apparent volume (V) of the material. The opposite of porosity is *roughness* that describes the external non-porous surface of the material. The total *specific area* (SA) is defined as the accessible area of solid surface per unit mass of material given in m^2/g units and represents the sum of external surface area and internal pore surface area.

According to IUPAC [32], the pores of a material can be classified based on their size, shape and availability to an external fluid. Based on their size, pores can be distinguished in three main types, (a) *micropores* with widths less than 2 nm, (b) *mesopores* with widths between 2 and 50 nm and (c) *macropores* with a width of more than 50 nm. A further subdivision of the micropores leads to *super-micropores* with widths between 0.7 and 2 nm and the *ultra-micropores* with a width less than 0.7 nm. In general, pores with widths less than 100 nm are commonly referred as *nanopores*. The H_2 physisorption mechanism is enhanced in materials with microporous structure due to the fact that the attractive potential fields from the opposite pore walls can overlap each other creating stronger binding sites for the adsorbed H_2 molecules [35]. Besides stronger physisorption, microporous materials exhibit larger specific areas and micropore volumes and thus can store effectively much more H_2. Based on their shape, pores can be cylindrical (as (c) and (f) in Fig. 3.3), ink-bottle (as (b) in Fig. 3.3), funnel-shaped (as (d) in Fig. 3.3) or slit-shaped. Thus, the pore size, which is the distance between the two opposite walls of a pore, can be defined as width in the case of a slit-shaped pore or as a diameter in the case of a cylindrical pore. The opposite of a pore is the external rough surface (as (g) in Fig. 3.3). Based on the availability to an external fluid, pores can be either closed (as (a) in Fig. 3.3) (a) or opened (as (b), (c), (d), (e) and (f) Fig. 3.3). Characterization techniques involving the use of a fluid such as N_2 adsorption at 77 K can evaluate only the open porosity of a material and not the closed one. Many porous materials can exist as an assemblage of rigid macroscopic particles known as *agglomerates*, while other particles can be less rigid and more loosely packed known as *aggregates*.

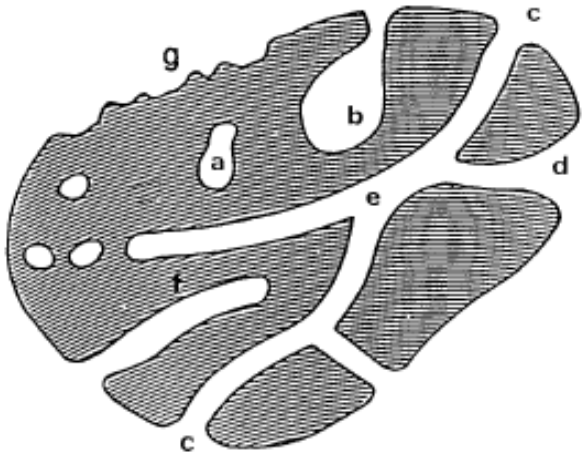

Fig. 3.3: Possible pore shapes in the cross-section of a porous material [40].

3.4 Physical adsorption mechanisms

There are four mechanisms of physical gas adsorption that can occur in a solid surface based on the geometrical characteristics of the pores and the operating temperature and pressure conditions, including (a) *micropore filling*, (b) *monolayer adsorption*, (c) *multilayer adsorption* and (d) *capillary condensation* [35], as seen in Fig. 3.4. At first, the micropores of a material (pore widths < 2 nm) are getting filled with gas molecules under vacuum pressures due to their enhanced interaction potential, a phenomenon known as *micropore filling.* By increasing the pressure, a single layer of gas molecules covers the rest of the internal pore surface (mesopores and macropores) and the external surface referring to *monolayer adsorption*. If the operating temperature is below the critical temperature of the employed gas, then the interactions between the gas molecules become more important and multiple layers of the adsorbate are formed along the surface, a process described as *multilayer adsorption*. Beyond multilayer formation, the adsorbed gas molecules can also be condensed to a liquid-like state inside the mesopores (pore widths between 2 and 50 nm) below the vapor pressure of the adsorbate, a phenomenon known as *capillary condensation*.

At temperatures above its critical temperature (i.e. 32.9 K), H_2 is considered as a supercritical fluid. In fact, the behavior of free H_2 at room temperature (i.e. 298 K) can be described on the basis of the van der Waals equation [15]:

$$P = \frac{n \cdot R \cdot T}{V - n \cdot b} - a \cdot \frac{n^2}{V^2} \qquad (3.3)$$

where P is the gas pressure, V is the volume, T is the absolute temperature, n is the mole number, R is the universal gas constant (i.e. 8.314 J mol^{-1} K^{-1}), a is the dipole interaction or repulsion constant (i.e. 2.476 × 10^{-2} m^6 Pa mol^{-2}) and b is the volume occupied by the H_2 molecule (i.e. 2.661 × 10^{-5} m^3 mol^{-1}).

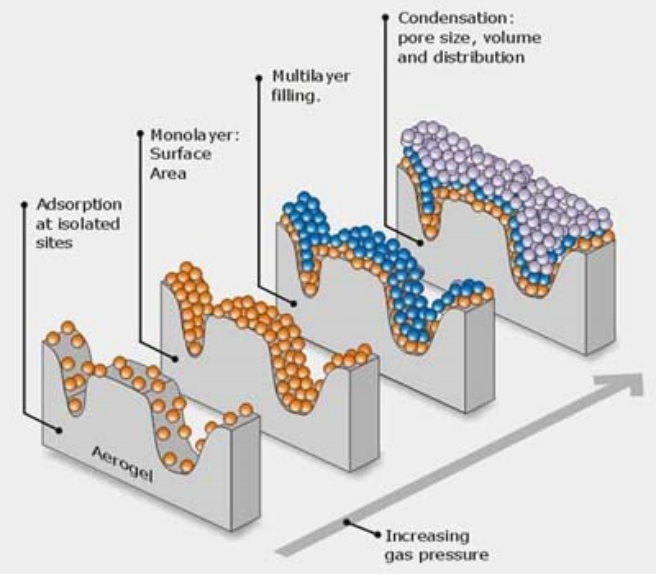

Fig. 3.4: Mechanisms of physical adsorption by increasing the pressure (below critical point) [42].

In case of H_2 adsorption at temperatures well above hydrogen's critical temperature (> 32.9 K), it is assumed that a thin film of adsorbed molecules is formed along the surface of the solid, known as *monolayer*, which has a thickness of a single H atom. If the temperature is equal or below the critical point of H_2 (i.e. ≤ 33 K), then the interactions between the H_2 molecules become more important due to potential liquid phase formation (on the basis of the applied pressure) and as a result the adsorption exceeds the monolayer coverage by forming multiple layers of the adsorbate, known as *multilayer*, which has a thickness of several H atoms. Therefore, a multilayer coverage or capillary condensation of H_2 in porous surfaces cannot be expected at temperatures well above its critical point, either cryogenic (77 K) or ambient (298 K). Instead, micropore filling and monolayer formation are the primary mechanisms involved during adsorption of supercritical H_2 gas. It is commonly referred that the physisorption of supercritical H_2 follows the Langmuir isotherm model [35] representing the adsorption of a monolayer onto the surface of a solid. The Langmuir equation correlates the surface coverage (θ) with the pressure (P):

$$\theta = \frac{b \cdot P}{1 + (b \cdot P)} \qquad (3.4)$$

where b is the adsorption efficient defined as:

$$b = K \cdot \exp\left(\frac{E}{R \cdot T}\right) \qquad (3.5)$$

There, K is an empirical parameter, E is the energy of adsorption, R is the universal gas constant (i.e. 8.314 J mol^{-1} K^{-1}) and T is the temperature. The Langmuir model is based on the assumptions that (a) each site on the surface can be occupied by only one adsorbate molecule, (b) the energy of adsorption (E) is equal for each site and (c) there are no interactions between adsorbate molecules. The linear form of the Langmuir equation can be extracted on the basis that the surface coverage (θ) is the ratio of the adsorbed amount (n) to the monolayer capacity (n_m). Thus, Eq. (3.4) becomes:

$$\frac{P}{n} = \frac{1}{n_m \cdot b} + \frac{P}{n_m} \qquad (3.6)$$

Besides the fact that physisorption strongly depends both on the nature of the adsorbate gas and the solid adsorbent, it is also proven, based on the Langmuir equation, that it is strongly depended by the operating conditions of temperature (T) and pressure (P). The amount of adsorbed gas is proportional to the pressure and inversely proportional to the temperature. Thus, the amount of adsorbed H_2 increases by increasing the pressure and decreasing the temperature as shown in Fig. 3.5. For this reason, the ultimate goal of a high H_2 uptake under low pressures and ambient temperatures is quite a challenge.

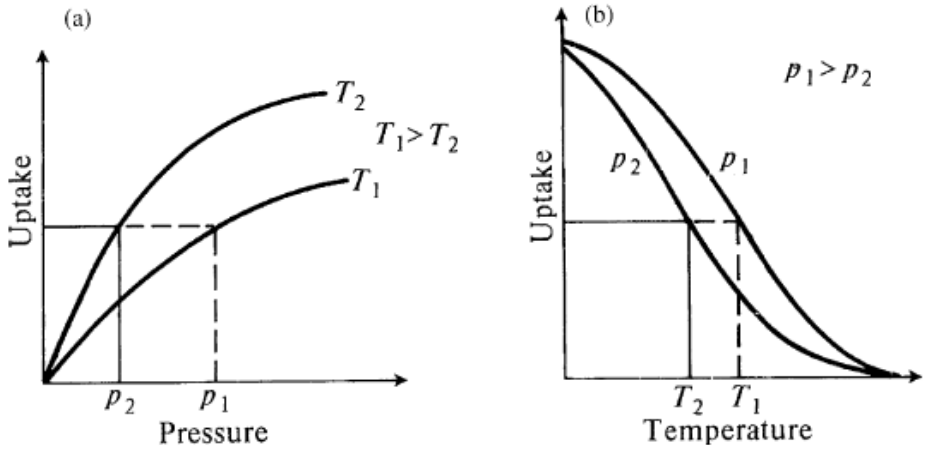

Fig. 3.5: Influence of the (a) temperature and (b) pressure on the H_2 uptake [32].

“I have always attached great importance to the manner in which an experiment is set up and conducted… the experiment should be set up to open as many windows as possible on the unforeseen”

Frederic Joliot-Curie, French Physicist (1900-1958)

4 Materials and experimental methods

4.1 Studied materials

A variety of carbon-based materials with different morphologies, surface chemistries and porous structures were studied in this thesis, including multi-walled carbon nanotubes, graphene oxide sponges and foams, few-layer graphene flakes, activated carbon cloths as well as hybrid materials such as metal-organic frameworks. Carbon materials are considered attractive adsorbents for H_2 storage applications as they are lightweight and exhibit high specific areas and pore volumes, excellent thermochemical stability, non-toxicity and can be produced with a plethora of methods at low cost [43-46].

4.1.1 Graphene-based nanostructures

Graphene, the newest member in the family of carbon allotropes [47], is visualized as a 2-D monolayer of hexagonally structured sp^2-bonded carbon atoms (see Fig. 4.1). Exfoliated graphene has been a subject of considerable research attributed to its unique electronic, thermal and mechanical properties. Characteristically, graphene exhibits high electrical and thermal conductivity, remarkable strength and stiffness as well as an impressively large area relative to its mass [45,46]. Based on theoretical calculations, an individual graphene sheet (non-porous) can provide a specific area as high as 2630 m^2/g (i.e. 1315 m^2/g for each side) [48]. However, single planar graphene sheets are thermodynamically unstable and usually form few- or multi-layer stacks and curved nanostructures (e.g. nanotubes, fibers, fullerenes, etc.), while they cannot be produced in bulk quantities using the currently available synthesis methods. Production of graphene has been reported over the last decade mostly through micro-mechanical exfoliation/peeling of pyrolytic graphite [49], epitaxial growth by chemical vapor deposition or high-temperature segregation using carbonaceous sources [50] and reduction of graphite- or graphene-oxide (GO) using thermal annealing, solvothermal, electrochemical or microwave radiation methods [51]. Few-layer graphene (FLG), an extremely "thin" graphitic analogue composed of a limited number of stacked graphene layers, can be also produced in a porous-like form, including 2-D nano-sized flakes and 3-D macroscopic structures, such as sponges and foams, and has attracted significant attention as a potential H_2 storage material. Impressive H_2 uptake values of up to 7.5 wt.% at 77 K and ~120 bar were reported for highly-nanoporous graphene scaffolds with high specific areas of up to ~3400 m^2/g prepared by KOH activation and H_2 annealing [52]. Alternative methods of producing nanoporous and high-

specific area graphene or GO materials, such as sponges, foams and flakes, using hydrothermal-, microwave- and plasma-induced exfoliation of graphite or graphite oxide, are presented within the publications of this thesis (see Publications I and II).

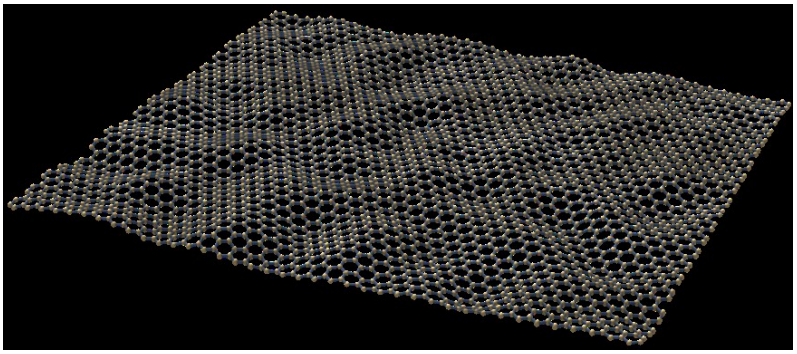

Figure 4.1: Visualization of a single planar layer of graphene [53].

4.1.2 Carbon nanotubes

Carbon nanotubes (CNTs) are considered an allotropic form of carbon consisting of a cylindrical/tubular nanostructure and belong to the family of fullerenes. CNTs can be distinguished to single-walled (SWCNT), consisting of a single graphene sheet rolled-up as a cylinder and multi-walled (MWCNT), composed of multiple rolled graphene sheets (2-50 tubes) coaxially arranged one inside each other (see Fig. 4.2). There are different variations in the nanotube formation based on the rolling angle of the graphene sheet, known as *chiral vector* [54]. The rolling direction determines the electrical and mechanical properties of the nanotube (e.g. conductivity, tensile strength, Young's modulus, etc.). Concerning the size characteristics, SWCNTs have diameters around 1 nm and MWCNTs have inner and outer diameters of 1.5-15 nm and 2.5-30 nm, respectively, while the interlayer distances between the coaxial tubes lie between 0.34 and 0.36 nm [33]. For both cases, the nanotube length ranges in the micrometer scale (i.e. 5-100 μm). The ends of a nanotube are normally closed by hemispherical structures, but they can open with proper chemical or ultra-sonication treatment. The carbon atoms of a nanotube are bonded together by sp^2 bonds forming hexagonal cells (similar to graphite or graphene), the walls of a MWCNT are weakly stacked together by van der Waals forces, while individual nanotubes tend to form bundles or ropes. CNTs are produced by vaporization of bulk carbon, a process that generates carbon molecules or atoms which then condense in the form of nanotubes. There are three common production methods: (a) arc discharge between two carbon electrodes, (b) laser ablation of a graphite target, and (c) chemical vapor deposition over a metal

catalyst. The nature, geometry and purity of the CNTs seem to have a crucial influence on their H_2 adsorption performance [55]. More specifically, SWCNTs of high-purity exhibit much higher specific areas (i.e. up to ~700 m^2/g), thus allowing larger H_2 amounts to be adsorbed. The H_2 gravimetric capacities of commercial MWCNTs at 77 K and up to ~1 bar are presented within the publications of this thesis (see Publication I).

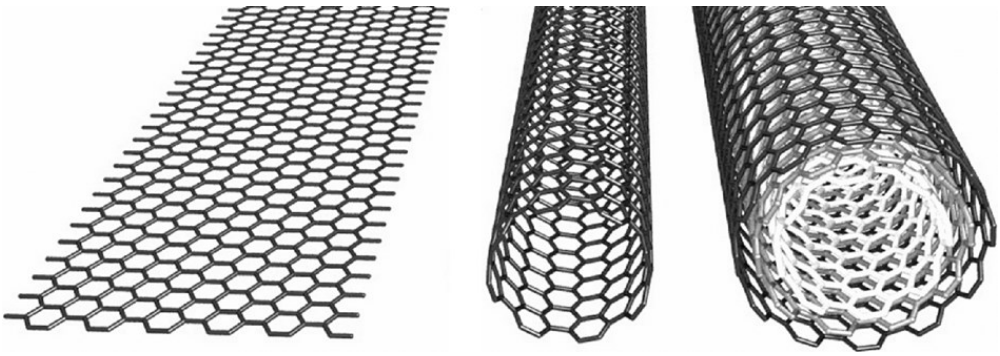

Figure 4.2: The formation of SWCNTs and MWCNTs by rolling graphene sheets [56].

4.1.3 Activated carbons

Activated carbons (ACs) constitute the most characteristic and extensively studied category of carbonaceous adsorbents produced on an industrial scale that stand for their large specific areas (> 1000 m^2/g) and pore volumes (> 0.5 cm^3/g) as well as their broad pore size distribution covering the micropore, mesopore and macropore region. A wide range of natural and synthetic materials can be used as precursors for the production of ACs, including biomass, such as wood, sawdust, fabrics and coconut shells, as well as carbonized byproducts, such as coal, coke, charcoal and biochar. Activation can be achieved either (a) physically by carbonization/pyrolysis in inert atmospheres (i.e. N_2, Ar, etc.) followed by gasification using oxidizing gases (i.e. air, O_2, CO_2 and steam) under high temperatures (i.e. up to 1000 ^oC), (b) chemically by using strong chemical agents (i.e. acids, bases or salts) or (c) using a combination of both [57]. The H_2 gravimetric capacities of ACs can be correlated to the available specific area and pore volume. In this respect, there is a general rule for microporous ACs, known as *Chahine's rule* (established by the Canadian scientist Richard Chahine in 1996), based on which a gravimetric H_2 uptake of 1 wt.% is expected per 500 m^2/g of SA or 0.2 cm^3/g of SPV at 77 K and ~35 bar [58]. Follow up studies, however, showed that in certain cases the H_2 adsorption behavior could deviate from the linear trend proposed by Chahine. A characteristic example was given by Gogotsi et al. [38], where a series of carbide-derived carbons with controllable porosity properties

were investigated for their H_2 uptake performance at 77 K and 60 bar. The conclusion was that carbon materials outperforming Chahine's rule usually exhibit a greater fraction of micropores with sizes smaller than 1.5 nm and/or an average pore size between 0.6 and 0.7 nm. Hence, maximizing the available specific area by retaining a high micropore volume and narrow ultra-micropore sizes is the suitable combination of properties for H_2 cryo-adsorption. However, the relatively weak Q_{st} values between molecular H_2 and carbon lead to a rather poor H_2 storage performance at room temperature. Theoretical studies indicated that the optimum Q_{st} value for efficient and reversible H_2 adsorption in ambient temperatures and moderate pressures (1.5-30 bar) lies at ~15 kJ/mol [59]. The Q_{st} values presented for standard ACs in the literature are usually found in the range of 5–8 kJ/mol [57], showing an average value of around 6 kJ/ mol [27]. For such a case, an optimum operating temperature of 115 K is required, which is far below the desired ambient temperatures (i.e. 298 K). The H_2 adsorption properties of an ultra-microporous and high-specific area/pore volume carbon cloth-like material derived by CO_2 activation of viscose rayon cloth is presented within the publications of the current thesis (see Publication III).

4.1.4 Beyond carbons – metal-organic frameworks

Metal-organic frameworks (MOFs) are crystalline and nanoporous hybrid materials composed of metal ions and organic ligands that form a great variety of 1-, 2- or 3-D nanostructures. MOFs have received considerable attention since the early 2000's mainly due to their low densities, impressively large specific areas and pore volumes, as well as the facile tuning of their pore sizes and shapes upon modification of their individual building blocks (i.e. metals and linkers) [60]. However, there are still technical difficulties upon their usage, including decomposition or structural collapse upon long-term atmospheric exposure, high sensitivity in moisture, lack of thermal stability as well as deformation of the pore structure under high-pressures [61,62]. The most characteristic and considerably studied MOF system is IRMOF-1, known as MOF-5 in previous years, consisting of Zn_4O clusters linked with 1,4-benzenedicarboxylate (BDC) linkers that overall form a 3-D cubic crystal lattice, as shown in Fig. 4.3. Production of IRMOF-1 type materials can be achieved mainly using room temperature mixing [63], solvothermal [62], sonochemical [64] and microwave irradiation methods [65]. MOFs in general are considered promising adsorbents for H_2 cryo-adsorption and storage applications due to their increased SA and SPV values and narrow ultra-microporosities (i.e. pore sizes below

0.7 nm) [66,67]. Specifically, impressive gravimetric H_2 uptake of ~6.9 wt.% at 77 K and 100 bar [68] and ~7.1 wt.% at 77 K and 40 bar [69] were reported for solvothermally-derived IRMOF-1 materials with very large Brunauer-Emmet-Teller (BET) SA of ~2449 and ~3800 m^2/g, respectively. An IRMOF-1 powder derived by solvothermal treatment and supercritical CO_2 activation, showing a high ratio of H_2 uptake relative to its BET SA, is presented within the publications of this thesis (see Publication IV).

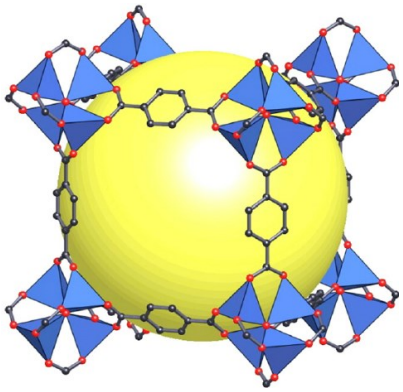

Figure 4.3: The structure of the IRMOF-1 material composed of Zn4O tetrahedral (blue) and BDC linkers consisting of carbon (black) and oxygen (red); the yellow sphere represents the available pore volume of the 3-D cubic framework [70].

4.2 Nitrogen adsorption and desorption at 77 K

The characterization by nitrogen (N_2) gas adsorption/desorption is a non-destructive volumetric/manometric-based technique that enables the evaluation of a solid's porosity-related properties, such as specific area, specific pore volume and pore size distribution. N_2 is used as the adsorbate gas with the applied pressures ranging from vacuum up to near-atmospheric (~1 bar) at a constant temperature of 77.3 K. Liquid nitrogen (LN_2) is also employed to cool down the system to the desirable cryogenic temperature of 77.3 K; i.e. the boiling point of N_2 under atmospheric pressure. The quantity of N_2 gas adsorbed onto the solid surface is recorded by gradually increasing (point by point) the pressure between 0-1 bar at 77.3 K, while in reverse the quantity of N_2 gas desorbed from the surface is measured by gradually decreasing the pressure. By the end of the cycle, *N_2 adsorption/desorption isothermal curves* are obtained and describe the relationship between the adsorbed/desorbed amount of N_2 gas and the equilibrium pressure at a constant temperature. More specifically, the equivalent graph consists of the amount of the adsorbed N_2 gas versus the relative pressure (P/P_0). The amount of adsorbed N_2 gas is expressed as gas volume at STP conditions (i.e. ~1 bar and 273 K) relative to the mass of

the sample given in cm^3/g units. The relative pressure is defined as the applied pressure (P) divided by the vapor pressure of N_2 at 77 K (i.e. $P_0 \sim 1$ bar).

The automatic volumetric gas sorption analyzer Autosorb 1-MP by Quantachrome Instruments was employed within the studies of this thesis (see Fig. 4.4), while N_2 gas of ultra-high purity (99.9999 %) was used. A sample quantity of 30-40 mg for each material was placed inside a Ø 6 mm bulb glass tube, known as the *sample cell*. The cell was weighed both as empty and with the sample inside to calculate the *non-degassed mass* of the sample. An elutriation cap was adjusted on the top of the sample cell to prevent the powder to drive off due to the rapid expansion of the gas during the de-gassing procedure. Then, the sample cell was adjusted on the de-gassing station of the instrument and placed inside a heating mantle. The samples were de-gassed under high-vacuum (10^{-6} mbar) with a constant heating at 250 ^oC for 24 h. The purpose of the de-gassing procedure is the removal of air, environmental impurities or synthesis remnants trapped inside the sample's pores. Upon this procedure, the sample cell was removed from the de-gassing station and weighed once again to calculate the *degassed mass* of the sample. A non-porous round glass rod was placed inside the sample cell to minimize the interior volume. The fully assembled sample cell (i.e. cell, degassed sample, glass rod and elutriation cap) was adjusted on the measuring station of the instrument and submerged inside a bath of liquid N_2. The applied pressure initiated from vacuum ($P/P_0 < 10^{-3}$) and terminated near the vapor pressure of N_2 ($P/P_0 \sim 0.99$), while the temperature was constantly recorded at 77.3 K by a reference tube. The analysis method was based on many extra points in the region P/P_0 = 0.6-0.95 and the equilibrium time on each point was set at 3 min. Helium (He) gas was used for balancing the interior pressure of the sample cell with the exterior atmospheric pressure during the placement or removal of the sample cell on or from the measuring station. The porosity-related properties were determined by using Quantachrome's ASiQWin software on the recorded adsorption and/or desorption data. The total SA was calculated by the multi-point *Brunauer-Emmet-Teller* (*BET*) method, the total SPV was estimated by the single-point *Gurvich* rule, while the micropore SPV and micropore SA were calculated based on the Carbon Black statistical thickness equation, also known as *t-plot*. The pore size distribution analysis was carried out using the *Barret- Joyner-Halenda* (*BJH*) method for mesoporous materials as well as the *Quenched Solid Density Functional Theory (QSDFT)* method for microporous materials or materials containing both micropores and mesopores.

Fig. 4.4: The volumetric gas sorption analyzer Autosorb 1-MP by Quantachrome Instruments; measuring station, vacuum cold trap and two de-gassing stations (from left to right) [71].

4.2.1 Adsorption/desorption isotherms

According to the IUPAC [32], the adsorption/desorption isotherms can be classified into six main groups (I-VI), as shown in Fig. 4.5. The type of the curve provides crucial information about the nature of the adsorption process and the porosity of the material. The most common isotherms are type I, II and IV, while types III, V and VI are rarely observed. The reversible type I isotherm, also known as Langmuir isotherm, is characteristic of microporous materials (pore widths < 2 nm) with small external surfaces. The adsorption increases abruptly at low relative pressures implying a micropore filling mechanism due to enhanced gas-solid interactions in narrow micropores (i.e. pores of molecular dimensions). At higher relative pressures it reaches a point of saturation (plateau) with the equivalent amount of adsorbed gas attributed to the accessible micropore volume instead of the internal surface area. A further subdivision can be performed between type I(a), given by microporous materials with narrow micropores below 1 nm in width, and type I(b), given by materials with a broader range of pore size distribution, including both micropores and small mesopores (pore widths < 2.5 nm). The reversible type II isotherm is characteristic of non-porous or macroporous materials. The isotherm's shape is a result of unrestricted monolayer-multilayer adsorption up to high relative pressures due to presence of macropores (> 50 nm) and/or external surface. The adsorption point B, shown in in Fig. 4.5 (II), indicates the limit at which monolayer

coverage is completed and multilayer formation begins. The type IV isotherm is characteristic of mesoporous materials (pore widths of 2-50 nm). The adsorption curve in the beginning is the same as in the case of a type II isotherm representing also monolayer-multilayer adsorption, followed by pore condensation at higher relative pressures; i.e. gas condenses within the pores in a liquid-like form at $P/P_0 < 1$. Type IV isotherms can be distinguished into non-reversible type IV(a) showing a hysteresis loop between adsorption and desorption, which is associated with capillary condensation in pores exceeding a certain critical width (e.g. for N_2 adsorption at 77 K hysteresis may occur for cylindrical-shape pores wider than 4 nm) and reversible type IV(b) for materials having small mesopores in width.

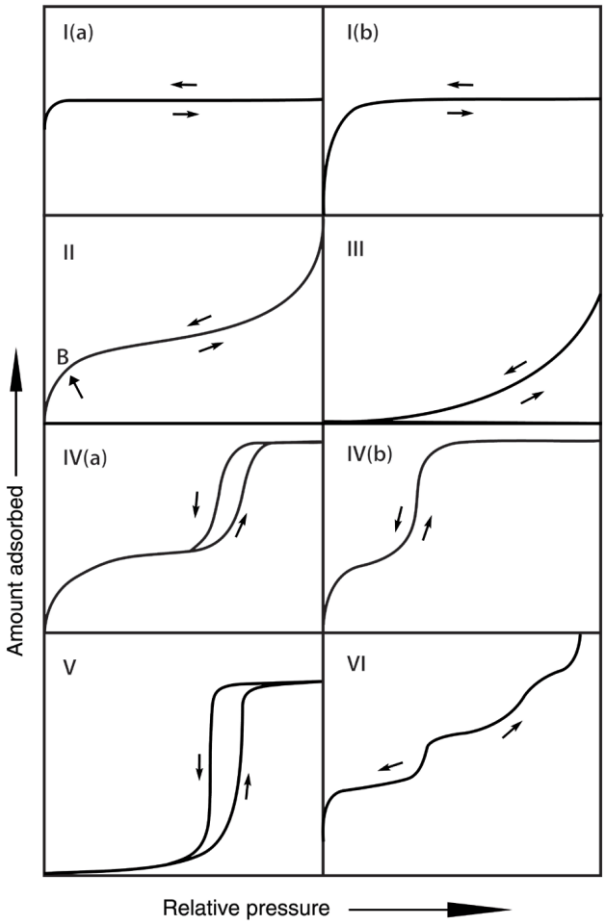

Fig. 4.5: Types of adsorption/desorption isotherms based on the IUPAC classification [32].

Furthermore, the type of the hysteresis loop can provide important information about the pore structure and shape in mesoporous materials. According to the IUPAC [32], hysteresis loops can be classified into five main types (H1-H5), as shown in Fig. 4.6. The type H1 loop

is associated with materials consisting of a uniform size of mesopores, as for example ordered mesoporous carbons. A steep and narrow loop indicates a delayed condensation during adsorption. The type H2 loop is presented in materials comprising of a complex porous structure and is formed due to pore blocking effects. Such loops can be distinguished to type H2(a), usually given by silica gels, porous glasses and other ordered mesoporous materials, and type H2(b), given by silica foams or hydrothermally-treated ordered mesoporous silica. The type H3 is related with materials consisting of non-rigid plate-like particles (aggregates) and/or having a macroporous network not completely filled with condensate. The characteristic step observed at the closure of the desorption curve implies that the mechanism of desorption involves a cavitation-induced evaporation. The effect of *cavitation* describes the spontaneous nucleation and growth of gas bubbles in the condensed fluid trapped within the mesopores [72]. As a result, the main body of the mesopores gets empty as the liquid N_2 is evaporated, while their pore neck still remains filled. The type H4 loop is observed in materials containing both micropores and mesopores, as for example zeolites and combined micro- and meso-porous carbons. The enhanced uptake at low relative pressures is attributed to micropore filling. Finally, the type H5 loop is not so common and refers to materials containing both open and partially blocked mesopores.

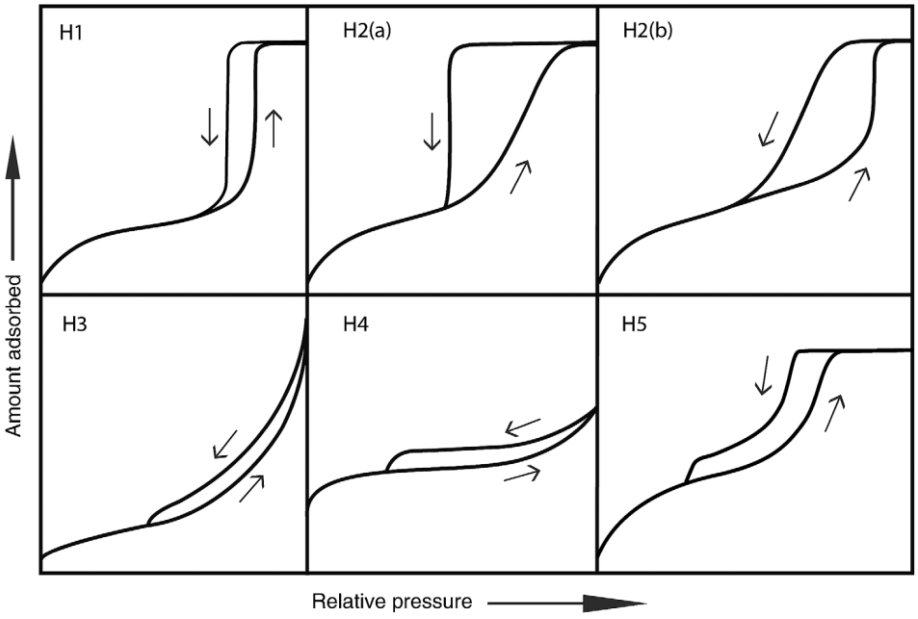

Fig. 4.6: Types of hysteresis loops based on the IUPAC classification [32].

4.2.2 Total specific area – multi-point BET method

The total specific area (SA) was estimated by applying the multi-point Brunauer-Emmet-Teller (BET) method in the adsorption isotherm data [35]. The method involves the determination of the amount of adsorbate required to cover both the external surface and the internal pore surface of a solid to a complete monolayer. However, the BET method is based on certain assumptions, including (a) adsorption on a homogeneous surface (well-defined sites), (b) lack of lateral interactions between the gas molecules, (c) the upper layer is in equilibrium with the gas phase, (d) the heat of adsorption should be provided for the first layer and the heat of condensation for the rest of layers and (e) the number of layers becomes infinite in saturation pressure. There are two main stages involved in the application of the BET method, (a) calculating the weight of the monolayer adsorbate (W_m) from the BET plot and (b) calculating the SA value. The linear form of the BET equation is:

$$\frac{1}{W \cdot \left[\left(\frac{P_0}{P}\right) - 1\right]} = \frac{1}{W_m \cdot C} + \frac{(C-1)}{W_m \cdot C} \cdot \left(\frac{P}{P_0}\right) \qquad (4.1)$$

where W is the weight of the adsorbed gas at a relative pressure P/P_0, W_m is the weight of the adsorbate forming a monolayer surface coverage and C is a BET constant indicating the magnitude of the adsorbent-adsorbate interactions in the first adsorbed layer (heat of adsorption). The multi-point BET plot is a linear plot consisting of the ratio $1/[W(P_0/P)-1]$ versus the relative pressure (P/P_0). For mesoporous and macroporous materials, the BET method is applied in the relative pressure range of $0.05 < P/P_0 < 0.35$ by choosing at least three points, while in the case of microporous materials a lower range is selected ($P/P_0 < 0.01$) in order to satisfy the BET consistency criteria (ISO 9277:2010) [74]. The weight of the monolayer is obtained by the slope (s) and the intercept (i) of the BET plot, based on the following equations:

$$s = \frac{C-1}{W_m \cdot C} \qquad (4.2)$$

$$i = \frac{1}{W_m \cdot C} \qquad (4.3)$$

Hence, combining Eqs. (4.2) and (4.3) lead to:

$$W_m = \frac{1}{s+i} \qquad (4.4)$$

The total BET area (S_t) can be expressed as:

$$S_t = \frac{W_m \cdot N \cdot A_{cs}}{M} \qquad (4.5)$$

There, N is the Avogadro's number (6.023×10^{23} molecules/mol), A_{cs} is the cross-sectional area of the adsorbate molecule (i.e. 0.162 nm^2 for N_2) and M the molecular weight of the adsorbate (i.e. 28.0134 amu for N_2 at 77K). Therefore, the BET SA (S_{BET}) can be calculated by dividing the BET area (S_t) to the weight of the sample (W). Thus, Eq. (4.5) becomes as following:

$$S_{BET} = \frac{S_t}{W} \qquad (4.6)$$

4.2.3 Total pore volume – single-point Gurvich rule

The total volume of the pores is estimated by applying the single-point Gurvich rule [35] in the adsorption isotherm. It is derived by the adsorbed volume of N_2 at a relative pressure close to the vapor pressure of N_2 (i.e. $P/P_0 \sim 0.99$), based on the assumption that the pores are filled with liquid N_2. The last point of the adsorption curve is selected at which adsorption ends and desorption begins. The adsorbed N_2 volume (V_{ads}) can be converted to liquid N_2 volume (V_{liq}) as following:

$$V_{liq} = \frac{P_a \cdot V_{ads} \cdot V_m}{R \cdot T} \qquad (4.7)$$

There, P_a is the ambient pressure, V_m is the molar volume of the liquid adsorbate (i.e. 34.7 cm^3/mol for N_2), R is the universal gas constant (i.e. 8.314 J mol^{-1} K^{-1}) and T is the ambient temperature. If the material contains no macropores or external surface, the adsorption isotherm reaches a clear plateau at high relative pressures and the total SPV can be calculated. Instead, in the presence of macropores or external surface, the adsorption isotherm rises indefinitely in a vertical direction at $P/P_0 \sim 0.99$ and therefore the total SPV cannot be extracted by using the Gurvich rule.

4.2.4 Micropore specific area and volume

The specific surface area and volume of the micropores were estimated by applying the Carbon Black statistical thickness equation in the total isotherm [75]. The process is similar to the BET method, but it extends to higher relative pressures (P/P_0) and depends on the micropore size distribution (< 2 nm). The t-plot is a linear plot consisting of the adsorbed

N_2 volume (V) versus the statistical thickness (t) of the adsorbed film. The calculation of the statistical thickness is based on the comparison to a non-porous solid using the following equation:

$$t_{CB}(\text{Å}) = 0.88 \cdot \left(\frac{P}{P_0}\right)^2 + 6.45 \cdot \left(\frac{P}{P_0}\right) + 2.98 \qquad (4.8)$$

The micropore volume (V_{MP}) is calculated by converting the intercept (i) of the t-plot to a liquid N_2 volume; i.e.:

$$V_{MP} = 0.001547 \cdot i \qquad (4.9)$$

The micropore specific surface area (S_{MP}) is extracted as a fraction of the total BET specific surface area by the slope (s) of the t-plot. Hence,

$$S_{MP} = S_{BET} - 15.47 \cdot s \qquad (4.10)$$

4.2.5 Pore size distribution

The distribution of the cumulative pore volume or differential pore volume with respect to the pore size is known as *pore size distribution* (*PSD*). In this study, the PSD graphs were extracted on the basis of two different methods, (a) the *Barret-Joyner-Halenda* (*BJH*) method [76] and (b) the *Quenched Solid Density Functional Theory* (*QSDFT*) method [77]. The BJH method was used for mesoporous materials, while the QSDFT method was used for materials containing both micropores and mesopores. No PSD analysis was carried out for macroporous or non-porous materials.

The BJH method is usually applied in the desorption branch of the isotherm. The method is based on two assumptions, (a) the cylindrical geometry of the pores and (b) that the pores are filled with liquid N_2 close to the vapor pressure of N_2 ($P/P_0 \sim 0.99$). A typical BJH-based PSD graph consists of the first derivative of the cumulative volume to the pore diameter (dV/dD) versus the pore diameter (D). The BJH analysis is based on the Kelvin equation:

$$r_K = \frac{-2\gamma \cdot V_m}{R \cdot T \cdot \ln(P/P_0)} \qquad (4.11)$$

where r_k is the Kelvin pore radius, γ is the surface tension of N_2 at its boiling point (i.e. 8.85 ergs/cm^2 at 77K), V_m is the molar volume of liquid N_2 (i.e. 34.7 cm^3/mol), R is the universal gas constant (i.e. 8.314 J mol^{-1} K^{-1}), T is the boiling point of N_2 (i.e. 77K) and P/P_0 is the

relative pressure. The actual pore radius (r_p) is the sum of the Kelvin pore radius (r_k) and the thickness of the adsorbed layer (t):

$$r_p = r_k + t \qquad (4.12)$$

The QSDFT method was applied in the adsorption isotherm by using the N_2-carbon equilibrium transition kernel at 77.4 K based on a slit-pore model. The QSDFT provides a more realistic approach of the micropore size distribution in contrary to other classical theories of mesoporosity (e.g. BJH method). It is widely used for disordered micro- and meso-porous carbons characterized by a heterogeneous surface chemistry [78]. A typical QSDFT-based PSD graph consists of the first derivative of the cumulative volume to the pore width (dV/dW) versus the pore width (W). The experimental adsorption isotherm of a porous solid can be analyzed based on the Generalized Adsorption Isotherm (GAI) equation [79]:

$$N\left(\frac{P}{P_0}\right) = \int_{W_{min}}^{W_{max}} N\left(\frac{P}{P_0}, W\right) f(W) dW \qquad (4.13)$$

where $N(P/P_0)$ represents the experimental adsorption isotherm data, W is the pore width, $N(P/P_0,W)$ is the isotherm on a single pore with a width W and $f(W)$ is the PSD function. The GAI equation is based on the assumption that the total isotherm consists of many individual single-pore isotherms $N(P/P_0,W)$ multiplied by their PSD function $f(W)$; a set of single-pore isotherms consists a *kernel*. The ASiQWin software extracts the PSD diagram by numerical calculation of the GAI equation through a non-negative least square algorithm.

4.2.6 Average pore size

PSD graphs usually provide a distribution of maximum peaks within a range of pore diameter or width. However, these peaks do not necessarily represent the average pore size (APS). Based on the assumption of an infinitely-extended slit-like pore system with an area (A) for one of the pore walls, this parameter would correspond to the slit width (W). In such a case, the specific pore volume (SPV) and specific area (SA) would correspond to:

$$SPV = A \cdot W \qquad (4.14)$$

$$SA = 2 \cdot A \qquad (4.15)$$

Hence, in order to obtain a rough measure for the average pore width (APW) value, the ratio given between Eqs. (4.14) and (4.15) has been evaluated:

$$APW = 2 \cdot \frac{SPV}{SA} \qquad (4.16)$$

The SA and SPV values used for this ratio could be either those derived by the BET method and the single-point Gurvich rule or the equivalent ones derived from the QSDFT method, as long as they are used consistently.

4.3 Hydrogen storage measurements

The available H_2 adsorption techniques can be categorized in three main groups, (a) gravimetric techniques, where the amount of stored H_2 is determined by the added mass, (b) volumetric or manometric techniques, where the amount of stored H_2 is determined by the change in pressure under a known volume, and (c) temperature-programmed desorption techniques, where the amount of desorbed H_2 is determined as function of temperature [8]. In the current work, volumetric/manometric adsorption methods were applied for the determination of the adsorbed H_2 quantity using low-(0-1 bar) and high-pressures (0-100 bar) in a wide range of temperatures (60-298 K). Experimentally, the "excess" H_2 mass (m_{excess}) is measured, which is the difference between the total H_2 mass (m_{total}) within the pore space and the bulk H_2 mass that would be present in the absence of adsorption. Hence,

$$m_{(excess)} = m_{(total)} - \rho_H \cdot V_a \qquad (4.17)$$

where ρ_H is the constant bulk density of H_2 and V_a is the volume of the adsorbed phase. The adsorbed H_2 content of a solid material is usually expressed in terms of mass as *H_2 gravimetric capacity*, which is defined as the adsorbed H_2 mass (adsorbate) divided by the sum of the adsorbent's and the adsorbate's mass given in wt.% units. Thus,

$$Capacity\ (wt.\%) = \left[\frac{(Mass\ of\ adsorbed\ H_2)}{(Mass\ of\ host\ material)+(Mass\ of\ adsorbed\ H_2)} \cdot 100\right] \% \qquad (4.18)$$

4.3.1 Low-pressure hydrogen adsorption

In this method, H_2 is used as an adsorbate gas with the applied pressures ranging from vacuum up to near-atmospheric (~1 bar) at a constant temperature ranging from 60 to 298 K. The same volumetric gas analyzer AUTOSORB 1-MP by Quantachrome Instruments was employed, as in the case of the N_2 adsorption measurements, coupled with a Gifford-McMahon two-stage closed-cycle refrigerator (cryo-cooler) and using H_2 gas of ultra-high

purity (99.9999%). The quantity of H_2 gas adsorbed onto the solid surface is recorded by gradually increasing (point by point) the pressure between 0-1 bar at 77.3 K, while in reverse the quantity of H_2 gas desorbed from the surface is measured by gradually decreasing the pressure. By the end of the measurement, H_2 *adsorption/desorption isothermal curves* are obtained and describe the relationship between the adsorbed/desorbed amount of H_2 gas and the equilibrium pressure at a constant temperature. More specifically, the equivalent graph consists of the amount of the adsorbed H_2 gas versus the pressure (P) in mbar units. The amount of adsorbed H_2 gas can be expressed either as adsorbed H_2 volume at STP conditions (i.e. 1 bar and 273 K) relative to the degassed mass of the sample (i.e. v_{gas}/m_{solid} in cm^3/g units), adsorbed H_2 mole relative to the degassed mass of the sample (i.e. n_{gas}/m_{solid} in mmol/g units) or as a total system capacity, which refers to the adsorbed H_2 mass relative to the sum of the adsorbed H_2 and degassed sample masses (i.e. $m_{gas}/(m_{gas} + m_{solid})$ in wt.% units). The preparation, de-gassing and measurement of the samples was carried out in a similar manner to the N_2 adsorption experiments, as described in section 4.2. The samples were de-gassed under high-vacuum (10^{-6} mbar) with a constant heating at 250 ^oC for 24 h.

4.3.2 High-pressure hydrogen adsorption

In this method, H_2 is used as an adsorbate gas with the applied pressures ranging from vacuum up to 100 bar at two different constant temperatures (i.e. 77 and 298 K). Liquid N_2 is also employed to cool down the system at the desirable cryogenic temperature of 77.3 K; i.e. the boiling point of N_2 under atmospheric pressure, while a water bath is used for the room temperature measurements. The quantity of H_2 gas adsorbed onto the solid surface is recorded by gradually increasing (point by point) the pressure between 0-100 bar at 77.3 or 298 K, while in reverse the quantity of H_2 gas desorbed from the surface is measured by gradually decreasing the pressure. By the end of the measurement, *H_2 adsorption/desorption isothermal curves* are obtained and describe a relationship between the adsorbed/desorbed amount of H_2 gas and the equilibrium pressure at a constant temperature. More specifically, the equivalent graph consists of the H_2 gravimetric capacity of the system (i.e. adsorbed H_2 mass relative to the sum of the adsorbed H_2 and degassed sample masses) in wt.% units versus the pressure (P) in bar. The operation of the instrument can be described based on a *Sievert's apparatus*, as shown in Fig. 4.7. The instrument contains two reservoirs of known volumes, one with H_2 gas and one with the

sample, connected by an isolation valve. A small dose of H_2 gas is admitted inside the sample's reservoir by opening the valve and an equilibrium pressure is reached between the two reservoirs. The pressure-drop inside the reservoir is directly attributed to the adsorption of H_2 gas by the sample. The amount of adsorbed gas can be calculated based on the real or non-ideal gas law by knowing the initial gas pressures and volumes of the system. Hence,

$$P \cdot V = n \cdot Z \cdot R \cdot T \qquad (4.19)$$

where P is the pressure, V is the volume, n is the number of moles, Z is the gas compressibility factor, R is the universal gas constant (i.e. 8.314 J mol^{-1} K^{-1}) and T is the temperature. The Z factor is related to the non-ideality correction factor (α) as following:

$$\alpha = \frac{(Z-1)}{P} \qquad (4.20)$$

For the case of H_2, the α factor corresponds to 2.2 × 10^{-6} $torr^{-1}$ at 77 K, 1.2 × 10^{-6} $torr^{-1}$ at 87 K and 0.1 × 10^{-6} $torr^{-1}$ at 298 K (i.e. 1 torr ~1.33 × 10^{-3} bar).

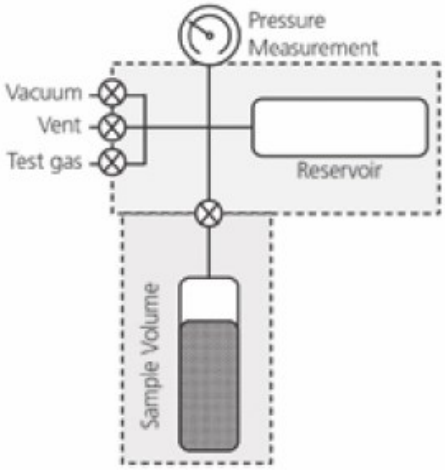

Fig. 4.7: The operating principle of a Sievert's apparatus [80].

The manually-handled volumetric gas sorption system Hy-Energy PCT Pro-2000 by SETARAM Instrumentation was employed for our studies (see Fig. 4.8), while H_2 gas of ultra-high purity (99.9999 %) was used. A sample quantity of 100-120 mg for each material was placed inside metal gasket face seal, known as the *VCR®*. The VCR was weighed both as empty and with the sample inside to calculate the *non-degassed mass* of the sample. A non-porous glass cylinder, known as *spacer*, was placed inside the VCR to minimize the interior volume and then the assembled VCR (i.e. VCR, sample and spacer)

was adjusted in the instrument. The evacuation of the VCR was achieved by an ultra-high vacuum pump, while the temperature was controlled by a thermocouple. The samples were de-gassed under strong vacuum (10^{-7}mbar) with a constant heating at 250 ^{o}C for 24 h. A volume calibration was carried out prior to the H_2 adsorption measurements using He gas. It is a standard procedure that enables the calculation of the free volumes inside the cell. In total three calibrations took place at the operating temperature of the instrument (303 K), at room temperature (298 K) and at the boiling point of N_2 (77 K). Each calibration included five adsorption/desorption cycles with He. The free volumes at each temperature were calculated for adsorption and desorption and an average of both. For the H_2 adsorption measurements, the VCR was submerged in a LN_2 bath at 77.3 K and in a water bath at 298 K. The instrumental HyData software allowed the configuration of the experimental parameters and the monitor of the whole procedure. The pressure dose and equilibrium time in each point were set to 2 bar and 5 min, respectively, for the measurements at 77 K and 2 bar and 7 min, respectively, for the measurements at 298 K. The applied pressure started from vacuum (10^{-7}) up to ~100 bar. In total four major evacuations took place for each sample during the high-pressure experiments. The first evacuation was carried out when the VCR was placed into the instrument and the second one after the volume calibration. The last two evacuations were competed after each measurement at 77 and 298 K. By the end of the measurements, the VCR was removed from the instrument and the *de-gassed mass* of the sample was weighed. Mathematical corrections were also applied to the results to minimize any experimental errors.

Fig. 4.8: High-pressure gas sorption analyzer Hy-Energy PCT Pro-2000 by SETARAM [81].

5. Summary, conclusions and future work

The main objectives of the present thesis are related to: (a) the fundamental understanding of the physisorption mechanism of molecular H_2 onto carbonaceous surfaces using different temperature and pressure conditions, (b) potential correlations between the porosity-related properties, such as specific area (SA), specific pore volume (SPV), pore size distribution (PSD) and average pore size/width (APS/APW), and the H_2 storage performance of carbon-based adsorbents, and (c) useful suggestions towards pore structure optimization of H_2 storage materials for increased H_2 adsorption uptake. All issues were investigated within the following publications through advanced characterization methods, including low-(0-1 bar) and high-pressure (0-100 bar) H_2 gas adsorption and desorption measurements at temperatures ranging from 60 up to 298 K, and porosity measurements by N_2 gas adsorption and desorption at 77 K. A series of mainly carbon-based materials with different morphologies, surface chemistries and porosities were investigated as potential H_2 adsorbents. The commercially available and lab-synthesized materials included a mixture of carbon nanoparticles, 1-D multi-walled carbon nanotubes, 2-D few-layer graphene-like flakes, 3-D graphene oxide foams and sponges, activated carbon fiber cloths as well as metal-organic framework nanocrystallites. These samples exhibited BET SAs from 44 up to 1205 m^2/g, micropore SA fractions of up to ~99 %, micropore volumes of up to 0.46 cm^3/g as well as PSDs covering the whole micropore, mesopore and macropore region. A selective summary of the aforementioned porosity-related properties, based on N_2 adsorption data recorded at 77 K, can be found in Table 6.1.

Physical gas adsorption in general is favored upon decreasing the operating temperature and increasing the applied pressure. The gas-solid interactions are promoted at lower temperatures due to the reduced kinetic energy of the gas molecules. For the case of H_2 adsorption in nanoporous materials (including carbons), cryogenic temperatures (i.e. below 100 K) are required to achieve significant H_2 storage capacities, a fact that is attributed to the poor polarizability and weak quadrupole moment of molecular H_2 [27]. Most of the studied materials exhibited an adequate H_2 gravimetric uptake at 77 K and up to ~1 bar relative to their available BET specific area value, a fact that was attributed to the greater fraction of micropore specific area and volume and/or to the mean micropore

sizes found in the sub-nanometer region. As already mentioned, such small micropores can act as "strong" adsorption sites for H_2 due to the overlapping of the potential fields of the opposite pore walls [27,38].

Table 6.1: Summary of porosity properties, based on N_2 adsorption data (77 K), for all the materials studied within the publications of this thesis. The commercial activated carbon powder YP-80 is included for comparison (unpublished data).

Publication (#)	Material	S_{BET} (m^2/g)	S_{Micro} (m^2/g)	S_{Micro}/S_{BET} (%)	$V_{Gurvich}$ (m^2/g)	V_{Micro} (m^2/g)	$V_{Micro}/V_{Gurvich}$ (%)	W_{Ave} (nm)	W_{Micro} (nm)
I	Ros1	44	0	0	NA	0	NA	NA	NA
I	MWCNTs	201	2	0.99	NA	0.001	NA	NA	NA
I	GS-75	348	88	25.28	NA	0.04	NA	NA	0.909
II	FLG-400	428	171	39.95	NA	0.076	NA	NA	0.888
IV	IRMOF-1	520	480	92.30	NA	0.190	NA	NA	0.791
I	mic-GO	626	5	0.79	NA	0.007	NA	NA	NA
I	FLG-700	724	275	37.98	NA	0.119	NA	NA	0.865
II	FLG-800	777	299	38.48	NA	0.132	NA	NA	0.869
III	ACC	1205	1190	98.75	0.470	0.460	97.87	0.780	0.773
NA	YP-80	2353	2182	92.73	1.173	0.974	83.03	0.997	0.892

S_{BET}: Brunauer-Emmet-Teller (BET) specific area (SA), S_{Micro}: micropore SA derived by the Carbon Black statistical thickness (t-plot) method, (S_{Micro}/S_{BET}): % fraction of micropore SA to BET SA $V_{Gurvich}$: total specific pore volume (SPV) at P/P_0 ~0.96 for pores smaller than 50 nm in width calculated by the single-point Gurvich rule, V_{Micro}: micropore SPV derived by the t-plot method, ($V_{Micro}/V_{Gurvich}$): % fraction of micropore SPV to total SPV, W_{Ave}: average pore width calculated by the ratio of $2\cdot(V_{Gurvich})/(S_{BET})$ assuming a slit pore model, W_{Micro}: average micropore width calculated by the ratio of $2\cdot(V_{Micro})/(S_{Micro})$ assuming a slit micropore model, NA: Not Applicable

A set of representative correlation graphs between the gravimetric H_2 storage capacities of all the tested materials at ~1 bar and 77 K and their porosity-related properties, such as BET SA and micropore volume, is given in Fig. 6.1. It can be clearly seen in Figs. 6.1(a) and 6.2(b) that the ACC material, which combines the largest values of BET SA and micropore volume (or micropore SA), exhibits also the highest H_2 uptake value at 77 K and 1 bar. It should be also highlighted that the FLG-800 and IRMOF-1 materials demonstrate a similar H_2 uptake of ~1 wt.% at 77 K and 1 bar (see Fig. 6.1(a)), even though the FLG-800 has a ~33 % higher BET SA compared to the IRMOF-1 sample (i.e. 777 vs. 520 m^2/g, respectively). This should be attributed mainly to the higher micropore SA fraction (i.e. ~92 vs. ~38 %) and micropore volume (0.19 vs. ~0.13 cm^3/g) of the IRMOF-1 sample compared to the FLG-800 sample.

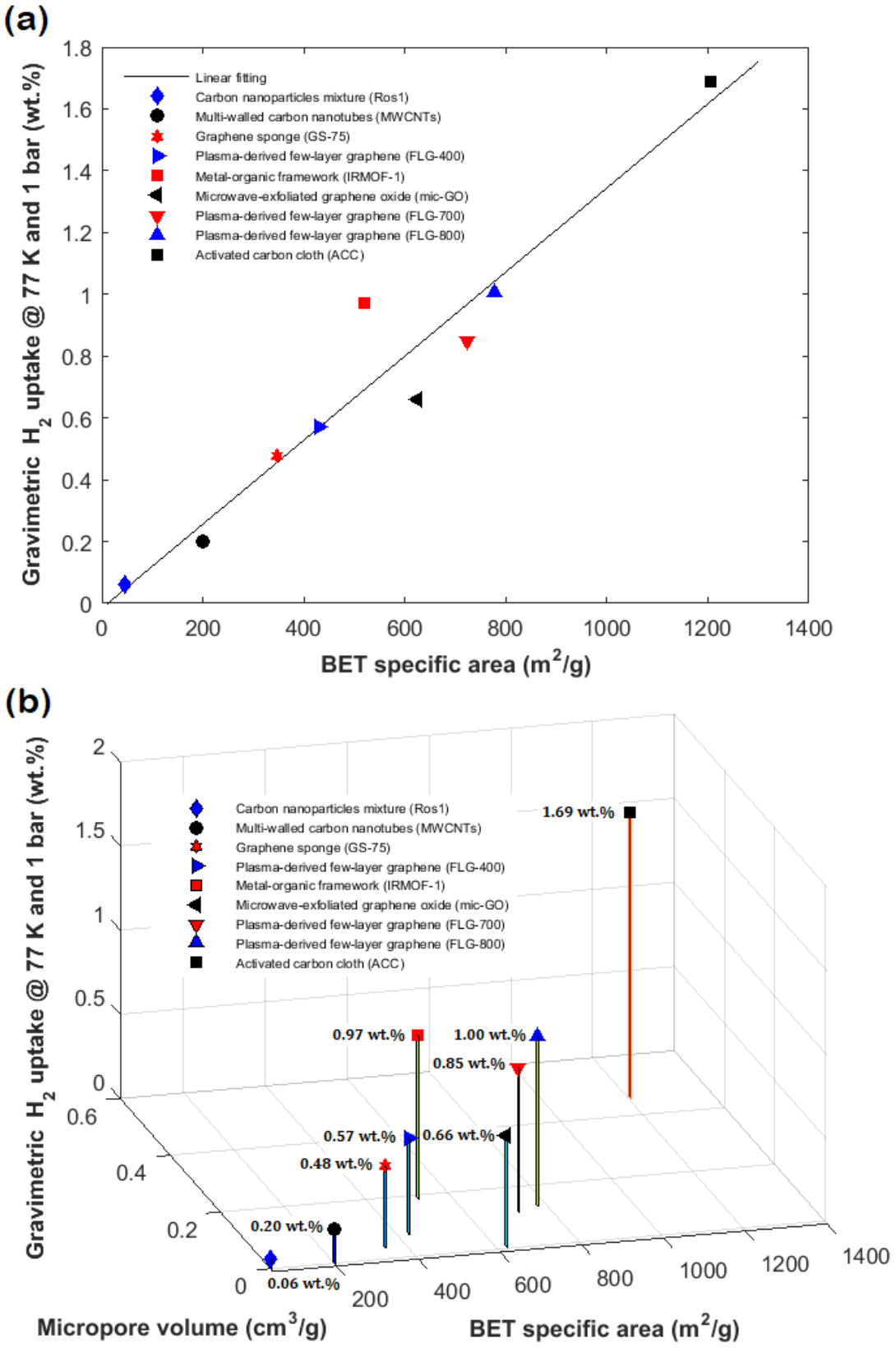

Fig. 6.1: (a) A collection of gravimetric H_2 uptake data at 77 K and 1 bar for all the materials studied within the publications of this thesis versus their available BET specific area values (fitted with a line) and (b) a 3-D graph including also the micropore volume values of these materials.

Furthermore, the most promising carbon materials evaluated from the low-pressure H_2 adsorption measurements (ACC, FLG-800 and FLG-400), along with a commercial and standard activated carbon powder (YP-80), were also investigated under a high-pressure regime up to ~100 bar both at 77 and 298 K. A selective summary of the H_2 storage properties of the aforementioned materials including H_2 gravimetric capacities and H_2 uptake to BET SA ratios can be found in Table 6.2.

Table 6.2: Summary of H_2 storage properties, based on low- and high-pressure H_2 adsorption data (77 and 298 K), for the best-performed materials studied within the publications of this thesis. The commercial activated carbon powder YP-80 is included for comparison (unpublished data).

Material (#)	$C_{@77K\&1bar}$ (wt.%)	$C_{@77K\&35bar}$ (wt.%)	$C_{max@77K}$ (wt.%)	$C_{@298K\&80bar}$ (wt.%)	$C_{@77K\&1bar}/S_{BET}$ (wt.%·m^{-2}·g)	$C_{@77K\&35bar}/S_{BET}$ (wt.%·m^{-2}·g)	$C_{@298K\&80bar}/S_{BET}$ (wt.%·m^{-2}·g)
FLG-400	0.57	1.09	1.14 @ 61 bar	NA	$1.331 \cdot 10^{-3}$	$2.546 \cdot 10^{-3}$	NA
FLG-800	1.00	1.94	2.01 @ 58 bar	NA	$1.287 \cdot 10^{-3}$	$2.496 \cdot 10^{-3}$	NA
ACC	1.69	2.99	3.14 @ 72 bar	0.31	$1.402 \cdot 10^{-3}$	$2.481 \cdot 10^{-3}$	$0.257 \cdot 10^{-3}$
YP-80	NA	4.46	4.52 @ 47 bar	0.49	NA	$1.895 \cdot 10^{-3}$	$0.208 \cdot 10^{-3}$

$C_{@77K\&1bar}$: H_2 gravimetric capacity at 77 K and 1 bar, $C_{@77K\&35bar}$: H_2 gravimetric capacity at 77 K and 35 bar (operating conditions described by Chahine's rule), $C_{max@77K}$: maximum H_2 gravimetric capacity at 77 K at the saturation pressure, $C_{@298K\&80bar}$: H_2 gravimetric capacity at 298 K and 80 bar (comparable maximum pressure), $C_{@77K\&1bar}/S_{BET}$: ratio of H_2 gravimetric capacity at 77 K and 1 bar to BET specific area (SA), $C_{@77K\&35bar}/S_{BET}$: ratio of H_2 gravimetric capacity at 77 K and 35 bar to BET SA, $C_{@298K\&80bar}/S_{BET}$: ratio of H_2 gravimetric capacity at 298 K and 80 bar to BET SA

Fully reversible gravimetric H_2 storage capacities from 1.14 up to 4.46 wt.% were recorded at 77 K and saturation pressures for these materials, as shown in Fig. 6.2(a). Higher H_2 uptake values were recorded for the higher-SA materials (YP-80, ACC, FLG-800 and FLG-400 in descending order). Instead, relative to the BET SA values of each material, the equivalent behavior seems to be reversed (FLG-400, FLG-800, ACC and YP-80 in descending order). Comparing only the ACC and YP-80 materials, due to the availability of all the porosity data for both, it seems that the higher fraction of micropore SA (i.e. ~99 vs. 93 %, respectively) and micropore volume (i.e. ~98 vs. 83 %, respectively) as well as the smaller average pore width (i.e. 0.78 vs. ~1 nm, respectively) provides an adequate explanation for the increased H_2 uptake to BET SA ratio of the ACC over YP-80; i.e. enhanced H_2 adsorption due to overlapping potential of the opposite micropore walls [27,38]. However, for the FLG-400 and FLG-800 materials not all the porosity data are available (i.e. total SPV and APW cannot be extracted by the N_2 adsorption method), while

a potential influence of the surface chemistry (i.e. presence of oxygen-based groups) cannot be excluded as well. The room temperature H_2 storage performance of the higher-SA materials was rather poor compared to the equivalent measurements at 77 K (see Fig. 6.2(a)) and consequently small gravimetric capacities of 0.31 and 0.49 wt.% were recorded at 298K and ~80 bar for ACC and YP-80, respectively, as clearly shown in Fig. 6.2(b). For this case as well, the H_2 uptake to BET SA ratio of the ACC exceeds the one of the YP-80 material due to the aforementioned reasons (see Table 6.2). Finally, the ACC, FLG-800 and FLG-400 materials also seem to exceed the theoretical capacity values extracted from Chahine's rule for standard activated carbons taking into consideration either the available BET SA or total SPV values, as shown in Figs. 6.2(c) and (d), respectively. Based on this general rule, a H_2 uptake of 1 wt.% is expected at ~35 bar and 77 K per 500 m^2/g of SA and/or 0.2 cm^3/g of SPV) [58]. For the case of the ACC material, this is surely attributed to the APW of 0.78 nm based on a slit-pore model. It should be noted that QSDFT data indicated an even lower APW value of 0.68 nm, while GCMC-based PSD analysis based on CO_2 adsorption data indicated a maximum around 0.57 nm. The aforementioned APW values lie between the mean pore size range of 0.6 to 0.7 nm suggested by Gogotsi et al. [38] for carbon materials that outperform Chahine's rule.

To sum up, H_2 storage in pure carbon-based nanoporous and high-SA materials via physical adsorption cannot be considered sustainable and practical towards applications in ambient temperatures due to the minor recorded H_2 gravimetric capacities even at high-pressures. However, such materials can be effectively combined with H_2 cryo-compression storage systems operating at 77 K using LN_2-based refrigeration systems and thus achieve higher H_2 uptake values. In this respect, the ideal H_2 adsorbent operating at cryogenic temperatures (< 100 K) should combine large SA and SPV values (as high as possible) together with dominant microporosities and narrow pore sizes in the sub-nanometer scale. Concerning room temperature applications, it is evident that alternative strategies should be employed with the aim to promote other sort of storage mechanisms and enhance the molecular H_2-carbon interactions, including surface modification either by functionalization with active redox groups and/or doping with active metal catalysts. In this respect, future studies will be mainly focused on investigating phenomena beyond classical physisorption, including "weak" chemisorption effects. The carbon-based nanoporous materials studied within this thesis need to be further treated using a plethora of physical and chemical methods, including plasma activation, microwave radiation,

physical vapor deposition, thermal annealing and wet chemical oxidation or reduction, with the aim to modify the energetic landscapes inside their pores. Acidic and basic groups, such as carboxyls (–COOH) and amines ($–NH_3$), as well as transition metal nanoparticles, such as Ru, Pd and Pt, will represent the potential functionalities and dopants, respectively, to be introduced onto the carbon surfaces towards improvement of their H_2 storage performance in ambient temperatures.

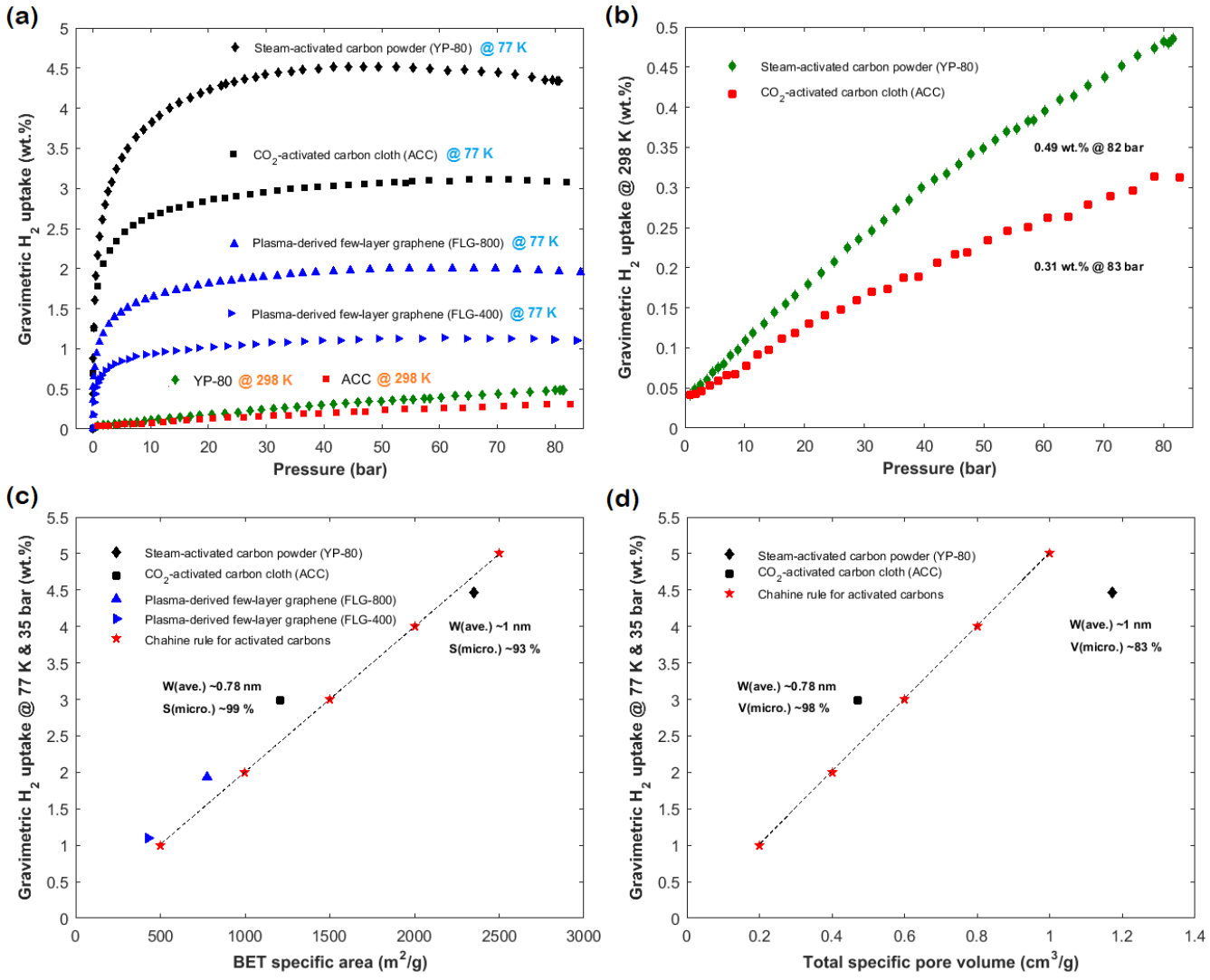

Fig. 6.2: (a) A collection of high-pressure H_2 adsorption isotherms recorded at 77 and 298 K for the materials performing best within this thesis, i.e. ACC, FLG-800 and FLG-400, compared to the activated carbon powder YP-80 (unpublished data), (b) comparison of H_2 adsorption performance at 298 K between ACC and YP-80 and gravimetric H_2 uptake at 77 K and 35 bar versus (c) BET specific area and (d) total specific pore volume compared to Chahine's rule.

6. References

[1] M. Aneke, M. Wang, Energy storage technologies and real life applications–a state of the art review, Applied Energy 79 (2016) 350–377.

[2] A. Zuttel, A. Remhof, A. Borgschulte, O. Friedrichs, Hydrogen: the future energy carrier, Philosophical Transactions of the Royal Society A 368 (2010) 3329–3342.

[3] G.W. Crabtree, M.S. Dresselhaus, The Hydrogen Fuel Alternative, MRS Bulletin 33 (2008) 421–428.

[4] M. Balat, Potential importance of hydrogen as a future solution to environmental and transportation problems, International Journal of Hydrogen Energy 33 (2008) 4013–4029.

[5] US Department of Energy, Report of the Hydrogen Production Expert Panel: A Subcommittee of the Hydrogen & Fuel Cell Technical Advisory Committee, https://www.hydrogen.energy.gov/pdfs/hpep_report_2013.pdf (October 2017).

[6] K. Zeng, D. Zhang, Recent progress in alkaline water electrolysis for hydrogen production and applications, Progress in Energy and Combustion Science 36 (2010) 307-326.

[7] J. Ren, N.M. Musyoka, H.W. Langmi, M. Mathe, S. Liao, Current research trends and perspectives on materials-based hydrogen storage solutions: a critical review, International Journal of Hydrogen Energy 42 (2017) 289–311.

[8] Q. Lai, M. Paskevicius, D.A. Sheppard, C.E. Buckley, A.W. Thornton, M.R. Hill, Q. Gu, J. Mao, Z. Huang, H.K. Liu, Z. Guo, A. Banerjee, S. Chakraborty, R. Ahuja, K.-F. Aguey-Zinsou, Hydrogen storage materials for mobile and stationary applications: current state of the art, ChemSusChem 8 (2015) 82789-82825.

[9] D.P. Broom, Hydrogen Storage Materials, Green Energy and Technology, Springer-Verlag London Limited, 2011.

[10] T.A. Steriotis, G.C. Charalambopoulou, A.K. Stubos, Advanced materials for hydrogen storage, in N. Kanellopoulos, Nanoporous materials: advanced techniques for characterization, modeling and processing, CRC Press Taylor & Francis, 2011.

[11] US Department of Energy, Module 1: Hydrogen Properties, https://www1.eere.energy.gov/hydrogenandfuelcells/tech_validation/pdfs/fcm01r0.pdf (October 2017).

[12] US Department of Energy, Module 2: Hydrogen Use, https://www1.eere.energy.gov/hydrogenandfuelcells/tech_validation/pdfs/fcm02r0.pdf (October 2017).

[13] US Department of Energy, Module 3: Hydrogen Use in Internal Combustion Engines, https://www1.eere.energy.gov/hydrogenandfuelcells/tech_validation/pdfs/fcm03r0.pdf (October 2017).

[14] US Department of Energy, Module 4: Fuel Cell Technology, https://www1.eere.energy.gov/hydrogenandfuelcells/tech_validation/pdfs/fcm04r0.pdf (October 2017).

[15] A. Zuttel, Hydrogen storage methods, Naturwissenschaften 91 (2004) 157–172.

[16] US Department of Energy, Hydrogen Storage, https://energy.gov/eere/fuelcells/hydrogen-storage (October 2017).

[17] M. Felderhoff, C. Weidenthaler, R. von Helmolt, U. Eberle, Hydrogen storage: the remaining scientific and technological challenges, Physical Chemistry Chemical Physics 9 (2007) 2643–2653.

[18] D.K. Ross, Hydrogen storage: the major technological barrier to the development of hydrogen fuel cell cars, Vacuum 80 (2006) 1084-1089.

[19] US Department of Energy, Multi-year Research, Development and Demonstration Plan 3.3, 2015, http://energy.gov/sites/prod/files/2015/05/f22/fcto_myrdd_storage.pdf (October 2017).

[20] D.J. Durbin, C. Malardier-Jugroot, Review of hydrogen storage techniques for on board vehicle applications, International Journal of Hydrogen Energy 38 (2013) 14595–14617.

[21] M. Kunowsky, J. P. Marco-Lózar, A. Linares-Solano, Material demands for storage technologies in a hydrogen economy, Journal of Renewable Energy 2013 (2013) 1–16.

[22] The Linde Group, http://www.linde.com/en/index.html (October 2017).

[23] US Department of Energy, Materials-Based Hydrogen Storage, https://energy.gov/eere/fuelcells/materials-based-hydrogen-storage (October 2017).

[24] R.A. Varin, T. Czujko, Z.S. Wronski, Nanomaterials for solid state hydrogen storage, Springer Science & Business Media, 2009.

[25] B. Sakintuna, F. Lamari-Darkrim, M. Hirscher, Metal hydride materials for solid hydrogen storage: A review, International Journal of Hydrogen Energy 32 (2007) 1121–1140.

[26] Hydrogen Components Inc., Chemistry, http://www.hydrogencomponents.com/Chemistry.htm (October 2017).

[27] D.P. Broom, C.J. Webb, K.E. Hurst, P.A. Parilla, T. Gennett, C.M. Brown, R. Zacharia, E. Tylianakis, E. Klontzas, G.E. Froudakis, T.A. Steriotis, P.N. Trikalitis, D.L. Anton, B. Hardy, D. Tamburello, C. Corgnale, B.A. van Hassel, D. Cossement, R. Chahine, M. Hirscher, Outlook and challenges for hydrogen storage in nanoporous materials, Applied Physics A 122 (2016) 1–21.

[28] J. Burress, M. Kraus, M. Beckner, R. Cepel, G. Suppes, C. Wexler, P. Pfeifer, Hydrogen storage in engineered carbon nanospaces, Nanotechnology 20 (2009) 204026.

[29] G.J. Kubas, Fundamentals of H_2 binding and reactivity on transition metals underlying hydrogenase function and H_2 production and storage, Chemical Reviews 107 (2007) 4152-4205.

[30] A. Gotzias, E. Tylianakis, G. Froudakis, Th. Steriotis, Theoretical study of hydrogen adsorption in oxygen functionalized carbon slit pores, Microporous and Mesoporous Materials 154 (2012) 38–44.

[31] L. Wang, A.J. Lachawiec, R.T. Yang, Nanostructured adsorbents for hydrogen storage at ambient temperature: high-pressure measurements and factors influencing hydrogen spillover, RSC Advances 3 (2013) 23935–23952.

[32] M. Thommes, K. Kaneko, A.V. Neimark, J.P. Olivier, F. Rodriguez-Reinoso, J. Rouquerol, K.S.W. Sing, Physisorption of gases, with special reference to the evaluation of surface area and pore size distribution (IUPAC Technical Report), Pure and Applied Chemistry 87 (2015) 1051–1069.

[33] R. Strobel, J. Garche, P.T. Moseley, L. Jorissen, G. Wolf, Hydrogen storage by carbon materials, Journal of Power Sources 159 (2006) 781–801.

[34] J.A. Dunne, R. Mariwala, M. Rao, S. Sircar, R.J. Gorte, A.L. Myers, Calorimetric heats of adsorption and adsorption isotherms 1. O_2, N_2, Ar, CO_2, CH_4, C_2H_6, and SF_6 on silicalite, Langmuir 12 (1996) 5888–5895.

[35] S.J. Gregg, K.S.W. Sing, Adsorption, surface area and porosity, 2nd edition, Academic Press, New York, 1982.

[36] J. E. Lennard-Jones, The equation of state of gases and critical phenomena, Physica 4 (1937) 941–956.

[37] M. Hirscher, B. Panella, Nanostructures with high surface area for hydrogen storage, Journal of Alloys and Compounds 404 (2005) 399–401.

[38] Y. Gogotsi, C. Portet, S. Osswald, J.M. Simmons, T. Yildirim, G. Laudisio, J.E. Fischer, Importance of pore size in high-pressure hydrogen storage by porous carbons, International Journal of Hydrogen Energy 34 (2009) 6314–6319.

[39] M. Dubinin, The potential theory of adsorption of gases and vapors for adsorbents with energetically nonuniform surfaces, Chemical Reviews 60 (1960) 235–241.

[40] J. Rouquerol, D. Avnir, C.W. Fairbridge, D.H. Everett, J.H. Haynes, N. Pernicone, J.D.F Ramsay, K.S.W. Sing, K.K. Unger, Recommendations for the characterization of porous solids (IUPAC Technical Report), Pure and Applied Chemistry 66 (1994)1739–1758.

[41] J. Rouquerol, F. Rouquerol, P. Llewellyn, G. Maurin, K.S. Sing, Adsorption by Powders and Porous Solids: Principles, Methodology and Applications, Academic Press, 2013.

[42] Union College, Accelerated Surface Area and Porosimetry System, https://muse.union.edu/aerogels/aerogel-lab-at-union/accelerated-surface-area-and-porosimetry-system/ (October 2017).

[43] G. Srinivas, X.G. Zheng, Graphene-based materials: synthesis and gas sorption, storage and separation, Progress in Materials Science 69 (2015) 1–60.

[44] Y. Xia, Z. Yang, Y. Zhu, Porous carbon-based materials for hydrogen storage: advancement and challenges, Journal of Materials Chemistry A 1 (2013) 9365–9381.

[45] K. Spyrou, D. Gournis, P. Rudolf, Hydrogen storage in graphene-based nanomaterials: Efforts towards enhanced hydrogen absorption. ECS Journal of Solid State Science and Technology 2 (2013) 3160–3169.

[46] Y. Yurum, A. Taralp, T.N. Veziroglu, Storage of hydrogen in nanostructured carbon materials, International Journal of Hydrogen Energy 34 (2009) 3784–3798.

[47] A. Geim, K.S. Novoselov, The rise of graphene, Nature Materials 6 (2007) 183.

[48] A. Peigney, Ch. Laurent, E. Flahaut, R.R. Bacsa, A. Rousset, Specific surface area of carbon nanotubes and bundles of carbon nanotubes, Carbon 39 (2001) 507–514.

[49] M. Yi, Z. Shen, A review on mechanical exfoliation for scalable production of graphene, Journal of Materials Chemistry A 3 (2015) 11700–11715.

[50] H. Tetlow, J.P. de Boer, I.J. Ford, D.D. Vvedensky, J. Coraux, L. Kantorovich, Growth of epitaxial graphene: theory and experiment, Physics Reports 542 (2014) 195–295.

[51] S. Pei, H.M. Cheng, The reduction of graphene oxide, Carbon 50 (2012) 3210–3228.

[52] A. Klechikov, G. Mercier, T. Sharifi, I. A. Baburin, G. Seifert, A.V. Talyzin, Hydrogen storage in high surface area graphene scaffolds, Chemical Communications, 51 (2015) 15280–15283.

[53] James Hedberg, A wavey sheet of graphene, http://www.jameshedberg.com/scienceGraphics.php?sort=all&id=graphene-sheet-wavey (October 2017).

[54] R. Saito, G. Dresselhaus, M.S. Dresselhaus, Physical properties of carbon nanotubes, World Scientific, 1998.

[55] G.E. Ioannatos, X.E. Verykios, H_2 storage on single- and multi-walled carbon nanotubes, International Journal of Hydrogen Energy 35 (2010) 622–628.

[56] F. Kreupl, A.P. Graham, G.S. Duesberg, W. Steinhögl, M. Liebau, E. Unger, W. Hönlein, Carbon nanotubes in interconnect applications, Microelectronic Engineering, 64 (2002) 399–408.

[57] M. Sevilla, R. Mokaya, Energy storage applications of activated carbons: supercapacitors and hydrogen storage, Energy & Environmental Science 7 (2014) 1250–1280.

[58] R. Chahine, T.K. Bose, Characterization and optimization of adsorbents for hydrogen storage, Hydrogen Energy Progress: Proceedings of the 11th World Hydrogen Energy Conference, International Association for Hydrogen Energy (1996) p. 1259–1264.

[59] S.K. Bhatia, A.L. Myers, Optimum conditions for adsorptive storage, Langmuir 22 (2006) 1688–1700.

[60] H. Furukawa, K.E. Cordova, M. O'Keeffe, O.M. Yaghi, The chemistry and applications of metal-organic frameworks. Science 341 (2013) 1230444.

[61] B. Panella, M. Hirscher, Hydrogen physisorption in metalorganic porous crystals, Advanced Materials 17 (2005) 538–41.

[62] L. Huang, H. Wang, J. Chen, Z. Wang, J. Sun, D. Zhao, Y. Yan, Synthesis, morphology control, and properties of porous metal-organic coordination polymers, Microporous and Mesoporous Materials 58 (2003)105–14.

[63] H. Zhao, H. Song, L. Chou, Facile synthesis of MOF-5 structure with large surface area in the presence of benzoyl peroxide by room temperature synthesis, Materials Chemistry Physics 43 (2014) 1005–1011.

[64] W.J. Son, J. Kim, J. Kim, W.S. Ahn, Sonochemical synthesis of MOF-5, Chemical Communications 47 (2008) 6336–6338.

[65] R. Sabouni, H. Kazemian, S. Rohani, A novel combined manufacturing technique for rapid production of IRMOF-1 using ultrasound and microwave energies, Chemical Engineering Journal 165 (2010) 966–73.

[66] H.W. Langmi, J. Ren, B. North, M. Mathe, D. Bessarabov, Hydrogen storage in metal-organic frameworks: a review, Electrochimica Acta 128 (2014) 368–392.

[67] M.P. Suh, H.J. Park, T.K. Prasad, D.W. Lim, Hydrogen storage in metal-organic frameworks, Chemical Reviews 112 (2011) 782–835.

[68] D. Saha, Z. Wei, S. Deng, Hydrogen adsorption equilibrium and kinetics in metal-organic framework (MOF-5) synthesized with DEF approach, Separation and Purification Technology 64 (2009) 280–287.

[69] S.S. Kaye, A. Dailly, O.M. Yaghi, J.R. Long, Impact of preparation and handling on the hydrogen storage properties of Zn_4O (1,4-benzenedicarboxylate)$_3$ (MOF-5), Journal of American Chemical Society 129 (2007) 14176–14177.

[70] M. O'Keeffe, M. Eddaoudi, H. Li, T. Reineke, O.M. Yagh, Frameworks for extended solids: geometrical design principles, Journal of Solid State Chemistry 152 (2000) 3.

[71] Helmholtz-Zentrum Berlin, Quantachrome Autosorb1-MP, https://www.helmholtz-berlin.de/user/experimental-infrastructures/lab-clusters/degas/degas-equipment/autosorb_en.html (October 2017).

[72] M. Thommes, Physical adsorption characterization of nanoporous materials, Chemie Ingenieur Technik 82 (2010) 1059–1073.

[73] S. Brunauer, P.H. Emmett, E. Teller, Adsorption of gases in multimolecular layers, Journal of the American Chemical Society 60 (1938) 309–319.

[74] International Standard Organization, Determination of the specific surface area of solids by gas adsorption — BET method, ISO 9277: 2010(E), 2nd edition, 2010.

[75] J.H. De Boer, B.G. Linsen, T. Van der Plas, G.J. Zondervan, Studies on pore systems in catalysts: VII. Description of the pore dimensions of carbon blacks by the t method, Journal of Catalysis 4 (1965) 649–653.

[76] E.P. Barrett, L.G. Joyner, P.P. Halenda, The determination of pore volume and area distributions in porous substances. I. Computations from nitrogen isotherms, Journal of the American Chemical Society 73 (1951) 373–380.

[77] J. Landers, G.Y. Gor, A.V. Neimark, Density functional theory methods for characterization of porous materials, Colloids and Surfaces A: Physicochemical and Engineering Aspects 437 (2013) 3–32.

[78] A.V. Neimark, Y. Lin, P.I. Ravikovitch, M. Thommes, Quenched solid density functional theory and pore size analysis of micro-mesoporous carbons, Carbon 47 (2009) 1617–1628.

[79] Quantachrome Instruments, Gas sorption system operation manual AUTOSORB AS-1/AS1Win, version 5.54, 2008.

[80] K.J. Gross, The PCTPro-2000–The Ultimate Tool for Gas Sorption Analysis, Material Matters, 2 (2007) 26–28.

[81] SETARAM Instrumentation, PCTPRO-2000, http://www.setaram.jp/?attachment_id=19410 (October 2017).

7 Publications

7.1 List of publications included in the current thesis

I. N. Kostoglou, V. Tzitzios, A. Kontos, K. Giannakopoulos, C. Tampaxis, A. Papavasiliou, G. Charalambopoulou, T. Steriotis, Y. Li, K. Liao, K. Polychronopoulou, C. Mitterer, C. Rebholz, Synthesis of nanoporous graphene oxide absorbents by freeze-drying or microwave radiation: characterization and hydrogen storage, *International Journal of Hydrogen Energy* 40 (2015) 6844-6852.

II. N. Kostoglou, A. Tarat, I. Walters, V. Ryzhkov, C. Tampaxis, G. Charalambopoulou, T. Steriotis, C. Mitterer, C. Rebholz, Few-layer graphene-like flakes derived by plasma treatment: a potential material for hydrogen adsorption and storage, *Microporous and Mesoporous Materials* 225 (2016) 482-487.

III. N. Kostoglou, C. Koczwara, C. Prehal, V. Terziyska, B. Babic, B. Matovic, G. Constantinides, C. Tampaxis, G. Charalambopoulou, T. Steriotis, S. Hinder, M. Baker, K. Polychronopoulou, C. Doumanidis, O. Paris, C. Mitterer, C. Rebholz, Nanoporous activated carbon cloth as a versatile material for hydrogen adsorption, selective gas separation and electrochemical energy storage, *Nano Energy* 40 (2017) 49-64.

IV. V. Tzitzios, N. Kostoglou, M. Giannouri, G. Basina, C. Tampaxis, G. Charalambopoulou, T. Steriotis, K. Polychronopoulou, C. Doumanidis, C. Mitterer, C. Rebholz, Solvothermal synthesis, nanostructural characterization and gas cryo-adsorption studies in a metal-organic framework (IRMOF-1) material, *International Journal of Hydrogen Energy* 42 (2017) 23719-23727.

7.2 Personal contribution to the publications included in the current thesis

➢ Publication I

The concept and planning of this publication was my original idea. The microwave-exfoliated graphene oxide material (mic-GO) was prepared by myself under the supervision of Dr. Vasileios Tzitzios from NCSR Demokritos. The low-pressure N_2 and H_2 gas adsorption measurements were carried out by myself under the instructions of Mr. Christos Tampaxis at the NCSR Demokritos facilities. The porosity-related properties of Table 1 were calculated by myself using the ASiQWin software. The SEM and TEM images were collected by Dr. Angeliki Papavassiliou and Dr. Konstantinos Giannakopoulos, respectively, at the NCSR Demokritos facilities under my guidance during the sessions. I

evaluated all the characterization data with the exception of the micro-Raman analysis which was done by Dr. Athanassios Kontos from NCSR Demokritos. Finally, I developed the structure of the paper, prepared almost every figure (except Fig. 2) and wrote the manuscript (except some parts of the Structural properties section), under the supervision and guidance of Prof. Claus Rebholz and Prof. Christian Mitterer.

- **Publication II**

The concept and planning of this publication was my original idea. The SEM and TEM images were collected by Dr. Angeliki Papavassiliou and Dr. Konstantinos Giannakopoulos, respectively, at the NCSR Demokritos facilities under my guidance during the sessions. I collected the X-ray diffractograms of the few-layer graphene (FLG) powders at the University of Cyprus, while the data interpretation (see Table 1) was carried out in collaboration with Dr. Vladislav Ryzhkov from Fibrtec Inc. The porosity-related properties of Table 2 were calculated by myself using the ASiQWin software. I evaluated all the characterization data with the exception of the XPS analysis which was done by Dr. Afshin Tarat from Perpetuus Carbon Technologies. Finally, I developed the structure of the paper, prepared three out of five figures (Figs. 1, 4 and 5) and wrote the whole manuscript, under the supervision and guidance of Prof. Claus Rebholz and Prof. Christian Mitterer.

- **Publication III**

The concept and planning of this publication was my original idea. I collected the X-ray diffractogram and Raman spectrum of the activated carbon cloth (ACC) material at the Montanuniversität Leoben, as well as the FT-IR spectrum at the University of Cyprus. The porosity-related properties of Table 1 were calculated by myself using the ASiQWin software. I evaluated all the characterization data except the ones referring to the electrochemical performance of the ACC material which was done by Mr. Christian Koczwara and Mr. Christian Prehal from the Institute of Physics of the Montanuniversität Leoben. Finally, I developed the structure of the paper, prepared all the figures and wrote the manuscript (except the parts related to the electrochemical performance of the ACC material), under the supervision and guidance of Prof. Claus Rebholz and Prof. Christian Mitterer.

- **Publication IV**

The concept and planning of this publication was my original idea. I suggested a potential approach/methodology, based on the literature, to synthesize the IRMOF-1 material, while the actual synthesis was performed by Dr. Vasileios Tzitzios from NCSR Demokritos. I collected the FT-IR spectrum of the IRMOF-1 material at the University of Cyprus. The porosity-related properties of Table 4 were calculated by myself using the ASiQWin

software. I evaluated all the characterization data with the exception of the XRD analysis which was done by Dr. Maria Giannouri and Dr. Georgia Basina from Demokritos NCSR. Finally, I developed the structure of the paper, prepared all the figures and wrote the manuscript (except few parts of the XRD analysis in the Morphology, surface chemistry and structure section), under the supervision and guidance of Prof. Claus Rebholz and Prof. Christian Mitterer.

Publication no. (#)	Manuscript concept & planning	Experimental Studies	Data analysis & interpretation	Manuscript preparation
I	100 %	70 %	80 %	80 %
II	100 %	40 %	70 %	90 %
III	100 %	30 %	65 %	80 %
IV	100 %	65 %	75 %	80 %

7.3 List of publications not included in the current thesis

- N. Kostoglou, K. Polychronopoulou, C. Rebholz, Thermal and chemical stability of boron nitride (h-BN) nanoplatelets, *Vacuum* 112 (2015) 42-45.
- N. Kostoglou, G. Constantinides, G. Charalambopoulou, T. Steriotis, K. Polychronopoulou, Y. Li, K. Liao, V. Ryzhkov, C. Mitterer, C. Rebholz, Nanoporous spongy graphene: Potential applications for hydrogen adsorption and selective gas separation, *Thin Solid Films* 596 (2015) 242-249.
- N. Kostoglou, J. Lukovic, B. Babic, B. Matovic, D. Photiou, G. Constantinides, K. Polychronopoulou, V. Ryzhkov, B. Grossmann, C. Mitterer, C. Rebholz, Few-step synthesis, thermal purification and structural characterization of porous boron nitride nanoplatelets, *Materials and Design* 110 (2016) 540-548.
- N. Kostoglou, E. Gunduz, T. Isik, V. Ortalan, G. Constantinides, A. Kontos, T. Steriotis, V. Ryzhkov, E. Bousser, A. Matthews, C. Doumanidis, C. Mitterer, C. Rebholz, Novel combustion synthesis of carbon foam-aluminum fluoride nanocomposite materials, "Under review".
- M. Aureli, A.S.M. Alzaabi, A.G.S. Hussien , C.C. Doumanidis, S.M. Jaffar, I.E. Gunduz, C. Rebholz, N. Kostoglou, Y. Liao, C.C. Doumanidis, Thermal observation and adaptive control of fractal structure in ball-milled materials, "Under review".

Publication I

Synthesis of nanoporous graphene oxide adsorbents by freeze-drying or microwave radiation: Characterization and hydrogen storage properties

N. Kostoglou, V. Tzitzios, A.G. Kontos, K. Giannakopoulos, C. Tampaxis, A. Papavasiliou, G. Charalambopoulou, T. Steriotis, Y. Li, K. Liao, K. Polychronopoulou, C. Mitterer, C. Rebholz

International Journal of Hydrogen Energy 40 (2015) 6844-6852

Synthesis of nanoporous graphene oxide adsorbents by freeze-drying or microwave radiation: Characterization and hydrogen storage properties

Nikolaos Kostoglou[a,b,*], Vasilios Tzitzios[c], Athanassios G. Kontos[c], Konstantinos Giannakopoulos[c], Christos Tampaxis[c], Aggeliki Papavasiliou[c], Georgia Charalambopoulou[c], Theodore Steriotis[c], Yuanqing Li[d], Kin Liao[d], Kyriaki Polychronopoulou[e,***], Christian Mitterer[b], Claus Rebholz[a,**]

[a] Department of Mechanical and Manufacturing Engineering, University of Cyprus, 1678 Nicosia, Cyprus

[b] Department of Physical Metallurgy and Materials Testing, Montanuniversität Leoben, 8700 Leoben, Austria

[c] National Center for Scientific Research Demokritos, Agia Paraskevi Attikis, 15310 Athens, Greece

[d] Department of Aerospace Engineering, Khalifa University of Science, Technology and Research, Abu Dhabi, United Arab Emirates

[e] Department of Mechanical Engineering, Khalifa University of Science, Technology and Research, Abu Dhabi, United Arab Emirates

Highlights

- High-surface area GOs were synthesized by freeze drying and microwave radiation
- Porosity, structure and morphology were studied by BET, Raman, SEM and TEM
- H_2 storage capacity was evaluated against commercial nanocarbons
- Reversible H_2 storage with gravimetric capacities 0.5-0.7 wt.% at 77 K and 1 bar
- H_2 storage behavior was correlated to specific textural/surface features

Abstract

In the present work, we synthesized and systematically characterized two novel graphene-based nanomaterials, a chemically reduced graphene oxide (GO) sponge and a microwave-exfoliated GO. Textural properties were determined by N_2 adsorption/desorption at 77 K, while additional characterization techniques were employed, such as Micro-Raman Spectroscopy, Field-Emission Scanning Electron Microscopy and High-Resolution Transmission Electron Microscopy, to elucidate further the structural and morphological

features. Both nanomaterials were additionally evaluated for their H_2 storage capacity and were critically compared to commercially available carbons (e.g. few-layer graphenes, carbon nanotubes) based on systematic H_2 adsorption/desorption measurements at 77 K between 0 and 1 bar. Maximum H_2 gravimetric capacities of ~0.5 wt.% and ~0.7 wt.% were recorded at 77 K and 1 bar for the reduced GO sponge and the microwave-exfoliated GO, respectively.

Keywords: Nanoporous sorbents; Graphene oxide; Hydrogen storage; Physical adsorption; Gravimetric capacity; Characterization

1. Introduction

The transition to a future hydrogen-fueled society requires a convenient, efficient and safe H_2 storage method, especially for on-board automotive applications [1]. In recent years, scientific research has been focused on the so-called "materials-based H_2 storage", in which supercritical hydrogen gas is physically or chemically sorbed by solid materials [2,3]. Nanoporous carbon sorbents, with the ability to bind molecular H_2 into their external surface and internal pores by the mechanism of physical adsorption, are considered an appealing storage solution [4]. The important advantages of complete reversibility and fast kinetics are attributed to the weak nature of van der Waals interactions between the solid surface and the gas molecules [5]. However, the cryogenic temperatures (e.g. 77 K) required to achieve significant storage capacities constitute the major drawback of physisorption processes [6].

A plethora of carbonaceous materials, ranging from amorphous activated carbons to carbon nanostructures (nanotubes, nanofibers, fullerenes, etc.), have attracted over the years significant attention as potential H_2 stores [7,8]. These materials are quite interesting as adsorbents, because they exhibit large surface areas and pore volumes, lightweight, chemical and thermal stability but also low manufacturing cost [4,7]. However, many controversial results have been reported concerning their H_2 storage capacity. It is well known that pore properties play a significant role in the adsorption mechanism; microporous carbons (pore size < 2 nm) can be more efficient for H_2 storage, as besides their larger surface areas and pore volumes, they favor stronger gas-solid interactions as the potential fields of the opposite pore walls overlap.

More recently, exfoliated graphene and graphene oxide (GO) started to be examined as potential materials for H_2 storage applications [9-14]. Especially GO combines the

advantages of graphene (i.e. high surface area, low density, environmental friendliness, low processing cost) with convenient surface chemistry that allow further modification/functionalization [15,16]. GO consists of highly-oxidized few-layer graphene sheets with multiple surface functional groups such as epoxides (-ROOH, -ROOR) and hydroxyls (-OH) as well carbonyls (C=O) and carboxyls (-COOH) at the edges. Based on experimental and theoretical studies [17-19], it has been proposed that the presence of such oxygen groups on the carbon surfaces may enhance the adsorbate-adsorbent interactions leading to increased H_2 storage capacity. Indeed, grand canonical Monte Carlo method (GCMC) simulations of H_2 adsorption isotherms at 77 K within graphene and graphene-oxide slit-like micropores showed that the presence of surface functionality can induce significant changes in the energetic landscapes inside the pores, while the density of the adsorbed phase increases with increasing surface oxygen content [17]. As such, GO materials present interesting systems for hydrogen storage processes.

In general, the facile, efficient and low-cost development of graphene-based nanostructures, including nanosheets [9,24,27], sponges [21-23] and foams [11,25], with narrow micropore sizes and large surface areas, are the subject of continuous effort. In this respect, nanoporous derivatives of GO have been reported from graphite oxide treatment either by wet chemical reduction [9,13,21-24], thermally-induced exfoliation (with or without gas stream) [10,12-14,20,24] or microwave-assisted thermal shock methods [26-29]. Srinivas et al. [9] synthesized graphene-like nanosheets with high-surface area (640 m^2/g) by chemically reducing graphite oxide using hydrazine hydrate (N_2H_4); a H_2 storage capacity of 0.64 wt % was reported at 77 K and 1 bar that reached up to 1.17 wt.% at 10 bar. Multi-layered GO with optimized interlayer distance (0.65 nm) was modulated by thermal annealing and showed an enhanced H_2 adsorption of 4.8 wt.% at 77 K and 90 bar [10]. Xia et al. [12] produced a series of hierarchical porous graphene-like sheets with large surface areas (up to 532 m^2/g) and pore volumes (up to 1.67 cm^3/g) by CO_2 activation of graphite oxide up to 950 ^oC; storage capacities of up to 0.75 wt.% H_2 were reported at 77 K and 1 bar. Recently, Hudson et al. [13] prepared an exfoliated GO (375 m^2/g) by thermally reducing graphite oxide that adsorbed 2.07 wt.% H_2 at 77 K and 50 bar.

In the present work, we have successfully produced two new nanoporous GO-based materials, in powder-form, following two entirely different exfoliation processes. The first one was a reduced spongy GO derived by hydrothermal treatment of graphite oxide (synthesized by Hummer's method) in combination with freeze drying; this type of

material has lately attracted a lot of interest due to its unique properties [21-23,30]. Nevertheless, it has not been characterized extensively. The second one was an exfoliated fluffy GO induced by microwave radiation of graphite oxide (synthesized by Staudenmaier's method), one of the most popular techniques to produce GO materials with relatively large surface areas [26-29]. We have demonstrated that a combined hydrothermal-freeze frying approach leads to a reduced GO material with a significant fraction of micropores (pore width ~0.7 nm), while the microwave-exfoliation approach provides a clearly mesoporous GO material that exhibits one of the largest surface areas (~630 m^2/g) ever reported in similar studies [26-29]. Apart from the thorough textural, structural and morphological characterization of these two interesting nanomaterials, emphasis was also placed on the evaluation of their H_2 sorption properties at 77 K and up to 1 bar. To our best knowledge, none of these two types of materials has previously been examined for H_2 storage. Therefore, we compared the H_2 storage capacities of the as-produced samples to well-established and commercially available nanocarbons such as few-layer graphenes and multi-walled carbon nanotubes, the surface of which contained a certain amount of oxygenated (e.g. -COOH) functional groups. The H_2 uptake of all the studied materials was correlated to their textural properties (i.e. specific surface area, micropore volume, etc.).

2. Materials and experimental methods

2.1 Synthesis

A sponge-like nanostructure was produced by hydrothermal treatment of graphite oxide with hydroiodic acid (HI) in combination with freeze drying. The original graphite oxide was synthesized from graphite powder using a modified Hummer's method [21,31]. The obtained suspension was then diluted in an aqueous solution (2 mg/ml) and treated by ultrasonication for 30 min. In a typical synthesis, 1 ml of HI (30 %) was added into 60 ml homogeneous graphite oxide aqueous solution (2 mg/ml) and then the mixture was sealed in a 100 ml PTFE-lined stainless steel autoclave, where it was maintained at 180 ^oC for 12 h. As soon as the reactor cooled down to room temperature, the as-prepared graphene hydrogel (GH) was taken out and instantly submerged into distilled water for 24 h to remove the residual HI. In order to control the density of the final product, water was removed by 75 wt.% from the original GH through evaporation at room temperature; Li et al. [21] showed that a higher surface area can be obtained by this way. In a final step, the

sample (denoted hereafter as GS-75) was freezed with liquid nitrogen (LN_2) and freeze-dried in vacuum to remove the remaining water and obtain the desirable sponge-like nanostructure.

An exfoliated graphene oxide (denoted hereafter as mic-GO) was produced by microwave radiation treatment of graphite oxide. The original graphite oxide was synthesized from graphite powder using a modified Staudenmaier's method [32,33]. In a typical synthesis, 10 g of powdered graphite (purum, powder ≤ 0.2 mm; Fluka) were added into a mixture of concentrated sulfuric acid (H_2SO_4, 400 ml, 95-97 wt.%) and nitric acid (HNO_3, 200 ml, 65 wt.%), while cooling in an ice-water bath. Potassium chlorate powder ($KClO_3$, 200 g, purum, > 98 %; Fluka) was added to the mixture in small portions, while stirring and cooling. The reactions were quenched after 18 h by pouring the mixture into distilled water and the oxidation product was washed until pH 6. The as-prepared graphite oxide was then dried at room temperature. Finally, the sample was placed in a microwave oven (Panasonic NE-1856, 1800 W) for less than 1 min, where it was expanded and transformed into a black powder with fluffy texture.

2.2 Commercial materials

Few-layer graphenes (FLGs), in the form of nanoplatelets with stacks of 3-6 layers, diameter < 2 mm, thickness < 3 nm, 4.0 wt.% -COOH content and 96 % purity, were provided by Perpetuus Advanced Materials, UK (product under development). The FLGs were produced through argon (Ar) plasma exfoliation of natural graphite [34]; they were also functionalized with -COOH groups via oxygen (O_2) plasma treatment.

Multi-walled carbon nanotubes (MWCNTs) with outer diameter 10-20 nm, inner diameter 5-10 nm, length 10-30 mm, 2.0 wt.% -COOH content and 95 % purity were obtained by Chengdu Organic Chemicals Co. Ltd, Chinese Academy of Sciences, China (product no. TNMC3). The MWCNTs were produced by chemical vapor deposition (CVD) through catalytic decomposition of natural gas (~90% CH_4) over a Ni-based catalyst; they were also purified through oxidation in a mixture of potassium permanganate ($KMnO_4$) and sulfuric acid (H_2SO_4).

Short multi-walled carbon nanotubes (sh-MWCNTs) with outer diameter 7-20 nm, inner diameter 3-7 nm, length 100-500 nm and low-purity (50-80 %) were provided by Rosseter Holdings Ltd, Cyprus (commercial product Ros1™). The Ros1 nanomaterial was actually a mixture of sh-MWCNTs, carbon polyhedral nanoparticles and graphene-like nanoplatelets.

It was produced by a self-regulated low-voltage arc-discharge method by employing ethanol (C_2H_6O) and graphitic anodes and cathodes [35]. The inner cores of the cathode deposits were collected and milled in a Hosokawa 100 AFG Fluidized Bed Jet Mill machine to reduce the size of the particles.

2.3 Characterization techniques

Micro-Raman measurements were performed in backscattering configuration on a Renishaw inVia Reflex microscope. Excitation was carried out with a Fantago diode-pumped solid-state laser emitting at 514.4 nm. The laser beam was focused onto the samples by means of an 50× objective at a power density of 0.1 mW/mm^2 in order to avoid local heating effects.

Surface morphology was studied with a JEOL JSM-7401F field emission scanning electron microscope (FE-SEM). A low acceleration voltage was applied (~2 kV) and a working distance was set to 6 mm and 3 mm. Powder samples were mounted onto round metallic (brass) substrates using a double coated conductive carbon tape. High resolution images of the materials were obtained by a Philips CM-20 transmission electron microscope (TEM) with a LaB_6 filament, equipped with an energy dispersive X-ray spectrometer (EDS). The instrument operated at 200 kV acceleration voltage, while the powders were dispersed in ethanol through ultra-sonication and then placed onto a holey carbon film mounted on a copper grid.

N_2 adsorption/desorption isothermal curves at 77 K were recorded using a volumetric gas analyzer Autosorb 1-MP by Quantachrome Instruments, while nitrogen gas of ultra-high purity was used (99.9999%). Prior to the measurements, the samples (30-40 mg) were out-gassed under high vacuum (10^{-6} mbar) at 250 ^{o}C for 12 h. Textural properties were determined using Quantachrome's ASiQWin software (version 2.0). The total specific surface area (SSA) was calculated by the Multi-point Brunauer-Emmet-Teller (BET) method in the relative pressure range $0.1 < P/P_0 < 0.35$. The micropore volume and the micropore surface area were estimated by the Carbon Black (CB) t-plot method. Pore size distribution (PSD) analysis was established on the basis of two different methods: (i) the Barret-Joyner-Halenda (BJH) method was applied on the desorption isotherm branch of the mesoporous materials; and (ii) the Quenched Solid Density Functional Theory (QSDFT), based on the nitrogen-carbon equilibrium transition kernel at 77.4 K for slit-shaped pores, was applied on the adsorption isotherm branch of the materials, containing

both micropores and mesopores. The same volumetric instrument was also employed to obtain H_2 adsorption/desorption isotherms curves at 77 K and pressures up to 1 bar; hydrogen gas of ultrahigh purity (99.9999%) was used.

3. Results and discussion

3.1 Porous properties

Low-pressure N_2 adsorption/desorption isothermal curves at 77 K for all the studied nanomaterials are presented in Fig. 1. The newly-synthesized GS-75 and mic-GO, as well as the commercial FLGs and MWCNTs, exhibited type IV isotherms according to the IUPAC classification [36] characteristic of mesoporous materials, while only Ros1 demonstrated type II isotherm typical of non-porous materials. The formation of hysteresis loops at the relative pressure range $0.45 < P/P_0 < 0.99$ is associated with nitrogen's capillary condensation inside the mesopores. None of the isotherms reached a plateau at $P/P_0 \sim 0.99$; instead they were extended indefinitely, representing unrestricted multilayer adsorption due to the existence of macropores or external rough surface. For this reason, the total pore volume cannot be properly estimated on the basis of the single-point Gurvich rule [37] by assuming that the pores are filled with LN_2 at a relative pressure close to unity ($P/P_0 = 0.99$). The textural characteristics of the studied materials are presented in Table 1.

The GS-75 demonstrated enhanced physisorption at lower relative pressures ($P/P_0 < 0.01$), probably due to microporosity (Fig. 1a). The total specific surface area was calculated at 348 m^2/g based on the Multi-point BET method, while the micropore surface area and volume corresponded to 88 m^2/g and 0.04 cm^3/g, respectively, on the basis of the Carbon Black V-t method. The PSD analysis through QSDFT provided a bimodal distribution with two distinct peaks at 0.7 nm and 3.4 nm, and thus confirmed the presence of super-micropores (0.7-2 nm) and small mesopores. Furthermore, the GS-75 exhibited a characteristic H3-type hysteresis loop related to slit-shaped pores, while the step at the closure of the loop implies that desorption is achieved through cavitation; spontaneous nucleation and growth of gaseous bubbles inside the condensed N_2, leading to evaporation from the mesopores [38].

Regarding the commercial carbons in Fig. 1a, the FLGs adsorbed even greater N_2 amounts for $P/P_0 < 0.01$, while super-micropores were also detected in this case as QSDFT revealed a maximum at 0.8 nm. The FLGs demonstrated also the largest BET surface area (724

m^2/g), as well as the largest micropore surface area (275 m^2/g) and micropore volume (~0.12 cm^3/g) within the context of this study. The MWCNTs had a smaller surface area and an insignificant micropore volume, while they were characterized mainly by large mesopores (20-50 nm), as BJH method indicated a broad peak around 18.9 nm. The Ros1 adsorbed minor N_2 amounts due to its macroporous/non-porous nature; its BET surface area was much lower compared to the other materials, while no micropore volume was detected. The mic-GO is presented separately from the rest of the materials (Fig. 1b), as it demonstrated a swelling behavior during N_2 adsorption [39]. The impressive size of the hysteresis loop and the large condensed N_2 volumes are associated with the expansion of the material's volume. More specifically, the exfoliated GO layers are moving apart as capillary condensation occurs and therefore an increased N_2 amount can be adsorbed inside the mesopores. Hence, a reliable PSD analysis is not feasible due to the swelling phenomenon. However, the H3-type hysteresis loop indicates pores with slit-shape, while the desorption mechanism involves cavitation (single-step closure), as described previously in the case of GS-75. Another interesting fact was the large BET surface area of the mic-GO that reached 626 m^2/g, but a minor micropore volume was detected based on the Carbon Black t-plots. Prior to microwave-treatment, the original GO produced by the modified Staudenmaier's method had a quite small surface area (~20 m^2/g); after applying microwave radiation the surface area increased dramatically (~31 times larger).

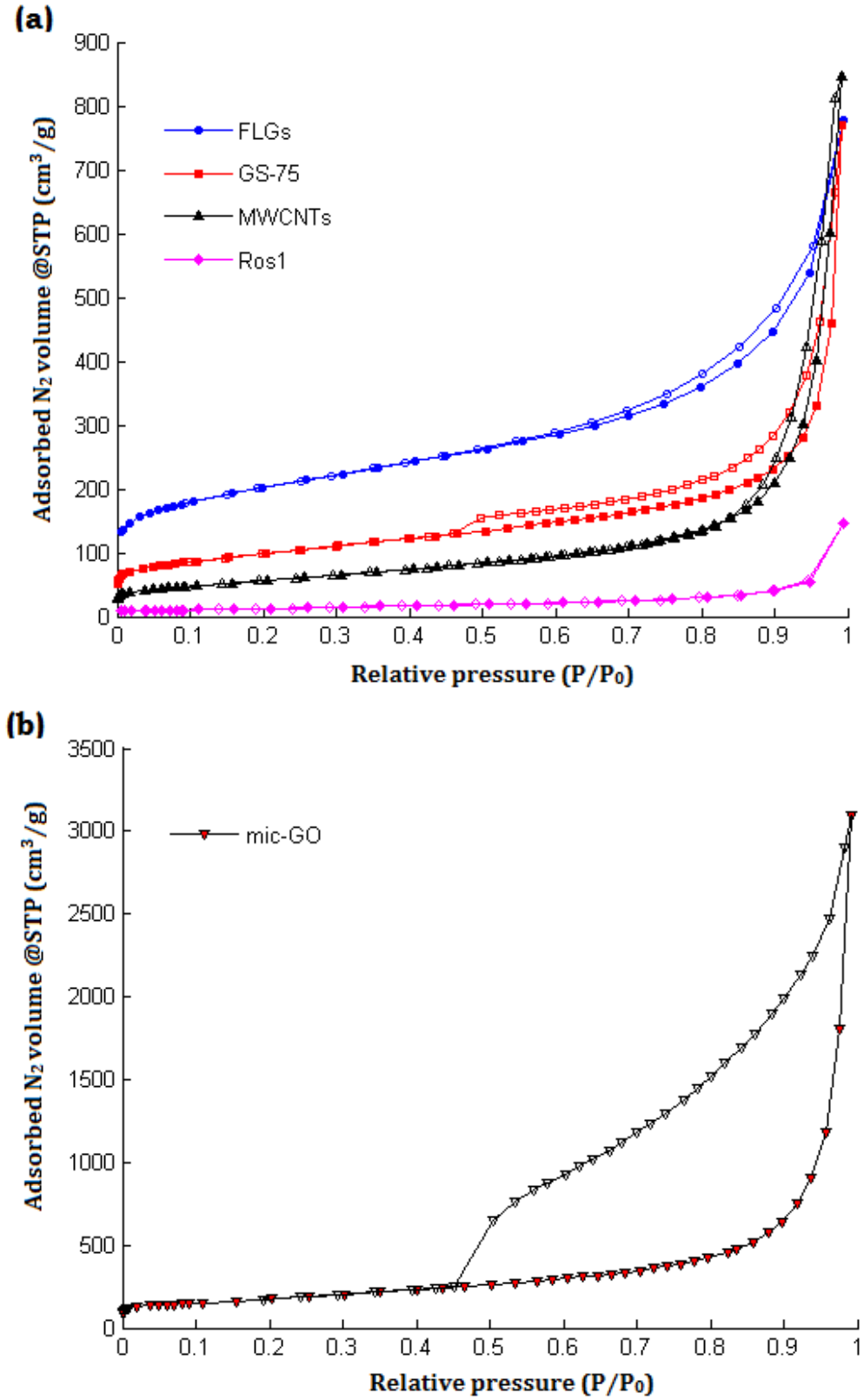

Fig. 1: (a) N_2 adsorption (colored symbols) and desorption (empty symbols) isothermal curves at 77 K for FLGs, GS-75, MWCNTs and Ros1 and (b) swelling behavior by the as-prepared mic-GO during N_2 adsorption at 77 K.

Table 1: Porosity properties based on N_2 adsorption/desorption isothermal curves at 77 K.

Materials	S_{BET} [m^2/g]	C_{BET}	V_{micro} [cm^3/g]	S_{micro} [m^2/g]	S_{micro}/S_{BET} [%]
FLGs	724	290	0.119	275	37.98
mic-GO	626	147	0.007	5	0.79
GS-75	348	238	0.04	88	25.28
MWCNTs	201	130	0.001	2	0.99
Ros1	44	124	0	0	0

S_{BET}: total specific surface area derived by the multi-point Brunauer-Emmet-Teller method, C_{BET}: BET constant, V_{micro}: micropore volume derived by the Carbon Black V-t method, S_{micro}: micropore specific surface area derived by the Carbon Black V-t method, (S_{micro}/S_{BET}): percentage (%) of microporous specific surface area relative to BET specific surface area

3.2 Structural properties

Raman spectra of the GO samples (GS-75 and mic-GO), in comparison with the commercial carbon nanomaterials, are shown in Fig. 2. All reference samples (FLGs, MWCNTs and Ros1) present three peaks in the 1200-1700 cm^{-1} range. The modes are attributed to the defect-activated D1 band at ~1353 cm^{-1} due to the vibrations of C atoms with dangling bonds, the graphitic G band at ~1580 cm^{-1} arising from the bond stretching of sp^2 carbon atoms in a two-dimensional hexagonal lattice and the higher frequency defect activated D2 band at ~1620 cm^{-1}. In the high frequency region, the materials exhibited the second order overtone of D1 band at ~2710 cm^{-1} and the defect activated combination mode (D1+D2) at ~2940 cm^{-1}. Table 2 shows values obtained after numerically fitting the raw spectra of the peak frequency (F), full width at half maximum (W) and relative integrated intensity ratio of the D1-band to that of the graphitic G-band, often taken as a measure of the disorder in the structure. Among the three different reference samples, Ros1 clearly outperformed in terms of less defected structure and narrow distribution of MWCNTs dimensions. For the other two samples (FLGs and MWCNTs) a weak peak at 3080 cm^{-1} was observed, which implies the existence of C-H stretching vibrations.

The prepared GO samples presented instead two broad Raman features in the 1200-1700 cm^{-1} range, the one retains the Lorenzian character and peak frequency of the D1-band, while the other is very broad and highly anisotropic with its peak frequency significantly blue shifted to that of the G-band in CNTs and graphite, to 1603 cm^{-1}. Eventually, this band is a merging of the superimposed G and D2 bands [40,41]. In addition, all bands (including

the first and the second order peaks) exhibited substantial broadening, characteristic of disorder in the structure and/or intense surface modification [41].

The characteristic parameters of the D and G bands as well their integrated intensity ratio obtained from the analysis of the GO spectra in our study (see Table 2) were very similar to those generally observed from pristine GO materials [40,42,43]. Reduced GO usually leads to increased $I_{D1/G}$ ratio [42,44], while a decrease has been also observed by appropriate chemical treatment that heals the structure [43]. Furthermore, in order to account for the anisotropy of the G band, we have fitted the spectra by adding a new broad spectral component (D3 band) at ~1550 cm^{-1}, which is related to the carbon vibrations by the extensive coverage of GO by oxygen groups, also observed before in GO [40,45]. Between the two prepared samples, the mic-GO presented larger $I_{D1/G}$ ratios and broader spectral lines, consistently with more defective graphene structure.

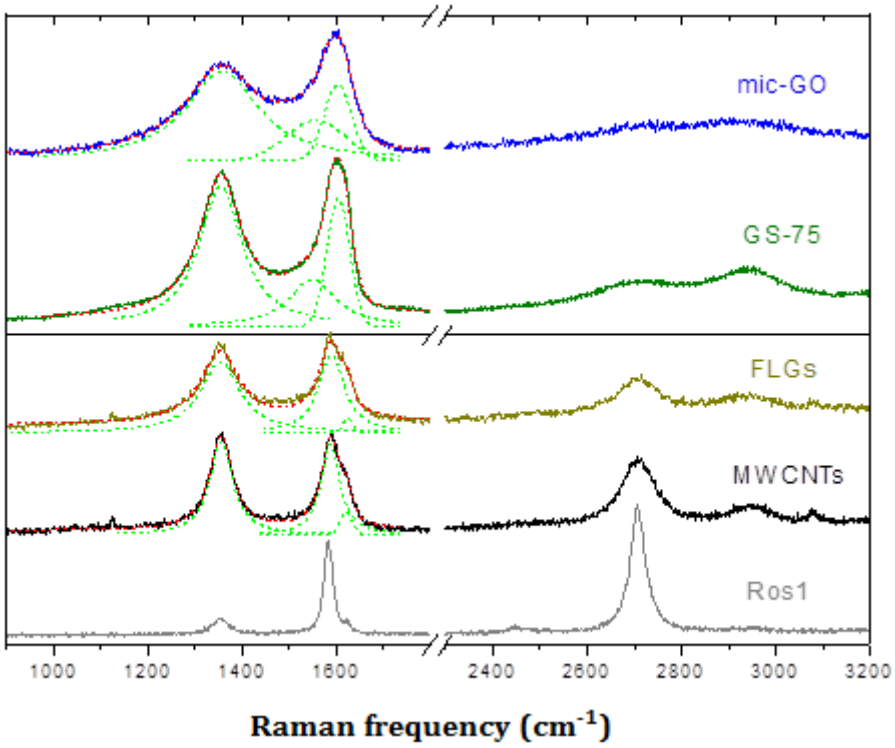

Fig. 2: Raman spectra of the as-prepared GOs (mic-GO, GS-75) and commercial samples (FLGs, MWCNTs, Ros1) obtained by excitation at 514.4 nm; spectral fitting curves and fitting components are shown with dashed lines.

Table 2: Peak frequencies (F) and full width at half maximum (W) of the various Raman bands (D1, G, D2 and D3) in the 1200-1700 cm^{-1} range.

Materials	D1		G		$I_{D1/G}$	D2	D3
	(F/cm^{-1})	(W/cm^{-1})	(F/cm^{-1})	(W/cm^{-1})		(F/cm^{-1})	(F/cm^{-1})
mic-GO	1357.8	188.5	1602.7	68.1	4.8	-	1555.8
GS-75	1354.9	108.5	1604.2	56.6	3.2	-	1551.3
FLGs	1353.2	100.3	1589.4	64.5	1.4	1624.1	-
MWCNTs	1355.8	57.9	1587.9	48.8	1.2	1621.3	-
Ros1	1354.7	42.1	1583.0	22.8	0.3	1621.1	-

$I_{D1/G}$: estimated integrated intensity ratios of the D1 vs. G bands

3.3 Morphological properties

FE-SEM images (Fig. 3) revealed different surface morphologies for each one of the materials under study. The mic-GO exhibited a fluffy structure of multiple exfoliated GO sheets (Fig. 3a), while the GS-75 demonstrated a sponge-like structure of multiple reduced GO sheets (Fig. 3b). The FLGs consisted of rigid aggregate particles with a platelet-like shape (Fig. 3c). The MWCNTs showed a typical nanotubular structure (Fig. 3d), while the Ros1 presented a non-uniform surface morphology due to the presence of various carbon nanoparticles such as sh-MWCNTs, polyhedrals and GNPs (Fig. 3e).

TEM analysis provided a more detailed description of the above morphological features. The mic-GO (Fig. 4a) was characterized by "wrinkles" formed due to the overlap of the exfoliated GO layers induced by the microwave radiation treatment [27]. Similarly, a wrinkled-structure with folded graphene regions was more evident in the case of GS-75 (Fig. 5a) with the reduced GO layers observed at higher magnifications (inset Fig. 5a). The high-magnification image of FLGs (Fig. 4b) revealed highly-defective graphene regions, while few curved tube-like graphene sheets were also observed (dark-colored components) as a result of the plasma exfoliation process. For the MWCNTs, tubes with length in mm scale and hollow-opened ends can be clearly observed in Fig. 5b. The multi-walled nature of the nanotubes was quite apparent at high-resolution images (inset Fig. 5b); their interlayer distance was ~0.360 nm, while their inner and outer tube diameter was ~5 nm and ~10 nm, respectively.

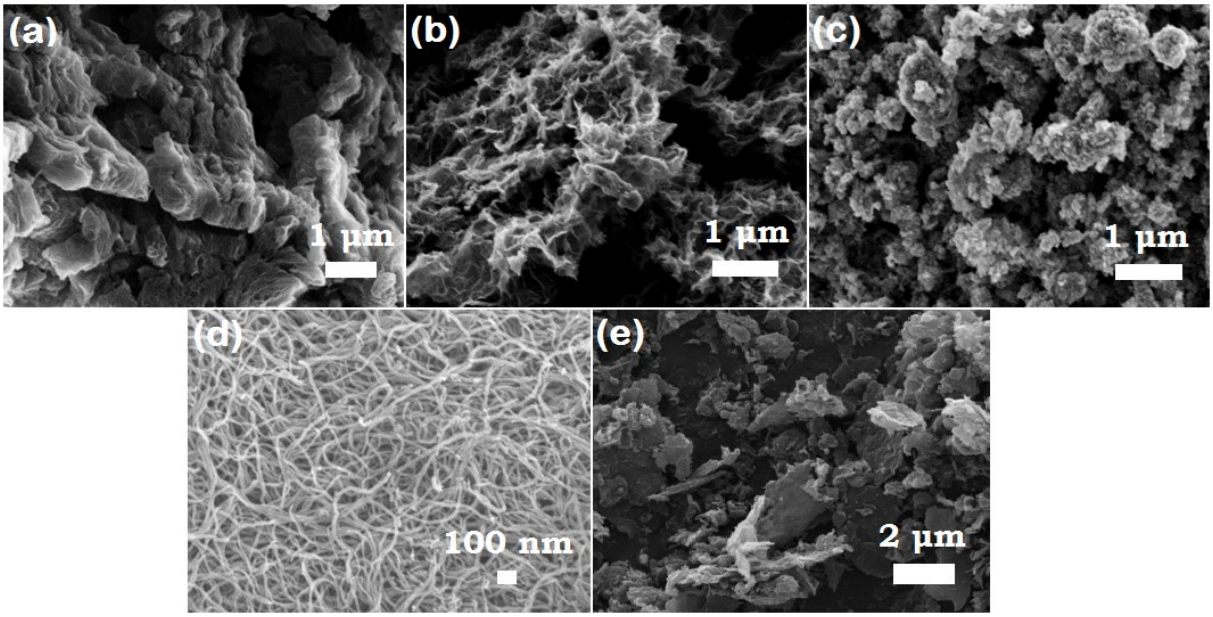

Fig. 3: FE-SEM images of (a) mic-GO, (b) GS-75, (c) FLGs, (d) MWCNTs and (e) Ros1.

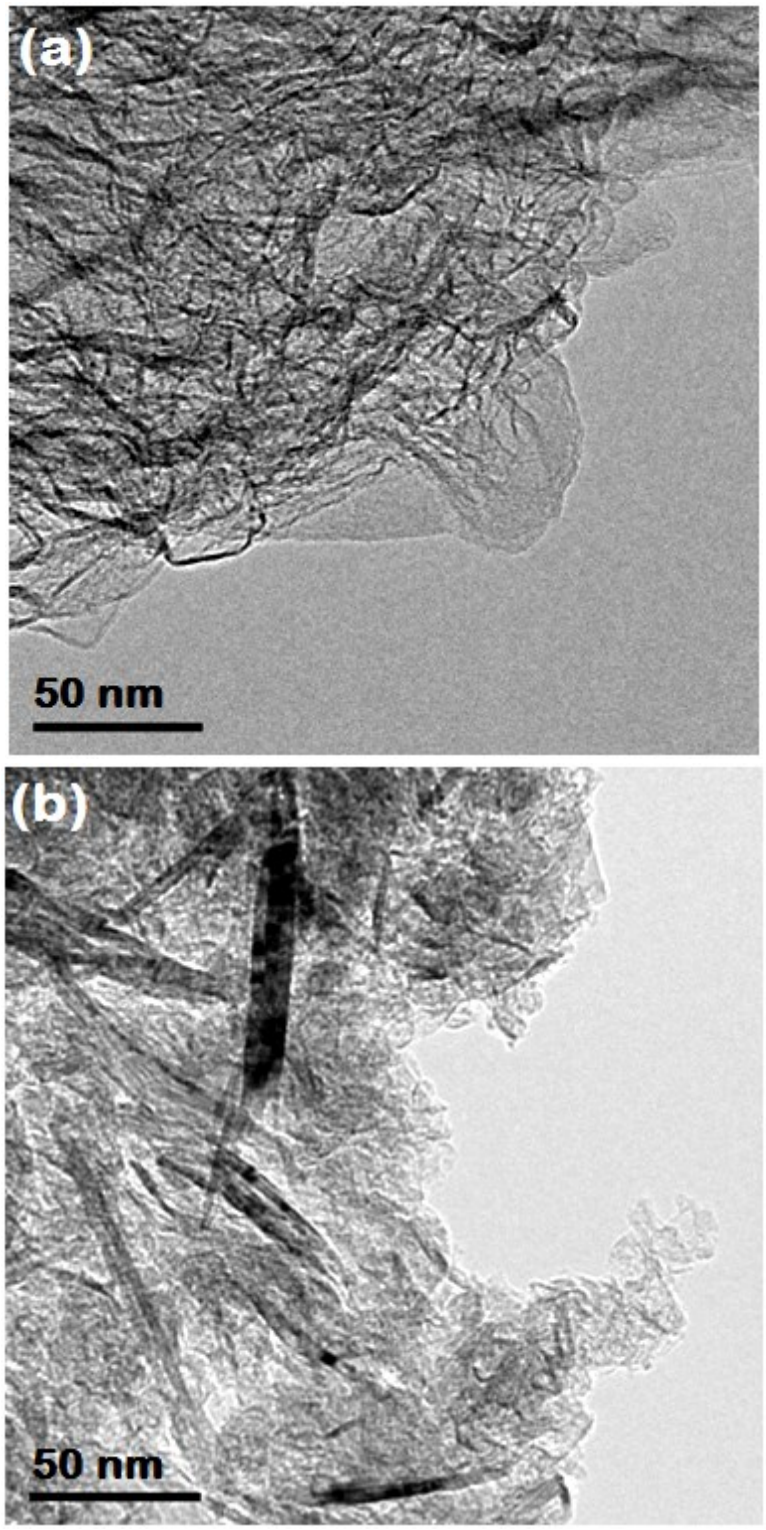

Fig. 4: High-magnification TEM images of the (a) as-prepared mic-GO and (b) commercial FLGs.

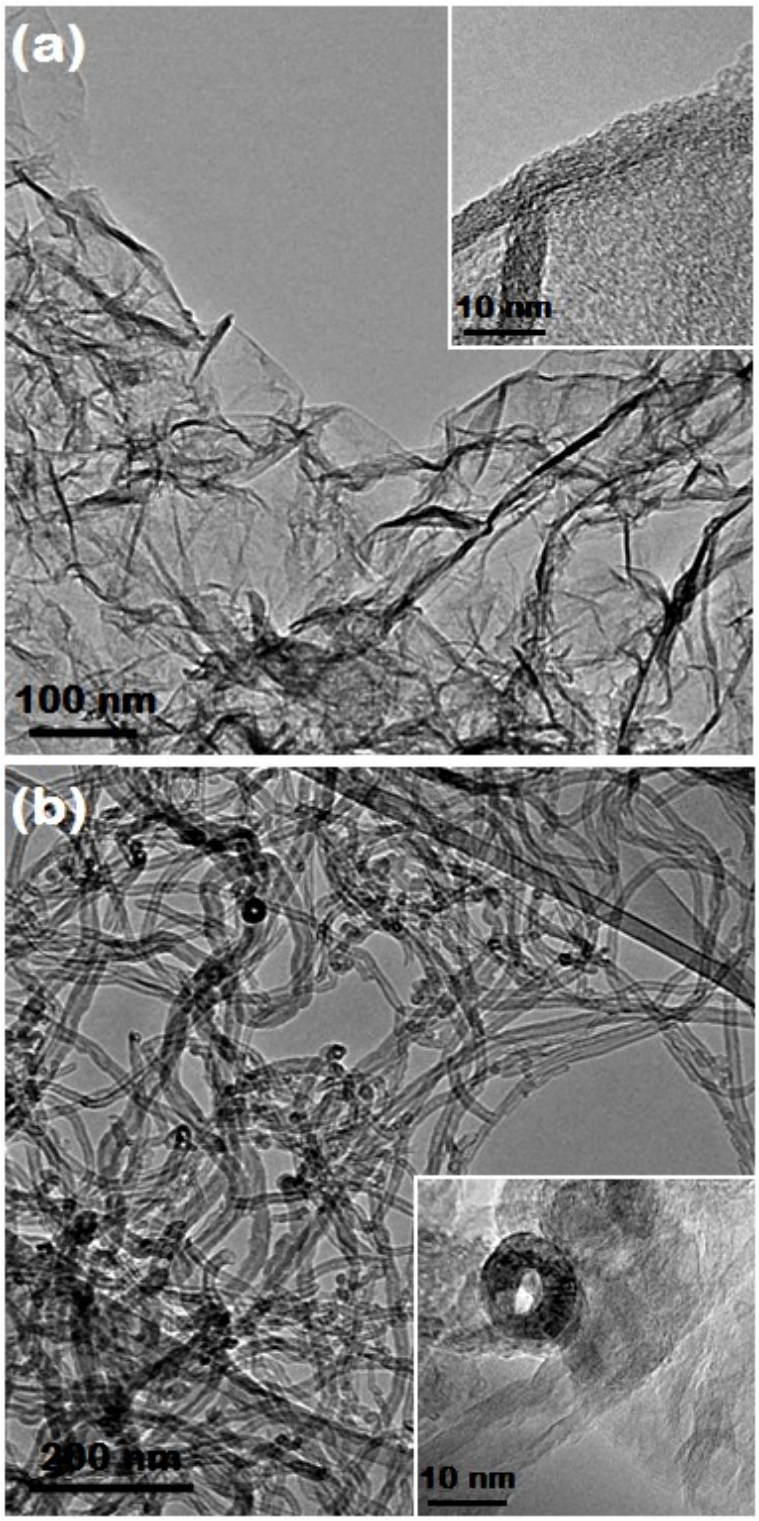

Fig. 5: Low- and high-magnification (insets) TEM images of the (a) as-prepared GS-75 and (b) commercial MWCNTs.

3.4 Hydrogen storage capacity

Low-pressure H_2 adsorption/desorption isothermal curves at 77 K are shown in Fig. 6. All materials exhibited type I isotherms based on the IUPAC classification [36] with the adsorbed amount increasing rapidly up to a certain point following the Langmuir equation; indicative of the fact that physical adsorption of supercritical H_2 cannot proceed beyond monolayer coverage. The process was fully reversible and no hysteresis loop was observed between adsorption/desorption branches. The H_2 gravimetric capacity was calculated based on the following equation:

$$Capacity\ (wt\%) = \left[\frac{m_{H_2}}{m_{sample}+m_{H_2}} \times 100\right]\% \qquad (1)$$

There, m_{H_2} is the adsorbed hydrogen mass and m_{sample} is the tested sample mass. Our newly-synthesized GS-75 and mic-GO reached maximum capacities of 0.48 wt.% and 0.66 wt.%, respectively, at 77 K and 1 bar. The commercial FLGs demonstrated a higher capacity (0.85 wt.%) under the same experimental conditions, mainly due to their larger SSA and micropore volume. Both FLGs and GS-75 presented enhanced H_2 physisorption at the lower operating pressures (<10 mbar), most likely attributed to the presence of super-micropores (width 0.7-0.8 nm) as detected by the QSDFT method. The high-purity MWCNTs reached a much smaller capacity (0.2 wt.%), while non-porous Ros1 adsorbed only minor amounts (<0.1 wt.%). Ioannatos and Verykios [46] examined the H_2 storage performance (at 77 K and up to 1 bar) of high-purity (96-99 %) single- and multi-walled CNTs produced by chemical vapor deposition. They concluded that H_2 adsorption strongly depends on the nature/geometry and the purity of the nanotubes. An overview of the low-pressure H_2 storage results for all the studied nanomaterials is presented in Table 3.

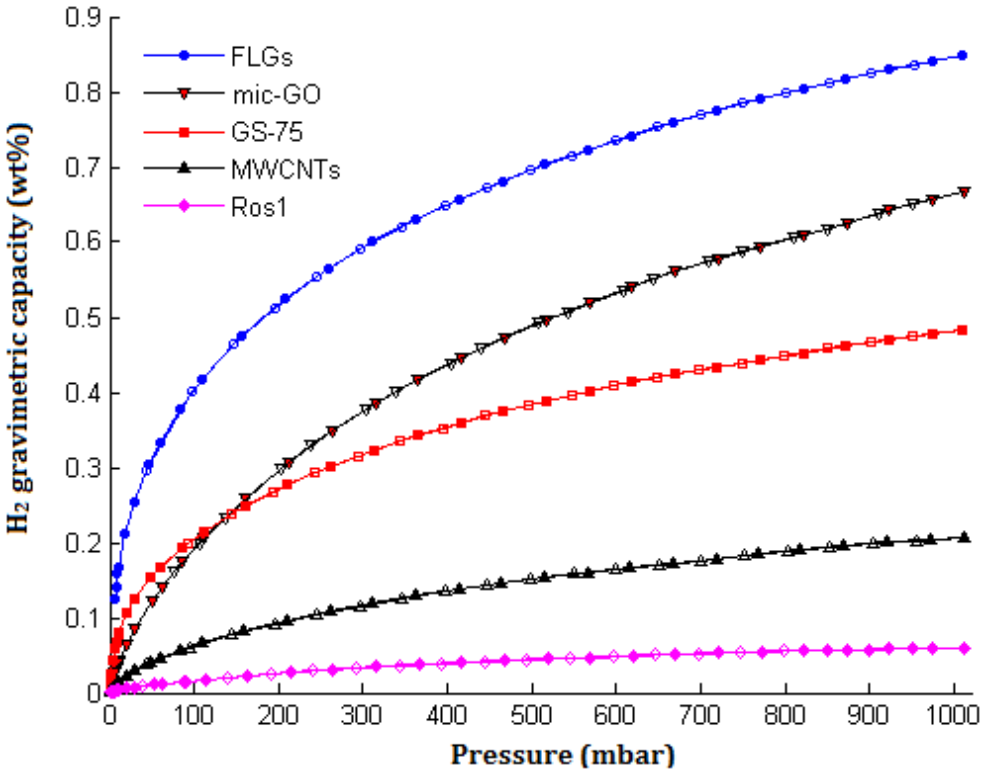

Fig. 6: Reversible H_2 adsorption (colored symbols) and desorption (blank symbols) isotherm curves at 77 K and up to 1 bar for the as-prepared GOs (mic-GO and GS-75) in comparison with the commercial samples (FLGs, MWCNTs and Ros1).

Table 3: Hydrogen storage capacities of the studied nanomaterials at 77 K and 1 bar.

Materials	C_H [wt.%]	V_H [cm^3/g]	C_H / S_{BET} [$wt.\%/m^2/g$]	V_H / S_{BET} [cm^3/m^2]
FLGs	0.85	95.2	0.001174	0.131491
mic-GO	0.66	74.5	0.001054	0.119009
GS-75	0.48	53.9	0.001379	0.154885
MWCNTs	0.20	23.1	0.000995	0.114925
Ros1	0.06	6.7	0.001363	0.152272

C_H: H_2 gravimetric capacity based on Eq. 1, V_H: adsorbed H_2 volume at standard temperature-pressure (STP) conditions, (C_H/S_{BET}): ratio between H_2 gravimetric capacity and BET SSA, (V_H/S_{BET}): ratio between adsorbed H_2 volume at STP conditions and BET SSA

In addition, the results confirmed the existing linear relationship between the H_2 gravimetric capacity and the BET SSA, as described by previous studies on high-surface area porous carbons [47,48]. Specifically, H_2 uptake increased almost proportionally to the SSA of the tested materials. As shown in Fig. 7, linear fitting was applied to the data and a straight line was obtained with a goodness of fit close to unity (R^2 = 0.9756) and a slope parameter equal to 1.121 × 10^{-3} wt %/m^2/g. In the context of this study, an equivalent linear equation for the micropore volume cannot be extracted, as only two of the examined nanomaterials exhibited microporosity (i.e. FLGs and GS-75). However, taking into consideration the enhanced physisorption behavior of these two samples (compared to the rest) at pressures < 10 mbar, it is clear that their higher fraction of micropores had a significant effect to their H_2 storage capacities, probably by providing stronger binding/adsorption sites for the H_2 molecules.

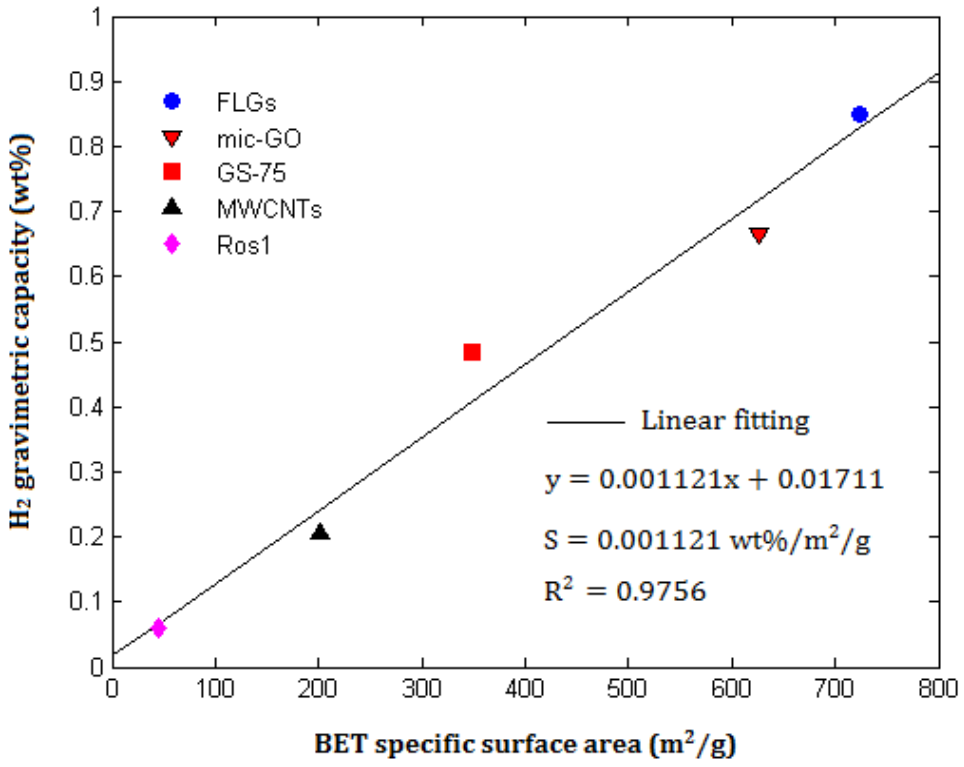

Fig. 7: Correlation plot between H_2 gravimetric capacity (wt.%) and BET specific surface area (m^2/g) at 77 K and 1 bar.

4. Conclusions

Two novel high-surface area graphene-based nanomaterials were synthesized based on different approaches: (a) a reduced graphene oxide (GO) sponge-like nanostructure (~350 m^2/g) through hydrothermal treatment combined with freeze drying; and (b) an exfoliated GO (~630 m^2/g) through microwave radiation. Both were fully characterized with respect to their texture, structure and morphology using a variety of techniques. Porosity properties (BET surface area, micropore surface area and volume and pore size distribution) were determined by N_2 adsorption/desorption measurements at 77 K. Raman spectra confirmed their graphitic-like structure and the presence of oxygen surface functionalities, while SEM and TEM images revealed a similar morphology of exfoliated GO wrinkles for both nanomaterials. Furthermore, their H_2 storage capacity was investigated at low (0-1 bar) pressures at 77 K in comparison to other commercial nanocarbons such as few-layer graphenes and multi-walled carbon nanotubes. The lab-synthesized GS-75 and mic-GO nanomaterials exhibited a reversible H_2 adsorption/desorption behavior and reached maximum capacities ~0.5 wt.% and ~0.7 wt %, respectively, at 77 K and 1 bar.

Acknowledgments

The present research was partially supported by the EC FP7-INFRASTRUCTURES project H2FC (GA No. 284522) and by Khalifa University Internal Research Fund (KUIRF L1 2013/210014 and KUIRF 2014/210047). The authors are very grateful to Mr. Ian Walters (Perpetuus Advanced Materials, UK) and Dr. Vladislav Ryzhkov (Fibrtec Inc., USA) for providing the commercial few-layer graphenes (FLGs) and Ros1™ products, respectively.

References

[1] Durbin DJ, Malardier-Jugroot C. Review of hydrogen storage techniques for on board vehicle applications. Int J Hydrogen Energy 2013;28:14595-617.

[2] Broom DP. Hydrogen storage materials. Green energy and technology. London: Springer-Verlag; 2011.

[3] Steriotis TA, Charalambopoulou GC, Stubos AK. Advanced materials for hydrogen storage. In: Kanellopoulos Nick, editor. Nanoporous materials: advanced techniques for characterization, modeling and processing. CRC Press Taylor & Francis; 2011.

[4] Xia Y, Yang Z, Zhu Y. Porous carbon-based materials for hydrogen storage: advancement and challenges. J Mater Ch A 2013;1:9365-81.

[5] Zuttel A, Remhof A, Borgschulte A, Friedrichs O. Hydrogen: the future energy carrier. Phil Trans R Soc A 2010;368:3329-42.

[6] Felderhoff M, Weidenthaler C, von Helmolt R, Eberle U. Hydrogen storage: the remaining scientific and technological challenges. Phys Chem Chem Phys 2007;9:2643-53.

[7] Strobel R, Garche J, Moseley PT, Jorissen L, Wolf G. Hydrogen storage by carbon materials. J Power Sources 2006;159:781-801.

[8] Yurum Y, Taralp A, Veziroglu TN. Storage of hydrogen in nanostructured carbon materials. Int J Hydrogen Energy 2009;34:3784-98.

[9] Srinivas G, Zhu Y, Piner R, Skipper N, Ellerby M, Ruoff R. Synthesis of graphene-like nanosheets and their hydrogen adsorption capacity. Carbon 2010;48:630-5.

[10] Kim BH, Hong WG, Yu HY, Han YK, Lee SM, Chang SJ, et al. Thermally modulated multilayered graphene oxide for hydrogen storage. Phys Chem Chem Phys 2012;14:1480-4.

[11] Lyth S, Shao H, Liu J, Sasaki K, Akiba E. Hydrogen adsorption on graphene foam synthesized by combustion of sodium ethoxide. Int J Hydrogen Energy 2014;39:376-80.

[12] Xia K, Tian X, Fei S, You K. Hierarchical porous graphene-based carbons prepared by carbon dioxide activation and their gas adsorption properties. Int J Hydrogen Energy 2014;39:11047-54.

[13] Hudson MSL, Raghubanshi H, Awasthi S, Sadhasivam T, Bhatnager A, Simizu S, et al. Hydrogen uptake of reduced graphene oxide and graphene sheets decorated with Fe nanoclusters. Int J Hydrogen Energy 2014;39:8311-20.

[14] Lee SY, Park SJ. Isothermal exfoliation of graphene oxide by a new carbon dioxide pressure swing method. Carbon 2014;68:112-7.

[15] Spyrou K, Gournis D, Rudolf P. Hydrogen storage in graphene-based nanomaterials: Efforts towards enhanced hydrogen absorption. ECS J Solid State Sci Technol 2013;2:3160-9.

[16] Srinivas G, Zheng XG. Graphene-based materials: synthesis and gas sorption, storage and separation. Prog Mater Sci 2015;69:1-60.

[17] Gotzias A, Tylianakis E, Froudakis G, Steriotis Th. Theoretical study of hydrogen adsorption in oxygen functionalized carbon slit pores. Microporous Mesoporous Mater 2012;154:38-44.

[18] Giasafaki D, Charalambopoulou G, Tampaxis C, Stubos A, Steriotis Th. Hydrogen sorption properties of Pd-doped molecular sieves. Int J Hydrogen Energy 2014;39:9830-6.

[19] Giasafaki D, Bourlinos A, Charalambopoulou G, Stubos A, Steriotis Th. Synthesis and characterisation of nanoporous carbon-metal composites for hydrogen storage. Microporous Mesoporous Mater 2012;154:74-81.

[20] Srinivas G, Burressa J, Yildirim T. Graphene oxide derived carbons (GODCs): synthesis and gas adsorption properties. Energy Environ Sci 2012;5:6453-9.

[21] Li Y, Samad YA, Polychronopoulou K, Alhassan SM, Liao K. Highly electrically conductive nanocomposites based on polymer-infused graphene sponges. Sci Rep 2014;4:46452-7.

[22] Bi H, Xie X, Yin K, Zhou Y, Wan S, He L, et al. Spongy graphene as a highly efficient and recyclable sorbent for oils and organic solvents. Adv Funct Mater 2012;21:4421-5.

[23] Zhao JP, Ren WC, Cheng HM. Graphene sponge for efficient & repeatable adsorption and desorption of water contaminations. J Mater Chem 2012;38:20197-202.

[24] Akhavan O. The effect of heat treatment on formation of graphene thin films from graphene oxide nanosheets. Carbon 2010;48:509-19.

[25] Zhao Y, Hu C, Song L, Wang L, Shi G, Dai L, et al. Functional graphene nanomesh foam. Energy Environ Sci 2014;7:1913-8.

[26] Chen W, Yang L, Bangal PR. Preparation of graphene by the rapid and mild thermal reduction of graphene oxide induced by microwaves. Carbon 2010;48:1146-52.

[27] Zhu Y, Murali S, Stoller MD, Velamakanni A, Piner RD, Ruoff RS. Microwave assisted exfoliation and reduction of graphite oxide for ultracapacitors. Carbon 2010;48:2118-22.

[28] Sridhar V, Jeon JH, Oh IK. Synthesis of graphene nano-sheets using eco-friendly chemicals and microwave radiation. Carbon 2010;48:2953-7.

[29] Shulga YM, Baskakov SA, Knerelman EI, Davidova GI, Badamshina ER, Shulga NY, et al. Carbon nanomaterial produced by microwave exfoliation of graphite oxide: new insights. RSC Adv 2014;4:587-92.

[30] Chabot V, Higgins D, Yu A, Xiao X, Chen Z, Zhang J. A review of graphene and graphene oxide sponge: material synthesis and applications to energy and the environment. Energy Environ Sci 2014;7:1564-96.

[31] Geng J, Jung H. Porphyrin functionalized graphene sheets in aqueous suspensions: from the preparation of graphene sheets to highly conductive graphene films. J Phys Chem C 2010;114:8227-34.

[32] Tsoufis T, Katsaros F, Sideratou Z, Romanos G, Ivashenko O, Rudolf P, et al. Tailor-made graphite oxide-DAB poly(propylene imine) dendrimer intercalated hybrids and their potential for efficient CO_2 adsorption. Chem Commun 2014;50:10967-70.

[33] Enotiadis A, Angjeli K, Baldino N, Nicotera I, Gournis D. Graphene-based nafi on nanocomposites membranes: enhanced proton transport and water retention by novel organo-functionalized graphene oxide nanosheets. Small 2012;8:3338-49.

[34] Perpetuus Research & Development Ltd Particles. UK Patent appl no. GB1405614.7 (pending status), 2014.

[35] Ryzhkov VA. Short carbon nanotubes. U. S Patent 7244408, 2007.

[36] Sing KSW, Everett DH, Hall RAW, Moscou L, Pierotti RA, Rouquerol J, et al. Reporting physisorption data for gas/solid systems with special reference to the determination of surface area and porosity. IUPAC 1985;57:603-19.

[37] Rouquerol F, Rouquerol J, Sing K. Adsorption by powders and solids: principles, methodology, and applications. London: Academic Press; 1999.

[38] Thommes M. Physical adsorption characterization of nanoporous materials. Chem Ing Tech 2010;82:1059-72.

[39] Hart KE, Springmeier JM, McKeownc NB, Colina CM. Simulated swelling during low-temperature N_2 adsorption in polymers of intrinsic microporosity. Phys Chem Chem Phys 2013;15:20161-9.

[40] Pastrana-Martinez LM, Morales-Torres S, Likodimos V, Figueiredo JL, Faria JL, Falaras P, et al. Advanced nanostructured photocatalysts based on reduced graphene oxide-TiO_2 composites for degradation of diphenhydramine pharmaceutical and methyl orange dye. Appl Catal B Environ 2012;123-4:241-56.

[41] Gokus T, Nair RR, Bonetti A, Bohmler M, Lombardo A, Novoselov KS, et al. Making graphene luminescent by oxygen plasma treatment. ACS Nano 2009;3:3963-8.

[42] Kim HJ, Lee S-M, Oh Y-S, Yang Y-H, Soo Lim Y, Yoon D-H, et al. Unoxidized graphene/alumina nanocomposite: Fracture- and wear-resistance effects of graphene on alumina matrix. Sci Rep 2014;4:5176.

[43] Some S, Kim Y, Yoon Y, Yoo H, Lee S, Park Y, et al. High-quality reduced graphene oxide by a dual-function chemical reduction and healing process. Sci Rep 2013;3:1929.

[44] Ramesha GK, Sampath S. Electrochemical reduction of oriented graphene oxide films: an in situ Raman spectroelectrochemical study. J Phys Chem C 2009;113:7985-9.

[45] Sadezky A, Muckenhuber H, Grothe H, Niessner R, Poschl U. Raman microspectroscopy of soot and related carbonaceous materials: spectral analysis and structural information. Carbon 2005;43:1731-42.

[46] Ioannatos GE, Verykios XE. H_2 storage on single- and multi-walled carbon nanotubes. Int J Hydrogen Energy 2010;35:622-8.

[47] Zuttel A, Sudan P, Mauron Ph, Kiyobayashi T, Emmenegger Ch, Schlapbach L. Hydrogen storage in carbon nanostructures. Int J Hydrogen Energy 2002;27:203-12.

[48] Panella B, Hirscher M, Roth S. Hydrogen adsorption in different carbon nanostructures. Carbon 2005;43:2209-14.

Publication II

Few-layer graphene-like flakes derived by plasma treatment: A potential material for hydrogen adsorption and storage

N. Kostoglou, A. Tarat, I. Walters, V. Ryzhkov, C. Tampaxis, G. Charalambopoulou, T. Steriotis, C. Mitterer, C. Rebholz

Microporous and Mesoporous Materials 225 (2016) 482-487

Few-layer graphene-like flakes derived by plasma treatment: A potential material for hydrogen adsorption and storage

Nikolaos Kostoglou[a,b,*], Afshin Tarat[c], Ian Walters[c], Vladislav Ryzhkov[d], Christos Tampaxis[e], Georgia Charalambopoulou[e], Theodore Steriotis[e], Christian Mitterer[a], Claus Rebholz[b,**]

[a] Department of Physical Metallurgy and Materials Testing, Montanuniversität Leoben, 8700 Leoben, Austria

[b] Department of Mechanical and Manufacturing Engineering, University of Cyprus, 1678 Nicosia, Cyprus

[c] Perpetuus Advanced Materials, Ammanford, SA183EZ Carmarthenshire, UK

[d] Nanotube Production Department, Fibrtec Incorporation, TX 75551 Atlanta, USA

[e] National Center for Scientific Research Demokritos, Agia Paraskevi Attikis, 15310 Athens, Greece

Graphical abstract

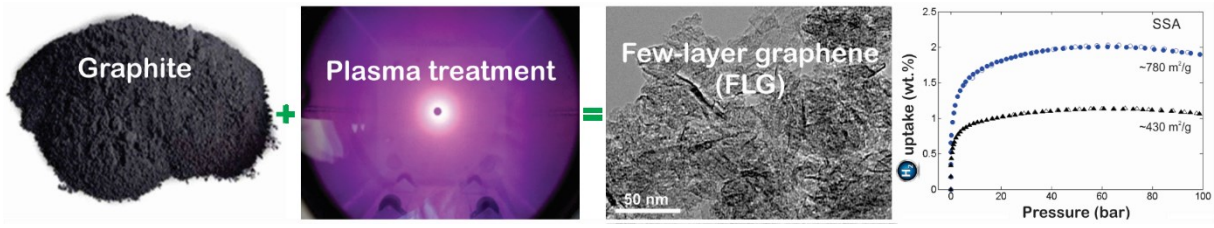

Highlights

- Few-layer graphene-like flakes were prepared by plasma-processing of natural graphite
- Demonstrated large surface areas (up to 800 m^2/g) and nanopore sizes (0.7-0.8 nm)
- Characterization was performed using SEM, TEM, XPS, XRD and N_2 porosimetry methods
- H_2 storage behavior was evaluated by adsorption/desorption at 77 K and up to 100 bar
- Reversible H_2 adsorption isotherms with maximum uptake of up to ~2 wt.% at ~60 bar

Abstract

A novel, one-step, wet-free, environmental friendly and high-yield method for producing few-layer graphene powders with large surface areas (up to 800 m^2/g) and narrow nanopore sizes (0.7-0.8 nm) using plasma-induced exfoliation of natural graphite is presented. Advanced characterization techniques were employed, including scanning and transmission electron microscopy, X-ray photoelectron spectroscopy, X-ray diffraction and N_2 gas adsorption/desorption measurements at 77 K, to investigate the morphological, elemental, structural and textural/porosity properties of these nanomaterials. Fully reversible H_2 gas adsorption/desorption isotherms with maximum gravimetric capacities of up to ~2 wt.% at 77 K and ~60 bar are reported here. The H_2 storage performance at 77 K is well correlated with certain textural features such as specific surface area and microporosity. The results of this work provide a valuable feedback for further research on plasma-processed graphene-based materials towards efficient H_2 storage via cryo-adsorption.

Keywords: Graphene; Plasma; Adsorption; Hydrogen storage; Nanoporous powders

1. Introduction

Exfoliated graphene has been a subject of considerable research during the last decade attributed to its unique electronic, thermal, optical and mechanical properties. Recently, porous graphene has also attracted significant attention as a potential solid-state medium for storing gases and especially a highly-dense energy carrier such as hydrogen (H_2) [1-11]. Few-layer graphene (FLG), an extremely "thin" graphitic analogue composed of a limited number of stacked carbon atomic layers, could become an efficient adsorbent material in applications related to H_2 cryo-adsorption and storage mainly due to the large surface areas achieved in combination with the tunable pore sizes. Density Functional Theory simulations by Yadav et al. [9] showed that defect-engineering of graphene could lead to effective H_2 gravimetric capacities of up to ~7 wt.%. Combined theoretical and experimental studies by Baburin et al. [10] indicated that graphene sheets with defect-induced porosities exhibit surface areas greater than that of single-layer graphene (i.e. 2630 m^2/g), thus leading to enhanced H_2 adsorption at cryogenic liquid nitrogen (N_2) temperature (i.e. 77 K). Indeed, Grand Canonical Monte-Carlo simulations in perforated graphene revealed capacities of up to 6.5 wt.% H_2, while volumetric measurements on a

thermally-exfoliated and chemically-activated high-surface area (~2900 m^2/g) graphene recorded 5.5 wt.% H_2 at 30 bar. Recently, Klechikov et al. [11] reported an impressive H_2 uptake of up to 7.5 wt.% at 77 K and ~120 bar for highly-porous graphene scaffolds with extremely high surface areas of up to ~3400 m^2/g prepared by KOH activation and H_2 annealing.

Micro-mechanical cleavage of graphite [12], catalytic chemical vapor deposition of carbonaceous sources [13] and reduction of graphite oxide are few of the principal methods currently used to produce graphene [14]. Despite the large variety of graphene-like materials presented in the literature [1-8,10,11], there are no references available describing the H_2 adsorption properties of FLG powders derived by direct plasma-assisted exfoliation of natural graphite. Plasma-processing technology is considered a novel, wet-free, cost-effective and environmental-friendly "top-down" method for producing graphene of high quality and purity in an industrial-commercial scale, while allowing its modification with a variety of surface functionalities (e.g. carboxyls, amines, etc.). The plasma interacts with and subsequently modifies a graphitic surface both physically (i.e. ablation) and chemically (i.e. functionalization) depending on the gas stream (e.g. argon, oxygen, etc.) and the operating power [15,16]. Herein, nanoporous and high-surface area FLG-like powder materials were produced based on a plasma-induced graphite-exfoliation process [17]. The presented method offers a series of advantages, including production of bulk quantities (i.e. 30 kg per batch), relatively low power consumption (i.e. maximum ~6 kW) during plasma formation, absence of metal catalysts usually employed in graphene industry as well as lack of wet chemical procedures for purification. The morphology, elemental composition, structure and porosity/texture was studied by scanning and transmission electron microscopy (SEM and TEM), X-ray photoelectron spectroscopy (XPS), X-ray diffraction (XRD) and N_2 gas adsorption/desorption measurements at 77 K, respectively. The characterization studies revealed that the controlled "destruction" of the graphitic surface using plasma could lead to three-layered graphene-like flakes with enhanced surface areas (up to 800 m^2/g) and defect-induced microporosities (pore sizes below 1 nm). Finally, the H_2 storage performance of these powders was systematically evaluated by high-pressure (i.e. 0-100 bar) H_2 gas adsorption/desorption measurements at 77 K. Even though the H_2 uptake values presented in this study are not superior to those reported for other graphene-like materials usually derived by wet chemical treatment of

graphene oxide (e.g. KOH activation) [2,5,7,10,11], it is the first time that the H_2 storage potential of plasma-processed carbon-based materials is explored in such detail.

2. Experimental

2.1 Plasma processing

Two FLG powder materials with large surface areas (denoted hereafter as FLG-400 and FLG-800) were prepared by plasma-processing of natural graphite using a custom-made multi-electrode dielectric barrier discharge (DBD) plasma reactor, as described elsewhere [17]. Flake graphite powders (30 kg; Asbury Carbons) were initially exposed in an argon (Ar) plasma (0.01 mbar pressure and 600 sccm flow) for 60 min using lower (~3 kW) and higher (~6 kW) power inputs, respectively. The process causes the exfoliation of graphite by generating Stone-Wales, single- and double-vacancy surface defects and consequently negating the van der Waals forces between the stacked graphene layers [10]. The as-produced FLG powders were subsequently treated in an oxygen plasma for 30 min, under similar conditions to the previous process, to introduce surface oxygen-based functionalities with the view to reduce agglomeration.

2.2 Characterization methods

Surface images were obtained by a JEOL JSM-7401F field emission SEM and a Philips CM-20 high-resolution TEM equipped with a LaB_6 filament. XPS studies were carried out by a Kratos Axis Ultra- DLD system equipped with a monochromatic Al Kα radiation, a dual Al-Mg anode and a delay-line detector. XRD patterns were collected in the 2θ region of 10-60° by a Shimadzu XRD-6000 equipped with Ni-filtered Cu Kα radiation (λ ~1.54 Å). The interlayer distances (d) and crystallite thicknesses (L_c) were estimated using Bragg's law and Scherrer's equation, respectively. Low-pressure (0-1 bar) N_2 adsorption/desorption isotherms were recorded at 77 K using a Quantachrome Autosorb 1-MP volumetric gas sorption analyzer and ultra-pure (99.999 %) N_2 gas. Prior to measurements, the samples (~40 mg) were degassed at 10^{-6} mbar and 250 °C for 12 h. Total specific surface area (SSA) was calculated by the multi-point Brunauer-Emmet-Teller (BET) method in the relative pressure (P/P_0) range of 0.05-0.15. Micropore SSA and volume were calculated by the Carbon Black statistical thickness equation (t-plot). Pore size distribution was estimated by the Quenched Solid Density Functional Theory (QSDFT) method using the N_2-carbon equilibrium transition kernel at 77.4 K for slit-shaped pores. High-pressure (0-100 bar) H_2

adsorption/desorption isotherms were recorded at 77 K using a Hy-Energy PCTPro- 2000 volumetric gas sorption analyzer and ultra-pure (99.9999 %) H_2 gas. The samples (~200 mg) were degassed at 10^{-6} mbar and 250 ^{o}C for 12 h. In order to avoid possible errors from helium (He) gas sorption at 77 K, volume calibrations with He were only carried out at room temperature (i.e. 298 K); the dead volumes at 77 K were calculated from a non-porous glass reference curve.

3. Results and discussion

3.1 Morphological studies

Field emission SEM images (Fig. 1) revealed a similar surface morphology for both FLG powders. At low magnifications (Fig. 1a), the surface is characterized by rigid aggregate particles with sizes of several mm. At higher magnifications (Fig. 1b), defects and voids are indicative of the plasma ablation process; defects in crystalline structures, such as graphene, are generally caused by dislocations, grain boundaries and phase interfaces [18]. By increasing almost twice the Ar plasma power (i.e. from ~3 kW to ~6 kW) more defects are introduced, leading to an increased surface area of FLG-800 relative to FLG-400. High-resolution TEM images (Fig. 1c) confirmed the SEM observations by indicating highly-defective graphene regions across the surface of both materials.

3.2 Elemental analysis

XPS analysis (Fig. 2a) provided an elemental composition of 92.19 and 7.81 at.% for carbon and oxygen, respectively. The C/O ratio of ~12:1 is attributed to the functionalization process using oxygen plasma for 30 min. The deconvoluted C1s and O1s XPS spectra of the FLG-800 sample are presented in Fig. 2b and c, respectively. For the C1s spectrum (Fig. 2b), the peaks at ~284 eV and ~285 eV represent C=C and C–C bonds, respectively; combined sp^2 and sp^3 hybridization is typically observed in functionalized graphene [15,16]. Functionalities such as hydroxyl (C–OH) and epoxy (C–O–C) groups with high binding energy may cause main peak chemical shifts to ~286.5 eV. In addition, the peak at ~289 eV is probably attributed to ester (O–C=O) and carboxyl (O–C=OH) groups; these high binding energy components may shift the peak to 3-4.5 eV above the main carbon peak. The last peak at ~291 eV could describe plasmon loss features. The O1s spectrum (Fig. 2c) indicates the presence of three oxygen species. The stronger peak at ~532.2 eV arises due to high binding energy bonds between oxygen and carbon such as the C=O bond

in ester and carboxyl groups. The second large peak at ~533.8 eV could be assigned to C–OH groups, while the weaker peak at ~530.7 eV is probably related to O–C=OH groups.

3.3 Structural features

Fig. 3a represents the XRD patterns of the FLG powders after subtraction of the background. The graphitic (002) reflection at around 2θ ~25° dominates both patterns while less intense peaks are observed at ~43° and ~54°, representing (100)/(101) and (004) crystal planes, respectively. The deconvoluted (002) reflections of FLG-400 and FLG-800 are presented in Fig. 3b and c, respectively. No wide reflections of amorphous carbon were observed at 2θ ~20° for both samples, which theoretically represent aliphatic carbon atoms [19,20]. In contrast, peaks at 24.57°, 25.75° and 26.03° for FLG-400 (Fig. 4b) and at 22.83°, 25.4° and 26.1° for FLG-800 (Fig. 3c) are considered signals of graphene-like nanoparticles with different thicknesses. Table 1 shows structural results for the two types of FLG crystallites based on the Gaussian deconvolution of the (002) reflections. For FLG-400, about 50 wt.% of its carbon fraction is composed of five-layered graphene-like crystallites with d ~0.362 nm and L_c ~1.364 nm. In contrast, three-layered crystallites having lateral thickness of just 0.761 nm represent about the 61 wt.% of the carbon in the FLG-800 sample. As expected, the crystallinity is reduced by moving from FLG-400 to FLG-800 (Fig. 3a), as the average number of graphene layers is decreasing.

Table 1: Structural features of the plasma-exfoliated FLG powders derived by the Gaussian deconvolution of the (002) XRD reflection.

Materials	Fractions	2θ [°]	d [Å]	L_c [Å]	FWHM [°]	RA [counts]	Layers [no.]	CF [wt.%]
FLG-400	1st	24.57	3.62	13.64	5.89	2514	5	50
	2nd	25.75	3.46	45	1.79	1675	14	33
	3rd	26.03	3.42	125.9	0.64	863	38	17
FLG-800	1st	22.83	3.89	7.61	10.53	4830	3	61
	2nd	25.40	3.51	21.7	3.71	1937	7	25
	3rd	26.10	3.41	66.1	1.22	1135	20	14

2θ: diffraction angle, d: interlayer distance calculated by Bragg's law, L_c: crystallite thickness estimated by Scherrer's equation, FWHM: full-width at half maximum, RA: reflection area, CF: % carbon fraction

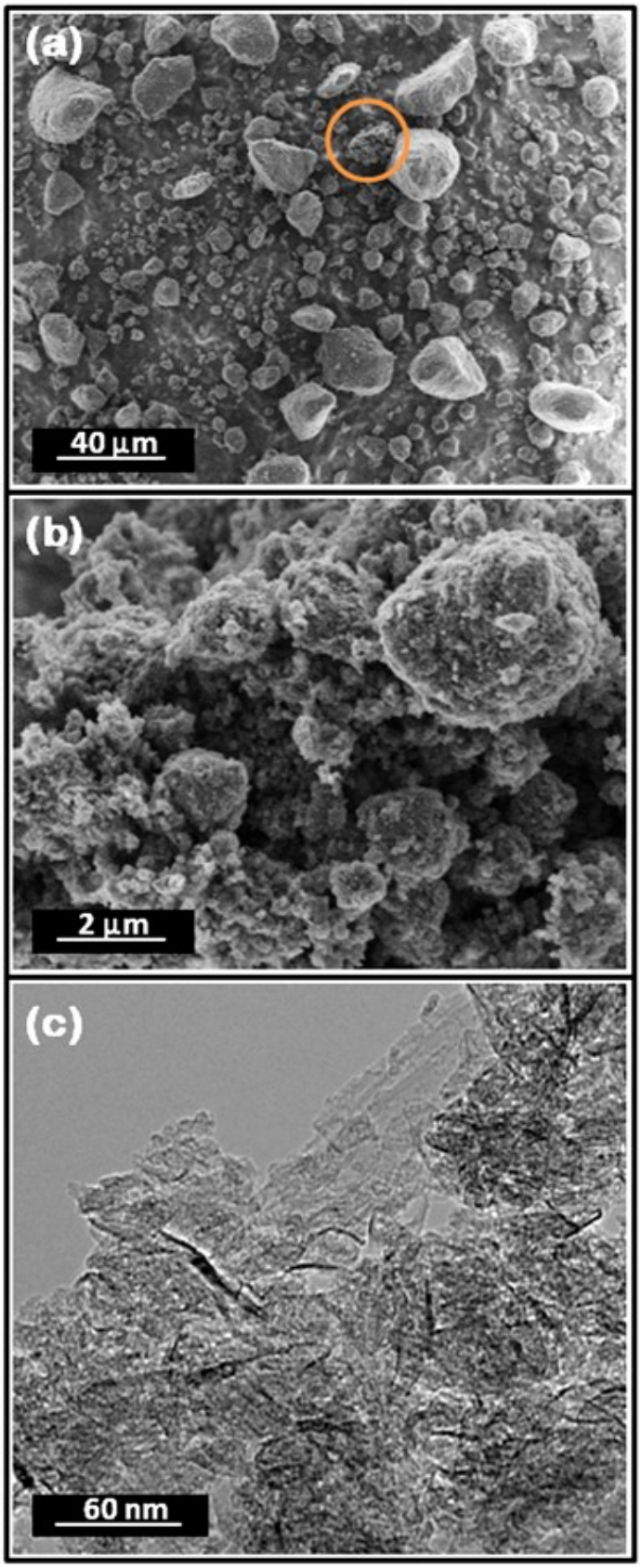

Fig. 1: Field emission SEM images at (a) low- and (b) high-magnification and (c) high-resolution TEM image of the FLG-800 powder.

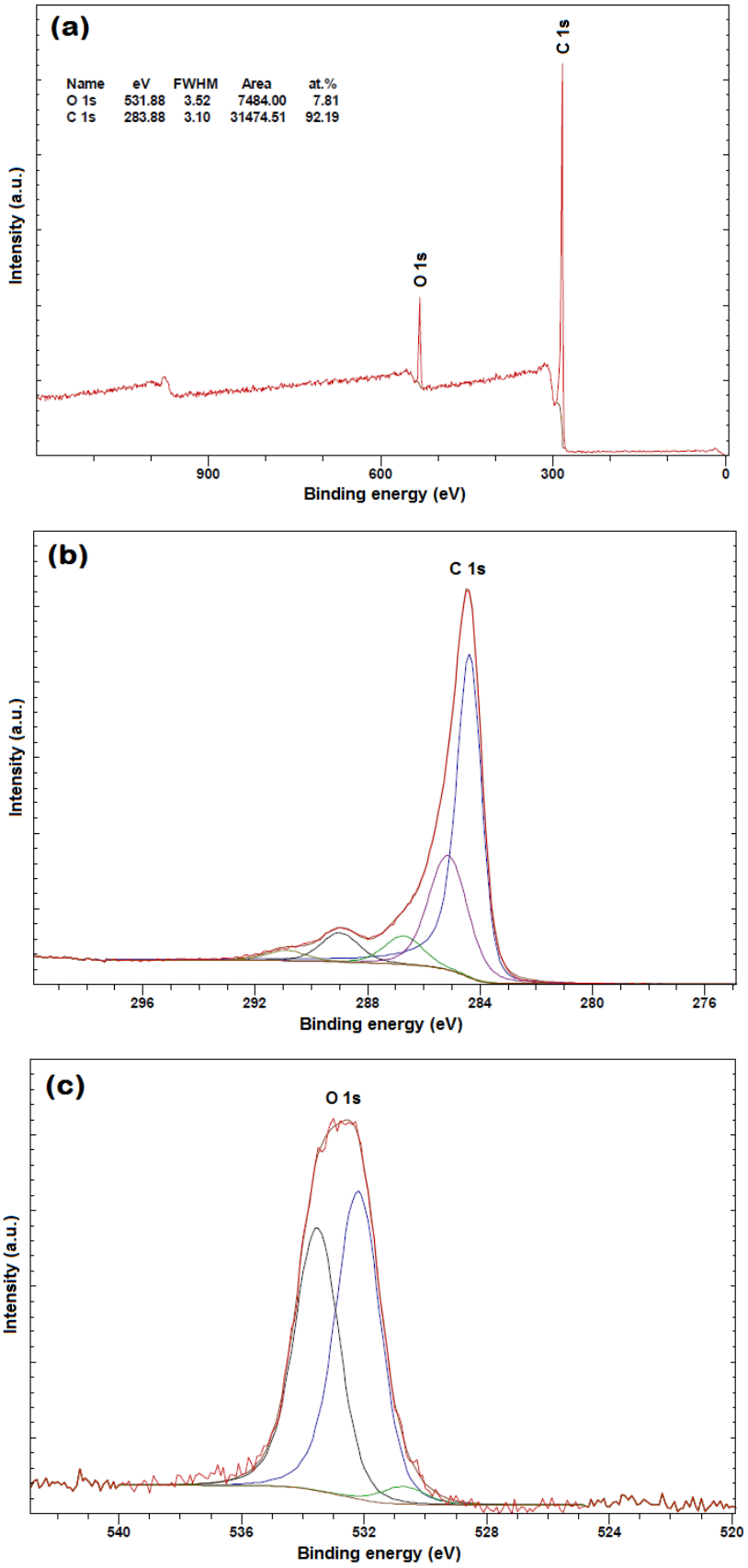

Fig. 2: (a) XPS and (b) deconvoluted C1s and (c) O1s spectra of the FLG-800 powder.

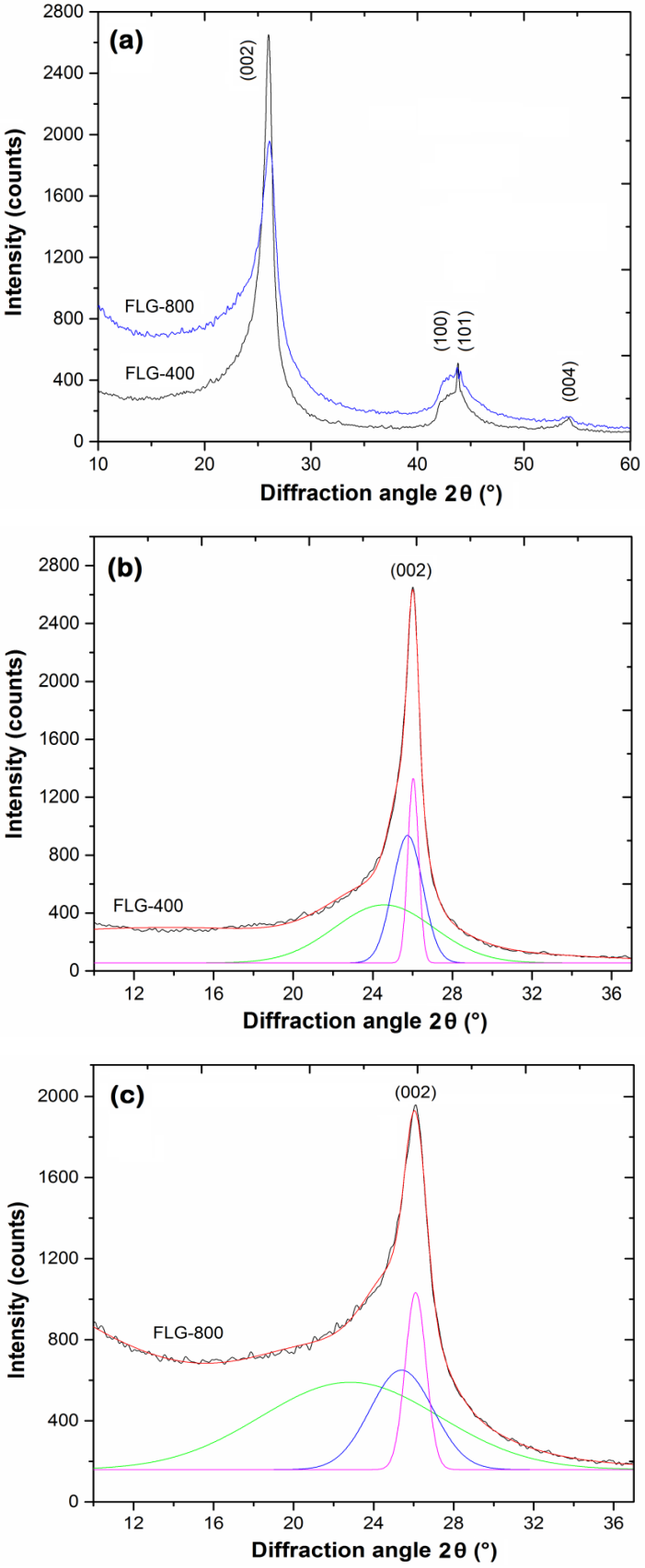

Fig. 3: (a) Background subtracted XRD patterns and deconvoluted (002) reflections of the (b) FLG-400 and (c) FLG-800 powders.

3.4 Textural properties

N_2 adsorption/desorption isotherms at 77 K of both FLG powders are presented in Fig. 4. The increased N_2 volumes at the lower relative pressures ($P/P_0 < 0.01$) are attributed to microporosity (i.e. pore sizes < 2 nm). The formation of a hysteresis loop between the adsorption and desorption curves is related to the capillary condensation of N_2 gas inside the mesopores (i.e. pore sizes 2-50 nm). The adsorbed N_2 amounts are increased abruptly at the higher relative pressures due to sorption at external or macropore surface (i.e. pore sizes > 50 nm). Table 2 summarizes the textural-porous properties of both FLG powders deduced by the N_2 sorption data. The BET SSA values for FLG-400 and FLG-800 were calculated at ~420 and ~780 m^2/g, respectively; the micropore SSA in both cases corresponds to the ~40 % of the total SSA (i.e. 170 and 300 m^2/g, respectively). The pore size distribution, as determined by the QSDFT method, revealed the presence of super-micropores (i.e. pore sizes 0.7-2 nm). A set of maxima were detected at ~0.7 and ~0.8 nm for FLG-400 and FLG-800, respectively, as clearly observed in the inset of Fig. 4.

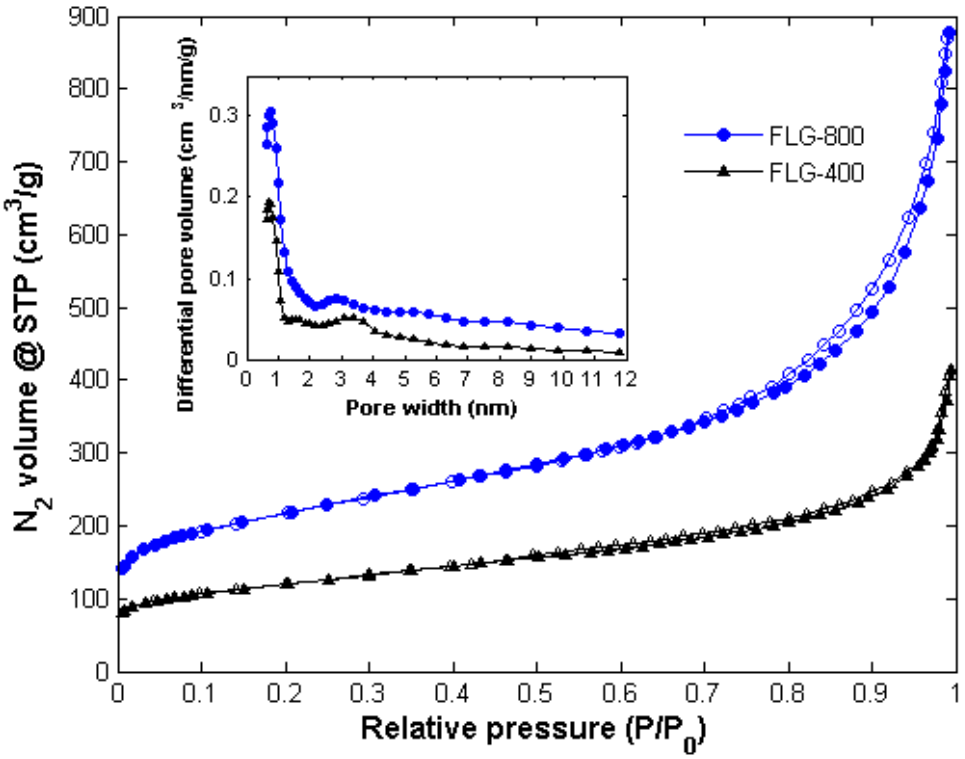

Fig. 4: (a) N_2 adsorption (colored symbols) and desorption (empty symbols) isotherms at 77 K of the plasma-exfoliated FLG powders; the inset shows the differential pore size distributions derived by the QSDFT method.

Table 2: Textural/porosity properties based on the N_2 adsorption/desorption isotherms recorded at 77 K.

Materials	S_{BET} [m^2/g]	S_{Micro} [m^2/g]	S_{Micro}/S_{BET} [%]	V_{Micro} [cm^3/g]	W_{QSDFT} [nm]
FLG-400	428.29	170.95	39.91	0.076	0.723
FLG-800	777.34	299.11	38.48	0.132	0.785

S_{BET}: total specific surface area (SSA) derived by the multi-point Brunauer-Emmet-Teller (BET) method, S_{Micro}: micropore SSA derived by the Carbon Black statistical thickness (t-plot) method, S_{Micro}/S_{BET}: % percentage of micropore SSA to BET SSA, V_{Micro}: micropore volume derived by the t-plot method, W_{QSDFT}: average pore width calculated by the Quenched Solid Density Functional Theory (QSDFT) method

3.5 Hydrogen sorption performance

High-pressure H_2 adsorption/desorption isotherms at 77 K are presented in Fig. 5a. Both samples exhibited a fully reversible adsorption-desorption behavior (i.e. absence of a hysteresis loop) in the pressure range of 0-100 bar. The H_2 gravimetric capacities were calculated by the ratio $m_h/(m_h + m_p)$, where m_h is the mass of the adsorbed H_2 gas and m_p is the mass of the FLG powder. The maximum capacities at 77 K reached 1.14 wt.% at ~61 bar for FLG- 400 and 2.01 wt.% at ~58 bar for FLG-800. The latter value (i.e. 2.0 wt.%) corresponds to the minimum gravimetric capacity for single-use H_2 storage systems in portable power applications established by the US Department of Energy for the year 2015, which is still much lower than the on-board automotive H_2 storage system target of 5.5 wt.% for the year 2020 [21]. It is important to note that the aforementioned targets refer to the operation of a complete H_2 storage system, which may include a tank, a storage material, valves, regulators, piping, mounting brackets, an insulation, an added cooling capacity, and probably other balance-of-plant components. In terms of surface area, FLG-400 showed a slightly higher maximum H_2 uptake to BET SSA ratio in comparison to FLG-800 (i.e. 2.662 and 2.586 × 10^{-3} wt.% m^{-2} g, respectively). This could be related to the slightly higher percentage of micropore SSA found in the FLG-400 sample (i.e. 39.91 against 38.48 %, respectively). The maximum H_2 uptake increases linearly with the BET SSA of the powders; i.e. almost doubles (~1.8 times) by increasing the available SSA approximately by a factor of two (~1.8 times). However, the H_2 adsorption behavior of the FLG materials seems to exceed "Chahine's rule" for activated carbons that roughly predicts 1 wt.% H_2 uptake at 77 K per 500 m^2/g BET SSA [22]. In both cases, the experimental

capacities are ~25 % larger compared to the theoretically expected ones. As the H_2 sorption data refer to "excess adsorption" beyond ~60 bar, the capacity starts to decrease due to bulk H_2 compression (i.e. the density value of the H_2 gas outside the pores exceeds the one inside the pores) and finally reaches 1.07 and 1.90 wt.% for FLG-400 and FLG-800, respectively, at ~100 bar (i.e. ~5.5 and ~6.2 % uptake drop, respectively).

Fig. 5b demonstrates the enhanced H_2 physisorption behavior of both samples at the lower pressures (< 1 bar), which is most likely attributed to microporosity; the micropores (< 2 nm) act as highly energetic adsorption sites for the H_2 molecules due to overlapping potential of the opposite pore walls [23]. This observation agrees well with the pore size distribution analysis based on the N_2 sorption data in which micropores with sizes of 0.7-0.8 nm were previously detected. The adsorbed H_2 amounts at ~1 bar represent almost 50 % of the maximum capacities (i.e. ~0.6 and ~1 wt.%, respectively). These low-pressure values are higher than the ones reported, under the same experimental conditions (i.e. 77 K and 1 bar), by Srinivas et al. [8] for a chemically-reduced graphene (H_2 uptake 0.64 wt.%, BET SSA ~640 m^2/g), by Xia et al. [6] for carbon dioxide-activated porous graphene-based carbons (H_2 uptake up to 0.75 wt.%, BET SSA up to ~530 m^2/g, micropore SSA up to ~210 m^2/g) and recently by Kostoglou et al. [3] for a hydrothermally-derived nanoporous spongy graphene (H_2 uptake 0.48 wt.%, BET SSA ~350 m^2/g and micropore SSA ~90 m^2/g).

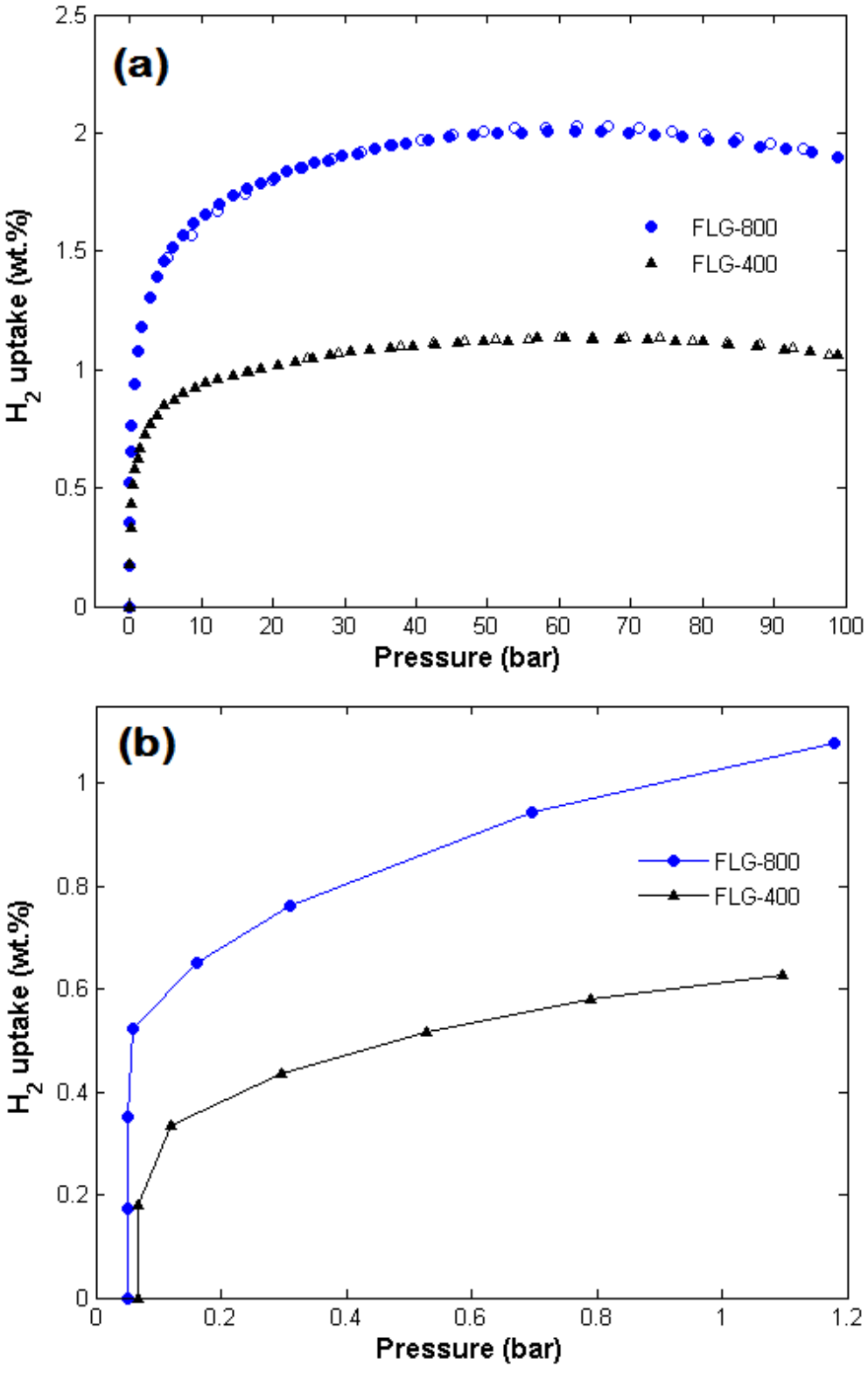

Fig. 5: (a) Reversible H_2 adsorption (colored symbols) and desorption (empty symbols) isotherms at 77 K and up to 100 bar of the plasma-exfoliated FLG powders and (b) enhanced adsorption behavior at the lower pressures (0-1 bar) due to microporosity.

4. Conclusions

In summary, plasma-processed FLG powders, with large surface areas up to ~800 m^2/g and micropore sizes less than 0.8 nm, were prepared in a DBD reactor, subsequently characterized via SEM, TEM, XPS, XRD and BET methods and finally evaluated for their H_2 storage potential at optimal temperature and pressure conditions (i.e. 77 K and up to 100 bar). A completely reversible H_2 cryo-adsorption behavior was recorded with maximum gravimetric capacities of up to ~2 wt.% at ~60 bar. The H_2 uptake was correlated to the powders' textural properties, including BET and micropore SSA. Future research will be focused on optimizing the plasma-exfoliation process to produce FLG materials with larger SSA values (>1000 m^2/g) and enhanced microporosities with the view to achieve even higher H_2 storage capacities.

Acknowledgments

The current work was partially supported by the EC FP7- INFRASTRUCTURES project H2FC (GA No. 284522). The authors are grateful to Dr. K. Giannakopoulos and Dr. A. Papavasiliou from NCSR "Demokritos" for their assistance with the TEM and SEM studies, respectively.

References

[1] G. Srinivas, X.G. Zheng, Prog. Mater. Sci. 69 (2015) 60.

[2] A.G. Klechikov, G. Mercier, P. Merino, S. Blanco, C. Merino, A.V. Talyzin, Micropor. Mesopor. Mat. 210 (2015) 46.

[3] N. Kostoglou, G. Constantinides, G. Charalambopoulou, T. Steriotis, K. Polychronopoulou, Y. Li, K. Liao, V. Ryzhkov, C. Mitterer, C. Rebholz, Thin Solid Films 596 (2015) 242.

[4] N. Kostoglou, V. Tzitzios, A.G. Kontos, K. Giannakopoulos, C. Tampaxis, A. Papavasiliou, G. Charalambopoulou, T. Steriotis, Y. Li, K. Liao, K. Polychronopoulou, C. Mitterer, C. Rebholz, Int. J. Hydrogen Energy 40 (2015) 6844.

[5] S. Lyth, H. Shao, J. Liu, K. Sasaki, E. Akiba, Int. J. Hydrogen Energy 39 (2014) 376.

[6] K. Xia, X. Tian, S. Fei, K. You, Int. J. Hydrogen Energy 39 (2014) 11047.

[7] G. Srinivas, J.W. Burress, J. Ford, T. Yildirim, J. Mater. Chem. 21 (2011) 11323.

[8] G. Srinivas, Y. Zhu, R. Piner, N. Skipper, M. Elerby, R. Ruoff, Carbon 48 (2010) 630.

[9] S. Yadav, Z. Zhu, C.V. Singh, Int. J. Hydrogen Energy 39 (2014) 4981.

[10] I.A. Baburin, A. Klechikov, G. Mercier, A. Talyzin, G. Seifert, Int. J. Hydrogen Energy 40 (2015) 6594.
[11] A. Klechikov, G. Mercier, T. Sharifi, I.A. Baburin, G. Seifert, A.V. Talyzin, Chem. Commun. 51 (2015) 15280.
[12] M. Yi, Z. Shen, J. Mater. Chem. A 3 (2015) 11700.
[13] H. Tetlow, J.P. de Boer, I.J. Ford, D.D. Vvedensky, J. Coraux, L. Kantorovich, Phys. Rep. 542 (2014) 195.
[14] S. Pei, H.M. Cheng, Carbon 50 (2012) 3210.
[15] G. Zhao, D. Shao, C. Chen, X. Wang, Appl. Phys. Lett. 98 (2011) 183114.
[16] N. McEvoy, H. Nolan, N.A. Kumar, T. Hallam, G. Duesberg, Carbon 54 (2013) 283.
[17] Perpetuus Research & Development Ltd, Particles, UK Patent appl. no. GB1405614.7 (pending status), 2014.
[18] C. Shen, J. Li, Y. Wang, Acta Mater. 74 (2014) 125.
[19] H. Takagi, K. Maruyama, N. Yoshizova, Y. Yamada, Y. Sato, Fuel 83 (2007) 2427.
[20] K.S. Binoy, R.K. Boruah, P.K. Gogoi, J. Chem. Sci. 103 (2009) 121.
[21] US Department of Energy, Multi-year Research, Development and Demonstration Plan 3.3 1, 2015 http://energy.gov/sites/prod/files/2015/05/f22/fcto_ myrdd_storage.pdf (accessed in August 2015).
[22] P. Bernard, R. Chahine, Int. J. Hydrogen Energy 26 (2001) 849.
[23] F. Rouquerol, J. Rouquerol, K. Sing, Adsorption by Powders and Solids: Principles, Methodology, and Applications, Academic Press, London, 1999.

Publication III

Nanoporous activated carbon cloth as a versatile material for hydrogen adsorption, selective gas separation and electrochemical energy storage

N. Kostoglou, C. Koczwara, C. Prehal, V. Terziyska, B. Babic, B. Matovic, G. Constantinides, C. Tampaxis, G. Charalambopoulou, T. Steriotis, S. Hinder, M. Baker, K. Polychronopoulou, C. Doumanidis, O. Paris, C. Mitterer, C. Rebholz

Nano Energy 40 (2017) 49-64

Nanoporous activated carbon cloth as a versatile material for hydrogen adsorption, selective gas separation and electrochemical energy storage

Nikolaos Kostoglou[a,b,*], Christian Koczwara[c], Christian Prehal[c], Velislava Terziyska[a], Biljana Babic[d,e,**], Branko Matovic[d], Georgios Constantinides[f], Christos Tampaxis[g], Georgia Charalambopoulou[g], Theodore Steriotis[g], Steve Hinder[h], Mark Baker[h], Kyriaki Polychronopoulou[i], Charalabos Doumanidis[i], Oskar Paris[c], Christian Mitterer[a], Claus Rebholz[a,b,*]

[a] Department of Physical Metallurgy and Materials Testing, Montanuniversität Leoben, 8700 Leoben, Austria

[b] Department of Mechanical and Manufacturing Engineering, University of Cyprus, 1678 Nicosia, Cyprus

[c] Institute of Physics, Montanuniversität Leoben, 8700 Leoben, Austria

[d] Vinča Institute of Nuclear Sciences, University of Belgrade, P.O. Box 522, 11000 Belgrade, Serbia

[e] Institute of Physics Belgrade, University of Belgrade, Pregrevica 118, 11000 Belgrade, Serbia

[f] Research Unit for Nanostructured Materials Systems, Department of Mechanical Engineering and Materials Science and Engineering, Cyprus University of Technology, 3036 Lemesos, Cyprus

[g] National Center for Scientific Research Demokritos, Agia Paraskevi Attikis, 15310 Athens, Greece

[h] Department of Mechanical Engineering Sciences, University of Surrey, GU27XH Guildford, UK

[i] Department of Mechanical Engineering, Khalifa University of Science, Technology & Research, P.O. Box 127788, Abu Dhabi, UAE

Graphical abstract

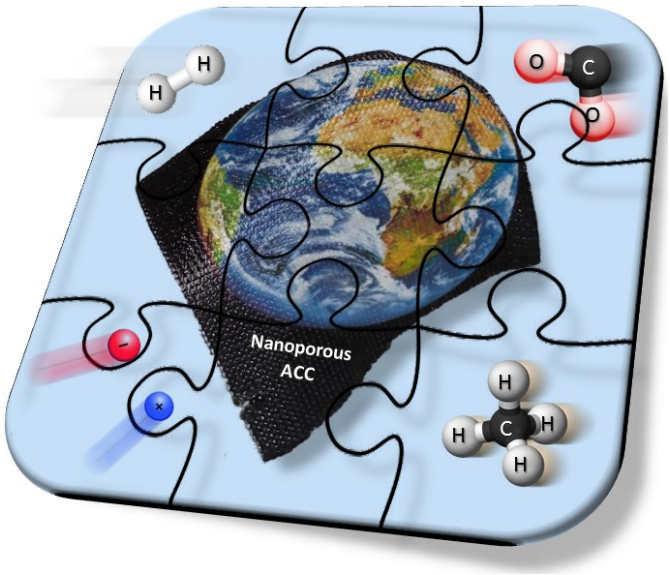

Research highlights

- CO_2 activation of carbonized viscose rayon leads to ultra-microporous carbon cloth.
- Strong interaction with H_2 and reversible uptake of 3.12 wt.% at 77 K and 72 bar.
- Predicted CO_2/CH_4 gas selectivity factor of 4.5 at 298 K and 1 bar using IAST model.
- Excellent specific area normalized supercapacitor performance using CsCl electrolyte.

Abstract

The efficient storage of energy combined with a minimum carbon footprint is still considered one of the major challenges towards the transition to a progressive, sustainable and environmental friendly society on a global scale. The energy storage in pure chemical form using gas carriers with high heating values, including H_2 and CH_4, as well as via electrochemical means using state-of-the-art devices, such as batteries or supercapacitors, are two of the most attractive alternatives for the combustion of finite, carbon-rich and environmentally harmful fossil fuels, such as diesel and gasoline. A few-step, reproducible and scalable method is presented in this study for the preparation of an ultra-microporous (average pore size around 0.6 nm) activated carbon cloth (ACC) with large specific area (> 1200 m^2/g) and pore volume (~0.5 cm^3/g) upon combining chemical impregnation, carbonization and CO_2 activation of a low-cost cellulose-based polymeric fabric. The ACC material shows a versatile character towards three different applications, including H_2

storage via cryo-adsorption, separation of energy-dense CO_2/CH_4 mixtures via selective adsorption and electrochemical energy storage using supercapacitor technology. Fully reversible H_2 uptake capacities in excess of 3.1 wt.% at 77 K and ~72 bar along with a significant heat of adsorption value of up to 8.4 kJ/mol for low surface coverage have been found. Upon incorporation of low-pressure sorption data in the ideal adsorbed solution theory model, the ACC is predicted to selectively adsorb about 4.5 times more CO_2 than CH_4 in ambient conditions and thus represents an appealing adsorbent for the purification of such gaseous mixtures. Finally, an electric double-layer capacitor device was assembled and tested for its electrochemical performance, constructed of binder-free and flexible ACC electrodes and aqueous CsCl electrolyte. The full-cell exhibits a gravimetric capacitance of ~121 F/g for a specific current of 0.02 A/g, which relative to the ACC's specific area, is superior to commercially available activated carbons. A capacitance retention of more than 97 % was observed after 10,000 charging/discharging cycles, thus indicating the ACC's suitability for demanding and high-performance energy storage on a commercial scale. The enhanced performance in all tested applications seems to be attributed to the mean ultra-micropore size of the ACC material instead of the available specific area and/or pore volume.

Keywords: Activated carbon cloth; Nanoporous material; Adsorption, H_2 storage, CO_2/CH_4 selectivity; Supercapacitor electrode

1. Introduction

Nanoporous carbons with high specific area (SA) and specific pore volume (SPV) have attracted considerable interest during recent years as adsorbent materials for the confinement and storage of highly-dense energy carriers, such as hydrogen (H_2) [1–10] and methane (CH_4) [11–14], capture and separation of unwanted greenhouse emissions such as carbon dioxide (CO_2) [4,5,15–17] as well as electrode materials for highly-efficient electrochemical energy storage devices such as supercapacitors [3,5,18–27]. Additional characteristics, including low densities, superior thermochemical stability, excellent electrical conductivity, affordable production cost and a plethora of manufacturing processes, make carbon-based materials even more attractive for such purposes [3,8]. According to recent reports [28,29], the worldwide demand for activated carbon (AC) is expected to grow over 12 % by 2019 due to the continuous awareness towards

environmental and energy issues, for which AC materials can play a key role, while the global AC market is forecasted to record revenues of up to 4.9 billion $ by 2021. However, most of the commercially-available and laboratory-produced carbon materials are systematically studied as loose and extremely fine powders, thus raising issues related to health [30], ease of handling and processing [3] as well as practical implementation in commercial-scale systems for stationary and mobile applications [31,32]. Even if some porous carbons are also produced in a "bulkier" compacted form, including granules, pellets, monoliths or blocks, there are still issues arising from a practical perspective. In addition, the preparation of carbon powders in the form of functional components, such electrodes, membranes, thin films or coatings using binders [11], hot pressing [13] and spark plasma sintering processes [21], may lead to a partial modification of their original textural and porosity properties, including the reduction of their SAs and SPVs, due to agglomeration and/or pore blocking mechanisms [11,24]. Such values certainly play a crucial role in the physical adsorption and selective separation of gases and/or mixtures thereof as well as in the potential-induced electrosorption of ions from aqueous or organic electrolytes on the surface of charged electrodes. For the case of supercapacitor electrodes, the use of an insulating binder may also increase the internal electrode resistance and lead to a drop in their performance [3,24].

Therefore, the major challenge lies in the facile and low-cost development of a lightweight, mechanically flexible and non-fragile carbon-based structure in compact form that could exhibit similar porosity properties (i.e. large SAs and SPVs combined with sub-nm pore sizes) to well-established standard ACs that are currently available on the market. Such an approach would not only permit safer and easier handling, but should also allow potential modifications through physical or chemical means without significantly altering important porosity features as well. Furthermore, this type of material could be more effectively introduced as a practical, self-supporting and efficient component in commercial-scale devices for gaseous and electrochemical energy storage. On the one side, it may be included, for example, as an adsorbent in cryo-compressed tanks with the aim to offer a more efficient combination of packing density and enhanced mass transfer compared to powders as well as drastically minimize attrition problems that lead to severe pressure drops and poor mass transfer after cycling or even pipeline clogging. On the other side, it may act, for instance, as a flexible and binder-free working electrode for electric-double layer capacitors. In this respect, the US Department of Energy (DOE) has established

specific targets towards the development of gaseous fuel storage systems for the automotive industry as well as grid energy storage technologies [32–34]. The gravimetric and volumetric capacities for H_2 storage lie at 5.5 wt.% H_2 (or 1.8 kWh/kg) and 0.04 kg H_2/L (or 1.3 kWh/L), respectively, for delivery temperatures between 233 and 358 K, respectively, as well as delivery pressures between 3 and 12 bar, respectively [33]. However, it should be clarified that the aforementioned values refer to the entire H_2 storage system implemented in a light-duty fuel cell vehicle and not the sorbent material itself. For CH_4 storage instead, the targets for potential adsorbent materials are more clear, thus referring to gravimetric and volumetric capacity values of 0.5 g/g (i.e. 0.5 g CH_4 per g of adsorbent) and 350 v/v (i.e. 350 cm^3 CH_4 at standard temperature and pressure (STP) conditions per cm^3 of adsorbent), respectively, at 298 K and up to 35 bar [34]. The latter value was set up 25 % higher than the one achieved by compressed natural gas storage at 298 K and 250 bar (i.e. 263 v/v or ~2.6 kWh/L), based on the assumption that the volumetric capacity will be reduced by 25 % as a result of packing an adsorbent in the interior of a compressed tank. The US DOE has also recognized the need for efficient electrical energy storage towards the planning and realization of a "smart" grid. Specifically, the long-term performance targets required for emerging energy storage technologies based on advanced materials and systems correspond to an efficiency of over 80 %, a lifetime of more than 5.000 cycles as well as a system capital cost of less than 150 $/kWh and a levelized cost under 0.1 $/kWh/cycle [35].

In the current study, an ultra-microporous (i.e. with sub-nanometer pore sizes) and flexible carbon cloth-like material with large SA (~1200 m^2/g) and SPV (~0.5 cm^3/g) was produced via a facile and few-step procedure, upon combining chemical impregnation, carbonization and CO_2 activation of a commercial cellulose-based fabric. In general, cellulose-based and polyacrylonitrile (PAN) fibers are the most common precursors for the production of carbon fiber materials. Cellulosic precursors in particular demonstrate attractive properties, such as large thermal conductivity, good mechanical flexibility and low cost [36]. However, natural cellulose-based materials (e.g. cotton, linen, ramie, etc.) are not considered appropriate precursors for carbonization due to their discontinuous filaments, low degree of orientation among their fibers, as well as large amount of impurities [36,37]. Such features may eventually lead to a low yield of carbon fibers that exhibit rather poor porosity characteristics. Instead, semi-synthetic (regenerated) cellulose-based fibers such as viscose rayon are preferentially selected for carbonization

and activation purposes as they transform to highly nanoporous and large surface area structures. Activated carbon cloth-like materials, as studied here, have frequently been investigated during the past years as adsorbents, filters and electrodes mostly for environmental purposes, including wastewater treatment from organic solvents and toxic pollutants [38,39], heavy metal ions [40,41] and acid and basic dyes [42,43], capacitive deionization for water desalination [44–46] as well as atmospheric air purification from volatile organic compounds and micro-pollutants [47–49]. More recent studies have focused on using such cloths as electrodes, substrates and catalyst supports for energy-related devices, such as photovoltaic cells for conversion of solar radiation into electricity [50], lithium-ion batteries and supercapacitors for electrochemical energy storage [19,24,26,27,51] as well as microbial fuel cells for electric power generation [52,53]. However, only limited experimental data are currently available in the literature describing the H_2, CO_2 and CH_4 adsorption properties of such nanopore-sized carbon cloth-, fabric- or textile-like materials [10,12], which lack systematic study over a wide range of temperature and pressure conditions as well as an in-depth analysis of the interaction strength and selective adsorption behavior with these gases. The material within this work was extensively studied for its morphological, structural and elemental composition properties using advanced characterization methods, including scanning electron microscopy (SEM), X-ray diffraction (XRD), Raman spectroscopy, small-angle X-ray scattering (SAXS), Fourier-transform infrared spectroscopy (FT-IR) and X-ray photoelectron spectroscopy (XPS). The porosity properties were deduced from low-pressure (0–1 bar) nitrogen (N_2) gas adsorption/desorption data collected at 77 K using empirical methods. The H_2 storage performance was evaluated by low- (0–1 bar) and high-pressure (0–100 bar) gas adsorption/desorption measurements at a series of temperatures between 60 and 298 K, while the equivalent CO_2 and CH_4 adsorption behavior was investigated at low-pressures (0–1 bar) between 273 and 323 K. Gas sorption-related properties, such as isosteric enthalpies of H_2, CO_2 and CH_4 adsorption as well as CO_2 over CH_4 selectivity values, were also calculated from the experimental data, using well-established physical-based models. Finally, the electrochemical performance was studied by cyclic voltammetry (CV), galvanostatic cycling with potential limitation (GCPL) and electrochemical impedance spectroscopy (EIS) measurements using half- and fully-assembled electrical double layer capacitor cells. Relevant properties to

supercapacitor performance were evaluated, including specific capacitance and galvanostatic cyclic stability, towards practical energy storage applications.

2. Materials and methods

2.1 Synthesis procedure

Fig. 1 demonstrates the basic steps of the production process of the nanoporous activated carbon cloth (denoted hereafter as ACC). The ACC material was prepared via chemical impregnation followed by carbonization and CO_2 activation in dynamic mode using a viscose rayon cloth of a whitish color as the carbon precursor (denoted hereafter as VRC; originally obtained from the Viskoza factory, Loznica, Serbia). All synthesis steps were initially proposed and optimized by Babic and co-workers [54,55] for laboratory conditions. In a typical synthesis procedure, the raw VRC material was first impregnated into a mixture of 4.0 wt.% ammonium chloride (NH_4Cl) and 4.0 wt.% zinc chloride ($ZnCl_2$) aqueous solution with the aim of increasing the reaction yield during carbonization as well as reducing the ash and volatile carbon content upon carbonization [39,55–57]. The soaked VRC sample was then dried in air at 80 °C for 40 min. In the next step, the VRC material was carbonized inside a vertical furnace from 30 up to 630 °C under an inert N_2 atmosphere using a heating rate of 5 °C/min (i.e. the carbonization process lasted for 2 h). When the temperature reached 600 °C, the N_2 flow was paused and then CO_2 was introduced into the furnace chamber, with the cloth sample being additionally activated from 630 to 930 °C using a heating rate of 5 °C/min (i.e. the activation process lasted for 1 h). When the maximum temperature of 930 °C was finally reached, the CO_2 flow was switched back to N_2 with the aim of avoiding further gasification and subsequently the furnace was switched off and left to physically cool down at room temperature. The resulting black-colored ACC material was thoroughly washed with distilled water to remove traces of chlorides and/or other soluble impurities, dried in air at 110 °C for 40 min and finally stored in a desiccator. It should be noted that the as-prepared ACC is non-fragile and maintains the cloth-like texture of the original VRC precursor.

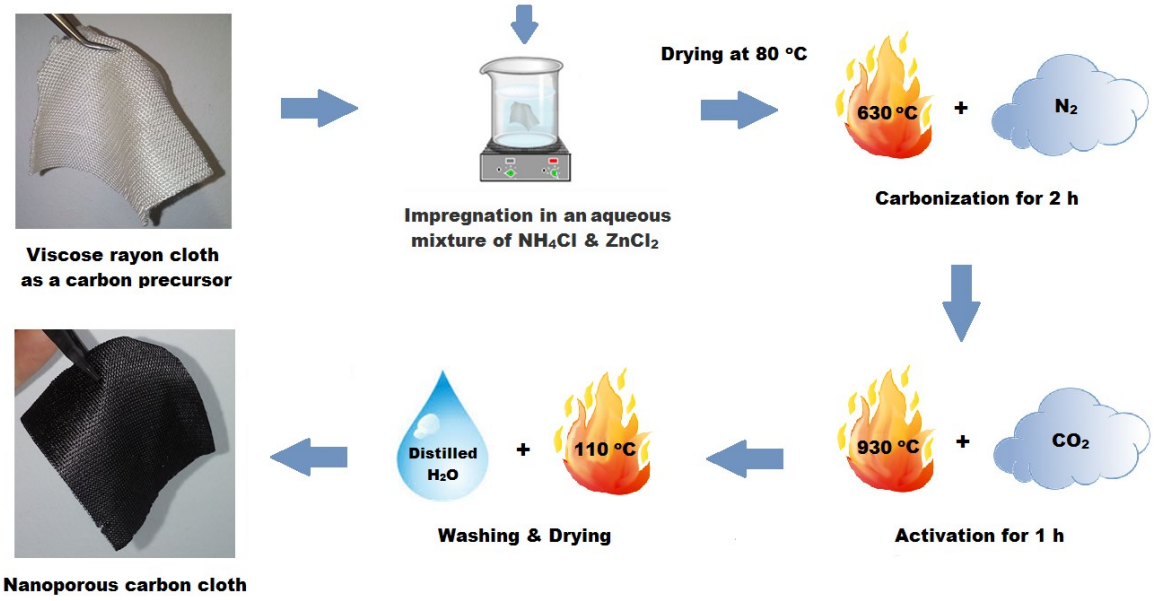

Fig. 1: Few-step synthesis of the nanoporous ACC material using a VRC as the raw material; the temperatures for carbonization and CO_2 activation procedures refer to the maximum values reached using a heating rate of 5 ^{o}C/min.

2.2 Characterization studies

Low- and high-magnification SEM images were collected by a FEI Quanta 200 microscope using acceleration voltages between 10 and 20 kV and a working distance of 10 mm. The X-ray diffractogram was recorded by a Bruker-AXS D8 Advance diffractometer operated with CuKα radiation (λ ~1.54 Å) using voltage and current values of 40 kV and 40 mA, respectively. The measurements were performed in the Bragg-Brentano geometry using a continuous scan speed mode between the diffraction angles (2θ) of 10 and 90°, a 0.01° step width and a 0.5°/min scan speed. The Raman spectrum was recorded by a Jobin-Yvon LABRAM confocal spectrometer equipped with a frequency-doubled Nd-YAG laser emitting at 532.2 nm. The laser beam was focused onto the sample by an Olympus BX 40 microscope fitted with a ×50 long-working distance objective lens at a power density of 0.1 mW/μm^2 and a spatial resolution of 1.5 cm^{-1}. The SAXS curve was recorded with a Bruker NANOSTAR SAXS facility operated with CuKα radiation (λ ~1.54 Å) using voltage and current values of 40 kV and 40 mA, respectively. The 2-D SAXS pattern was recorded with a Vantec 2000 detector and was then spherically averaged and corrected for background, transmission and measurement time. Using an analytical model fitted to the measured SAXS intensity, a 3-D real-space visualization of the nanopore structure could be generated. The FT-IR spectrum was recorded by a JASCO 4100 spectrometer in the mid-

infrared region between 3600 and 1000 cm^{-1} with a spatial resolution of 4 cm^{-1}. The studied sample (~1 mg) was prepared in the form of potassium bromide (KBr) pellets, and the raw FT-IR data were smoothed. XPS analysis was carried out by a Thermo Scientific Theta Probe spectrometer equipped with a monochromated AlKα radiation source (h_ν = 1486.6 eV) using an X-ray spot of ~400 μm in radius. Survey spectra were acquired by using a pass energy of 300 eV, while a high-resolution core level spectrum for the C1s component was acquired with a pass energy of 50 eV. All spectra were charge referenced against the C1s peak at 284.5 eV (sp^2 hybridized carbon) to correct for charging effects during acquisition. Quantitative chemical compositions were determined from the high-resolution core level spectra following the removal of a nonlinear Shirley background. The Thermo Scientific Avantage software was used for peak fitting of the C1s peak, which incorporates the appropriate sensitivity factors and corrects for the electron energy analyzer transmission function.

Low-pressure (0–1 bar) N_2 adsorption/desorption isotherms were recorded at 77 K by a Quantachrome Autosorb MP-1 volumetric gas sorption analyzer using a liquid N_2 bath and ultra-pure (99.999 %) N_2 gas. The total SA was calculated using the multi-point Brunauer-Emmet-Teller (BET) and Langmuir methods in the lower relative pressure (P/P_0) region between 0.01 and 0.04 of the adsorption data, following the BET consistency criteria of the International Standard Organization (ISO 9277:2010) [58]. The total SPV for pores smaller than ~50 nm was estimated using the single-point Gurvich rule at P/P0 ~0.96 [59]. The micropore SA and SPV values were extracted by using the carbon black statistical thickness equation (t-plot) [59,60]. A series of low-pressure (0–1 bar) H_2 adsorption/desorption isotherms were recorded between 60 and 100 K using the aforementioned analyzer (Quantachrome Autosorb MP-1) coupled with a Gifford-McMahon two-stage closed-cycle refrigerator (cryo-cooler). Prior to the low-pressure N_2 and H_2 adsorption measurements, samples of ~50 mg were degassed under vacuum (10^{-6} mbar) at 250 °C for 12 h with the aim of removing any physisorbed species and/or synthesis remnants from the material's surface. High-pressure (0–100 bar) H_2 adsorption/desorption isotherms were recorded at 77 and 298 K using a Hy-Energy PCTPro-2000 volumetric gas sorption analyzer and ultra-pure H_2 gas (99.9999 %). Prior to the measurements, a sample of ~200 mg was degassed under vacuum (10^{-6} mbar) at 250 °C for 12 h. Volume calibrations with helium gas (He) were carried out at 303 K to avoid potential errors from He adsorption at 77 K. The dead volumes at 77 K were consequently calculated based on a non-porous glass reference curve

(i.e. V_{77K} vs. V_{303K}). Low-pressure (0–1 bar) CO_2 and CH_4 adsorption/desorption isotherms were recorded at 273, 298 and 323 K by a Micromeritics 3Flex volumetric gas sorption analyzer using a PolyScience circulating bath (water/ethylene glycol mixture; 50/50 vol%.) and ultra-pure (99.9999 %) CO_2 and CH_4 gases. The studied samples (~50 mg) were also degassed prior to these measurements using the same conditions as the ones previously described (i.e. 10^{-6} mbar and 250 °C for 12 h). A pore size distribution (PSD) analysis was carried out for the degassed ACC sample by applying the Quenched Solid Density Functional Theory (QSDFT) and the Grand Canonical Monte Carlo (GCMC) kernels for slit-like shape pores in the N_2 (77 K) and CO_2 (273 K) adsorption data, respectively. Methods like QSDFT take into account the energetic and geometrical heterogeneities of nanoporous carbon surfaces [61,62]. All the gas uptake quantities reported in this study (i.e. H_2, CO_2 and CH_4) were expressed as excess gravimetric uptakes, either as the volume of adsorbed gas, at STP conditions, relative to the degassed mass of the sample (i.e. v_{gas}/m_{solid} in cm^3/g units), or as the mole of adsorbed gas relative to the degassed mass of the sample (i.e. n_{gas}/m_{solid} in mmol/g units), or as the total capacity of the system, which refers to the mass of adsorbed gas relative to the sum of the adsorbed gas and degassed sample masses (i.e. $m_{gas}/(m_{gas} + m_{solid})$ in wt.% units). The isosteric enthalpies of adsorption (Q_{st}) at a constant surface coverage (θ) were estimated for H_2, CO_2 and CH_4 by fitting the low-pressure adsorption data for three different operating temperatures with a high-order polynomial equation and subsequently using the Clausius-Clapeyron equation [63]. Hence,

$$Q_{st} = -R\left[\frac{\partial \ln(P)}{\partial(1/T)}\right]_{\theta}, \qquad (1)$$

where R is the universal gas constant (i.e. 8.314 J mol^{-1} K^{-1}), P is the pressure and T is the temperature given in K. Additionally, Q_{st} calculations were carried out by using a multiple Virial fitting of all the experimental adsorption curves measured at different temperatures. The two methods (i.e. Clausius-Clapeyron and Virial) produced identical results, however the latter allowed for a more accurate estimation of the adsorption enthalpy at zero coverage. The CO_2/CH_4 adsorption selectivity factor (S) for two different gaseous mixtures (i.e. landfill gas with 50/50 and natural gas with 5/95) was estimated by using the Ideal Adsorbed Solution Theory (IAST) model [64] and the low-pressure adsorption data at all three operating temperatures (i.e. 273, 298 and 323 K). Hence,

$$S = \frac{q_a/q_b}{p_a/p_b} \quad , \quad (2)$$

where q_a, q_b and p_a, p_b are the molar fractions of the two components in the adsorbed and bulk gas phase, respectively.

Electrochemical measurements were performed with a Gamry Reference 600 potentiostat using a custom-built cell with a polyether ether ketone (PEEK) housing and titanium pistons for the electrical contact. The pistons are spring loaded in order to apply consistent pressure. The cell is built up as a multilayered assembly with two platinum current collectors, a counter-electrode, a working electrode and a glass fiber separator in between the electrodes (Whatman GF/A). An aqueous 1 M cesium chloride (CsCl) solution was used as the electrolyte and the ACC as the electrode. Compared to organic electrolytes or ionic liquids, aqueous CsCl has the advantage of non-toxicity, low cost and environmental friendliness [65]. Due to the mechanical stability and flexibility of the ACC material, no additional polymer binder was needed for the preparation of the electrodes for all electrochemical characterization measurements. All the half-cell measurements were performed with a two-electrode setup using an oversized activated carbon electrode as quasi-reference. More specifically, the half-cell design consists of the ACC working electrode (WE), 5 mm in diameter (4.2 mg), punched out of the ACC material and a counter electrode (CE), 12 mm in diameter, made of a commercial AC (YP-80F from Kuraray Chemical Co.) with 5 wt.% polytetrafluoroethylene (PTFE) as binder. The CE has about six times the mass of the WE and can be treated as a quasi-reference electrode. The full-cell design on the other hand consists of equivalent electrodes (i.e. both of them are ACC in a symmetric setup) having a diameter of 12 mm and equal mass of 29 mg. CV, GCPL and EIS methods were applied in order to characterize the electrochemical (double-layer) performance of the supercapacitor cells. Half-cell CV and GCPL measurements were done in a voltage range between −0.6 and +0.6 V against the YP-80F pseudo-reference electrode. The CV curve was recorded with a scan rate of 10 mV/s, while the GCPL profile was measured with a constant specific current of 0.1 A/g and the data were analyzed for the discharging process only. The specific capacitance was calculated as follows,

$$C = \frac{\int_{t_0}^{t} I\, dt}{m \cdot \Delta U} \quad , \quad (3)$$

where I is the discharging current, m the WE mass and ΔU the voltage change during the discharging process. The capacitance values were calculated by correcting for the voltage drop due to the internal resistance and the polarity reversal of the current. The CV curve of the full-cell was also recorded with a scan rate of 10 mV/s and the equivalent GCLP power handling test was performed using different specific currents in the range from 0.02 to 10 A/g (based on the weight of one electrode). However, a factor of ½ has to be considered in Eq. (3) in order to properly calculate the specific capacitance of a full-cell. EIS studies were performed around 0 V with a root-mean-square (RMS) value of ± 5 mV over a frequency range from 100 kHz to 10 mHz with 10 points per decade. Finally, the full-cell stability test consists of 10000 GCPL cycles from 0 to 1.2 V using a specific current of 1 A/g. During this stability test, the columbic efficiency was also tracked over time. As the specific current for the charging and discharging processes was similar, the coulombic efficiency (η) was calculated as follows,

$$\eta = \frac{t_d}{t_c} \quad , \qquad (4)$$

where t_c and t_d represent the charging and discharging time, respectively.

3. Results and discussion

3.1 Carbonization and activation mechanism

The transformation of regenerated cellulose-based fibers (e.g. viscose rayon) into carbon fibers (CFs) is considered a complex procedure; the most simplified mechanism was proposed by Bacon and Tang [66,67]. Specifically, the carbonization process consists of four stages depending on the processing temperature range: (a) physical desorption of water (25–150 °C), dehydration from the cellulose unit (150–240 °C), thermal cleavage of the glycosidic linkage and scission of C–O and C–C bonds through free radical reaction (240–400 °C) and (d) aromatization (from 400 °C and above). Hence, the yield of the final CF-based product depends on the conditions of carbonization as well as on the type of the starting material. The step of impregnation in Lewis acid catalysts prior carbonization, including a combination of NH_4Cl and $ZnCl_2$ within this study, drastically modifies the pyrolysis mechanism of the cellulose precursor by primarily favoring dehydration over depolymerization, thus reducing the time of treatment as well as providing a higher carbon yield [56,57]. Further activation of the obtained CF material (after carbonization) by chemical and/or physical methods considerably increases the overall SA and SPV. Physical

activation, in particular, involves oxidation of the CF material's external surface and inner porous structure by CO_2 or water vapor at high temperatures (850–1100 °C) [68]. The yield of the ACC product was calculated at ~34 % by considering the mass change of the raw VRC precursor upon carbonization and CO_2 activation. As expected, the aforementioned value lies below the theoretical carbon yield of 44.4 % for pyrolyzed cellulose, which is determined stoichiometrically from its molecular formula $(C_6H_{10}O_5)_n$ [36].

3.2 Surface morphology and geometry

Fig. 2 shows SEM images of the hierarchical structure of the ACC material over a wide range of magnifications that cover three orders of magnitude in length (i.e. from mm to μm). From a macroscopic view (Fig. 2a), the ACC appears to maintain the original woven chain-like morphology of the VCR precursor upon carbonization and CO_2 activation. In Fig. 2b, it is clear that the material is woven from yarns that form a continuous fabric, while each yarn spans several hundreds of microns (i.e. 200–500 μm) in width and is composed of tens of individual CFs. The geometrical characteristics of the main building block (i.e. CF) can be resolved at even higher magnifications (Fig. 2c, d and e). Each CF has a diameter in the range of 10–15 μm (Fig. 2c and d), while it exhibits a corrugated circumference with wavelengths on the order of 1–2 μm (Fig. 2e). Finally, Fig. 2f shows a fractured CF surface, which appears to be dense in the interior, suggesting that the presence of porosity should exist at even smaller scales and most probably at the level of nanometers, which however cannot be resolved by SEM. Such porous structure appears as another key factor contributing to the high SPV attributes of the ACC material.

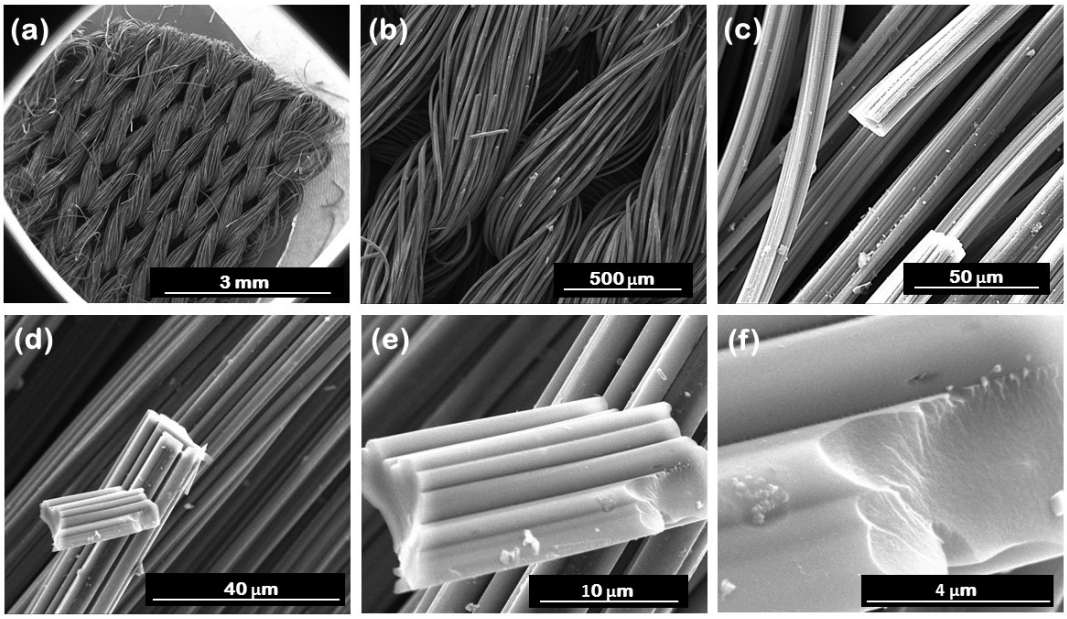

Fig. 2: SEM images at different magnifications showing (a), the ACC cloth, (b) woven yarns, (c) and (d) carbon fibers , (e) fiber corrugations and (f) fractured fiber surface.

3.3 Structural features

Fig. 3a presents the X-ray diffractogram of the as-prepared ACC material, which is characteristic of activated CFs demonstrating a turbostratic disorder (i.e. random orientation among the stacked hexagonal- structured graphene sheets). Hence, the broad peaks at the diffraction angles (2θ) of around 23° and 43° correspond to the (002) and (100) reflections of turbostratic carbon, respectively [36,37]. These two peaks are shifted to lower 2θ values compared to those of crystalline graphite, which are originally located at 26.5° and 44.3°, respectively, based on the Joint Committee on Powder Diffraction Standards (JCPDS) card no. 75-1621. This means that the in-plane crystallographic structure of the graphene layers and their stacking are considerably distorted. The Raman spectrum, shown in Fig. 3b, indicates the carbonaceous nature of the as-prepared ACC material. Two characteristic modes are observable in the wavelength region of 600 and 2000 cm^{-1}, i.e. the defect-activated D band at ~1338 cm^{-1} due to disordered structure and the graphitic G band at ~1593 cm^{-1} associated with bond stretching vibration of sp^2 carbon atoms in a two-dimensional hexagonal lattice [37,69]. The SAXS intensity versus the scattering vector length (Q) of the pure ACC powder is shown in the left side of Fig. 3c (i.e. black data points). The position and shape of the "hump" around 2 nm^{-1} contains information about the mean pore width and possible correlations in-between neighboring pores [70,71]. The concept of Gaussian Random Fields (GRFs) can be used in order to

visualize a porous structure in 3-D [72,73]. Following a recent study [71], an analytic function (i.e. red curve) is fitted to the measured SAXS data using fit parameters subsequently employed as input for the pore structure generation. The 3-D visualization of the ACC pore structure, presented in the right side of Fig. 3c, shows that the nanopores are rather randomly shaped, similarly to common ACs [74]. A subsequent Fast Fourier Transformation (FFT) and spherical averaging of the 3-D pore structure yields again a scattering curve with the same shape as the experimentally recorded curve, thus verifying the statistical resemblance of the modeled structure.

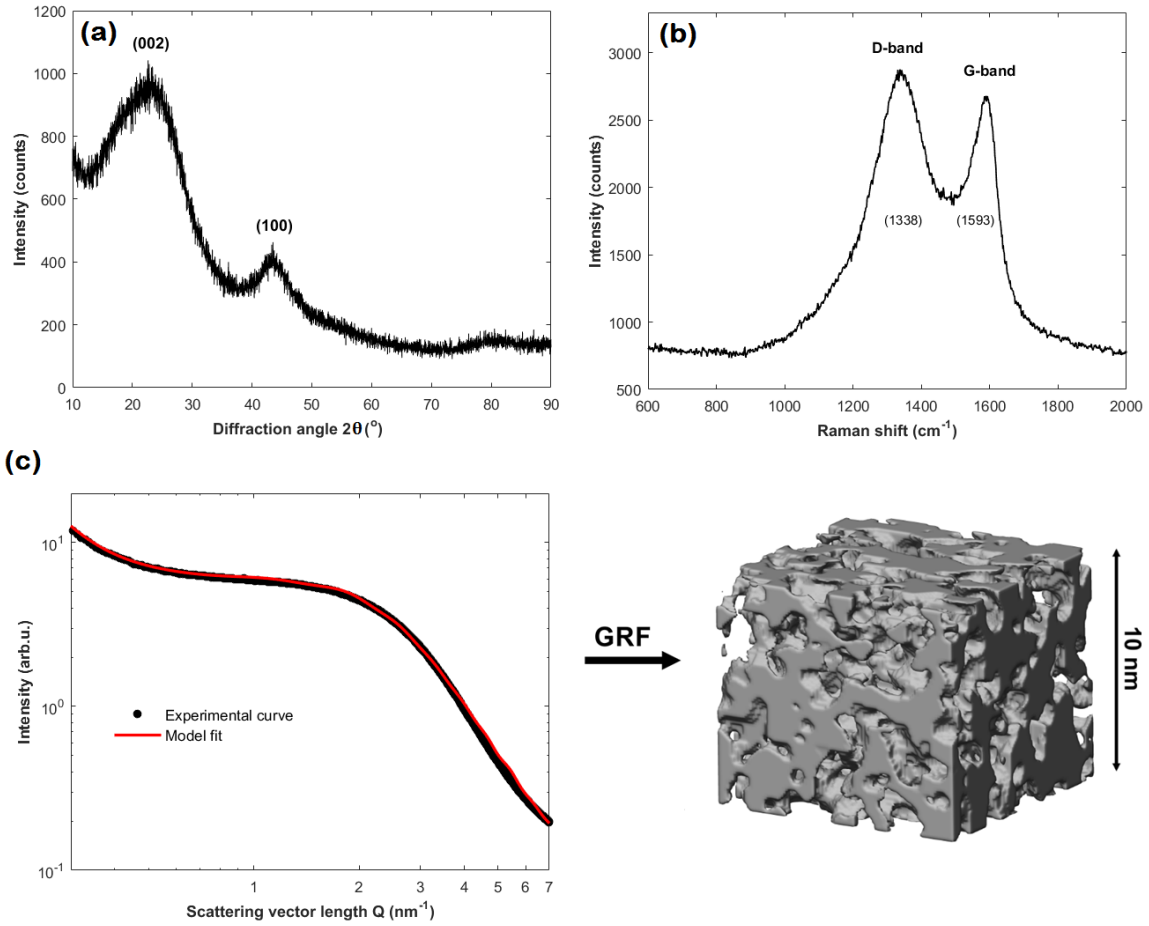

Fig. 3: (a) X-ray diffractogram, (b) Raman spectrum and (c) SAXS intensity vs. scattering vector length Q (black line) and model fit (red line) of the ACC material. A 3-D visualization of the modeled ACC pore structure created via Gaussian Random Fields (GRFs) is shown on the right.

3.4 Surface chemistry and composition

The smoothed FT-IR spectrum within the mid-infrared region, given in Fig. 4a, provides qualitative information about the nature of chemical bonds existing in the as-prepared ACC material. A series of continuous vibrational bands arises in the lower wavelength region of

1000–1650 cm^{-1}, most of which are related to the presence of surface functionalities due to the CO_2 activation procedure. The weak band at ~1194 cm^{-1} may arise from the C–O vibrations of oxygen-based groups (e.g. carboxyls, phenols, ethers, alcohols, etc.) [41]. The strongest band at ~1396 cm^{-1} probably corresponds to the symmetric –COO– vibration mode of carboxylic (–COOH) groups [75]. The less visible bands from 1569 to 1627 cm^{-1}, due to the low signal-to-noise ratio arising from the intense absorption of IR radiation from the CFs and the low concentration of surface functionalities, could be assigned to the C=C and/or C=O stretching vibration modes of aromatic sp^2 carbon and/or –COOH groups conjugated with aromatic rings, respectively [50,75]. Finally, the band at ~2375 cm^{-1} is due to atmospheric CO_2, while the broader band around 3400 cm^{-1} can be attributed to the O–H vibrations of oxygen-related surface groups and adsorbed moisture. The wide survey XPS analysis of the as-prepared ACC material (Fig. 4b) gives an elemental composition of ~83 at.% for carbon (C1s peak at ~284.5 eV) and ~13 at.% for oxygen (O1s peak at ~531.6 eV), thus suggesting a C/O ratio of ~6:1 as a result of the CO_2 activation procedure. There is a low level (~4 at.%) of impurities (e.g. N, Cl and Zn) derived mainly from the impregnation and carbonization stages of the synthesis procedure, but also from external contamination (e.g. presence of Ca). The deconvoluted high-resolution C1s spectrum, shown in Fig. 4c, was fitted with the main sp^2 carbon peak (i.e. C=C bond) at ~284.5 eV and five other components shifted from + 0.7 to + 5.4 eV relative to the main peak. It should be noted that assigning components and peak fitting of an oxidized carbon surface with such a C1s peak shape is not straightforward due to the number of possible functional groups with similar binding energies which could be present at the surface. Nevertheless, a good peak fit was obtained employing the following assignments. The component observed at ~285.2 eV can be attributed to the presence of sp^3 hybridized carbon (i.e. C–C bond) [76]. The peak at ~286.0 eV is assigned to the C–O bond of ether, phenol and/or alcohol surface groups [55,77]. It should be noted that this particular peak has an enhanced intensity that accounts for the additional C–N bonding features due to the presence of ~2 at.% N [77]. The following two components at ~286.9 and ~288.2 eV are most likely associated with carbonyl (C=O) and carboxyl (O—C=OH) functional groups, respectively, even though these peaks are slightly shifted to lower binding energies relative to those reported by Desimoni et al. [76] and Biniak et al. [77] for oxygen-containing carbon fiber and granulated activated carbon surfaces, respectively. This may be explained by the presence of additional oxygen-based functional groups around these binding energies that may give rise to peak

broadening. Finally, the broader peak region extended around 289.9 eV has been assigned to the π-π* satellite.

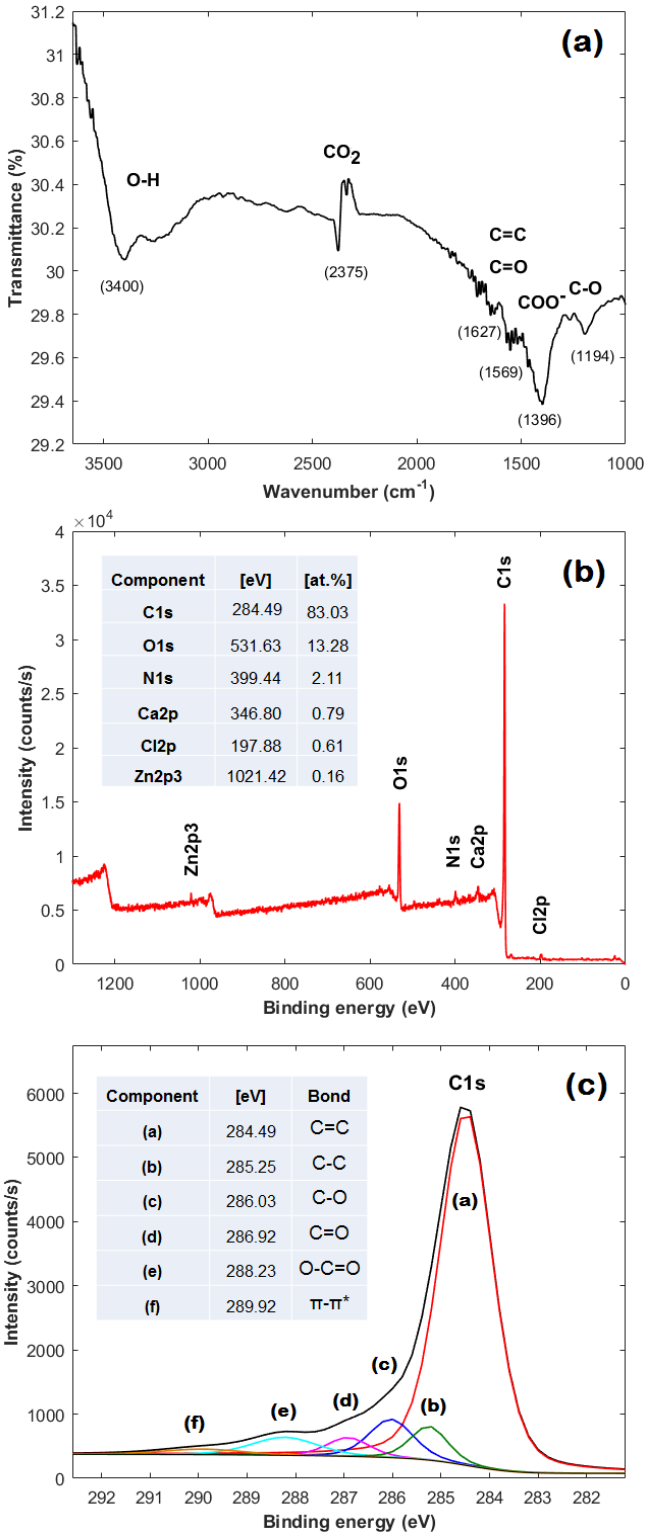

Fig. 4: (a) FT-IR spectrum in the mid-infrared region, (b) wide survey XPS analysis and (c) peak fitted high-resolution C1s spectrum of the ACC material.

3.5 Porosity properties

The low-pressure N_2 adsorption and desorption isotherms recorded at 77 K are shown in Fig. 5a. The degassed ACC material demonstrates a fully reversible type I isotherm, as defined by the classification of the International Union of Pure and Applied Chemistry (IUPAC) [78], which is characteristic of microporous materials (i.e. pore sizes below 2 nm) with a relatively small external surface. The steep N_2 uptake at the lower relative pressures ($P/P_0 < 0.01$) is indicative of the enhanced gas-solid interactions in narrow micropores (i.e. pore sizes below 1 nm) due to the micropore filling mechanism [59,79]. The adsorption isotherm reaches a plateau beyond the point of P/P_0 ~0.01 and the equivalent amount of adsorbed N_2 is attributed to the accessible micropore volume instead of the internal surface area of the material. Table 1 includes a summary of the porosity properties (i.e. SAs, SPVs and average pore sizes) of the ACC material deduced from the recorded N_2 adsorption data, as described in Section 2.2. The total SA was calculated to be 1205, 1275 and 1319 m^2/g based on the multi-point BET (denoted hereafter as S_{BET}), Langmuir and QSDFT methods, respectively. The inset of Fig. 5a shows the linear seven-point BET plot extracted for the lower P/P_0 region between 0.01 and 0.04 with a correlation coefficient of close-to-unity (r ~1). The total SPV (denoted hereafter as $V_{Gurvich}$) was calculated at 0.47 cm^3/g at P/P_0 ~0.96 for pores smaller than 51.8 nm in width. The micropore SA and SPV, as determined by the t-plot method, corresponds to the ~99 and ~98 % of the total SA and SPV values, respectively, clearly indicating the predominant microporous nature of the ACC material. The minor remaining percentage (~1 %) can be attributed to the external rough surface of the micrometer-sized CFs. In order to obtain a rough measure for the average pore size (D) we have simply evaluated the ratio $D = 2 \cdot (SPV)/(SA)$. For an infinitely extended slit-like pore, this parameter would correspond to the slit width. By inserting the values given in Table 1, the relationship provides a D value of 0.78 nm if the $V_{Gurvich}$ and the S_{BET} are included, and even 0.68 nm if the values of the corresponding QSDFT method are considered. In addition, a PSD analysis of the N_2 adsorption isotherm using the QSDFT kernel for carbon slits, shown in Fig. S1, indicates that there are no pores larger than 1.5 nm and points to ultra-microporosity with sizes below 0.61 nm (in width). These observations were further supported through the analysis of CO_2 adsorption data recorded at 273 K and up to 1 bar (presented in Fig. 6a), using the GCMC kernel for carbon slits (also shown in Fig. S1), which revealed a mean pore size around 0.57 nm.

3.6 H_2 adsorption and storage

The low-pressure (0–1 bar) H_2 cryo-adsorption and desorption isotherms recorded at 60, 70, 77, 90 and 100 K are shown in Fig. 5b. The ACC material demonstrates completely reversible gas sorption isotherms for all the temperatures; i.e. the desorption process (open symbols) follows the same pathway as adsorption (solid symbols). The gravimetric H_2 uptake at atmospheric pressure (~1 bar) reaches its highest value of 2.26 wt.% or 11.46 mmol/g at 60 K, then moves down to 1.68 wt.% or 8.47 mmol/g at 77 K (i.e. liquid N_2 temperature) and finally shows its lowest value of 0.82 wt.% or 4.11 mmol/g at 100 K. Hence, the H_2 uptake at ~1 bar drops significantly (i.e. by ~64 %) upon increasing the temperature of the system from 60 to 100 K (i.e. only by 40 degrees). The reduction rate of the H_2 uptake in this particular case seems to correspond to a value of ~0.04 wt.% K^{-1} or ~0.18 mmol/g K^{-1}, upon consideration of the low-pressure data from all five temperatures. Finally, the fact that none of the isotherms reached a clear saturation point up to ~1 bar implies that H_2 uptake can be further increased under a higher pressure regime. Fig. 5c describes the strength of interaction between the gaseous H_2 and the solid ACC surface, as estimated by using the low-pressure data at 60, 70 and 77 K and the Clausius-Clapeyron equation (Eq. (1)). The Qst value corresponds to ~8.4 kJ/mol for a low surface coverage (~0.84 mmol/g), which subsequently decreases and remains almost stable at ~5.6 kJ/ mol for higher loadings (~8.4 mmol/g), most probably due to saturation of energetically "strong" adsorption sites on the ACC surface [9]. Additionally, the Q_{st} value at zero coverage, as estimated from the Virial fitting of the low pressure isotherms, corresponds to ~9.2 kJ/mol. The aforementioned values are slightly higher than the Q_{st} values presented for standard activated carbons, which are usually found in the range of 5–8 kJ/mol [3] and show an average value of around 6 kJ/mol [31]. This is mostly attributed to the dominant ultra-microporous characteristics of the ACC material (i.e. narrow micropore sizes), however an influence of the enriched surface chemistry features (i.e. presence of oxygen surface groups as determined FT-IR and XPS studies) cannot be excluded. Even if the physical adsorption mechanism facilitates a fully reversible H_2 uptake and release, characterized by fast adsorption and desorption kinetics, the low Q_{st} values between carbon and H_2 compared to other gases (e.g. CO_2 and CH_4) are still an important challenge towards efficient storage under non-cryogenic conditions. Theoretical studies have shown that the optimum Q_{st} value for efficient and reversible H_2 adsorption in ambient temperatures and operating pressures between 1.5 and 30 bar lies at ~15 kJ/mol

[80]. For pure carbon materials with an average Q_{st} value of around 6 kJ/mol, an optimum operating temperature of 115 K is required for maximizing the H_2 delivery, which is however far below the desired ambient temperature range (i.e. from 273 to 298 K).

Further H_2 adsorption studies were performed under higher pressures up to ~100 bar with the aim to explore the full H_2 storage potential of the ACC material and the respective excess adsorption isotherms recorded at 77 and 298 K are presented in Fig. 5d. The adsorption curve at 77 K follows a Langmuir-like behavior and a maximum excess H_2 uptake of 3.12 wt.% or 15.97 mmol/g is reached at ~72 bar. Based on Chahine's rule for microporous activated carbons [81], an uptake of 1 wt.% H_2 is expected at 77 K and ~35 bar per 500 m^2/g of SA or 0.2 cm^3/g of SPV. In the case of our ACC, however, the experimentally-derived H_2 uptake at 77 K and ~ 35 bar (i.e. 3.0 wt.%) exceeds by ~25 % the theoretically-predicted value for an S_{BET} of ~1205 m^2/g (i.e. 2.41 wt.%). Gogotsi et al. [9] studied a series of carbide-derived carbons with controllable SA, SPV and PSD values with the aim to systematically investigate the correlation between such properties and the H_2 uptake performance at 77 K and 60 bar. They concluded that materials outperforming Chahine's rule (i.e. showing deviation from the linear trend) usually exhibit a greater fraction of micropores with diameter smaller than 1.5 nm and/or a 0.6–0.7 nm mean pore size, similar to our ACC sample (i.e. ~0.6 nm based on GCMC analysis of CO_2 adsorption data collected at 273 K). Furthermore, the amount of adsorbed H_2 seems to almost double by increasing the pressure up to ~72 bar in comparison to the low-pressure data presented in Fig. 5a (i.e. the equivalent uptake at 77 K and ~1 bar was 1.68 wt.% using the low-pressure equipment). This observation is also supported by the steep increase of the high-pressure isotherm up to ~1 bar (i.e. four adsorption points were recorded up to ~0.8 bar with the slope of the curve being almost vertical to the pressure axis), a trend that is certainly explained by the presence of enhanced and narrow microporosity across the ACC surface, as already indicated by the N_2 sorption and porosimetry studies (see Section 2.2). It is well-known that narrow micropores act as highly-energetic adsorption sites for molecular H_2 as the potential fields of the opposite pore walls overlap each other [31,82]. The H_2 adsorption isotherm at 77 K seems to reach a point of saturation (i.e. plateau) beyond the pressure of ~75 bar, while no significant drop of the adsorbed excess amounts can be observed up to ~100 bar due to bulk H_2 densification [83]. On the other hand, the equivalent H_2 adsorption performance at room temperature conditions was rather poor and the maximum H_2 uptake of 0.35 wt.% or 1.75 mmol/g reached at 298 K and ~95 bar

cannot be considered a sufficient value for practical H_2 storage applications. The adsorption curve at 298 K follows a Henry-like behavior, thus increasing almost linearly by increasing the applied pressure. The inset of Fig. 5d shows a comparison of the H_2 uptake performance at 77 and 298 K under relatively moderate pressures (i.e. up to ~21 bar). It is evident that the ACC material stores almost 22 times less H_2 at 298 K than 77 K (i.e. ~0.13 vs. ~2.86 wt.% H_2 at ~21 bar). This is attributed to the weak quadrupole moment and poorly polarizable nature of the molecular H_2, which leads to a rather weak adsorption in ambient conditions [31].

Table 1 – Porosity properties of the ACC material deduced from the N_2 adsorption and desorption isotherms recorded at 77 K.

S_{BET} [m^2/g]	$S_{Langmuir}$ [m^2/g]	S_{Micro} [m^2/g]	$S_{Micro(p)}$ [%]	S_{QSDFT} [m^2/g]	$V_{Gurvich}$ [cm^3/g]	V_{Micro} [cm^3/g]	$V_{Micro(p)}$ [%]	V_{QSDFT} [cm^3/g]	D_A [nm]	D_B [nm]
1205	1275	1190	98.76	1319	0.47	0.46	97.87	0.45	0.78	0.68

S_{BET}: Brunauer-Emmet-Teller (BET) specific area (SA), $S_{Langmuir}$: Langmuir SA, S_{Micro}: micropore SA derived by the Carbon Black statistical thickness (t-plot) method, $S_{Micro(p)}$: % percentage of micropore SA to BET SA ((S_{Micro}/S_{BET}) × 100%), S_{QSDFT}: cumulative SA for pores smaller than 1.5 nm in width calculated by the Quenched Solid Density Functional Theory (QSDFT) method, $V_{Gurvich}$: total specific pore volume (SPV) at P/P_0 ~0.96 for pores smaller than 51.8 nm in width calculated by the single-point Gurvich rule, V_{Micro}: micropore SPV derived by the t-plot method, $V_{Micro(p)}$: % percentage of micropore SPV to total SPV (($V_{Micro}/V_{Gurvich}$) × 100%), V_{QSDFT}: cumulative SPV for pores smaller than 1.5 nm in width derived by the QSDFT method, D_A: average pore size calculated by the ratio of $2\cdot(V_{Gurvich})/(S_{BET})$ assuming a slit pore model, D_B: average pore size calculated by the ratio of $2\cdot(V_{QSDFT})/(S_{QSDFT})$ assuming a slit pore model.

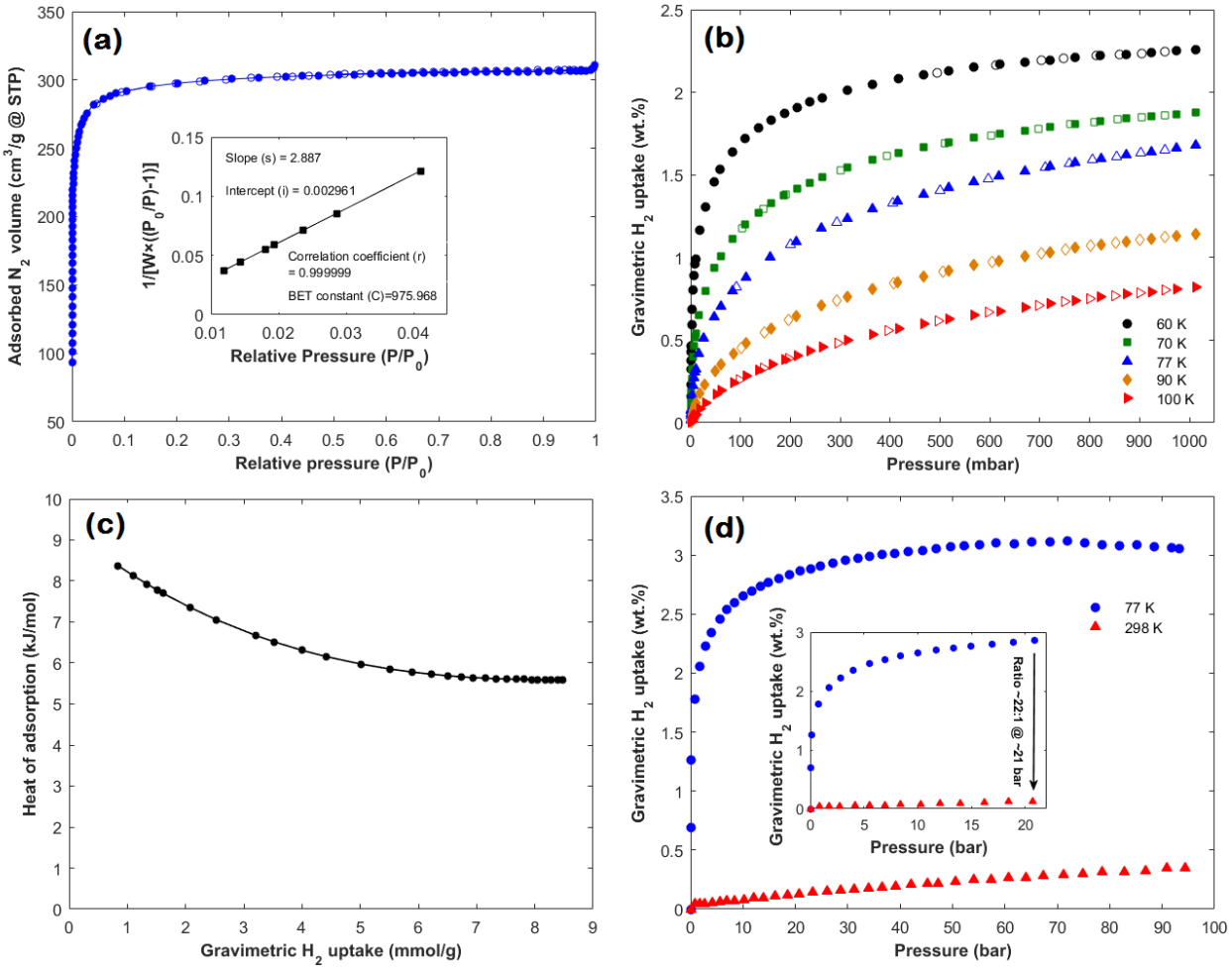

Fig. 5: (a) Fully reversible N_2 adsorption (solid symbols) and desorption (open symbols) isotherms recorded at 77 K for the ACC material; the inset shows the multi-point BET plot calculated at the lower P/P_0 range of 0.01 and 0.04, (b) fully reversible H_2 adsorption (solid symbols) and desorption (open symbols) isotherms recorded between 60 and 100 K and up to 1 bar, (c) equivalent isosteric heat of H_2 adsorption plot calculated by using the Clausius-Clapeyron equation and (d) high-pressure (up to ~100 bar) excess H_2 adsorption isotherms recorded at 77 and 298 K; the inset shows a comparison of the H_2 uptake amounts at 77 and 298 K for the lower pressure region between 0 and 20 bar.

3.7 CO_2/CH_4 adsorption and selectivity

The low-pressure (0–1 bar) CO_2 and CH_4 adsorption and desorption isotherms recorded at 273, 298 and 323 K are shown in Fig. 6a and b, respectively. Similar to the case of H_2 adsorption, the ACC material exhibits fully reversible isotherms for both gases at all studied temperatures. As expected, the gravimetric CO_2 and CH_4 uptakes at atmospheric pressure (~1 bar) reach their highest values at 273 K (i.e. 2.68 mmol/g or 10.55 wt.% for CO_2 and 0.99 mmol/g or 1.56 wt.% for CH_4). The adsorbed CO_2 and CH_4 amounts at ~1 bar decrease by 37 % and 23 %, respectively, upon increasing the operating temperature to 323 K. Fig. 6c and d includes the Q_{st} curves for CO_2 and CH_4, respectively, as estimated using the low-pressure data and Clausius-Clapeyron equation (Eq. (1)). The Q_{st} values range from ~18.9 down to ~13.4 kJ/mol by increasing the CO_2 loading amounts from 0.1 up to 1.6 mmol/g, as well as from ~14.9 to ~10.4 kJ/mol for CH_4 coverage between 0.04 and 0.6 mmol/g. Concerning the interactions between pure carbon and a non-polar molecule such as CH_4, Bhatia and Myers [80] predicted an optimum Q_{st} value of around 19 kJ/mol for ambient operating temperatures (i.e. from 273 to 298 K). This value could drop around to 16 kJ/mol, however an optimum operating temperature of 254 K is required to maximize the delivery of CH_4. Table 2 includes a summary of all the recorded excess gas uptake values of the degassed ACC material (expressed in terms of volume, mole or mass) for H_2, CO_2 and CH_4 adsorption at different temperature and pressure conditions.

The CO_2/CH_4 selectivity plots of the ACC material for two different gaseous mixtures (i.e. landfill and natural gas) were predicted at 273, 298 and 323 K by using the equivalent low-pressure adsorption data and the IAST model (Eq. (2)), as shown in Fig. 6e and f, respectively. As expected, the IAST CO_2/CH_4 selectivity values for both molar mixtures were reduced upon increasing the operating temperature from 273 to 323 K. Specifically, as shown in Fig. 6e, the estimated S values for landfill gas conditions (i.e. 50/50 M mixture) correspond to 5.3, 4.6 and 3.5 for 273, 298 and 323 K, respectively, at a given pressure of 1 bar. A similar picture can be seen in Fig. 6f for the case of natural gas (i.e. 5/95 M mixture), where the equivalent S values at 1 bar are 5.2, 4.5 and 3.7 for 273, 298 and 323 K, respectively. In addition, the equivalent S values for both mixtures seem to be slightly higher at the lower applied pressures (e.g. 5.5 and 5.8, respectively, at 273 K and 0.05 bar), which however show a small drop and mostly remain constant by increasing the pressure up to 1 bar. Hence, based on the IAST calculations, the ACC material should selectively adsorb CO_2 over CH_4 with a ratio of ~4.5:1 at room temperature and atmospheric pressure,

which makes it suitable for purification of such energy-dense gaseous mixtures. This kind of selective behavior from the ACC material for preferential adsorption of CO_2 over CH_4 is mainly attributed to the different electronic properties of the employed gases and more specifically due to the fact that CO_2 exhibits a significant quadrupole moment (i.e. 13.40 $\times 10^{-40}$ C m^2) compared to the non-polar CH_4 [17,84]. In comparison to other types of carbon adsorbents, as for example an ordered mesoporous carbon (OMC) presented in a recent study [17] having much higher S_{BET} and $V_{Gurvich}$ values (i.e. 2255 m^2/g and 2.17 cm^3/g, respectively), although larger pore sizes (i.e. bimodal PSD centered at 2.3 and 6.8 nm), the ACC shows a better selectivity (i.e. a lower S value of 2.9 at 298 K and 1 bar was predicted for the OMC sample using the IAST model). This clearly suggests that the dominant ultra-microporous features of the ACC material (i.e. mean pore size around 0.6 nm; see Section 3.5) play a crucial role towards a higher degree of selectivity, which most probably arises from the increased overlapping potential of the opposite micropore walls.

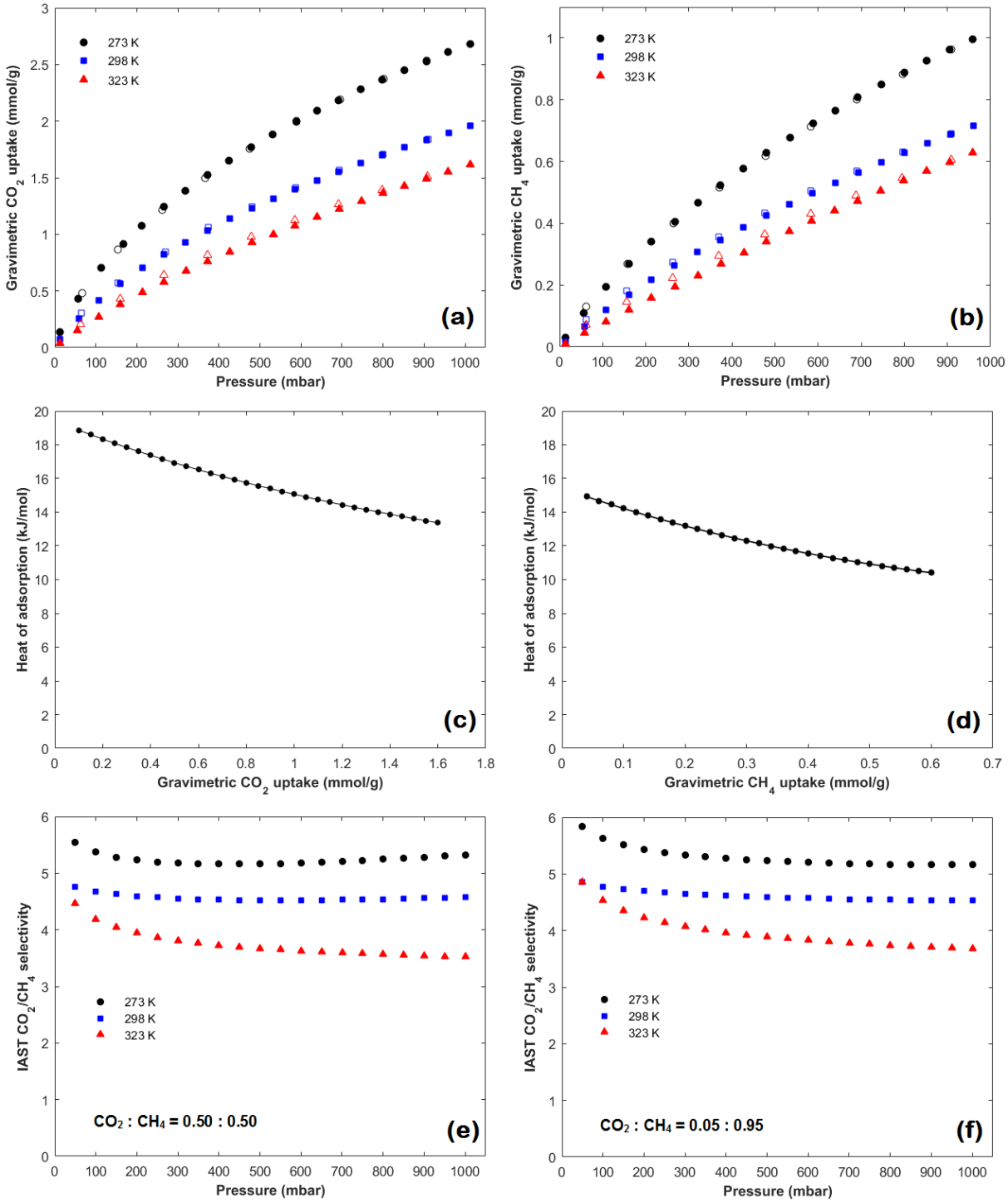

Fig. 6: Fully reversible (a) CO_2 and (b) CH_4 adsorption (solid symbols) and desorption (open symbols) isotherms recorded between 273 and 323 K and up to 1 bar, equivalent isosteric Q_{st} plots for (c) CO_2 and (d) CH_4 calculated by using the Clausius-Clapeyron equation and CO_2 over CH_4 gas selectivity plots of the ACC material at 273, 298 and 323 K for (e) landfill gas and (f) natural gas conditions, as calculated from the low-pressure (0-1 bar) CO_2 and CH_4 adsorption data by applying the IAST model.

Table 2: Summary of the excess gas adsorption capacities of the ACC material for H_2, CO_2 and CH_4 adsorption at different temperature and pressure conditions.

Gas	Temperature [K]	Pressure [bar]	C_v [cm^3/g]	C_n [mmol/g]	C_g [wt.%]
H_2	60	1	256.90	11.46	2.26
H_2	70	1	212.80	9.49	1.88
H_2	77	1	189.80	8.47	1.68
H_2	77	72	358.12	15.97	3.12
H_2	90	1	128.70	5.74	1.14
H_2	100	1	92.14	4.11	0.82
H_2	298	95	38.94	1.75	0.35
CO_2	273	1	60.10	2.68	10.55
CO_2	298	1	43.95	1.96	7.94
CO_2	323	1	36.33	1.62	6.65
CH_4	273	1	22.19	0.99	1.56
CH_4	298	1	16.14	0.72	1.14
CH_4	323	1	14.12	0.63	1.00

C_v: volume of adsorbed gas at STP conditions per mass of degassed sample, C_n: mole of adsorbed gas per mass of degassed sample, C_g: mass of adsorbed gas per mass of system (mass of adsorbed gas plus mass of degassed sample); i.e. $m_{gas}/(m_{gas}+m_{sample})$.

3.8 Electrochemical performance

The electrochemical performance of the ACC material in the form of a supercapacitor electrode using 1 M CsCl aqueous electrolyte is presented in detail in Fig. 7. The CV curve of the half-cell design, shown in Fig. 7a, deviates significantly from rectangular shape, suggesting a small additional pseudocapacitive contribution from active surface groups in addition to pure electrical double-layer capacitance [20,85,86]. Such surface functionalities (mainly oxygen-based) were previously detected by FT-IR and XPS studies, as described in Section 3.4. As a consequence, the specific capacitance of the half-cell becomes smaller for positive potentials (i.e. down to ~73 F/g at + 0.6 V vs. reference carbon), a trend properly indicated in the GCPL profile of Fig. 7b. However, the half-cell electrode exhibits its maximum capacitance value of ~115 F/g for a negative potential of – 0.6 V vs. reference carbon (Fig. 7b). Compared to standard and high-performance ACs [3,18,25,87] and ACCs [19,22,24,26], both gravimetric and specific area normalized capacitance of the herein studied ACC electrode perform reasonably well. Besides the CO_2-activation method presented in this work, other approaches have been recently published

in the literature for the preparation of carbon-based cloth-like materials for supercapacitors, including common woven textiles coated with porous carbons using dip coating and screen printing methods [22] as well as commercial carbon cloths activated either by wet chemical treatment and thermal annealing under a H_2/N_2 atmosphere [19] or by chemical oxidation followed by reduction in hydrazine and ammonia [26]. In the context of our studies, the ACC outperforms the commercial AC material YP-80F (S_{BET} ~2353 m^2/g and $V_{Gurvich}$ ~1.2 cm^3/g) in terms of half-cell capacitance (i.e. ~115 vs. ~96 F/g at – 0.6 V against the same reference carbon) upon employing the same electrolyte (i.e. CsCl) and following exactly the same experimental conditions described in Section 2.2. This difference is more pronounced upon normalization of the capacitance to the S_{BET} of both materials, which appears to correspond to more than a factor of two (i.e. ~0.10 vs. ~0.04 F/m^2). Such a larger SA normalized capacitance for our ACC material is most probably caused by the smaller average pore size compared to YP-80F (i.e. a larger D value of 1.02 nm is given for YP-80F vs. the 0.78 nm for ACC by using the ratio $D = 2\cdot(V_{Gurvich})/(S_{BET})$ mentioned in Section 3.5), a case systematically described in previous studies related to nanoporous carbon-based supercapacitor electrodes [88,89]. Due to the enhanced screening of the coulombic repulsion between ions of the same sign, the ion charge storage works more effectively in pores not much larger than the ions themselves [90]. In other words, ionic charge is stored most localized and, thus, most effectively in sub-nanometer pores with highest possible degree of confinement, as recently confirmed by experimental and simulation studies [71,91]. As expected, the CV curve for the full-cell design, shown in Fig. 7c, looks rather symmetric. This provides a good indication of the proper capacitive behavior followed by the ACC material and its suitability as an electrode material for supercapacitor devices. The maximum capacitance for the full-cell corresponds to ~121 F/g at 0.02 A/g, as presented in the equivalent GCPL profile (Fig. 7d). In terms of power handling, the full-cell capacitance at 10 A/g is about 50 % decreased compared to its highest value at 0.02 A/g, as clearly shown in the inset of Fig. 7d. The corresponding galvanostatic discharge curves are shown in the Supplementary information (see Fig. S2). The Nyquist plot, demonstrated in Fig. 7e, reveals common electrical double-layer behavior and nearly ideal capacitive behavior above the value of 2 Ω cm^2 for the real impedance axis. For the highest frequencies, an impedance value as small as 0.81 Ω cm^2 is given (inset of Fig. 7e), which indicates good conductivity and low internal resistance for the full-cell design [19]. The cycling stability test reveals a superior stable behavior of the

ACC electrode and the aqueous CsCl electrolyte (Fig. 7f). Within 10000 charge/discharge cycles between 0 and 1.2 V (using a specific current of 1 A/g) the initial capacitance drops only by 3 % (i.e. 97 % capacitance retention), as clearly observed in the inset of Fig. 7f. Finally, the coulombic efficiency of the full-cell setup at 1 A/g charging and discharging specific current is estimated at ~99 % using Eq. (4) and does not change during the 10000 cycle lasting stability test.

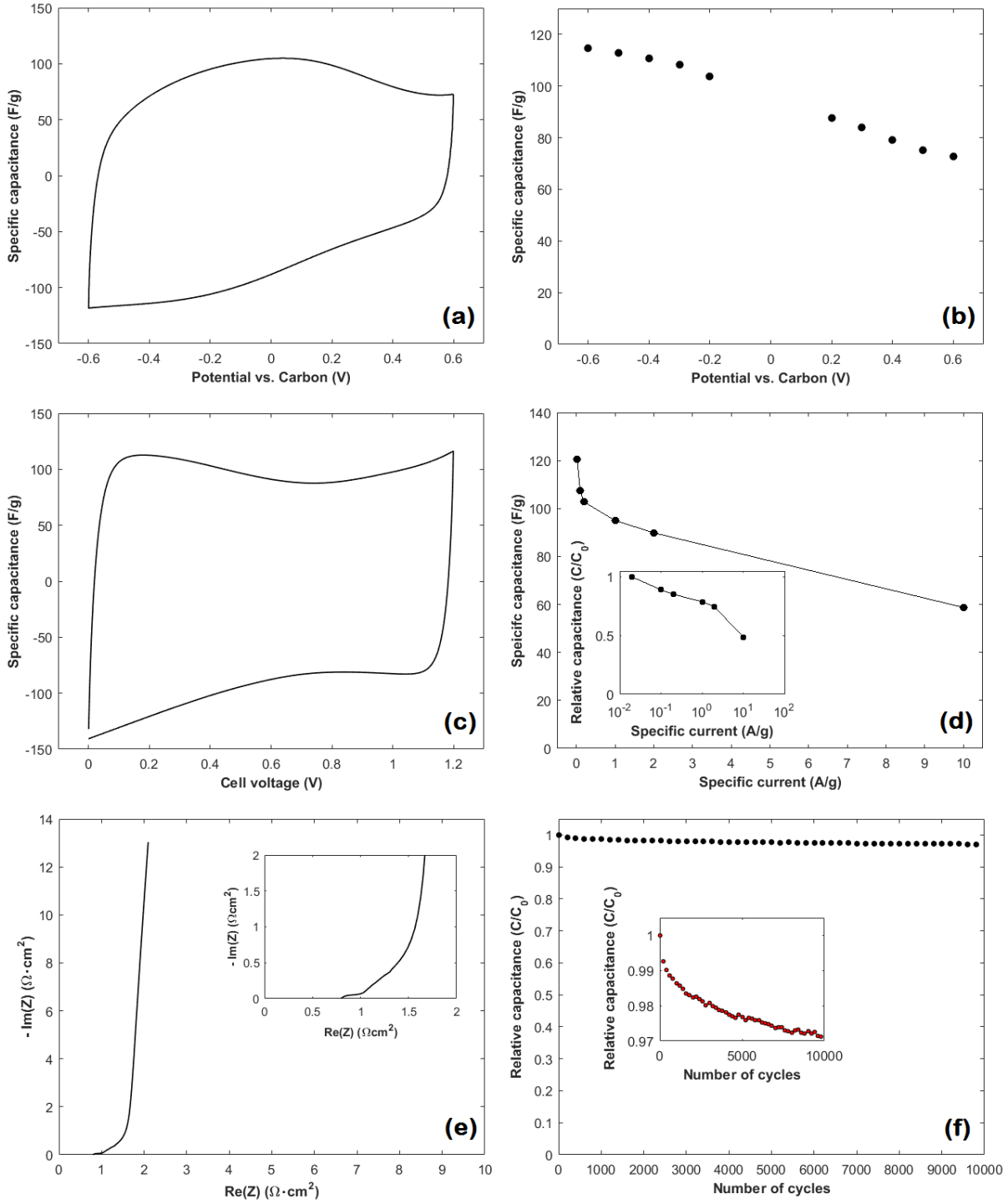

Fig. 7: Electrochemical characterization of the ACC material in an aqueous 1M CsCl electrolyte using (a), (b) a half-cell and (c), (d), (e), (f) a full-cell design. Specifically, (a) CV with 10 mV/s scan rate, (b) GCPL measurements with a specific current of 0.1 A/g, (c) CV with 10 mV/s scan rate, (d) GCPL power handling tests with specific currents from 0.02 to 10 A/g, (e) EIS with an RMS value of ±5 mV around 0 V and (f) cyclic stability tests between 0 and 1.2 V with a specific current of 1 A/g.

4. Summary and conclusions

The development of nanoporous and high-surface area carbon materials showing good performance for a variety of applications is a significant challenge, as the textural, porosity and surface chemistry features may have a different influence on its process. However, the average pore size and pore size distribution, as well as the specific area and pore volume seem to be the most important parameters for the adsorption of both gaseous molecules and charged ions. In the context of this study, a mechanically stable and flexible ACC material was prepared via chemical impregnation in an aqueous mixture of $ZnCl_2$ and NH_4Cl catalysts, followed by carbonization under N_2 for 2 h and activation under CO_2 for 1 h. The as-prepared ACC was studied for its morphology, structure and composition using a series of advanced characterization methods, including SEM, XRD, Raman, SAXS, FT-IR and XPS. In summary, the material comprises woven yarns and micro-sized carbon fibers (i.e. 10–15 μm in width), exhibits a turbostratic structure, shows Raman D and G bands characteristic of its carbon nature as well as presents surface oxygen-based functionalities attributed to the CO_2 activation procedure. A 3-D representation of the ACC pore structure created via GRF analysis of the fitted SAXS data suggests randomly-shaped pores. The S_{BET} and $V_{Gurvich}$ values were estimated at ~1205 m^2/g and ~0.47 cm^3/g by processing low-pressure N_2 sorption data recorded at 77 K, while the t-plot micropore SA and SPV fractions exceed the 98 % of the total. The PSD analysis based on the QSDFT and GCMC kernels indicated pores in the ultra-micropore region (i.e. below 0.7 nm). The ACC material was evaluated for three different applications, including H_2 storage using experimental gas adsorption measurements in a wide range of temperatures and pressures, selective CO_2 over CH_4 separation for different temperatures under low-pressures on the basis of the IAST model as well as electrochemical energy storage in supercapacitor devices. At first, it showed fully reversible H_2 uptake capacities ranging from 0.82 up to 2.26 wt.% between 100 and 60 K under atmospheric pressure. The H_2 gravimetric capacity at liquid N_2 temperature conditions (i.e. 77 K) corresponds to 1.68 wt.% at 1 bar and almost doubles up to 72 bar, thus reaching an excess value of 3.12 wt.%. However, the equivalent performance at room temperature was rather poor and the ACC material hardly reached a capacity of ~0.35 wt.% at pressures up to ~95 bar. The strength of interaction between H_2 and ACC was characterized on the basis of the Clausius-Clayperon equation using low-pressure data and the Q_{st} value was estimated as 9.2 kJ/mol at zero coverage and at 8.4 kJ/mol for low surface coverage, which is slightly higher than that of standard ACs and

most likely arises from the ultra-microporous nature of the material. Fully reversible CO_2 and CH_4 adsorption isotherms were recorded at three different temperatures (i.e. 273, 298 and 323 K) under a low-pressure regime (0–1 bar) and respective uptake values of up to ~2.7 and ~1 mmol/g were obtained at 273 K and 1 bar. The corresponding Q_{st} values for low adsorbed amounts were calculated at ~19 and ~15 kJ/mol for CO_2 and CH_4, respectively, using the Clausius-Clayperon equation. A theoretical prediction of the CO_2/CH_4 selective behavior of the ACC material for two different gaseous mixtures (i.e. landfill (50/50) and natural gas (5/95)) was carried out upon combining the low-pressure experimental data with the IAST model. A selectivity factor of ~ 4.5:1 was given for both gas compositions at ambient conditions (i.e. 298 K and 1 bar), while this value can increase to more than ~5:1 by reducing the temperature to 273 K. Finally, the ACC material was tested as a binder-free working electrode in supercapacitor half- and full-cells using a 1 M CsCl aqueous electrolyte. The gravimetric capacitance of a half-cell corresponds to ~115 F/g for a −0.6 V potential vs. reference carbon, while the equivalent value for a full setup reaches as high as ~121 F/g for a specific current of 0.02 A/g, which is higher than well-established ACs (e.g. YP-80F). However, the full-cell capacitance seems to drop by ~50 % upon increasing the current up to 10 A/g. The cyclic stability of the full-cell is superior as it retains its original capacitance by more than 97 % after 10,000 charge/discharge cycles, while its coulombic efficiency is estimated around 99 % using a specific current of 1 A/g. The overall electrochemical performance of the ACC electrode using aqueous CsCl electrolyte is promising, with respect to its porosity features (i.e. SA and SPV), and might be further improved in future by using different electrolytes and systematically adding sources of pseudo-capacitance such as surface functionalities. In conclusion, the mean pore size (~0.6 nm) seems to be an inherent parameter determining the effectivity of the ACC material towards H_2 storage, gas mixture selectivity and ion charge storage. Therefore, its versatile character as a gas and ion adsorbent in combination with its fabric-like texture make it an attractive option for practical and large-scale green energy-related and environmental applications.

Acknowledgments

The present study was partially supported by the EC FP7-INFRASTRUCTURES project H2FC (GA No. 284522) and by a Khalifa University Internal Research Fund (Level 1). N.K. is grateful to Montanuniversität Leoben for providing financial support for his Ph.D. research activities in the first semester of 2016. O.P., C.P. and C.K. acknowledge financial support from the Austrian Klima- und Energiefonds via the FFG program "Energieforschung" (Project: Hybrid Supercap). C.P. and C.K. thank Nicolas Jäckel (INM Saarbrücken, Germany) for discussions.

References

[1] J. Ren, N.M. Musyoka, H.W. Langmi, M. Mathe, S. Liao, Current research trends and perspectives on materials-based hydrogen storage solutions: a critical review, Int. J. Hydrog. Energy 42 (2017) 289–311.

[2] E. Callini, K.F. Aguey-Zinsou, R. Ahuja, J.R. Ares, S. Bals, N. Biliškov, S. Chakraborty, G. Charalambopoulou, A.L. Chaudhary, F. Cuevas, B. Dam, P. de Jongh, M. Dornheim, Y. Filinchuk, J.G. Novakovic, M. Hirscher, T.R. Jensen, P.B. Jensen, N. Novakovic, Q. Lai, F. Leardini, D.M. Gattia, L. Pasquini, T. Steriotis, S. Turner, T. Vegge, A. Zuttel, A. Montone, Nanostructured materials for solid-state hydrogen storage: a review of the achievement of COST Action MP1103, Int. J. Hydrog. Energy 41 (2016) 14404–14428.

[3] M. Sevilla, R. Mokaya, Energy storage applications of activated carbons: supercapacitors and hydrogen storage, Energy Environ. Sci. 7 (2014) 1250–1280.

[4] B. Adeniran, R. Mokaya, Compactivation: a mechanochemical approach to carbons with superior porosity and exceptional performance for hydrogen and CO_2 storage, Nano Energy 16 (2015) 173–185.

[5] S.N. Talapaneni, J.H. Lee, S.H. Je, O. Buyukcakir, T.W. Kwon, K. Polychronopoulou, J.W. Choi, A. Coskun, Chemical blowing approach for ultramicroporous carbon nitride frameworks and their applications in gas and energy storage, Adv. Funct. Mater. (2016), http://dx.doi.org/10.1002/adfm.201604658.

[6] N. Kostoglou, A. Tarat, I. Walters, V. Ryzhkov, C. Tampaxis, G. Charalambopoulou, T. Steriotis, C. Mitterer, C. Rebholz, Few-layer graphene-like flakes derived by plasma treatment: a potential material for hydrogen adsorption and storage, Microporous Mesoporous Mater. 225 (2016) 482–487.

[7] N. Kostoglou, V. Tzitzios, A.G. Kontos, K. Giannakopoulos, C. Tampaxis, A. Papavasiliou, G. Charalambopoulou, T. Steriotis, Y. Li, K. Liao, K. Polychronopoulou, C. Mitterer, C. Rebholz, Synthesis of nanoporous graphene oxide adsorbents by freeze-drying or microwave radiation: characterization and hydrogen storage properties, Int. J. Hydrog. Energy 40 (2015) 6844–6852.

[8] Y. Xia, Z. Yang, Y. Zhu, Porous carbon-based materials for hydrogen storage: advancement and challenges, J. Mater. Chem. A 1 (2013) 9365–9381.

[9] Y. Gogotsi, C. Portet, S. Osswald, J.M. Simmons, T. Yildirim, G. Laudisio, J.E. Fischer, Importance of pore size in high-pressure hydrogen storage by porous carbons, Int. J. Hydrog. Energy 34 (2009) 6314–6319.

[10] L. Zubizarreta, E.I. Gomez, A. Arenillas, C.O. Ania, J.B. Parra, J.J. Pis, H_2 storage in carbon materials, Adsorption 14 (2008) 557–566.

[11] D. Lozano-Castello, D. Cazorla-Amorós, A. Linares-Solano, D.F. Quinn, Activated carbon monoliths for methane storage: influence of binder, Carbon 40 (2002) 2817–2825.

[12] D. Lozano-Castello, J. Alcaniz-Monge, M.A. De la Casa-Lillo, D. Cazorla-Amorós, A. Linares-Solano, Advances in the study of methane storage in porous carbonaceous materials, Fuel 81 (2002) 1777–1803.

[13] C. Guan, L.S. Loo, K. Wang, C. Yang, Methane storage in carbon pellets prepared via a binderless method, Energ. Convers. Manag. 52 (2011) 1258–1262.

[14] N. Bimbo, A.J. Physick, A. Noguera-Diaz, A. Pugsley, L.T. Holyfield, V.P. Ting, T.J. Mays, High volumetric and energy densities of methane stored in nanoporous materials at ambient temperatures and moderate pressures, Chem. Eng. J. 272 (2015) 38–47.

[15] S. García, M.V. Gil, C.F. Martín, J.J. Pis, F. Rubiera, C. Pevida, Breakthrough adsorption study of a commercial activated carbon for pre-combustion CO_2 capture, Chem. Eng. J. 171 (2011) 549–556.

[16] G. Srinivas, V. Krungleviciute, Z.X. Guo, T. Yildirim, Exceptional CO_2 capture in a hierarchically porous carbon with simultaneous high surface area and pore volume, Energy Environ. Sci. 7 (2014) 335–342.

[17] B. Yuan, X. Wu, Y. Chen, J. Huang, H. Luo, S. Deng, Adsorption of CO_2, CH_4, and N_2 on ordered mesoporous carbon: approach for greenhouse gases capture and biogas upgrading, Environ. Sci. Technol. 47 (2013) 5474–5480.

[18] F. Béguin, V. Presser, A. Balducci, E. Frackowiak, Carbons and electrolytes for advanced supercapacitors, Adv. Mater. 26 (2014) 2219–2251.

[19] S. Jiang, T. Shi, X. Zhan, H. Long, S. Xi, H. Hu, Z. Tang, High-performance all-solid-state flexible supercapacitors based on two-step activated carbon cloth, J. Power Sources 272 (2014) 16–23.

[20] L. Wei, G. Yushin, Nanostructured activated carbons from natural precursors for electrical double layer capacitors, Nano Energy 1 (2012) 552–565.

[21] B. Daffos, G. Chevallier, C. Estournès, P. Simon, Spark plasma sintered carbon electrodes for electrical double layer capacitor applications, J. Power Sources 19 (2011) 1620–1625.

[22] K. Jost, C.R. Perez, J.K. McDonough, V. Presser, M. Heon, G. Dion, Y. Gogotsi, Carbon coated textiles for flexible energy storage, Energy Environ. Sci. 4 (2011) 5060–5067.

[23] P. Simon, Y. Gogotsi, Materials for electrochemical capacitors, Nat. Mater. 7 (2008) 845–854.

[24] B. Xu, F. Wu, S. Chen, C. Zhang, G. Cao, Y. Yang, Activated carbon fiber cloths as electrodes for high performance electric double layer capacitors, Electrochim. Acta 52 (2007) 4595–4598.

[25] E. Raymundo-Pinero, K. Kierzek, J. Machnikowski, F. Béguin, Relationship between the nanoporous texture of activated carbons and their capacitance properties in different electrolytes, Carbon 44 (2006) 2498–2507.

[26] G. Wang, H. Wang, X. Lu, Y. Ling, M. Yu, T. Zhai, Y. Li, Solid-state supercapacitor based on activated carbon cloths exhibits excellent rate capability, Adv. Mater. 26 (2014) 2676–2682.

[27] G. Zhang, Y. Song, H. Zhang, J. Xu, H. Duan, J. Liu, Radially aligned porous carbon nanotube arrays on carbon fibers: a hierarchical 3D carbon nanostructure for high-performance capacitive energy storage, Adv. Funct. Mater. 26 (2016) 3012–3020.

[28] TechSci Research, Global activated Carbon Market Forecast and Opportunities, 2019. ⟨https://www.techsciresearch.com⟩ (Accessed 27 November 2016), 2014.

[29] TechSci Research, Global Activated Carbon Market By Type (Powdered Activated Carbon, Granular Activated Carbon and Others), By Raw Material (Wood, Coconut Shells, Coal and Others), By Application, Competition Forecast and Opportunities, 2011–2021. ⟨https://www.techsciresearch.com⟩ (Accessed 27 November 2016).

[30] A. Schinwald, F.A. Murphy, A. Jones, W. MacNee, K. Donaldson, Graphene-based nanoplatelets: a new risk to the respiratory system as a consequence of their unusual aerodynamic properties, ACS Nano 6 (2012) 736–746.

[31] D.P. Broom, C.J. Webb, K.E. Hurst, P.A. Parilla, T. Gennett, C.M. Brown, R. Zacharia, E. Tylianakis, E. Klontzas, G.E. Froudakis, T.A. Steriotis, P.N. Trikalitis, D.L. Anton, B. Hardy, D. Tamburello, C. Corgnale, B.A. van Hassel, D. Cossement, R. Chahine, M. Hirscher, Outlook and challenges for hydrogen storage in nanoporous materials, Appl. Phys. A 122 (2016) 1–21.

[32] J. Ren, B.C. North, Shaping porous materials for hydrogen storage applications: a review, J. Technol. Innov. Renew. Energy 3 (2014) 12–20.

[33] US Department of Energy, Multi-year Research, Development and Demonstration Plan 3.3, 2015. ⟨http://energy.gov/sites/prod/files/2015/05/f22/fcto_myrdd_storage.pdf⟩ (Accessed 27 November 2016).

[34] Advanced Research Project Agency-Energy (ARPA-E), US Department of Energy, Methane Opportunities for Vehicular Energy (MOVE) program overview. ⟨https://arpa-e.energy.gov/sites/default/files/documents/files/MOVE_ProgramOverview.pdf⟩, 2012 (Accessed 27 November 2016).

[35] US Department of Energy, Grid energy storage. ⟨http://energy.gov/sites/prod/files/2014/09/f18/Grid%20Energy%20Storage%20December%202013.pdf⟩, 2013 (Accessed 27 November 2016).

[36] A.G. Dumanlı, A.H. Windle, Carbon fibres from cellulosic precursors: a review, J. Mater. Sci. 47 (2012) 4236–4250.

[37] E. Frank, L.M. Steudle, D. Ingildeev, J.M. Spörl, M.R. Buchmeiser, Carbon fibers: precursor systems, processing, structure, and properties, Angew. Chem. Int. Ed. 53 (2014) 5262–5298.

[38] C.O. Ania, F. Béguin, Mechanism of adsorption and electrosorption of bentazone on activated carbon cloth in aqueous solutions, Water Res. 41 (2007) 3372–3380.

[39] S. Masson, M. Gineys, S. Delpeux-Ouldriane, L. Reinert, S. Guittonneau, F. Béguin, L. Duclaux, Single, binary, and mixture adsorption of nine organic contaminants onto a microporous and a microporous/mesoporous activated carbon cloth, Microporous Mesoporous Mater. 234 (2016) 24–34.

[40] B.M. Babić, S.K. Milonjić, M.J. Polovina, S. Čupić, B.V. Kaludjerović, Adsorption of zinc, cadmium and mercury ions from aqueous solutions on an activated carbon cloth, Carbon 40 (2002) 1109–1115.

[41] L.L. Matović, N.S. Vukelić, U.D. Jovanović, K.R. Kumrić, J.B. Krstić, B.M. Babić, A.B. Đukić, Mechanochemically improved surface properties of activated carbon cloth for the removal of As (V) from aqueous solutions, Arab. J. Chem. (2016), http://dx.doi.org/10.1016/j.arabjc.2016.07.004.

[42] H. Métivier-Pignon, C. Faur-Brasquet, P. Le Cloirec, Adsorption of dyes onto activated carbon cloths: approach of adsorption mechanisms and coupling of ACC with ultrafiltration to treat coloured wastewaters, Sep. Purif. Technol. 31 (2003) 3–11.

[43] N. Hoda, E. Bayram, E. Ayranci, Kinetic and equilibrium studies on the removal of acid dyes from aqueous solutions by adsorption onto activated carbon cloth, J. Hazard. Mater. 137 (2006) 344–351.

[44] M.W. Ryoo, G. Seo, Improvement in capacitive deionization function of activated carbon cloth by titania modification, Water Res. 37 (2003) 1527–1534.

[45] H.J. Oh, J.H. Lee, H.J. Ahn, Y. Jeong, Y.J. Kim, C.S. Chi, Nanoporous activated carbon cloth for capacitive deionization of aqueous solution, Thin Solid Films 515 (2006) 220–225.

[46] H.J. Ahn, J.H. Lee, Y. Jeong, J.H. Lee, C.S. Chi, H.J. Oh, Nanostructured carbon cloth electrode for desalination from aqueous solutions, Mater. Sci. Eng. A 449 (2007) 841–845.

[47] D. Das, V. Gaur, N. Verma, Removal of volatile organic compound by activated carbon fiber, Carbon 42 (2004) 2949–2962.

[48] M.E. Ramos, P.R. Bonelli, A.L. Cukierman, M.R. Carrott, P.J.M. Carrott, Adsorption of volatile organic compounds onto activated carbon cloths derived from a novel regenerated cellulosic precursor, J. Hazard Mater. 177 (2010) 175–182.

[49] M.A. Sidheswaran, H. Destaillats, D.P. Sullivan, S. Cohn, W.J. Fisk, Energy efficient indoor VOC air cleaning with activated carbon fiber (ACF) filters, Build. Environ. 47 (2012) 357–367.

[50] M. Tathavadekar, M. Biswal, S. Agarkar, L. Giribabu, S. Ogale, Electronically and catalytically functional carbon cloth as a permeable and flexible counter electrode for dye sensitized solar cell, Electrochim. Acta 123 (2014) 248–253.

[51] X. Hou, X. Wang, B. Liu, Q. Wang, T. Luo, D. Chen, G. Shen, Hierarchical $MnCo_2O_4$ nanosheet arrays/carbon cloths as integrated anodes for lithium-ion batteries with improved performance, Nanoscale 6 (2014) 8858–8864.

[52] F. Zhao, N. Rahunen, J.R. Varcoe, A. Chandra, C. Avignone-Rossa, A.E. Thumser, R.C. Slade, Activated carbon cloth as anode for sulfate removal in a microbial fuel cell, Environ. Sci. Technol. 42 (2008) 4971–4976.

[53] I. Merino-Jimenez, C. Santoro, S. Rojas-Carbonell, J. Greenman, I. Ieropoulos, P. Atanassov, Carbon-based air-breathing cathodes for microbial fuel cells, Catalysts 6 (2016) 127.

[54] B.M. Babić, S.K. Milonjić, M.J. Polovina, B.V. Kaludierović, Point of zero charge and intrinsic equilibrium constants of activated carbon cloth, Carbon 37 (1999) 477–481.

[55] M. Polovina, B. Babić, B. Kaluderović, A. Dekanski, Surface characterization of oxidized activated carbon cloth, Carbon 35 (1997) 1047–1052.

[56] A. Huidobro, A.C. Pastor, F. Rodrıguez-Reinoso, Preparation of activated carbon cloth from viscous rayon: Part IV. Chemical activation, Carbon 39 (2001) 389–398.

[57] X. Huang, Fabrication and properties of carbon fibers, Materials 2 (2009) 2369–2403.

[58] International Standard Organization, Determination of the specific surface area of solids by gas adsorption — BET method, ISO 9277: 2010(E), 2nd edition, 2010.

[59] J. Rouquerol, F. Rouquerol, P. Llewellyn, G. Maurin, K.S. Sing, Adsorption by Powders and Porous Solids: Principles, Methodology and Applications, Academic Press, 2013.

[60] J.H. De Boer, B.G. Linsen, T. Van der Plas, G.J. Zondervan, Studies on pore systems in catalysts: VII. Description of the pore dimensions of carbon blacks by the t method, J. Catal. 4 (1965) 649–653.

[61] A.V. Neimark, Y. Lin, P.I. Ravikovitch, M. Thommes, Quenched solid density functional theory and pore size analysis of micro-mesoporous carbons, Carbon 47 (2009) 1617–1628.

[62] J. Landers, G.Y. Gor, A.V. Neimark, Density functional theory methods for characterization of porous materials, Colloids Surf. A: Physicochem Eng. Asp. 437 (2013) 3–32.

[63] J.A. Dunne, R. Mariwala, M. Rao, S. Sircar, R.J. Gorte, A.L. Myers, Calorimetric heats of adsorption and adsorption isotherms 1. O_2, N_2, Ar, CO_2, CH_4, C_2H_6, and SF_6 on silicalite, Langmuir 12 (1996) 5888–5895.

[64] A.L. Myers, J.M. Prausnitz, Thermodynamics of mixed-gas adsorption, AIChE J. 11 (1965) 121–127.

[65] M. Lu, F. Beguin, E. Frackowiak, Supercapacitors: Materials, Systems and Applications, John Wiley & Sons, 2013.

[66] M.M. Tang, R. Bacon, Carbonization of cellulose fibers — I. Low temperature pyrolysis, Carbon 2 (1964) 211–220.

[67] R. Bacon, M.M. Tang, Carbonization of cellulose fibers — II. Physical property study, Carbon 2 (1964) 221–225.

[68] F. Rodrıguez-Reinoso, A.C. Pastor, H. Marsh, M.A. Martnez, Preparation of activated carbon cloth from viscous rayon: Part II. Physical activation processes, Carbon 38 (2000) 379–395.

[69] G.A. Zickler, B. Smarsly, N. Gierlinger, H. Peterlik, O. Paris, A reconsideration of the relationship between the crystallite size La of carbons determined by X-ray diffraction and Raman spectroscopy, Carbon 44 (2006) 3239–3246.

[70] A. Gibaud, J.S. Xue, J.R. Dahn, A small angle X-ray scattering study of carbons made from pyrolyzed sugar, Carbon 34 (1996) 499–503.

[71] C. Prehal, C. Koczwara, N. Jäckel, A. Schreiber, M. Burian, H. Amenitsch, M.A. Hartmann, V. Presser, O. Paris, Quantification of ion confinement and desolvation in nanoporous carbon supercapacitors with modelling and in situ X-ray scattering, Nat. Energy 2 (2017) 16215.

[72] N.F. Berk, Scattering properties of a model bicontinuous structure with a well defined length scale, Phys. Rev. Lett. 58 (1987) 2718.

[73] C.J. Gommes, A.P. Roberts, Structure development of resorcinol-formaldehyde gels: microphase separation or colloid aggregation, Phys. Rev. E 77 (2008) 041409.

[74] P. Pré, G. Huchet, D. Jeulin, J.N. Rouzaud, M. Sennour, A. Thorel, A new approach to characterize the nanostructure of activated carbons from mathematical morphology applied to high resolution transmission electron microscopy images, Carbon 52 (2013) 239–258.

[75] M.S. Shafeeyan, W.M.A.W. Daud, A. Houshmand, A. Shamiri, A review on surface modification of activated carbon for carbon dioxide adsorption, J. Anal. Appl. Pyrolysis 89 (2010) 143–151.

[76] E. Desimoni, G.I. Casella, A. Morone, A.M. Salvi, XPS determination of oxygen-containing functional groups on carbon-fibre surfaces and the cleaning of these surfaces, Surf. Interface Anal. 15 (1990) 627–634.

[77] S. Biniak, G. Szymański, J. Siedlewski, A. Światkowski, The characterization of activated carbons with oxygen and nitrogen surface groups, Carbon 35 (1997) 1799–1810.

[78] M. Thommes, K. Kaneko, A.V. Neimark, J.P. Olivier, F. Rodriguez-Reinoso, J. Rouquerol, K.S.W. Sing, Physisorption of gases, with special reference to the evaluation of surface area and pore size distribution (IUPAC Technical Report), Pure Appl. Chem. 87 (2015) 1051–1069.

[79] M. Thommes, Physical adsorption characterization of nanoporous materials, Chem. Ing. Tech. 82 (2010) 1059–1073.

[80] S.K. Bhatia, A.L. Myers, Optimum conditions for adsorptive storage, Langmuir 22 (2006) 1688–1700.

[81] R. Chahine, T.K. Bose, Characterization and optimization of adsorbents for hydrogen storage, Hydrog. Energy Prog. 2 (1996) 1259–1264.

[82] M. Dubinin, The potential theory of adsorption of gases and vapors for adsorbents with energetically nonuniform surfaces, Chem. Rev. 60 (1960) 235–241.

[83] J. Burress, M. Kraus, M. Beckner, R. Cepel, G. Suppes, C. Wexler, P. Pfeifer, Hydrogen storage in engineered carbon nanospaces, Nanotechnology 20 (2009) 204026.

[84] D.M. D'Alessandro, B. Smit, J.R. Long, Carbon dioxide capture: prospects for new materials, Angew. Chem. Int. Ed. 49 (2010) 6058–6082.

[85] M. Seredych, D. Hulicova-Jurcakova, G.Q. Lu, T.J. Bandosz, Surface functional groups of carbons and the effects of their chemical character, density and accessibility to ions on electrochemical performance, Carbon 46 (2008) 1475–1488.

[86] Z. Tabti, R. Ruiz-Rosas, C. Quijada, D. Cazorla-Amorós, E. Morallón, Tailoring the surface chemistry of activated carbon cloth by electrochemical methods, ACS Appl. Mater. Interfaces 6 (2014) 11682–11691.

[87] S. Kondrat, A.A. Kornyshev, Superionic state in double-layer capacitors with nanoporous electrodes, J. Phys. Condens. Matter 23 (2011) 022201.

[88] J. Chmiola, G. Yushin, Y. Gogotsi, C. Portet, P. Simon, P.L. Taberna, Anomalous increase in carbon capacitance at pore sizes less than 1 nm, Science 313 (2006) 1760–1763.

[89] N. Jäckel, P. Simon, Y. Gogotsi, V. Presser, Increase in capacitance by subnanometer pores in carbon, ACS Energy Lett. 1 (2016) 1262–1265.

[90] C. Merlet, C. Péan, B. Rotenberg, P.A. Madden, B. Daffos, P.L. Taberna, P. Simon, M. Salanne, Highly confined ions store charge more efficiently in supercapacitors, Nat. Commun. 4 (2013) 2701.

[91] K. Fic, G. Lota, M. Meller, E. Frackowiak, Novel insight into neutral medium as electrolyte for high-voltage supercapacitors, Energy Environ. Sci. 5 (2012) 5842–5850.

Supporting information

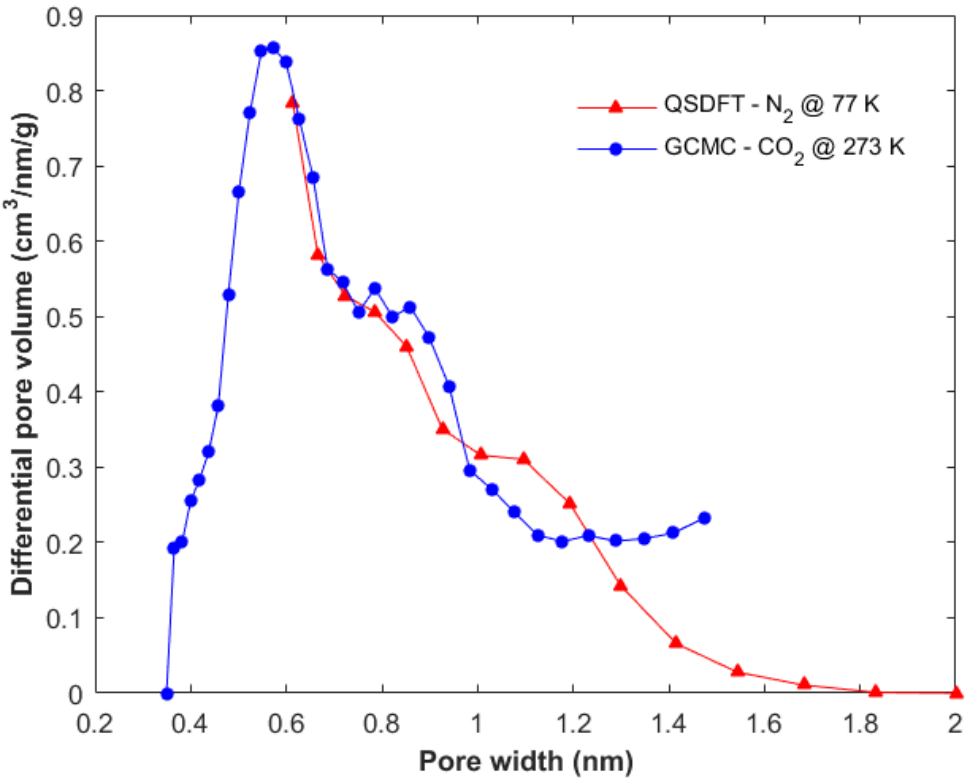

Fig. S1: Differential pore size distribution analysis of the degassed ACC material using the Quenched Solid Density Functional Theory (QSDFT) and Grand Canonical Monte Carlo (GCMC) methods for slit-like shape pores in the recorded N_2 (77 K) and CO_2 (273 K) adsorption data, respectively.

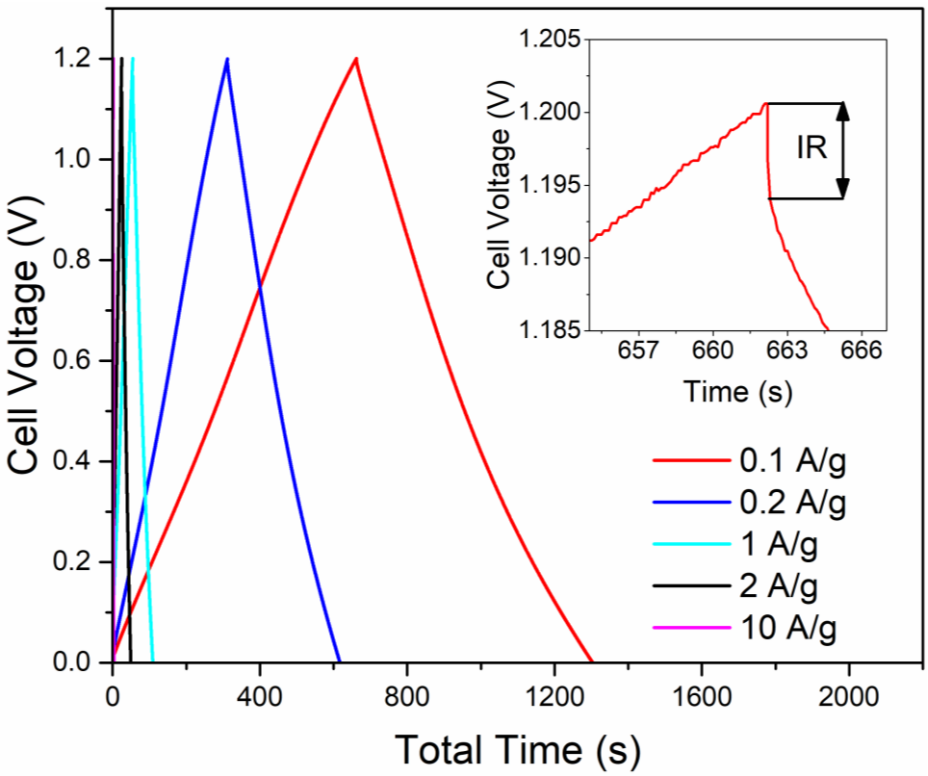

Fig. S2: Galvanostatic charging and discharging curves for different current densities. The inset shows a magnification of the curve recorded with 0.1 A/g; the voltage drop due to internal resistance (IR drop) is indicated.

Publication IV

Solvothermal synthesis, nanostructural characterization and gas cryo-adsorption studies in a metal-organic framework (IRMOF-1) material

V. Tzitzios, N. Kostoglou, M. Giannouri, G. Basina, C. Tampaxis, G. Charalambopoulou, T. Steriotis, K. Polychronopoulou, C. Doumanidis, C. Mitterer, C. Rebholz

International Journal of Hydrogen Energy 42 (2017) 23899-23907

Solvothermal synthesis, nanostructural characterization and gas cryo-adsorption studies in a metal-organic framework (IRMOF-1) material

Vasileios Tzitzios[a,**], Nikolaos Kostoglou[b,c,*], Maria Giannouri[a], Georgia Basina[a,d], Christos Tampaxis[a], Georgia Charalambopoulou[a], Theodore Steriotis[a], Kyriaki Polychronopoulou[e], Charalambos Doumanidis[e], Christian Mitterer[b], Claus Rebholz[b,c]

[a] National Center for Scientific Research Demokritos, Agia Paraskevi Attikis, 15310 Athens, Greece

[b] Department of Physical Metallurgy and Materials Testing, Montanuniversität Leoben, 8700 Leoben, Austria

[c] Department of Mechanical and Manufacturing Engineering, University of Cyprus, 1678 Nicosia, Cyprus

[d] Department of Chemistry, University of Crete, Voutes Campus, 71003 Heraklion, Greece

[e] Department of Mechanical Engineering, Khalifa University of Science, Technology and Research, P.O. Box 127788 Abu Dhabi, United Arab Emirates

Highlights

- IRMOF-1 powder synthesized by solvothermal method and supercritical CO_2 activation.
- Cubic nano-sized crystals with ~520 m^2/g specific area and ~0.2 cm^3/g pore volume.
- Fully reversible H_2 sorption isotherms with an uptake of ~1 wt.% at 77 K and ~1 bar.
- High ratio of H_2 uptake to specific area under low pressures compared to other MOFs.

Abstract

A nanoporous metal-organic framework material, exhibiting an IRMOF-1 type crystalline structure, was prepared by following a direct solvothermal synthesis approach, using zinc nitrate and terephthalic acid as precursors and dimethylformamide as solvent, combined with supercritical CO_2 activation and vacuum outgassing procedures. A series of advanced characterization methods were employed, including scanning electron microscopy, Fourier-transform infrared radiation spectroscopy and X-ray diffraction, in order to study the morphology, surface chemistry and structure of the IRMOF-1material directly upon its synthesis. Porosity properties, such as Brunauer-Emmet-Teller (BET) specific area (~520 m^2/g) and micropore volume (~0.2 cm^3/g), were calculated for the activated sample based on N_2 gas sorption data collected at 77 K. The H_2 storage performance was preliminary

assessed by low-pressure (0-1 bar) H_2 gas adsorption and desorption measurements at 77 K. The activated IRMOF-1 material of this study demonstrated a fully reversible H_2 sorption behavior combined with an adequate gravimetric H_2 uptake relative to its BET specific area, thus achieving a value of ~1 wt.% under close-to-atmospheric pressure conditions.

1. Introduction

Metal-organic frameworks, widely known by the acronyms MOF and/or MOFs, are considered a special class of crystalline and porous materials composed of metal ions or clusters and organic ligands or struts, giving rise to a great variety of one-, two- or three-dimensional nanoscale structures. These hybrid nanostructured solids, consisting of both organic and inorganic components, have received considerable attention during the past two decades mainly due to their low densities, impressively large specific areas (SAs) and pore volumes (PVs), as well as the ease of tuning their pore sizes and shapes upon modification of their individual building blocks (i.e. metals and linkers) [1-4]. Therefore, MOFs have been extensively studied as powder and membrane materials for a plethora of advanced applications, including gas sensing and catalysis [5,6], pressurized gas adsorption and storage of highly-dense energy carriers such as hydrogen (H_2) and methane (CH_4) [4,7,8], capture and sequestration of unwanted green-house emissions such as carbon dioxide (CO_2) gas [9,10], as well as selective separation of gaseous mixtures in industrial applications such as natural gas purification [9,11]. However, partial decomposition or complete structural collapse upon long-term exposure in atmospheric air, high sensitivity in moisture, lack of stability under elevated temperatures, as well as potential pore structure deformations under high-pressures of the MOF materials are still few of the major technical obstacles towards their development and large-scale implementation in stationary and mobile applications [12-15].

The most characteristic and considerably studied MOF system is IRMOF-1, known as MOF-5 in previous years, consisting of Zn_4O clusters linked with 1,4-benzenedicarboxylate (BDC) groups that overall form a three-dimensional cubic crystal lattice. Production of IRMOF-1 type materials has been reported using direct-mixing at room temperature [16,17], solvothermal [18,19], sonochemical [20,21] and microwave irradiation methods [20,22]. Great emphasis was given on the increased SA and PV values (i.e. ~250 to ~3800 m^2/g) and ~0.1 to ~1.2 cm^3/g, respectively) as well as on the enhanced and narrow microporosities (i.e. pore sizes between 0.4 and 2 nm) of IRMOF-1 materials, as reported

in several studies [12,16,23-33], thus making them promising porous adsorbents for materials-based H_2 cryo-adsorption and storage applications. In general, highly microporous materials consisting of small and narrow pores below 2 nm in size/width are considered ideal for physical H_2 adsorption due to the fact that their pores act as strong binding sites for the H_2 molecules, attributed to the overlapping of the potential fields of the opposite pore walls [34]. Over a decade ago, Panella and Hirscher [12] synthesized an IRMOF-1 material upon mixing zinc nitrate ($Zn(NO_3)_2$), terephthalic acid ($C_6H_4(CO_2H)_2$; TPA) and triethylamine ($N(CH_2CH_3)_3$; TEA) in dimethylformamide (C_3H_7NO; DMF) solution. They reported a Brunauer-Emmet-Teller (BET) SA of ~572 m^2/g and a micropore SA contribution of ~91 %, while a saturation H_2 uptake of 1.6 wt.% was reached at 77 K and pressures above 10 bar. A year later, the same group produced another IRMOF-1 sample with a much larger BET SA (i.e. ~2296 m^2/g), following an optimized method to the previous one, that demonstrated a high H_2 uptake of ~5.1 wt.% at 77 K and pressures above 50 bar [31]. Even more impressive values of ~6.9 wt.% at 77 K and 100 bar [28] and ~7.1 wt.% at 77 K and 40 bar [30] were later reported regarding solvothermally-derived IRMOF-1 powders with extremely large BET SAs of ~2449 and ~3800 m^2/g, respectively. Li et al. [27] produced IRMOF-1 materials by three different approaches, including solvothermal treatment of a $Zn(NO_3)_2$, TPA and DMF mixture, direct mixing with TEA and slow diffusion of TEA, that showed BET SAs from ~500 to ~840 m^2/g and pore volumes from 0.19 to 0.34 cm^3/g. Relative to the aforementioned values, these samples adsorbed significant amounts of H_2 gas, as capacities between 2.63 and 3.60 wt.% were recorded at 77 K and 17.4 bar. Recently, Zhao et al. [16] prepared a series of IRMOF-1 samples with quite large BET SAs (up to ~3210 m^2/g) and pore volumes (up to ~1.1 cm^3/g), but the reported H_2 storage capacities were not exceeding the value of 1.24 wt.% at 77 K and 1 bar. A selective summary of different IRMOF-1 type materials presented in the literature over the last decade, including the ones described above, and their respective porosity and H_2 adsorption properties at 77 K can be seen in Table 1. It should be noted that in addition to the aforementioned studies mainly focused on the development of IRMOF-1 powder materials with a high H_2 gravimetric uptake, significant efforts have been devoted on increasing their relatively low H_2 volumetric capacities (i.e. adsorbed H_2 mass per volume of material) using powder densification in the form of pellets [35,36].

Table 1: Selective summary including porosity properties and H_2 adsorption performance data at 77 K of IRMOF-1 type materials presented in the literature over the last decade.

Year	S_{BET} [m^2/g]	$S_{Langmuir}$ [m^2/g]	V_{Total} [cm^3/g]	P_H [bar]	C_H [wt.%]	C_H /S_{BET} [wt.% m^{-2} g]	Reference
2005	572	1014	-	10	1.60	2.797×10^{-3}	[12]
2006	2296	3840	-	50	5.10	2.221×10^{-3}	[31]
2006	2885	-	1.18	1	1.15	0.398×10^{-3}	[32]
2006	3534	4171	-	45.4	4.95	1.400×10^{-3}	[33]
2007	3800	4400	-	40	7.10	1.868×10^{-3}	[30]
2008	2360	-	-	20	4.40	1.864×10^{-3}	[29]
2009	261	778	0.32	1	0.21	0.804×10^{-3}	[26]
2009	311	840	0.08	1	0.44	1.414×10^{-3}	[26]
2009	350	1157	0.08	1	0.50	1.428×10^{-3}	[26]
2009	481	590	0.19	17.4	2.63	5.467×10^{-3}	[27]
2009	501	606	0.19	17.4	3.20	6.387×10^{-3}	[27]
2009	840	1029	0.34	17.4	3.60	4.285×10^{-3}	[27]
2009	2449	3917	1.39	1-100	1.46-6.90	$0.596\text{-}2.817 \times 10^{-3}$	[28]
2010	725	954	0.40	1	1.54	2.124×10^{-3}	[25]
2010	756	990	0.35	1	1.82	2.407×10^{-3}	[25]
2010	797	1052	0.40	1	1.79	2.245×10^{-3}	[25]
2012	2800	-	1.13	1-40	1.30-5	$0.464\text{-}1.785 \times 10^{-3}$	[24]
2013	2750	3058	1.15	1	1.33	0.418×10^{-3}	[23]
2014	2024	2145	0.68	1	0.76	0.375×10^{-3}	[16]
2014	2540	2693	0.84	1	0.91	0.358×10^{-3}	[16]
2014	2858	3029	0.95	1	1.12	0.391×10^{-3}	[16]
2014	3210	3402	1.07	1	1.24	0.386×10^{-3}	[16]

S_{BET}: total specific area (SA) derived by the Brunauer-Emmet-Teller (BET) method, $S_{Langmuir}$: total SA derived by the Langmuir method, V_{Total}: total pore volume, P_H: applied pressure, C_H: H_2 gravimetric uptake, C_H/S_{BET}: ratio of H_2 gravimetric uptake to BET SA

In the current work, a nanoporous IRMOF-1 material was synthesized in powder-form by direct solvothermal reaction of $Zn(NO_3)_2$ and TPA in DMF solution at the temperature of 150 ^oC. To the best of our knowledge, the combination of the reaction parameters, mainly those of Zn^{2+}/TPA ratio and temperature, has not been previously reported in the literature. The as-synthesized IRMOF-1 material was subsequently studied for its morphology, surface chemistry and nanostructure using scanning electron microscopy (SEM), Fourier-transform infrared radiation spectroscopy (FT-IR) and X-ray diffraction

(XRD), respectively. Prior to the characterization of its porosity using nitrogen (N_2) gas adsorption and desorption measurements at liquid N_2 temperature (i.e. 77 K), the IRMOF-1 dispersion was dried and activated using a supercritical CO_2-flow method at 50 ^oC under 110 bar, followed by an outgassing procedure at 200 ^oC under 10^{-6} mbar. The facile synthesis method and consequent activation approach resulted in IRMOF-1 colloidal particles with a cubic-like shape in nm-scale (i.e. particle sizes around ~50 nm), a large BET SA and micropore volume (i.e. ~520 m^2/g and ~0.20 cm^3/g, respectively), as well as a significant (i.e. micropore SA of ~92.5 %) and narrow (i.e. pore sizes below 1.6 nm) microporosity. A primary evaluation of the H_2 storage performance was also carried out using low-pressure (0-1 bar) H_2 gas adsorption and desorption measurements at 77 K. The activated IRMOF-1 crystals demonstrated a fully reversible H_2 sorption behavior combined with an adequate H_2 uptake to BET SSA ratio at ~1 bar, which is superior to most of the IRMOF-1 materials described in the literature.

2. Materials and methods

2.1 IRMOF-1 synthesis

The IRMOF-1 material was prepared by direct solvothermal reaction of $Zn(NO_3)_2$ and TPA in the presence of DMF. In a typical synthesis procedure, 1.5 mmol of $Zn(NO_3)_2 \cdot 6H_2O$ dissolved in 10 ml DMF (used as it is without any further purification) was mixed with 2 mmol of TPA in DMF solution. The mixture was stirred for a couple of minutes, then transferred inside a polytetrafluoroethylene (PTFE)-lined stainless steel autoclave reactor and heated for 24 h at 150 ^oC. As soon as the autoclave was cooled down to room temperature, the product was collected, thoroughly washed with DMF, ethanol (C_2H_6O) and chloroform ($CHCl_3$) and finally dried at 50 ^oC. The obtained colorless crystals were stored in $CHCl_3$ solution to avoid any contamination from atmospheric species. No further treatment followed prior to the activation procedure.

2.2 Structural characterization methods

SEM images were collected by a FEI Inspect microscope equipped with a tungsten filament using an acceleration voltage of 25 kV. The studied sample was sputter-coated with gold in order to improve surface conductivity and avoid potential charging effects during imaging. The mean particle size was estimated through a statistical analysis of different high-magnification images, including Fig. 1b. Both low- and high-magnification SEM images

were analyzed via standard image processing algorithms for grayscale edge detection, blob segmentation and feature identification of the crystallite assemblies. The fractal dimension of their contours projecting 3-D surfaces was computed by box-counting methods [37]. The FT-IR spectrum was collected by a JASCO 4100 spectrometer in the mid-infrared region of 4400 and 400 cm^{-1} with a spatial resolution of 4 cm^{-1}. The studied sample was prepared in the form of potassium bromide (KBr) pellets using a minor quantity (< 1 mg), while the recorded spectrum was smoothed properly upon the completion of the measurements. The XRD pattern was recorded by a Siemens D500 diffractometer equipped with a secondary graphite monochromator and copper (Cu Kα) radiation (λ ~1.54 Å) and using acceleration voltage and applied current values of 40 kV and 35 mA, respectively. The measurements were performed in Bragg-Brentano geometry between the diffraction angles (2θ) of 5° and 25°, using a continuous scan speed mode, a 0.04° step width and a 0.6°/min scan speed.

2.3 Gas cryo-adsorption studies and activation procedure

Low-pressure (0-1 bar) N_2 and H_2 adsorption and desorption isothermal curves were recorded at 77 K by a Quantachrome Autosorb 1-MP volumetric gas sorption analyzer and ultra-pure N_2 (99.999 %) and H_2 (99.9999 %) gases were used. Prior to the gas cryo-adsorption measurements, the prepared MOF dispersion was dried following a supercritical CO_2 activation procedure with the aim to remove all solvents, including $CHCl_3$ and DMF. In detail, the $CHCl_3$ dispersion was transferred to a leak-tight high-pressure cell which was further fully-filled with $CHCl_3$. The cell was attached to a flowing supercritical CO_2 extractor unit and flushed for 1.5 h continuously with liquid CO_2 (1.5 ml/min) at room temperature. Consequently, the temperature of the extractor was raised to 50 °C so that CO_2 becomes supercritical. A back pressure regulator attached to the extractor maintained the pressure at around 110 bar. Under these conditions the sample was flushed with flowing supercritical CO_2 (1.5 ml/min) for 1.5 h. Finally, the CO_2 pressure was slowly released for 3 h to ambient pressure and then the dried MOF sample was transferred sealed to a glove box. From there, a sample of ~30 mg was transferred to a measuring cell, which was sealed using Quantachrome's cell-seal system and attached to the volumetric analyzer, and was further degassed for 6 h at 200 °C under high vacuum (10^{-6} mbar). The material before and after activation is denoted hereafter as as-synthesized and activated, respectively. The total SA was calculated from the N_2 adsorption data using the multi-point

BET and Langmuir methods in the lower relative pressure (P/P_0) range of 5×10^{-3} and 0.05, following the BET consistency criteria of the International Standard Organization (ISO 9277:2010) [38]. An approximate estimate of the micropore SA and PV values was extracted using the statistical thickness equation (t-plot) [39]. A qualitative pore size distribution (PSD) analysis was carried out in the adsorption branch of the isotherm using the Quenched Solid Density Functional Theory (QSDFT) kernel [40]. The H_2 uptake value was recorded as the volume of adsorbed H_2 gas, at standard temperature and pressure (STP) conditions, relative to the degassed mass of the sample (i.e. v_{gas}/m_{solid} in cm^3/g units), as well as expressed as the ratio between the adsorbed H_2 mass relative to the sum of the adsorbed H_2 mass and degassed sample mass (i.e. $m_{gas}/(m_{gas} + m_{solid})$ in wt.% units).

3. Results and discussion

3.1 Morphology, surface chemistry and structure

Fig. 1 presents SEM images of the as-synthesized IRMOF-1 material at two different magnifications, covering an order of magnitude in length from microns to nanometers. At lower magnifications (Fig. 1a), the powder seems to exhibit a well-ordered particle morphology. The geometric features of the main building block can be resolved at higher magnifications (Fig. 1b), which are described as cubic-like shape crystals, a characteristic three-dimensional structure for IRMOF-1 type materials [3,12]. A statistical measurement of 250 cubic particles from high-magnification SEM images, including the representative Fig. 1b, provided sizes ranging from ~10 up to ~110 nm with the mean particle size estimated at ~44 nm. A comparative analysis of the fractal (Hausdorff) dimension attributes (i.e. capacity, information, correlation and probability) [41,42] of the material's structure under low and high magnification is given in Table 2. The diminishing values of these self-similarity attributes with magnification indeed confirm the degree of structural ordering by powder crystallization.

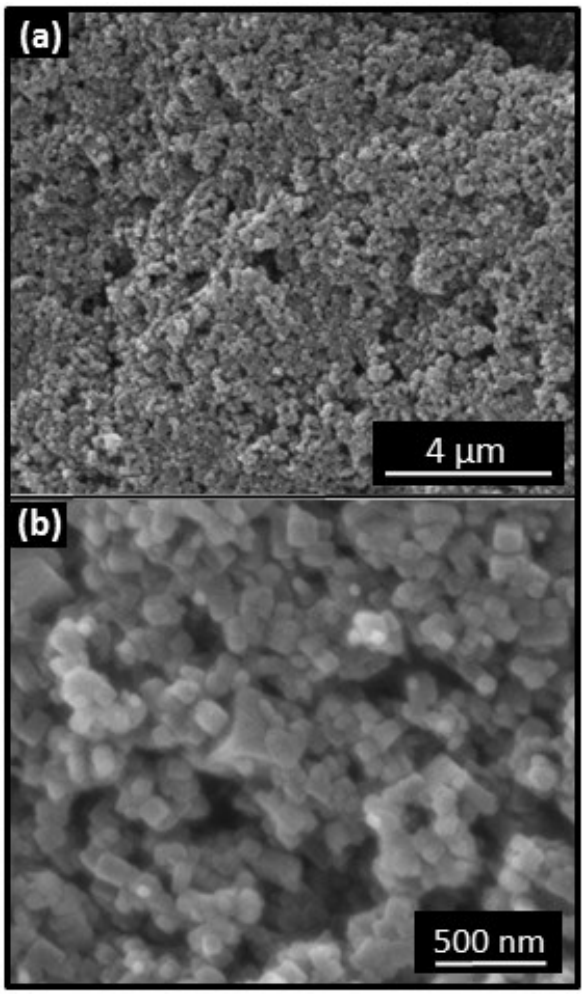

Fig. 1: SEM images of the as-synthesized IRMOF-1 material in (a) low- and (b) high-magnifications.

Table 2: Fractal (Hausdorff) dimension attributes of the crystalline IRMOF-1 powder derived from SEM images, including those shown in Fig. 1.

	Low resolution (Fig. 1a)	High resolution (Fig. 1b)	Ratio (High/Low)
Capacity	2.57	2.34	0.91
Information	2.51	2.25	0.90
Correlation	2.35	2.14	0.91
Probability	2.47	2.26	0.91

The smoothed FT-IR spectrum of the as-synthesized material in the mid-infrared region (Fig. 2) demonstrated characteristic phonon vibration modes of the IRMOF-1 structure that were similar to previously reported studies [13,18,20,43]. At first, the absorption band at ~523 cm^{-1} could be assigned to the Zn–O vibration of the tetrahedral coordinated Zn_4O cluster [20,43]. Next, several bands found between the wavenumbers of 600 and 1200 cm^{-}

^{1} are generally ascribed to the fingerprint region of terephthalate-based compounds. Specifically, the three larger bands at 657, 797 and 817 cm^{-1} and the three smaller ones at 1011, 1098 and 1145 cm^{-1} correspond to the out-of-plane and in-plane bending vibration modes of the C–H bond, respectively, which is present in the benzene (C_6H_6) ring of the 1,4-BDC linker [13,20,43]. Further bands arising in the wavenumber region of 1400 and 1700 cm^{-1} are usually related to the C–O bond of the carboxylic groups (–COOH) coordinated to Zn. Hence, the set of stronger and almost identical bands of the spectrum at ~1377 and ~1585 cm^{-1} represent the C–O symmetric and asymmetric stretching vibrations, respectively [18,20,43]. The broader band region around 3400 cm^{-1} is typically assigned to the O–H vibrations of the adsorbed atmospheric moisture/H_2O [13,18]. Finally, the less intense and sharp band at ~3605 cm^{-1} is probably related to the presence of DMF [13]. This is anticipated, as FTIR spectra were collected for the as-synthesized material.

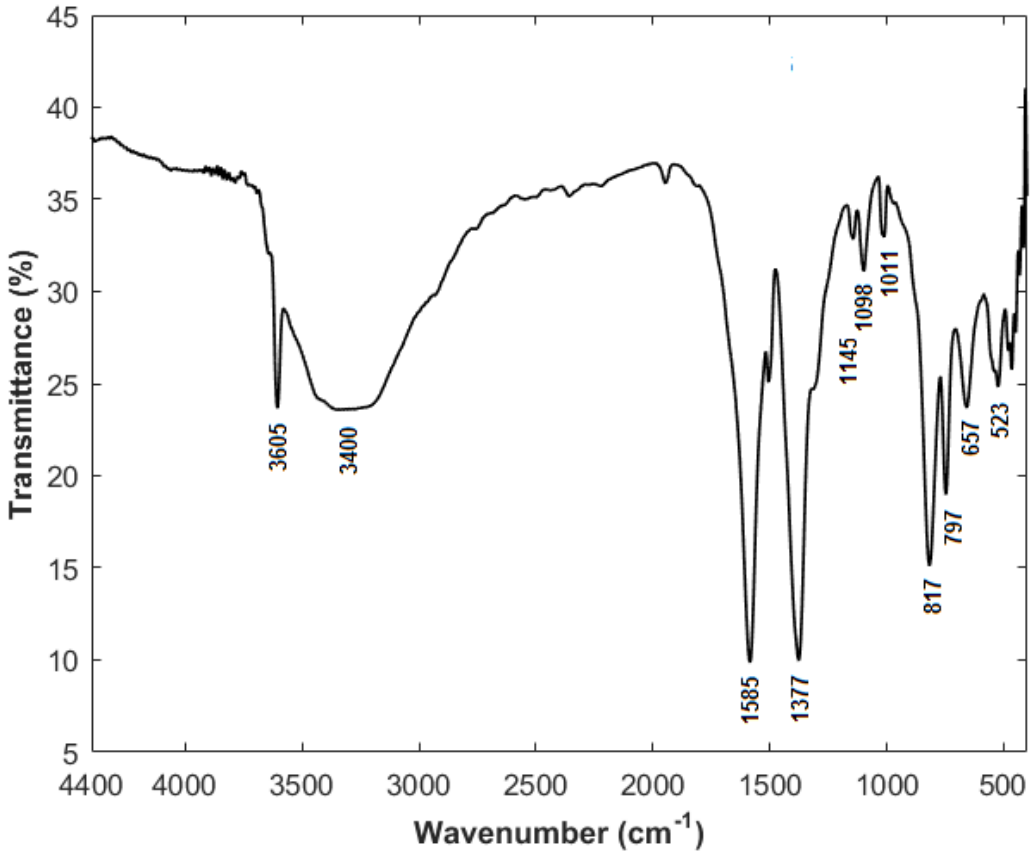

Fig. 2: FT-IR spectrum of the as-synthesized IRMOF-1 material in the mid-infrared region.

The X-ray diffractogram of the as-synthesized material, shown in Fig. 3, reveals an ordered crystalline structure in the 2θ range of 5° to 25°. The peak positions in specific diffraction

angles (i.e. 2θ ~6.8°, ~9.6°, ~13.6° and ~15.3°) show a good agreement with the characteristic structure of the IRMOF-1 material, as reported by Yaghi and co-authors [44]. However, the diffraction peak intensities reveal clear differences with emphasis on the first two and most intense peaks of the pattern; i.e. at 2θ ~6.8° and ~9.6°, representing the (100) and (110) crystallographic planes of the cubic structure with interlayer distances of 13.1 and 9.2 Å, based on Bragg's law, respectively. Specifically, the intensities of these two peaks seems to be inverted between each other. In this respect, Hafizovic et al. [45] and Huang et al. [13] studied XRD patterns of nanocrystalline IRMOF-1 materials and reported a strong shift in the relative intensities of the low-angle reflections. In a theoretical IRMOF-1 model with empty pores, the (220) reflection at 2θ ~9.6° exhibits the lowest intensity. Filling the pores with solvent molecules, such as DMF, increases the relative intensity of the reflection at ~9.6° from 15 % to 75 % [45]. Both research groups also found out that the intensity ratio of the peaks at 2θ ~9.6° to that of ~6.8° (referred as R1 value) can be used to predict the porosity of IRMOF-1materials; i.e. the lower the R1 value, the greater the porosity and consequently the SA. Low SA values are likely to suggest either lower crystallinity in the presence of impurities, such as entrapped Zn species or solvent molecules, or the presence of an interpenetrated structure (i.e. refers to the physical entanglement of two or more identical frameworks) [25,46]. Additionally, a high intensity ratio between the peaks at 2θ ~13.6° and ~6.8° (named as R2 value), referring to the (400) and (200) reflections, respectively, may also suggest an interpenetrated structure, especially when the R1 value is low. In this study, the R1 and R2 ratio values calculated from the XRD pattern of the as-synthesized material (Fig. 3) were ~2.27 and ~0.55, respectively. The standard R1 value of IRMOF-1 is around 0.20, while the R2 value is even lower [18]. Hence, the estimated R1 ratio of ~2.27 is far higher than the aforementioned standard value, which implies that the as-synthesized material should exhibit a relatively low SA compared to the ideal IRMOF-1 structure. As previously mentioned, this might be attributed to the existence of solvent molecules (i.e. $CHCl_3$ and DMF) or Zn species entrapped inside the IRMOF-1 framework upon the synthesis procedure and storage in $CHCl_3$ solution. In any case, it can be concluded that the purification (i.e. washing and drying) and storage (i.e. dispersion in $CHCl_3$) processes, followed upon synthesis, were not sufficient to remove DMF molecules still existing in the porous structure of the material. Therefore, the supercritical CO_2 activation procedure followed prior the N_2 and H_2 adsorption measurements was necessary for the definitive removal of any potential

solvents. Finally, the crystallite size was estimated in the range of 23-31 nm by applying Scherrer's formula on the (200), (220), (400) and (420) reflections. This suggests that the material probably consists of many smaller crystallites which are not clearly observable in the SEM images (i.e. below the measured mean size of ~44 nm). Thus, fractal attributes of a potentially self-similar crystalline structure (e.g. by molecular ordering and aggregation into a Menger sponge-like framework [47]) could not be compared with the microscale values of Table 2. The structural properties of the as-synthesized IRMOF-1 crystals derived by the analysis of the main XRD reflections are summarized in Table 3.

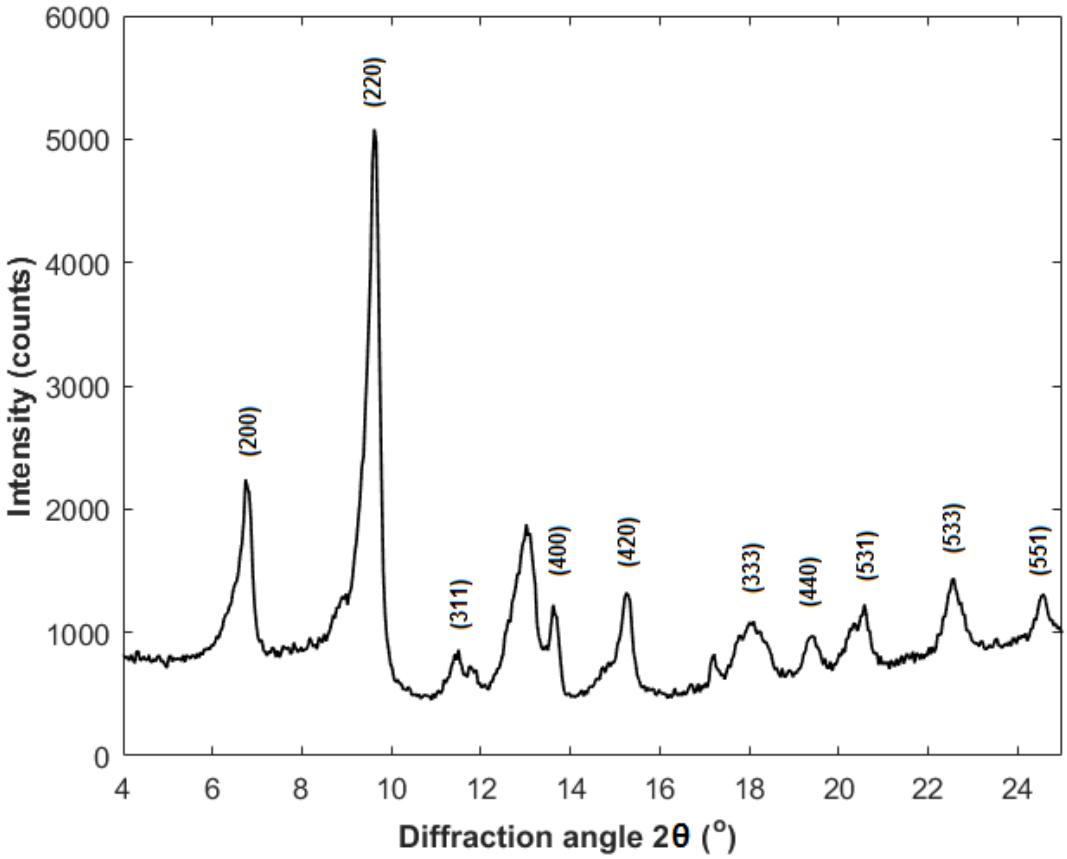

Fig. 3: X-ray diffractogram of the as-synthesized IRMOF-1 material.

Table 3: Structural properties of the as-synthesized IRMOF-1 crystals based on the XRD analysis.

Reflection [hkl]	Simulated 2θ [°]	Experimental 2θ [°]	d [nm]	A [counts]	FWHM [°]	D [nm]
200	6.80	6.74	1.313	2240	0.31	26
220	9.70	9.62	0.918	5081	0.34	24
400	13.80	13.62	0.649	1223	0.26	31
420	15.40	15.26	0.579	1321	0.35	23

Simulated 2θ: diffraction angles based on a theoretical IRMOF-1 model, Experimental 2θ: diffraction angles based on the recorded XRD pattern (Fig. 3), d: interlayer distance calculated by Bragg's law, A: intensity, FWHM: full-width at half maximum, D: crystallite size calculated by Scherrer's formula.

3.2 Porosity and gas adsorption behavior

Low-pressure N_2 adsorption and desorption isothermal curves at 77 K are shown in Fig. 4a. The activated IRMOF-1 material demonstrated features of type I and IV isotherms, as determined by the International Union of Pure and Applied Chemistry (IUPAC), which are usually associated with microporous (i.e. pore sizes below 2 nm) and mesoporous materials (i.e. pore sizes between 2 and 50 nm), respectively [48]. The physical adsorption initiated from high N_2 volumes (i.e. ~115 cm^3/g) for the lower P/P_0 value (i.e. 6×10^{-3}), as clearly observed in the inset of Fig. 4b, thus indicating the predominant microporous features of the studied sample. The relatively small hysteresis loop formed upon desorption (empty circle symbols) for P/P_0 values beyond ~0.85 reveals very limited mesoporosity presumably due to packing of the IRMOF-1 crystallites. This hysteresis behavior is usually attributed to capillary condensation of N_2 gas within the mesopores [39]. Finally, the adsorption isotherm did not reach a point of saturation (plateau) at the maximum P/P_0 point of ~0.99, but it extended without limit in an almost vertical direction, a trend that could be attributed to condensation in macropores (i.e. pore sizes above 50 nm) and/or multi-layer formation of N_2 onto the powder's external surface. Such larger pores may represent empty spaces between finely divided IRMOF-1 crystallites, as clearly observed in the SEM images (Fig. 1) and especially at high magnifications (Fig. 1b). Table 4 includes a summary of the porosity properties (i.e. SAs and PVs, respectively) of the activated IRMOF-1 material as determined by different mathematical and empirical methods applied on the recorded N_2 sorption data. The total SSA was estimated at ~520 and ~550 m^2/g based on the multipoint BET and Langmuir methods, respectively. A linear BET plot was extracted, as shown in Fig. 4b, by using five sorption points in the lower P/P0

range of 5×10^{-3} and 0.05 (i.e. micropore region) with a correlation coefficient (r) close to unity. Similar BET SAs for IRMOF-1 materials were also reported from Panella and Hirscher [12] and Li and co-authors [27]. The micropore SA was estimated by the t-plot method at ~480 m^2/g, thus representing a very significant fraction of the total BET SA (i.e. ~92.5 %). The remaining minor percentage (i.e. ~7.5 %) represents the sum of mesopore, macropore and external SA. In addition to the previous calculations, a rough qualitative analysis of the adsorption isotherm, based on the QSDFT kernel, revealed pores with sizes around 1.6 nm or less (see Fig. S1). This result provides an adequate explanation to the enhanced N_2 adsorption behavior in the lower P/P_0 region of 6×10^{-3} and 0.1, as shown in Fig. 4b. The micropore volume defined by the QSDFT method as the cumulative value for pore sizes below 2 nm agreed quite well with the one estimated by the t-plot method (i.e. 0.19 cm^3/g in both cases).

Table 4: Textural/porosity properties of the activated IRMOF-1 material based on the N_2 sorption data recorded at 77 K (Fig. 4a).

S_{BET} [m^2/g]	$S_{Langmuir}$ [m^2/g]	S_{Micro} [m^2/g]	S_{Ext} [m^2/g]	$S_{Micro(p)}$ [%]	$S_{Ext(p)}$ [%]	V_{Micro} [cm^3/g]	V_{QSDFT} [cm^3/g]
519.5	550.5	480.2	39.3	92.4	7.6	0.19	0.19

S_{BET}: total specific area (SA) derived by the multi-point Brunauer-Emmet-Teller (BET) method, $S_{Langmuir}$: total SA derived by the Langmuir method, S_{Micro}: micropore SA derived by the statistical thickness (t-plot) method, S_{Ext}: sum of mesopore, macropore and external SA given as the difference between BET SA and micropore SA (S_{BET}-S_{Micro}), $S_{Micro(p)}$: % percentage of micropore SA to BET SA, $S_{Ext(p)}$: % percentage of mesopore, macropore and external SA to BET SA, V_{Micro}: micropore volume derived by the t-plot method, V_{QSDFT}: Cumulative micropore volume for pores smaller than 2 nm derived by the Quenched Solid Density Functional Theory (QSDFT) method.

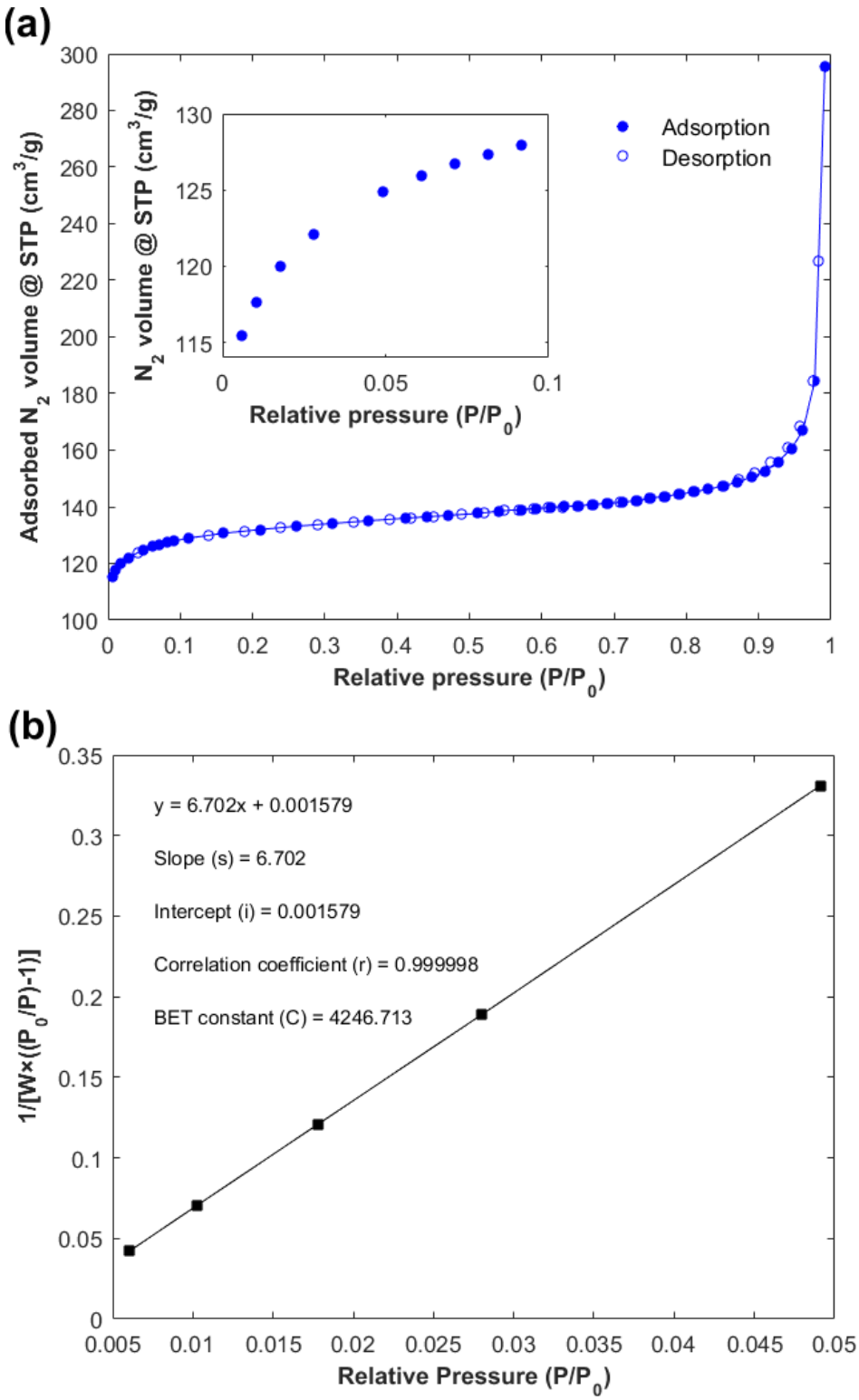

Fig. 4: (a) Low-pressure N_2 adsorption and desorption isothermal curves at 77 K of the activated IRMOF-1 material; the inset shows the increased volumes of adsorbed N_2 at the lower relative pressures ($P/P_0 < 0.1$) due to microporosity (pore sizes < 2 nm) and (b) linear multi-point BET plot with a correlation coefficient close to unity ($r \sim 1$).

Low-pressure (0-1 bar) H_2 cryo-adsorption and desorption isothermal curves at 77 K are shown in Fig. 5. The activated IRMOF-1 sample demonstrated a completely reversible type I isotherm, based on IUPAC's classification [48], as desorption of H_2 (empty circle symbols) followed the exact same path with its adsorption (colored circle symbols); i.e. no hysteresis loop was apparent between the two procedures. The H_2 uptake in gravimetric terms reached ~0.97 wt.% or ~109.3 cm^3/g at 77 K and ~1 bar, which could be considered a moderate value relative to high-surface area IRMOF-1 materials described in the literature [24,28,30,31,33]. In any case, this specific value is comparable to recently published results for other type of adsorbent materials under similar experimental conditions (i.e. 77 K and 1 bar), such as a solvothermally-derived magnesium- based formate [49] and plasma-derived few-layer graphene flakes [50] with BET SAs as high as ~496 and ~777m^2/ g, respectively. However, taking into consideration the estimated BET SA value of ~520 m^2/g, based on the N_2 sorption data, as well as the low-pressure regime up to ~1 bar, the IRMOF-1 sample exhibited an adequate ratio of H_2 uptake to BET SA of 1.874 × 10^{-3} wt.% m^{-2} g at 77 K and ~1 bar, which is superior to several other IRMOF-1 materials [16,23,24,26,28,32]. This increased ratio could be attributed to the significant and narrow microporosity, as estimated by the t-plot and QSDFT methods. As already mentioned, pores with sizes below 2 nm are considered highly energetic sites of enhanced H_2 adsorption due to the overlapping potential fields of the opposite pore walls [34]. This comes in good agreement with the enhanced adsorption behavior observed at the lower pressures (i.e. below 100 mbar), as clearly shown in the inset of Fig. 5. Specifically, the adsorbed H_2 volume at ~90 mbar was ~53.1 cm^3/g (or 0.47 wt.%), corresponding to the ~48 % of the overall H_2 uptake at ~1 bar. Hence, it would be safe to assume that the recorded H_2 uptake value at 77 K is attributed not only to the available BET SA of the IRMOF-1 material, but also on its increased values of microporosity (i.e. micropore SA and volume), as well as on its small and narrow pore sizes. Finally, the fact that the adsorption curve did not reach a plateau at ~1 bar implies that H_2 uptake could be further increased at higher pressures.

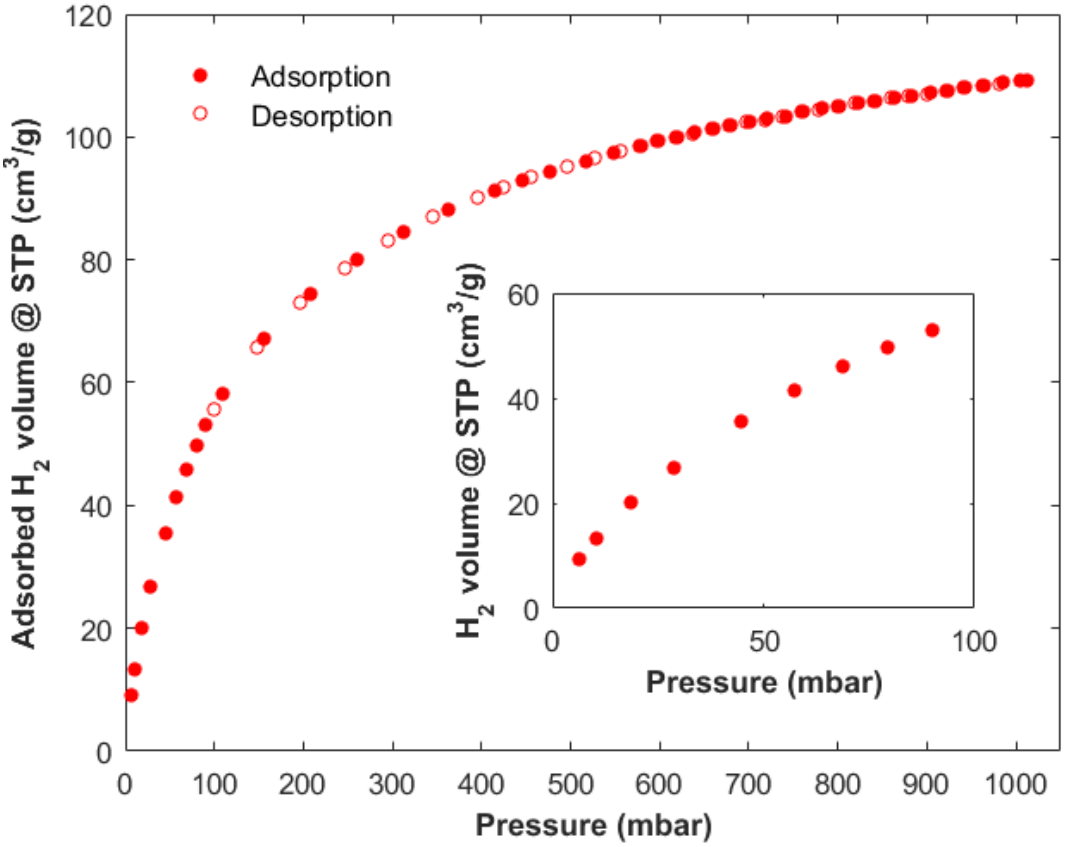

Fig. 5: Fully reversible low-pressure (0-1 bar) H_2 adsorption and desorption isothermal curves at 77 K of the activated IRMOF-1 material. The inset shows the enhanced H_2 adsorption at the lower pressures (P < 100 mbar) due to microporosity (pore sizes < 2 nm).

4. Conclusions

A rather simple and few-step solvothermal reaction method was adopted with the aim to produce a nanoporous IRMOF-1 type material. A mixture of $Zn(NO_3)_2$ and TPA dissolved in DMF solution was thermally treated at 150 ^oC for 24 h inside a PTFE autoclave reactor. The as-synthesized crystals were properly washed, dried and stored in $CHCl_3$ solution to avoid any contamination. A series of advanced materials characterization methods were used to investigate nanoparticle morphology, chemical bonding, crystalline structure and porosity. SEM images revealed a continuous network of cubic-like shape particles with a mean size around 50 nm. FT-IR analysis indicated the characteristic vibration modes of the Zn–O, C–H and C–O bonds related to the IRMOF-1 framework around 523, 600 to 1200 and 1400 to 1700 cm^{-1}. XRD patterns presented the characteristic (200) and (220) reflections of the cubic IRMOF-1 structure at the diffraction angles of ~6.8^o and ~9.6^o, corresponding to interlayer distances of 13.1 and 9.2 Å, respectively. The crystallite size was estimated

around 25 nm by applying Scherrer's formula on the XRD data. Prior the low-pressure (0-1 bar) N_2 and H_2 adsorption and desorption measurements, the IRMOF-1 crystals were further dried and activated by supercritical CO_2-flow under high-pressures (i.e. 1.5 ml/min for 1.5 h under 110 bar) and constant heating under high vacuum (i.e. at 200 ^oC for 6 h under 10^{-6} mbar) to remove any residual solvents from its porous structure, including $CHCl_3$ and DMF. The N_2 sorption data provided BET SA and micropore volume values of ~520 m^2/g and ~0.2 cm^3/g, respectively, a predominant micropore SA of ~480 m^2/g (i.e. ~92.5 % fraction of the total) and micropore sizes below 1.6 nm. Fully reversible H_2 sorption isotherms were recorded at 77 K without showing a point of saturation up to ~1 bar. The H_2 uptake, expressed in gravimetric terms, reached up to ~1 wt.% at 77 K and ~1 bar. Future work will be focused on optimizing the synthesis procedure of the presented IRMOF-1 material with the aim to increase even further the available BET SA value and maintain the significant micropore features towards the overall improvement of its H_2 adsorption performance at 77 K.

Acknowledgments

The current work was partially supported by the EC FP7- INFRASTRUCTURES project H2FC (GA No. 284522) and by Khalifa University Internal Research Fund – L1 (210108). N.K. would like to thank Dr. Vladislav Ryzhkov from Fibrtec Inc. (Atlanta, US) for his helpful discussions on the interpretation of the SEM and XRD data.

References

[1] Ren J, Musyoka NM, Langmi HW, Mathe M, Liao S. Current research trends and perspectives on materials-based hydrogen storage solutions: a critical review. Int J Hydrogen Energy 2017;42(1):289-311.

[2] Callini E, Aguey-Zinsou KF, Ahuja R, Ares JR, Bals S, Biliškov N, et al. Nanostructured materials for solid-state hydrogen storage: a review of the achievement of COST Action MP1103. Int J Hydrogen Energy 2016;41(32):14404-28.

[3] Furukawa H, Cordova KE, O'Keeffe M, Yaghi OM. The chemistry and applications of metal-organic frameworks. Science 2013;341(6149):1230444.

[4] Suh MP, Park HJ, Prasad TK, Lim DW. Hydrogen storage in metal-organic frameworks. Chem Rev 2011;112(2):782-835.

[5] Lee J, Farha OK, Roberts J, Scheidt KA, Nguyen ST, Hupp JT. Metal-organic framework materials as catalysts. Chem Soc Rev 2009;38(5):1450-9.

[6] Achmann S, Hagen G, Kita J, Malkowsky IM, Kiener C, Moos R. Metal-organic frameworks for sensing applications in the gas phase. Sensors 2009;9(3):1574-89.

[7] Langmi HW, Ren J, North B, Mathe M, Bessarabov D. Hydrogen storage in metal-organic frameworks: a review. Electrochim Acta 2014;128:368-92.

[8] Peng Y, Krungleviciute V, Eryazici I, Hupp JT, Farha OK, Yildirim T. Methane storage in metal-organic frameworks: current records, surprise findings, and challenges. J Am Chem Soc 2013;135(32):11887-94.

[9] Hong DH, Suh MP. Enhancing CO_2 separation ability of a metal-organic framework by post-synthetic ligand exchange with flexible aliphatic carboxylates. Chem Eur J 2014;20(2):426-34.

[10] Sumida K, Rogow DL, Mason JA, McDonald TM, Bloch ED, Herm ZR, et al. Carbon dioxide capture in metal-organic frameworks. Chem Rev 2011;112(2):724-81.

[11] Zhao Z, Ma X, Kasik A, Li Z, Lin YS. Gas separation properties of metal organic framework (MOF-5) membranes. Ind Eng Chem Res 2012;52(3):1102-8.

[12] Panella B, Hirscher M. Hydrogen physisorption in metalorganic porous crystals. Adv Mater 2005;17(5):538-41.

[13] Huang L, Wang H, Chen J, Wang Z, Sun J, Zhao D, et al. Synthesis, morphology control, and properties of porous metal-organic coordination polymers. Microporous Mesoporous Mater 2003;58(2):105-14.

[14] Ren J, Langmi HW, North BC, Mathe M. Review on processing of metal-organic framework (MOF) materials towards system integration for hydrogen storage. Int J Energy Res 2015;39(5):607-20.

[15] Lai Q, Paskevicius M, Sheppard DA, Buckley CE, Thornton AW, Hill MR, et al. Hydrogen storage materials for mobile and stationary applications: current state of the art. ChemSusChem 2015;8(17):2789-825.

[16] Zhao H, Song H, Chou L. Facile synthesis of MOF-5 structure with large surface area in the presence of benzoyl peroxide by room temperature synthesis. Mater Chem Phys 2014;143(3):1005-11.

[17] Tranchemontagne DJ, Hunt JR, Yaghi OM. Room temperature synthesis of metal-organic frameworks: MOF-5, MOF-74, MOF-177, MOF-199, and IRMOF-0. Tetrahedron 2008;64(36):8553-7.

[18] Wu ZP, Wang MX, Zhou LJ, Yin ZL, Jin TAN, Zhang JL, et al. Framework-solvent interactional mechanism and effect of NMP/DMF on solvothermal synthesis of $[Zn_4O(BDC)_3]_8$. Trans Nonferrous Met Soc China 2014;24(11):3722-31.

[19] Nguyen NPT, Nguyen TTN, Le TTT, Nguyen QC, Ton TQ, Nguyen TH, et al. Synthesis and characterization of zinc-organic frameworks with 1,4-benzenedicarboxylic acid and azobenzene-4,4'-dicarboxylic acid. Adv Nat Sci Nanosci Nanotechnol 2011;2(2):02500.

[20] Sabouni R, Kazemian H, Rohani S. A novel combined manufacturing technique for rapid production of IRMOF-1 using ultrasound and microwave energies. Chem Eng J 2010;165(3):966-73.

[21] Son WJ, Kim J, Kim J, Ahn WS. Sonochemical synthesis of MOF-5. Chem Commun 2008;47:6336-8.

[22] Choi JY, Kim J, Jhung SH, Kim H, Chang J, Chae HK. Microwave synthesis of a porous metal-organic framework, zinc terephthalate MOF-5. Bull Korean Chem Soc 2006;27(10):1523-4.

[23] Yang J, Grzech A, Mulder FM, Dingemans TJ. The hydrogen storage capacity of mono-substituted MOF-5 derivatives: an experimental and computational approach. Microporous Mesoporous Mater 2013;171:65-71.

[24] Marco-Lozar JP, Juan-Juan J, Suarez-Garcia F, Cazorla- Amoros D, Linares-Solano A. MOF-5 and activated carbons as adsorbents for gas storage. Int J Hydrogen Energy 2012;37(3):2370-81.

[25] Chen B, Wang X, Zhang Q, Xi X, Cai J, Qi H, et al. Synthesis and characterization of the interpenetrated MOF-5. J Mater Chem 2010;20(18):3758-67.

[26] Saha D, Deng S, Yang Z. Hydrogen adsorption on metal-organic framework (MOF-5) synthesized by DMF approach. J Porous Mater 2009;16(2):141-9.

[27] Li J, Cheng S, Zhao Q, Long P, Dong J. Synthesis and hydrogen-storage behavior of metal-organic framework MOF-5. Int J Hydrogen Energy 2009;34(3):1377-82.

[28] Saha D, Wei Z, Deng S. Hydrogen adsorption equilibrium and kinetics in metal-organic framework (MOF-5) synthesized with DEF approach. Separ Pur Tech 2009;64(3):280-7.

[29] Schmitz B, Muller U, Trukhan N, Schubert M, Férey G, Hirscher M. Heat of adsorption for hydrogen in microporous high-surface-area materials. ChemPhysChem 2008;9(15):2181-4.

[30] Kaye SS, Dailly A, Yaghi OM, Long JR. Impact of preparation and handling on the hydrogen storage properties of Zn_4O (1,4-benzenedicarboxylate)$_3$ (MOF-5). J Am Chem Soc 2007;129(46):14176-7.

[31] Panella B, Hirscher M, Putter H, Muller U. Hydrogen adsorption in metal-organic frameworks: Cu-MOFs and Zn- MOFs compared. Adv Funct Mater 2006;16(4):520-4.

[32] Dailly A, Vajo JJ, Ahn CC. Saturation of hydrogen sorption in Zn benzenedicarboxylate and Zn naphthalenedicarboxylate. J Phys Chem B 2006;110(3):1099-101.

[33] Wong-Foy AG, Matzger AJ, Yaghi OM. Exceptional H_2 saturation uptake in microporous metal-organic frameworks. J Am Chem Soc 2006;128(11):3494-5.

[34] Dubinin M. The potential theory of adsorption of gases and vapors for adsorbents with energetically nonuniform surfaces. Chem Rev 1960;60(2):235-41.

[35] Ren J, Musyoka NM, Langmi HW, Swartbooi A, North BC, Mathe M. A more efficient way to shape metal-organic framework (MOF) powder materials for hydrogen storage applications. Int J Hydrogen Energy 2015;40(13):4617-22.

[36] Purewal JJ, Liu D, Yang J, Sudik A, Siegel DJ, Maurer S, et al. Increased volumetric hydrogen uptake of MOF-5 by powder densification. Int J Hydrogen Energy 2012;37(3):2723-7.

[37] Falconer K. Fractal geometry: mathematical foundations and applications. John Wiley & Sons; 1990. p. 38-47.

[38] International Standard Organization. Determination of the specific surface area of solids by gas adsorption d BET method, ISO 9277:2010(E). 2nd ed. 2010.

[39] Rouquerol J, Rouquerol F, Llewellyn P, Maurin G, Sing KS. Adsorption by powders and porous solids: principles, methodology and applications. Academic Press; 2014.

[40] Landers J, Gor GY, Neimark AV. Density functional theory methods for characterization of porous materials. Colloids Surfaces A Physicochem Eng Aspects 2013;437:3-32.

[41] Hausdorff F. Dimension und äußeres Maß. Math Ann 1918;79(1-2):157-79.

[42] Reuter M, Franz P, Wolter E. Fraktaldimension von Grauwertbildern, Studienarbeit. Universitat Hannover; 1999.

[43] Hermes S, Schroder F, Amirjalayer S, Schmid R, Fischer RA. Loading of porous metal-organic open frameworks with organometallic CVD precursors: inclusion compounds of the type $[L_nM]_a$@MOF-5. J Mater Chem 2006;16(25):2464-72.

[44] Eddaoudi M, Kim J, Rosi N, Vodak D, Wachter J, O'Keeffe M, et al. Systematic design of pore size and functionality in isoreticular MOFs and their application in methane storage. Science 2002;295(5554):469-72.

[45] Hafizovic J, Bjørgen M, Olsbye U, Dietzel PDC, Bordiga S, Prestipino C, et al. The inconsistency in adsorption properties and powder XRD data of MOF-5 is rationalized by framework interpenetration and the presence of organic and inorganic species in the nanocavities. J Am Chem Soc 2007;129(12):3612-20.

[46] Kim H, Das S, Kim MG, Dybtsev DN, Kim Y, Kim K. Synthesis of phase-pure interpenetrated MOF-5 and its gas sorption properties. Inorg Chem 2011;50(8):3691-6.

[47] Menger K. Allgemeine Räume und Cartesische Räume. I. communications to the Amsterdam Academy of Sciences (1926); English translation reprinted in: Edgar GA. Classics on fractals, studies in nonlinearity. Boulder, CO: Westview Press. Advanced Book Program; 2004.

[48] Thommes M, Kaneko K, Neimark AV, Olivier JP, Rodriguez-Reinoso F, Rouquerol J, et al. Physisorption of gases, with special reference to the evaluation of surface area and pore size distribution (IUPAC Technical Report). Pure Appl Chem 2015;87(9-10):1051-69.

[49] Spanopoulos I, Bratsos I, Tampaxis C, Kourtellaris A, Tasiopoulos A, Charalambopoulou G, et al. Enhanced gas-sorption properties of a high surface area, ultramicroporous magnesium formate. Cryst Eng Comm 2015;17(3):532-9.

[50] Kostoglou N, Tarat A, Walters I, Ryzhkov V, Tampaxis C, Charalambopoulou G, et al. Few-layer graphene-like flakes derived by plasma treatment: a potential material for hydrogen adsorption and storage. Microporous Mesoporous Mater 2016;225:482-7.

Supplementary material

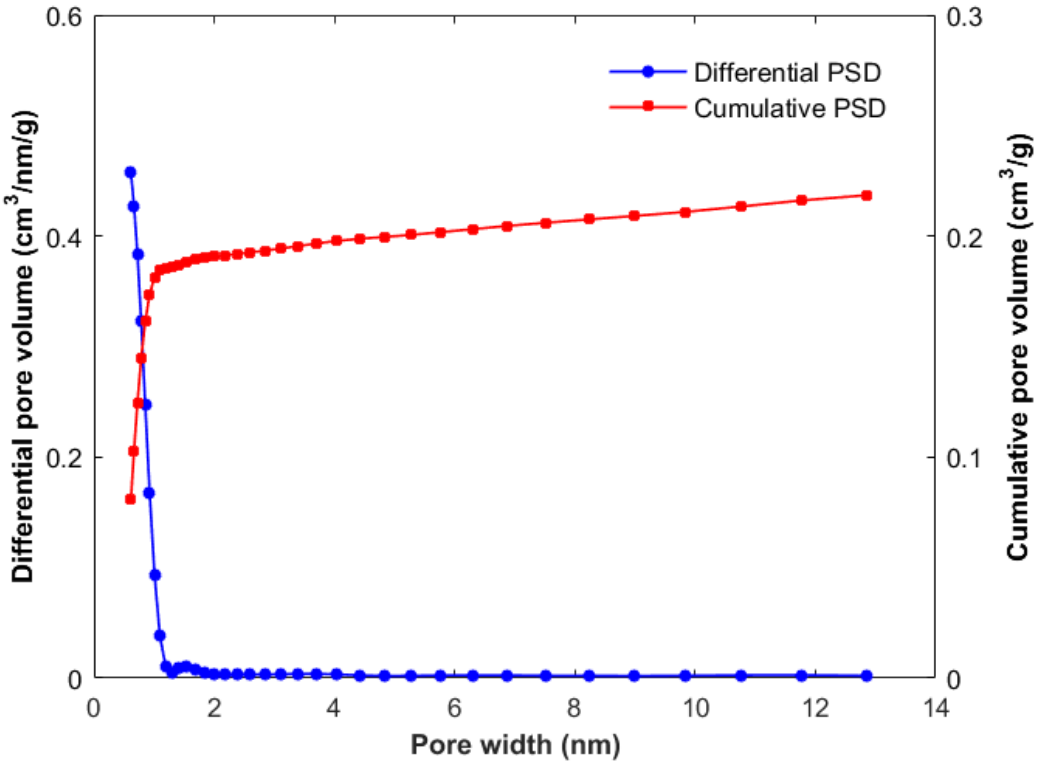

Fig. S1: Differential and cumulative pore size distribution analysis of the activated IRMOF-1 material using the Quenched Solid Density Functional Theory (QSDFT) method in the N_2 adsorption data.

.